Phase field and Cosserat simulation of recrystallization in polycrystals

Flavien Ghiglione

PSL
UNIVERSITÉ PARIS

THÈSE DE DOCTORAT
DE L'UNIVERSITÉ PSL

Préparée à MINES Paris

Modélisation de la recristallisation dans les polycristaux par un modèle couplé champ de phase et milieu de Cosserat

Phase field and Cosserat simulation of recrystallization in polycrystals

Soutenue par
Flavien GHIGLIONE
Le 8 Décembre 2023

École doctorale n°621
Ingénierie des Systèmes, Matériaux, Mécanique, Energétique

Spécialité
Mécanique

Composition du jury :

Jean SULEM Ecole des Ponts	*Président*
Håkan HALLBERG Lund University	*Rapporteur*
Vincent TAUPIN Université de Lorraine CNRS	*Rapporteur*
Anna ASK Onera DMAS	*Examinateur*
Fabrice BARBE INSA Rouen	*Examinateur*
Patrizia TROVALUSCI Sapienza Università di Roma	*Examinateur*
Benoît APPOLAIRE Université de Lorraine	*Directeur de thèse*
Samuel FOREST Mines Paris CNRS	*Directeur de thèse*

MINES PARIS | PSL

Remerciements

I want to express my sincere gratitude to the members of the jury for taking the time to examine my work. I am truly grateful for the invaluable feedback provided by the reviewers, Professor Håkan Hallberg and Doctor Vincent Taupin, on my manuscript. I would also like to extend my thanks to the examiners, Professors Patrizia Trovalusci, Jean Sulem and Fabrice Barbe, for their meticulous assessment of my work.

I want to express my sincere gratitude to my supervisors Samuel Forest, Benoit Appolaire, Anna Ask, and Kais Ammar for their invaluable contributions to this work. I am especially grateful to Kais for his assistance with the software Zset implementation and debugging, and to Anna for her kindness, sympathy and guidance on the KWC and coupled models. Your explanations have greatly enhanced my understanding of these complex topics. Benoit, thank you for taking the time to help me understand the physics of the phase-field models and perform the stability analysis, even with your busy schedule. I also really liked your sense of humor and funny jokes! Samuel, I wanted to express my heartfelt gratitude for your unwavering guidance and support over the past three years. You are truly an exceptional scientist and an amazing human being. It has been a pleasure and an honor working with you all and I hope I will have the opportunity to collaborate with you again in the future.

I would also like to thank my friends at Centre des Matériaux and from the association YouRPSL for their moral support and the good times we shared together. Special thanks go to Lili, Baptiste, Wajih, Manon, Daniel I., Rawad, Aubin, Jean-Michel and Mathias, as well as Daniel W., Nicolas, Alok and Manu.

Je souhaiterais également remercier mes amis d'enfance Clément, Younès et Antoine pour avoir été mes côtés durant plus de dix ans. J'adresse aussi un grand merci à Orane pour m'avoir accompagné et soutenu pendant presque quatre ans.

Enfin, je souhaiterais remercier du fond du cœur toute ma famille–sans qui rien n'aurait été possible–pour leur soutien et leurs encouragements indéfectibles. J'ai également une pensée émue pour mon arrière grand-mère Marie-Rose et mon oncle Gilles malheureusement décédés pendant ces années de doctorat. A toutes et tous, je leur adresse ma reconnaissance et mon amour.

Abstract

Thermomechanical treatment of crystalline materials induces significant microstructural changes that must be understood in order to control the resulting macroscopic properties. In particular, recrystallization, i.e. the nucleation and growth of grains with low dislocation density, is of industrial interest for microstructure optimization during metal forming. Despite its importance, the modelling of this phenomenon remains fragmentary. While numerous models have been developed to efficiently simulate the growth phase (Monte-Carlo Potts, cellular automata, level sets, phase-fields, etc.), the simulation of nucleation traditionally involves the ad hoc introduction of new spherical or circular grains linked to a critical value of strain, stress or dislocation density. It is therefore necessary to develop models that spontaneously account for the appearance of new grains. During thermomechanical processes, the (visco)plastic deformation of the material can lead to a significant reorientation of the crystal lattice and a heterogeneous distribution of orientations can appear within grains that are initially homogeneously oriented. At the mesoscopic scale, these phenomena are well accounted for by models of crystal plasticity. An enriched description of matter, such as that of Cosserat continua, also allows size effects to be taken into account. In this theory, additional degrees of freedom are introduced in the form of microrotations, which can be identified with the rotations of the crystal lattice by means of internal constraints. We propose new analytical solutions to the problems of torsion of an isotropic elastic-plastic cylinder and shear of a single crystal. For the latter, different formulations of the free energy potential exploring various dependencies on the curvature-torsion tensor are studied. Among the available grain growth models, only the two-phase-field approach proposed by Kobayashi-Warren-Carter (KWC) can model an intragranular orientation gradient induced by deformation. Since phase-field models are based on a thermodynamic formulation, coupling to mechanics via the free energy potential is particularly straightforward. The full-field mesoscopic model used in this work, developed by Ask et al., thus combines Cosserat crystal plasticity and the KWC phase-field model of grain growth. One of the features of the model studied is the inclusion of inelastic relaxation behaviour at the grain boundary in addition to the (visco)plastic deformation of the grain. Therefore, the choice of the relaxation function on the formation and movement of grain boundaries is investigated. In particular, the existence of a threshold stress in the relaxation function is shown to potentially hinder the formation and movement of grain boundaries. We also show through finite element simulations that KWC-type models can spontaneously simulate the nucleation of new (sub)grains due to the presence of crystal orientation gradients. A three-dimensional torsional calculation of a single-crystal copper rod with a circular cross section of axis [111] shows the nucleation of subgrains along the rod due to lattice orientation gradients induced by mechanical loading. This observation is qualitatively confirmed by comparison with experimental results on the torsion of an aluminium single crystal obtained by M.E. Kassner.

Keywords

Crystal plasticity, Phase field, Cosserat mechanics, Grain boundary migration, Recrystallization, Finite element method

Résumé

Les traitements thermomécaniques des matériaux cristallins provoquent d'importants changements microstructuraux qu'il convient de maitriser pour contrôler les propriétés macroscopiques qui en résultent. En particulier, la recristallisation, i.e la germination et croissance de grains possédant une faible densité de dislocations, est d'intérêt industriel pour l'optimisation de microstructures lors la mise en forme des métaux. Malgré son importance, la modélisation de ce phénomène reste parcellaire. En effet, si de nombreux modèles ont été développés afin de reproduire efficacement la phase de croissance (méthodes de Monte-Carlo Potts, automates cellulaires, level-sets, champs de phase...), la simulation de la germination passe traditionnellement par l'introduction ad hoc de nouveaux grains sphériques ou circulaires en lien avec une valeur critique de déformation, contrainte ou densité de dislocations. Il convient donc de développer des modèles rendant compte spontanément de l'apparition de nouveaux grains. Lors des procédés thermomécaniques, la déformation (visco)plastique du matériau peut engendrer une réorientation importante du réseau cristallin et une distribution hétérogène d'orientations peut apparaître au sein de grains initialement orientés de façon homogène. À l'échelle mésoscopique, ces phénomènes sont bien pris en compte par des modèles de plasticité cristalline. Une description enrichie de la matière, telle que celle des milieux de Cosserat, permet en outre de prendre en compte des effets de taille. Dans cette théorie, des degrés de liberté additionnels de microrotations sont introduits et peuvent être identifiés aux rotations du réseau cristallins par le biais de contraintes internes. Nous proposons de nouvelles solutions analytiques aux problèmes de la torsion d'un cylindre en elastoplasticité isotrope et du cisaillement d'un monocristal. Pour ce dernier, différentes formulations du potentiel d'énergie libre explorant diverses dépendances vis-à-vis du tenseur de courbure-torsion sont étudiées. Parmi les modèles de croissance de grains, seule l'approche à deux champs de phases proposée par Kobayashi-Warren-Carter (KWC) peut modéliser un gradient d'orientation intragranulaire induit par la déformation. Les modèles à champs de phase s'appuyant sur une formulation thermodynamique, le couplage avec la mécanique via le potentiel d'énergie libre est particulièrement aisé. Le modèle mésoscopique en champs complets utilisé dans cette thèse, développé par Ask et al., combine ainsi la plasticité cristalline des milieux de Cosserat et le modèle à champs de phase de croissance de grains de KWC. Une des particularités du modèle étudié est d'ajouter à la déformation (visco)plastique du grain un comportement inélastique de relaxation du joint de grain. L'influence du choix de la fonction de relaxation aux joints de grain sur la formation et le mouvement de ceux-ci est ainsi étudiée. En particulier, il est montré que la présence d'une contrainte seuil dans la fonction de relaxation peut ralentir la formation et le mouvement des joints. Nous montrons également par des simulations éléments finis que les modèles de type KWC peuvent simuler de façon spontanée de la germination de nouveaux (sous)grains en raison de la présence de gradients d'orientation cristalline. Un calcul tridimensionnel de torsion d'une barre monocristalline de cuivre à section circulaire d'axe [111] montre ainsi la formation de sous-grains le long de la barre en raison du développement d'un gradient d'orientation du réseau dû au chargement. Cette observation est confortée qualitativement par une comparaison aux résultats expérimentaux sur la torsion d'un monocristal d'aluminium obtenus par M.E. Kassner.

Mots clés

Plasticité cristalline, Champs de phase, Mécanique des milieux de Cosserat, Migration de joint de grains, Recristallisation, éléments finis

Contents

Nomenclature

Abbreviations

1D	one dimensional
2D	two dimensional
3D	three dimensional
BC	boundary conditions
CPFE	crystal plasticity finit element
CSL	coincident site lattice
FCC	face centered cubic
FE	finite element
FEA	finite element analysis
FEM	finite element method
GB	grain boundary
GND	geometrically necessary dislocations
HAGB	high angle grain boundary
IC	initial conditions
KWC	Kobayashi-Warren-Carter
LAGB	low angle grain boundary
MPF	multi phase field
SIBM	strain-induced boundary migration
SSD	statistically stored dislcations

Notations

a	scalar
$\underline{a} = a_i \underline{e}_i$	vector
$\underset{\sim}{A} = A_{ij} \underline{e}_i \otimes \underline{e}_j$	second order tensor
$\underline{\underline{A}} = A_{ijk} \underline{e}_i \otimes \underline{e}_j \otimes \underline{e}_k$	third order tensor
$\underline{\underline{\underline{A}}} = A_{ijkl} \underline{e}_i \otimes \underline{e}_j \otimes \underline{e}_k \otimes \underline{e}_l$	fourth order tensor
$\underset{\sim}{A}^T = A_{ji} \underline{e}_i \otimes \underline{e}_j$	transpose of a second order tensor
$\mathrm{Tr}\left(\underset{\sim}{A}\right) = A_{ii}$	trace of a second order tensor
$\underset{\sim}{A}' = \underset{\sim}{A} - \mathrm{Tr}\left(\underset{\sim}{A}\right)/3$	deviatoric part of a second order tensor
$\underset{\sim}{I} = \delta_{ij} \underline{e}_i \otimes \underline{e}_j$	second order identity tensor
$\underline{\underline{\underline{I}}} = \delta_{ik}\delta_{jl} \underline{e}_i \otimes \underline{e}_j \otimes \underline{e}_k \otimes \underline{e}_l$	fourth order identity tensor
$\underline{a} \cdot \underline{b} = a_i b_i$	scalar product
$\underset{\sim}{A} \cdot \underset{\sim}{B} = A_{ik} B_{kj} \underline{e}_i \otimes \underline{e}_j$	simple contraction
$\underset{\sim}{A} : \underset{\sim}{B} = A_{ij} B_{ij}$	double contraction
$\underline{a} \otimes \underline{b} = a_i b_j$	dyadic product
$\mathrm{sym}(\underset{\sim}{A}) = A^{\mathrm{sym}} = \frac{1}{2}\left(\underset{\sim}{A} + \underset{\sim}{A}^T\right)$	symmetric part of a second order tensor
$\mathrm{skew}(\underset{\sim}{A}) = A^{\mathrm{skew}} = \frac{1}{2}\left(\underset{\sim}{A} - \underset{\sim}{A}^T\right)$	skew-symmetric part of a second order tensor
$\underline{\underline{\underline{\epsilon}}}$	third order Levi-Civita tensor
$\overset{\times}{\underline{A}} = -\frac{1}{2}\underline{\underline{\underline{\epsilon}}} : \underset{\sim}{A}^{\mathrm{skew}}, \quad \underset{\sim}{A}^{\mathrm{skew}} = -\underline{\underline{\underline{\epsilon}}} \cdot \overset{\times}{\underline{A}}$	axial pseudo-vector

Introduction

Résumé en français

A l'échelle mésoscopique, la microstructure des métaux subit d'importants changements lors des opérations de mise en forme. Ces évolutions ont un impact direct sur les propriétés macroscopiques du matériau. Dès lors, l'intérêt industriel et scientifique de la compréhension et la maîtrise de ces évolutions microstructurales est clair. Un phénomène de restauration appelé recristallisation peut se produire au cours de la mise en forme à chaud ou après déformation à froid suivie d'un recuit. Ce phénomène peut grossièrement être décrit comme la germination et croissance de nouveaux grains. Dans la compréhension actuelle de la germination, les grains sont déjà présents dans l'état déformé et sont localisés, notamment, aux hétérogénéités de déformation.

Du point de vue de la modélisation, cela nécessite une description prenant en compte les inhomogénéités locales de déformation, telles que les théories continues de la plasticité cristalline. En particulier, les modèles de plasticité cristalline des milieux généralisés, tels que la théorie de Cosserat, présentent un certain attrait. Ils permettent en effet de palier à certaine limitations du milieu continu de Cauchy par l'introduction de longueurs internes, ce qui permet de rendre compte des effets de taille par exemple.
Ces modèles de plasticité cristalline sont classiquement couplés à des modèles de croissance de grains pour simuler la recristallisation. On observe notamment un certain engouement pour les méthodes à champs de phase, qui se basent sur une description continue des interfaces (ici les joints de grains). Ces modèles ont pour avantage d'être formulé dans un cadre thermodynamique, ce qui permet des couplages multiphysiques relativement simples *via* l'énergie libre. Le modèle à deux champs de Kobayashi-Warren-Carter (KWC) [Kobayashi et al., 2000] est le seul permettant de prendre en compte des gradients d'orientation intragranulaires susceptibles de mener à la germination au sein des grains.

Malgré son importance, la germination reste actuellement un point bloquant majeur dans la simulation de la recristallisation. En effet, dans l'immense majorité des cas, des germes circulaires ou sphériques sont introduits dans la microstructure en se basant sur des critères de densité de dislocation, déformation ou contrainte critique. En conséquence, l'objectif principal de cette thèse est de modéliser, à l'échelle mésoscopique et en champs complets, les évolutions microstructurales des métaux en prenant en compte de façon "spontanée" la germination. Pour ce faire, le modèles KWC et KWC-Cosserat Ask et al. [2018b] sont utilisés pour étudier la germination en lien avec une localisation hétérogène de la courbure du réseau cristallin. Nous nous limitons au cadre des petites déformations, rotations et courbure pour des processus isothermes.

Afin de faciliter la compréhension du modèle couplé utilisé, ses différentes composantes sont abordées de manière isolées. Ainsi, le premier chapitre de ce manuscrit est consacré à quelques rappels concernant les joints de grains et la recristallisation. Le deuxième chapitre aborde la théorie de Cosserat et présente de nouvelles solutions analytiques au problème de la torsion d'un cylindre à section circulaire et au cisaillement du monocristal. Dans ce cas, différentes formulations de l'énergie libre vis-à-vis de la courbure sont envisagées pour se rapprocher du modèle à champ de phase de KWC, présenté au chapitre 3. La deuxième partie de ce chapitre est consacrée au modèle couplé KWC-Cosserat, où l'effet de la mécanique sur le joint de grain est également étudié. Les modèles KWC et KWC-Cosserat sont ensuite appliqués, au chapitre 4, au phénomène de germination dans les monocristaux en présence de gradients d'orientation cristalline. Enfin, le cinquième chapitre présente quelques extensions aux polycristaux et autres cas d'application.

General context

Thermomechanical processing and microstructure evolution in crystalline materials

Metals and metallic alloys consist of grains, which are typically between 1-500 μm in size, separated by grain boundaries that usually measure about 0.1-1 nm in thickness. Alongside the chemical composition and crystalline structure, the size, morphology, and orientation of the grains (i.e. the microstructure) have a direct influence on the macroscopic properties of the material. One example of this is the effect of grain size on yield strength and fracture toughness, as demonstrated by the work of Hall and Petch in the early 1950s.

To achieve the intended shape for the end product, a sequence of heating and shaping procedures known as thermomechanical processing is usually carried out. The microstructure of the material also undergoes significant changes during these thermomechanical treatments. Indeed, the process of metal forming induces inelastic deformation of the material and introduces dislocations into the microstructure. Subsequent heating results in the reorganisation and elimination of these defects by thermally activated mechanisms. This process, referred to as recovery, partially restores the microstructure to its original state. An additional restoration process, known as recrystallization, leads to the nucleation and growth of new dislocation-free grains and is critical in metal forming processes. Once the material is fully recrystallised, grain growth can occur on further annealing to reduce the energy stored in the form of grain boundaries.

These significant microstructural evolutions, especially recrystallization, must therefore be controlled. This necessity has been well understood from the industrial standpoint and from the 1960s onwards, companies began incorporating microstructural features to enhance the final product through thermomechanical treatment [Montheillet, 2009]. Optimisation of the microstructure to achieve the desired macroscopic properties can be achieved, for example, by hot forming prior to forming the final product. For example, hot rolling can notably refine the grain size, thereby enhancing the yield strength. Similarly, a combination of cold rolling and annealing is employed to increase the formability of aluminium sheets.

Some physical and phenomenological aspects of recrystallization

As mentioned, recrystallization consists of the nucleation and growth of new grains with low dislocation content. More specifically, it involves the formation and migration of high angle grain boundaries (HAGBs) to reduce the stored energy. This process can occur during the deformation, typically during hot working operations: it is then referred to as dynamic recrystallization. Conversely, annealing of a metal that has been previously cold worked leads to static recrystallization. In addition, depending on whether the nucleation and growth stages are clearly identifiable, recrystallization is termed discontinuous or continuous. This work focuses on discontinuous static recrystallization.

The nucleation of recrystallization cannot be explained by the classical nucleation theory of thermodynamics based on thermal fluctuations, but nuclei are already present in the deformed state. Three main nucleation processes have been identified in the literature for single phase materials: strain induced boundary migration (SIBM), subgrain coarsening and subgrain coalescence.

Strain induced boundary migration [Beck and Sperry, 1950] consists of a pre-existing grain boundary growing into a grain with a higher dislocation content. The migration of grain boundaries creates defect-free zones in its wake and increases the total area of the HAGB. The orientation of the nucleus will be close to that of the grain from which it grew [Rollett et al., 2017]. Subgrain coarsening [Beck, 1949; Cahn, 1950] describes the thermally assisted growth of a subgrain at the expense of its surrounding neighbours to reduce the stored energy by dislocation annihilation and rearrangement. By absorbing dislocations, the subgrain increases its misorientation with respect to the surrounding subgrains, forming HAGBs. Subgrain coalescence is the rotation of two adjacent subgrains to align their lattices and form a larger subgrain with increased orientation difference with respect to the surrounding matrix, forming HAGBs. However, it is debated whether this is a recrystallization or recovery mechanism prior to SIBM [Rollett et al., 2017].

Due to the intricacy of the phenomena involved, controlling and predicting microstructural changes that occur during thermomechanical processing of metals and metallic alloys presents a significant industrial and scientific challenge. From a modelling perspective, mean field and macroscopic full-field models are limited since they are unable to characterise local phenomena that are crucial to microstructure evolution, such as intragranular lattice orientation gradients that occur during deformation. Consequently, it is imperative to develop and employ full-field models at the mesoscale.

Existing approaches to full-field modelling of microstructure evolution

The deformed state: crystal plasticity and generalised continua

Recrystallisation is closely linked to the deformed state of a material, necessitating a description that takes into account local strain heterogeneities as these are preferential sites for the nucleation of new dislocation-free grains. Physically, plastic deformation of crystalline materials occurs through slip along specific crystallographic planes (typically the densest ones at low temperature) induced by the motion of crystal defects called dislocations. Classically, dislocations are divided into statistically stored dislocations (SSDs) that accumulate due to interactions with other dislocations or precipitates, and geometrically necessary dislocations (GNDs) required to accommodate plastic strain gradients and ensure deformation compatibility. GNDs are therefore intrinsically linked to lattice curvature [Ashby, 1970]. From the modelling standpoint, several approaches exist depending on the chosen length scale. Typically, interactions between a few dislocations are studied using atomic models. On a coarser scale, discrete dislocation dynamics or continuum crystal plasticity models are used. In the latter, dislocations are not individually represented but rather only the quantity of plastic slip on each slip system, due to the collective motion of dislocations, is retained. This is currently the preferred approach for modelling microstructure evolutions at the mesoscale.

However, classical continuum crystal plasticity models have limitations. For instance, they cannot account for the size effects that are experimentally observed during the torsion of wires [Fleck et al., 1994]. These size effects stem from strain gradients, which induce a density of GNDs that contribute, in addition to the SSDs, to the work hardening. Consequently, the thinner the wire, the higher the strain gradient and thus the higher the density of GNDs and hardening. Models that propose an enriched description of matter, such as Cosserat continua [Cosserat and Cosserat, 1909] or strain gradient plasticity [Fleck et al., 1994], can capture these size effects. In the Cosserat theory, additional degrees of freedom are introduced in the form of microrotations (that are *a priori* independent of the displacement), which are identified with rotations of the crystal lattice by means of internal constraints [Forest et al., 1997, 2000]. Thus, the Cosserat curvature can be seen as an approximate measure of GND density.

Simulation of recrystallization: normal grain growth models and coupling with mechanics

In the available literature, crystal plasticity models are used to obtain the deformed state of the material and coupled with grain growth models to simulate recrystallization. Various grain growth models have been developed to describe microstructure evolution, including Monte-Carlo Potts [Anderson et al., 1984], cellular automata [Hesselbarth and Göbel, 1991], level sets [Bernacki et al., 2008], and phase-field methods. The latter relies on a continuous representation of interfaces, in which grain boundaries are diffuse. Two major approaches for phase-field modelling of microstructure evolution exist: one with one phase-field variable per grain [Chen and Yang, 1994; Steinbach and Pezzolla, 1999], and one with only two independent phase-field variables for the entire polycrystalline microstructure [Kobayashi et al., 2000; Warren et al., 2003], known as the Kobayashi-Warren-Carter (KWC) model. Only the latter is capable of accounting for intragranular orientation gradients that may lead to the emergence of new (sub)grains. Furthermore, the thermodynamic framework of phase-field models is highly adaptable to the integration of other physical phenomena such as mechanics [Steinbach and Apel, 2006]. This is conventionally achieved by adding physical contributions to the free energy density. Classically, the multiphysics problem is solved using staggered schemes. Only Ask et al. [2018b] and Admal et al. [2018] have proposed a unified framework for

the evolution of microstructure and concurrent (visco)plastic deformation.

Shortcomings of the current modelling approaches

The modelling of the nucleation stage of recrystallization, despite its importance, remains incomplete. While several models have been developed to efficiently simulate the growth phase, the simulation of nucleation is still inadequate. The classical theory of nucleation, used to model solidification, employs thermal fluctuations for the emergence of new phases. In full-field models, this is typically done by adding noise to the field equations. However, the renormalisation of these equations in the presence of strong noise prevents quantitative modelling of nucleation processes [Plapp, 2011]. It has long been recognised that explaining the nucleation process during recrystallization with the classical theory of nucleation is inadequate. Indeed, recrystallization nuclei are not *stricto sensu* thermodynamic nuclei but small pre-existing volumes in the deformed microstructure [Rollett et al., 2017]. Thus, simulating the nucleation stage of recrystallization has traditionally involved the ad hoc introduction of new spherical or circular grains linked to a critical value of strain, stress or dislocation density. There is therefore a need for models that spontaneously account for the appearance of new grains. We consider that orientation phase-field models combined with mechanics are capable of capturing such phenomena.

Objective

The main aim of this work is the full-field modelling of microstructure evolution at the mesoscale accounting for spontaneous nucleation. More specifically, the objective is to demonstrate that, in the presence of lattice orientation gradients, spontaneous nucleation (i.e without the introduction of spherical/circular nuclei) can be simulated with the orientation phase-field models [Kobayashi et al., 2000; Ask et al., 2018b] in single crystals. In the simulations that will be discussed, nucleation spontaneously arises to accommodate these gradients. Therefore, the modelling of strain induced boundary migration or subgrain coarsening/coalescence is not addressed in the present work.

Methodology

The model of Ask et al. [2018b] used in this work combines in a unified framework the Cosserat theory to describe the deformed state of the material and the grain growth phase-field model of Kobayashi et al. [2000]. The simulation of spontaneous nucleation in the presence of lattice orientation gradients is first carried out using the original KWC model. The instability induced by these gradients introduced as initial conditions is assessed both analytically, via a linear perturbation analysis, and numerically through finite element simulations. The numerical study is then extended to the KWC-Cosserat model,whose coupling is achieved through the free energy density, to verify that this nucleation capability is retained. The physical relevance of the simulation is demonstrated by conducting a three-dimensional computation in which the lattice orientation gradients are generated through the torsional loading of a single crystal rod with axis [111]. This simulation is validated based on a comparison with experimental results found in the literature. In addition, simulations of deformation and subsequent relaxation of polycrystalline aggregates are carried out to evidence the link between curvature localisation and nucleation of new (sub)grain boundaries.

Outline

This work is organized as follows. Chapter I presents essential notions about the structure, properties and motion of grain boundaries as well as recrystallization and its full-field modelling.
The KWC-Cosserat model being somewhat intricate, its two components are first presented separately for an easier understanding. Thus, the mechanics of Cosserat continua at small deformation is introduced in

chapter II and illustrated on simple examples. This work provides new analytical solutions to the problems of torsion of isotropic elastic-plastic rods and shear of a single crystal. In the latter, several formulations of the Helmholtz free energy density are explored in order to get closer to that of the orientation phase-field models [Kobayashi et al., 2000; Ask et al., 2018b]. Size effects that emerge during mechanical loading are also addressed.
In chapter III KWC-type microstructure evolution models are presented and the static and dynamic properties of grain boundaries are studied. The effect of the grain boundary inelastic behaviour in the coupled model is scrutinized and a finite element extension to the three-dimensional case is discussed.
Chapter IV addresses nucleation due to lattice orientation gradients in single crystals. An analytic linear stability analysis and finite element simulations are performed in this purpose. Most notably, a three-dimensional calculation of the torsion of a single crystal rod is presented and the outcomes are qualitatively compared to experimental results in the literature.
Finally, chapter V presents applications of the orientation phase-field models to bicrystals and polycrystalline aggregates. They represent first steps towards full-field simulation of thermomechanical processes in a unified, thermodynamically consistent framework.

Funding

This work is funded by the CNRS, the French national centre for scientific research, as part of the 80 Prime interdisciplinary program. The project involves the Centre for Materials (Mines Paris-PSL, CNRS), Institut Jean Lamour (Université de Loraine, CNRS) and ONERA. It combines advanced continuum mechanics and metallurgical approaches.

Chapter I

Essentials about the structure, properties and motion of grain boundaries

Résumé en français

Ce premier chapitre présente un bref résumé des connaissances nécessaires à la compréhension des prochains chapitres du manuscrit. Ainsi, nous abordons la structure et les propriétés des joints de grains. L'énergie et la mobilité des joints de grains ainsi que la distinction entre joint de faible désorientation et joint de grande désorientation sont rappelées. En particulier, la formulation de type Read-Schockley de l'énergie des joints de grain de faible désorientation et la proportionalité entre vitesse du joint et force motrice sont évoquées.

Dans un second temps, quelques aspects physiques et phénoménologiques de la recristallisation et croissance de grains sont présentés. Ainsi, la cinétique de recristallisation (loi de Johnson-Avrami-Kolmogorv (JMAK)) et de croissance des grains (loi de Burke-Turnbull) sont rappelées. Les principaux mécanismes de germination identifiés dans la littérature sont également abordés. Ceux-ci comprennent le SIBM et la croissance/coalescence de sous-grains.

Nous dressons également un état de l'art succinct des différents modèles à champs moyens et champs complets principaux utilisés pour la simulation de la recristallisation, en nous attardant sur les méthodes à champs de phases de Kobayashi-Warren-Carter (KWC) et multi-phase field (MPF). Enfin, nous présentons quelques aspects de la simulation de la germination en mentionnant certains travaux qui proposent une approche différente de la traditionnelle étape d'introduction de germes circulaires.

Contents

I.1 Introduction

The purpose of this chapter is to provide a brief summary of the structure and properties of grain boundaries and recrystallization processes in single-phase, single-component crystalline materials. This is not a comprehensive review, only the elements relevant to the rest of the thesis are presented.
The first part is largely based on the work of Rollett et al. [2017]; Gottstein and Shvindlerman [2009]; Priester [2012]; Han et al. [2018] and deals with the description of grain boundaries and their properties. The second part is devoted to grain nucleation and growth, its is mostly based on the work of Doherty et al. [1997]; Rios et al. [2005]; Raabe [2014]; Ferdinand Knipschildt [2022]; Rollett et al. [2017]. The third part then shortly introduces historical and more recent mean-field models of recrystallization and grain growth. Finally, the fourth part deals with the full-field continuum modelling, at the mesoscopic scale, of grain growth and recrystallization, with a brief introduction to the main simulation techniques, in order to position this work in relation to the literature. Monte Carlo Potts, cellular automata, phase field, and level sets methods are discussed, with emphasis on phase-field models. The main purpose is to present the advantages and drawbacks of each model. More detailed reviews are available elsewhere, for example in Rollett [1997]; Hallberg [2011]; Raabe [2014]; Rollett et al. [2017].

I.2 Structure, energy and mobility of grain boundaries

The migration of grain boundaries is the dominant process during microstructure evolution induced by thermomechanical processing and is heavily influenced by the grain boundaries' properties, which in turn are related to their structure. Therefore, a concise presentation of grain boundaries and their properties is given in this section in order to apprehend more readily recrystallization and grain growth described in section I.3.

I.2.1 Structure of grain boundaries

A grain boundary is defined as a lattice defect separating two regions of the same crystal structure but with different orientations. In the two-dimensional case, four degrees of freedom (DOFs) are required to describe a grain boundary mathematically. These are divided into macroscopic and microscopic parameters. The macroscopic DOFs are the misorientation θ between the two crystals and an angle defining the orientation of the boundary plane with respect to one of the crystals. The microscopic parameters define the translation vector, which describes the translation of one crystal with respect to the other. This becomes more complicated in 3D, where 8 DOFs are required:

- 5 macroscopic parameters: 3 characterising the orientation relationship between the two crystals (2 for the rotation axis and one for the rotation angle θ or 3 Euler-Bunge angles), 2 describing the orientation of the boundary plane using its normal unit vector.
- 3 microscopic parameters describing the translation vector.

Grain boundaries are usually divided into low angle grain boundaries (LAGBs) and high angle grain boundaries (HAGBs) according to their misorientation. The usual threshold for misorientation is $\theta_m \sim 15°$, where grain boundaries with a misorientation lower or higher than θ_m are called LAGBs and HAGBs respectively. Subgrain boundaries are LAGBs formed within a grain by the rearrangement of dislocation cells during hardening. Grain boundaries are also often referred to as tilt, twist or mixed grain boundaries, depending on whether the misorientation axis is parallel, perpendicular or has no particular relationship to the boundary plane. The term symmetric tilt boundaries is used to describe tilt boundaries where the two crystals are mirror images of each other. Illustrations of a 2D grain boundary and a twist and symmetric tilt boundary are given in figures 1.1 and 1.2.

A periodic arrangement of dislocations can be used to represent low angle grain boundaries. Symmetric tilt boundaries, for example, can be described as a wall of edge dislocations with a single set of Burgers vectors, as illustrated in Fig. 1.3.

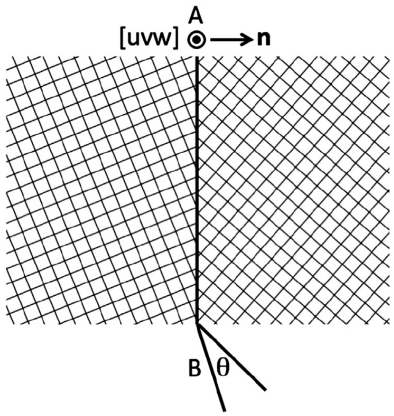

Figure 1.1: *A grain boundary between two crystals misoriented by an angle θ about an axis normal to the page [Rollett et al., 2017].*

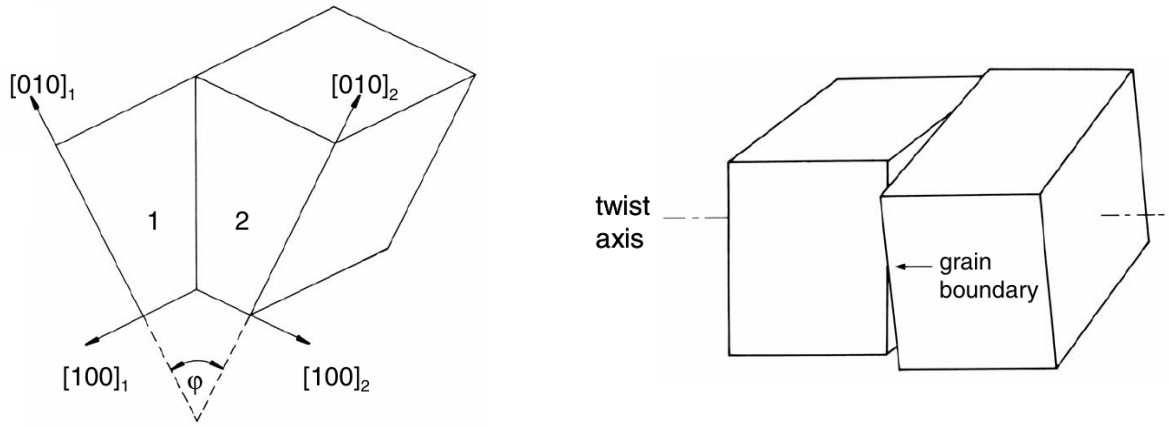

(a) *A symmetrical tilt boundary.* (b) *A twist boundary.*

Figure 1.2: *Schematic representation of twist and symmetrical tilt boundaries from Gottstein and Shvindlerman [2009].*

It has been established by Read and Shockley [1950] that for such grain boundaries the Burgers vector b and the dislocation spacing d are related to the disorientation angle θ by

$$\frac{b}{d} = 2\sin\left(\frac{\theta}{2}\right) \simeq \theta. \tag{1.1}$$

In the more general case where several sets of Burgers vectors are involved, their interaction leads to 2D networks of dislocations whose character depends on the type of dislocations. The shape of the network is influenced by the angle between the grain boundary plane and the crystals. Similar to the Read-Shockley approach, a continuous description of any grain boundary as a surface dislocation was proposed by Bilby [1955]; Bilby et al. [1955].

For HAGBs the Read-Shockley approach is no longer valid. There is however an important feature related to the orientation relationship that is used to describe some HAGBs: the coincident site lattice (CSL). It is obtained by extending the lattice of one of the grains into that of the other, the coincident sites forming the CSL. A reciprocal coincident site density Σ is defined to characterize these coincident boundaries:

$$\Sigma = \frac{\text{size of a unit cell of the CSL}}{\text{size of the unit cell of the primitive lattice}}. \tag{1.2}$$

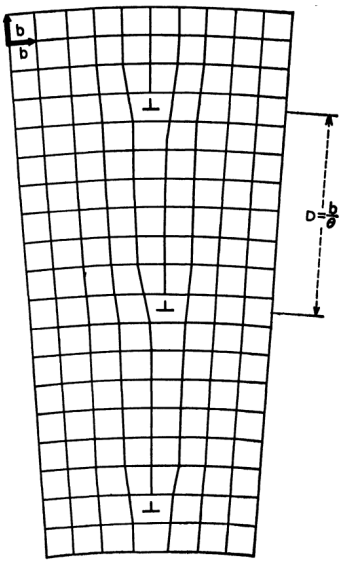

Figure 1.3: *A symmetrical tilt low angle grain boundary comprised of edge dislocations denoted by* ⊥ *from Read* [1953].

Coincident grain boundaries correspond to a coincidence relationship and can be associated with local minima or maxima of grain boundary energy. However, there is no one-to-one relationship between the value of Σ and that of the energy.
In some cases, the atomic arrangement at the grain boundary is such that well-defined structural units can be formed. This is illustrated in Fig. 1.4.

Other descriptions of grain boundaries such as disconnections and disclinations are not discussed here but are addressed for instance by Fressengeas et al. [2011] Han et al. [2018], Hirth et al. [2020], Sun et al. [2018].

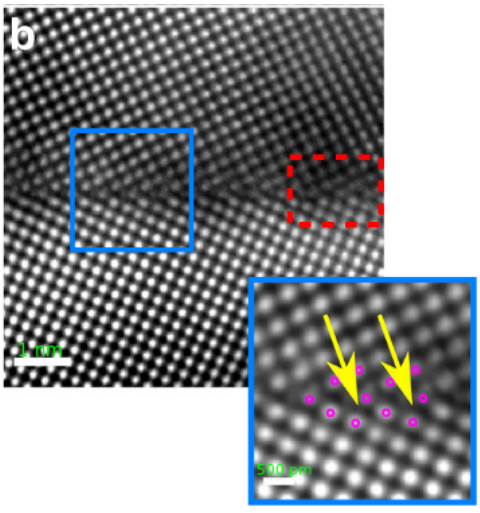

Figure 1.4: *High-angle annular dark field scanning electron microscopy Fourier-filtered image of a grain boundary exhibiting kite-like structural units in* α*-Fe at 4% Al [Ahmadian et al., 2021].*

I.2.2 Energy of grain boundaries

The presence of a grain boundary induces an excess of energy - compared to that of a pristine crystal - which depends on the macroscopic and microscopic parameters of the boundary. For LAGBs the interfacial

energy γ follows the Read-Shockley equation [Read and Shockley, 1950]:

$$\gamma = \gamma_0 \theta (A - \log(\theta)), \tag{1.3}$$

$$\gamma_0 = \frac{\mu b}{4\pi(1-\nu)}, \quad A = 1 + \log\left(\frac{b}{2\pi r_0}\right), \tag{1.4}$$

with μ the shear modulus, ν Poisson's ratio and r_0 the radius of the dislocation core ($b \leq r_0 \leq 5b$). A normalized grain boundary energy can also be defined as

$$\frac{\gamma}{\gamma_m} = \frac{\theta}{\theta_m}\left(1 - \log\frac{\theta}{\theta_m}\right) \tag{1.5}$$

where γ_m is the energy corresponding to a boundary of misorientation θ_m or to the maximum energy measured. This form of the Read-Shockley equation is convenient as it allows to measure energies in relative units. The Read-Shockley equation has been proven to successfully model the energy-misorientation relation of LAGB, as illustrated in Fig. 1.5 which shows a good agreement between experiment and theory. This formula is restricted to LAGBs due to overlapping of the dislocation cores for $\theta > \theta_m$.

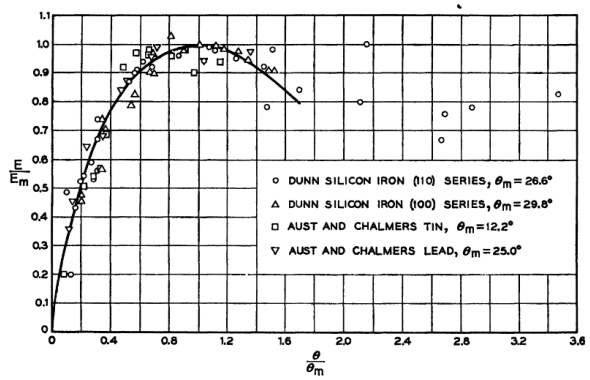

Figure 1.5: *Experimental (markers) and Read-Shockley (solid line) grain boundary energy [Read, 1953]*

The energy of HAGBs is much more complex as there is no simple relationship between the energy of a boundary and its geometry. The energy-misorientation curve can exhibit a plateau (Fig. 1.6a) or deep cusps (Fig. 1.6b). An empirical extension of the Read-Shockley equation was proposed in [Wolf, 1989]:

$$\gamma = \gamma_0 \sin(\theta)\,(A - \log(\sin(\theta)))\,, \tag{1.6}$$

which is able to accurately predict HAGB energy in some cases (Fig. 1.6a.)

Based on CSL theory, it is expected that the energy would be a minimum for an exact coincidence relationship, and that any deviation from this coincidence would increase the energy. Moreover, low values of Σ would indicate low energies. However, this is not what is observed experimentally or computationally, as shown in [Rohrer, 2011] and [Ratanaphan et al., 2015], which suggest that grain boundary anisotropy is influenced more by the orientation of the boundary plane than by misorientation.

Experimental measures of grain boundary energy are obtained from the geometry of interface junctions at equilibrium [Rohrer, 2011]. For triple junctions, simplifications of the Herring [Herring and Kingston, 1951] equation are used. It is often assumed that only the tangential forces are equilibrated, this simplified Herring equation is then referred to as Young's equation:

$$\frac{\gamma_1}{\sin(\theta_{2,3})} = \frac{\gamma_2}{\sin(\theta_{1,3})} = \frac{\gamma_3}{\sin(\theta_{1,2})}, \tag{1.7}$$

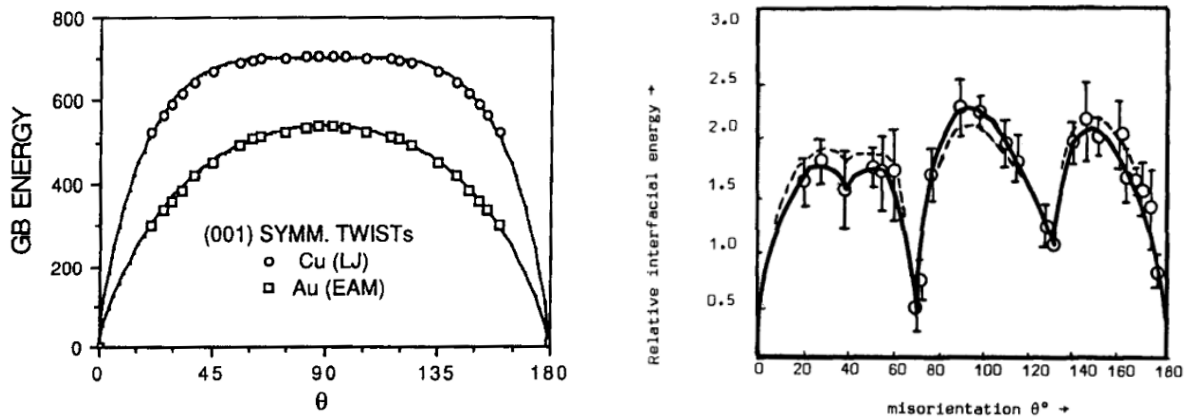

(a) *Energy of <100> symmetrical twist boundaries. Markers denote energies computed with molecular dynamics and solid lines are computed with the extended Read-Shockley equation [Wolf, 1989].*

(b) *Relative energies of <110> tilt boundaries measured in Al [Hasson and Goux, 1971].*

Figure 1.6: *Examples of grain boundary energy-misorientation curves*

where γ_i is the energy of the i^{th} grain boundary and $\theta_{i,j}$ is the contact angle between grains i and j. This approach allows relative grain boundary energies to be obtained simply by measuring the contact angles between grains. For more details on experimental measurements of grain boundary energy, a catalogue of different techniques is given in Gottstein and Shvindlerman [2009]. Grain boundary energies can also be obtained from atomistic calculations, often at 0K as in Wolf [1990].

I.2.3 Grain boundary mobility

The migration of grain boundaries plays a key role in thermomechanical processes. Migration of LAGB occurs during recovery and the nucleation stage of recrystallization whereas HAGB migrate during and after primary recrystallization. Despite the importance of this phenomenon, the understanding of the process is only partial and experimental measurements of grain boundary mobility are complex.
It is generally assumed that the mobility M relates the grain boundary velocity v to the driving force responsible for grain boundary migration P by

$$v = MP. \tag{1.8}$$

The mobility usually follows an Arrhenius law with respect to temperature

$$M = M_0 \exp\left(-\frac{Q}{RT}\right). \tag{1.9}$$

Based on dislocation theory, it is assumed that LAGB migrate through climb and glide of the dislocations belonging to the grain boundary. The dependence of mobility of LAGBs on misorientation is complex. For aluminium for instance, in [Bainbridge et al., 1954] a decrease in the mobility with increasing misorientation is reported, whereas in [Huang and Humphreys, 2000] the mobility increases with the misorientation. In some cases the mobility may be independent of the misorientation, as stated in [Winning et al., 2001].
For HAGBs, the dominant mechanism is thought to be atomic jumps across the boundary. Their mobility is usually higher than that of LAGBs and seems to be largely independent of misorientation, as visible in Fig. 1.7.
Experimental measurements are preferably conducted in bicrystals due to the reproducibility associated with this technique, compared to polycrystals [Gottstein and Shvindlerman, 2009]. Based on curvature driven motion of grain boundaries, this provides the advantage of the driving force being almost independent of temperature due to the weak dependence of the surface tension of the grain boundary on this variable. It is

however rather complex to produce these bicrystals.

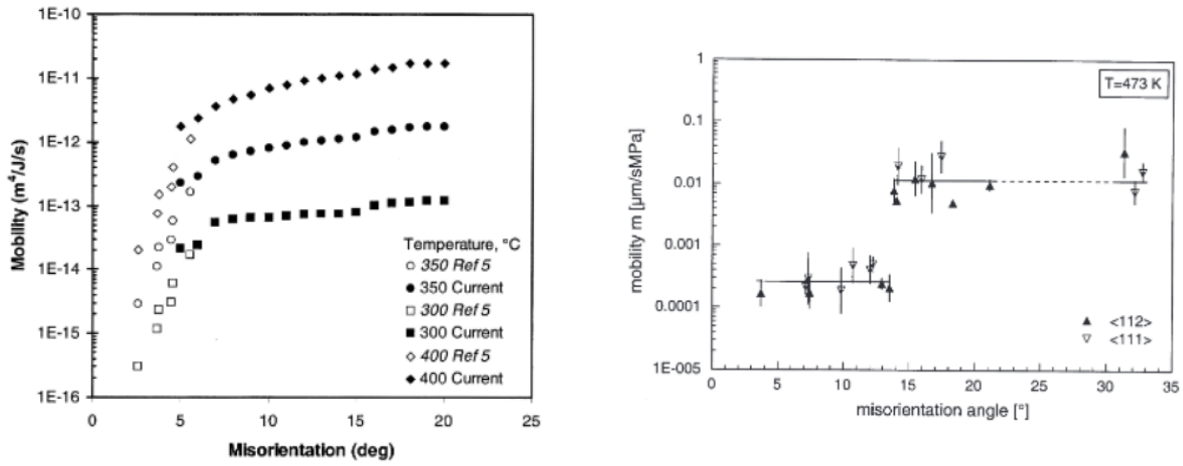

(a) *Grain boundary mobility as a function of misorientation and temperature in Al-0.05% Si [Huang et al., 2000].*

(b) *Grain boundary mobility as a function of misorientation in high purity Al [Winning et al., 2001].*

Figure 1.7: *Grain boundary mobilities as a function of misorientation*

In the literature, experimental and numerical identification of grain boundary properties have been carried out, in particular, for high purity copper and aluminium. Typical values of grain boundary properties for copper are reported in table 1.1.

Parameter	Approximate value for Cu	Misorientation [°]	Temperature [°C]	Means of measurement	Reference
Energy γ [J/m^{-2}]	0-0.8	0-30	-273	Computation	[Wolf, 1990]
Mobility $\mathscr{M}$ [m^{4}s^{-1}MJ^{-1}]	6.31×10^{-10}	36.4	121	Experiment	[Vandermeer et al., 1997]
Reduced mobility $\mathscr{M}_r = \gamma\mathscr{M}$ [cm^{2}s^{-1}]	$1 - 4000 \times 10^{-9}$	2-32	275-1025	Experiment	[Viswanathan and Bauer, 1973]

Table 1.1: *Experimental or computed values of grain boundary energy, mobility and reduced mobility for copper.*

I.3 Recrystallisation

The thermomechanical processing of crystalline materials involves a relatively wide variety of phenomena, the terminology of which is recalled here after Rollett et al. [2017].
During cold working, plastic deformation introduces dislocations into the material, increasing the free energy of the crystal. When the work piece is heated to a high temperature - a process called annealing - the dislocations can annihilate or rearrange into lower energy configurations. During annealing, a partial restoration of microstructure and properties can occur in a process called recovery, which preserves the shape of the deformed grains and gives rise to a subgrain structure. A separate restoration process called recrystallisation is also possible, in which new dislocation-free grains are nucleated. Recrystallisation involves the formation and migration of HAGBs to reduce the stored energy, resulting in a new grain structure. A third process that occurs during annealing is grain growth, which results in a reduction in the total grain boundary area. In some cases, a few large grains will grow at the expense of the others in a process known as abnormal grain growth or secondary recrystallization. These processes are referred to as either static or dynamic, depending on whether they occur after or during plastic deformation. If the nucleation and growth stages are clearly identifiable, they are referred to as discontinuous processes, otherwise they are termed continuous. Discontinuous or primary recrystallization usually occurs at relatively low or moderate strain ($\varepsilon \lesssim 1$) and will be the focus of the remainder of this thesis.

I.3.1 Nucleation stage of recrystallization

The nucleation stage of recrystallization is driven by the stored energy E due to dislocation density ρ which is estimated as

$$E \simeq \frac{1}{2}\mu b^2 \rho. \tag{1.10}$$

For copper ($\rho \sim 10^{15} - 10^{16}\ m^{-2},\ G \sim 42\ GPa,\ b \sim 0.26\ nm$) the driving force due to stored energy is about 2-20 MPa. Since the driving force is low and the interfacial energy is high ($\gamma \sim 0.5 - 1\ J.m^{-2}$), the nucleation of recrystallization cannot be explained by the classical nucleation theory of thermodynamics based on thermal fluctuations, but is already present in the deformed state. Three main nucleation processes have been identified in the literature for single phase materials [Doherty et al., 1997; Raabe, 2014; Rollett et al., 2017; Ferdinand Knipschildt, 2022]: strain induced boundary migration (SIBM), subgrain coarsening and subgrain coalescence. They are shown schematically in Figure 1.8.
Strain induced boundary migration [Beck and Sperry, 1950] consists of a pre-existing grain boundary growing into a grain with a higher dislocation content. The migration of the grain boundary creates defect-free zones in its wake and increases the total area of the HAGB. It has been reported to occur in regions of large strain differences on either side of the grain boundary and is the main recrystallization mechanism for relatively small strains (up to 40%). The orientation of the nucleus will be close to that of the grain from which it grew [Rollett et al., 2017].
Subgrain coarsening [Beck, 1949; Cahn, 1950] describes the thermally assisted growth of a subgrain at the expense of its surrounding neighbours to reduce the stored energy by dislocation annihilation and rearrangement. By absorbing dislocations, the subgrain increases its misorientation with respect to the surrounding subgrains, forming HAGBs. This mechanism occurs at large strains, high annealing temperatures and large orientation spreads [Rios et al., 2005].
Subgrain coalescence is the rotation of two adjacent subgrains to align their lattices and form a larger subgrain with increased orientation difference with respect to the surrounding matrix, forming HAGBs. It is associated with transition bands, moderate strains and relatively low annealing temperatures. However, it is debated whether this is a recrystallization or recovery mechanism prior to SIBM [Rollett et al., 2017].

Recrystallisation occurs preferentially at sites of large lattice curvature, such as grain boundaries and triple junctions. The reason advanced in [Rollett et al., 2017] is the presence of stress gradients across the boundary due to differences in the active slip systems, leading to an accumulation of lattice misorientations.

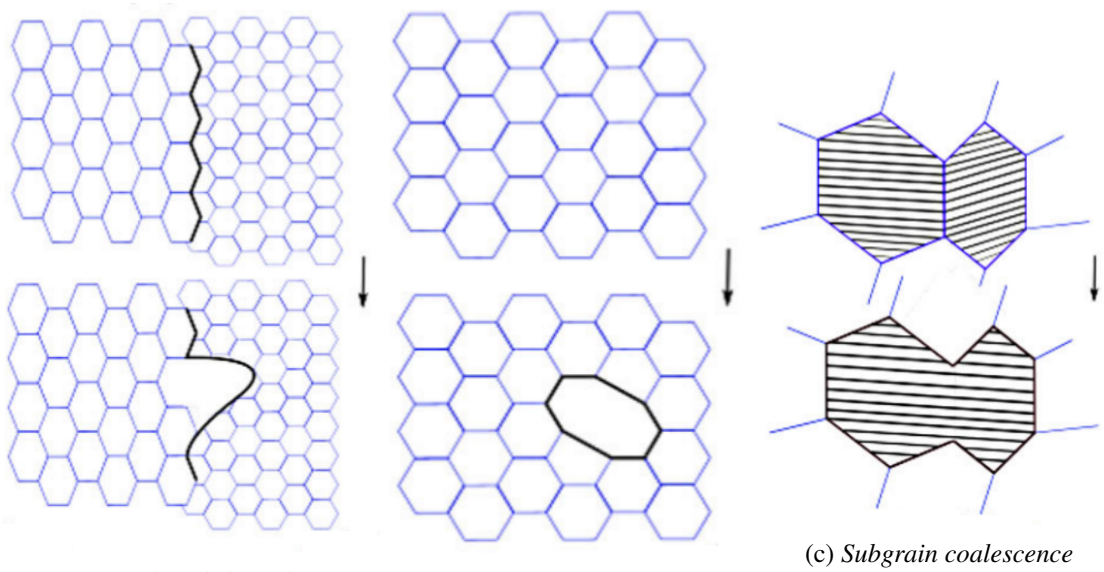

(a) *Strain-induced boundary migration*

(b) *Subgrain coarsening*

(c) *Subgrain coalescence*

Figure 1.8: *Schematic illustration of SIBM, subgrain coarsening and subgrain coalescence [Ferdinand Knipschildt, 2022]*

Large orientation gradients can also result from heterogeneous deformation. For example, transition bands are bands of high lattice strain that separate regions of different orientations of a grain that has split during deformation. Shear bands are another example of preferential nucleation sites due to heterogeneous deformation. They consist of thin regions of highly strained material associated with large stored energy and orientation gradients across the band.

I.3.2 Grain boundary migration: growth of nuclei and grain growth following recrystallization

For single phase, single component materials under isothermal annealing the main driving forces for grain boundary motion are the stored energy due to dislocations and the grain boundary energy/curvature, as summed up in table 1.2.

Source	Equation	Approximate value of parameters	Estimated driving force
Stored deformation energy	$P = \frac{1}{2}\rho\mu b^2$	ρ = dislocation density $\sim 10^{15}/\mathrm{m}^{-2}$ $\frac{\mu b^2}{2}$ = dislocation energy $\sim 10^{-8}$ J/m	10 (MPa)
Grain boundary energy	$P = \frac{2\gamma}{R}$	γ = grain boundary energy ~ 0.5 J/m^2 R = grain boundary radius of curvature $\sim 10^{-4}$ m	10^{-2} (MPa)

Table 1.2: *Driving forces for grain boundary motion [Gottstein and Shvindlerman, 2009]*

Once formed, a nucleus can grow into the strained microstructure by stored energy driven migration of the HAGB. Due to the curvature and energy of this newly formed grain of radius R, a retarding pressure P is exerted on the boundary, inducing shrinkage of the grain as it drives migration of the grain boundary towards its centre of curvature:

$$P = \frac{2\gamma}{R}. \tag{1.11}$$

As a result, the driving force induced by the accumulation of stored energy must overcome the retarding pressure caused by the curvature of the boundary. This results in a critical radius for nucleus growth [Bailey and Hirsch, 1962]. With $\gamma \sim 0.5\, J/m^2$ and $P \sim 1-10\, MPa$, the critical grain size is therefore $0.1-1\ \mu m$.

However, once the material is fully recrystallised, the microstructure is relatively defect-free but still unstable due to the presence of grain boundaries. Grain growth, which is the curvature driven migration of HAGBs, can occur to reduce this excess energy. During grain growth, the smaller grains are consumed by the larger grains so that the average grain size increases. The kinetics is often described by the Burke-Turnbull law [Burke and Turnbull, 1952]

$$\bar{R} = Bt^{1/n}, \tag{1.12}$$

with $\bar{R}$ the mean grain size, n is the grain growth exponent and B is a constant.

I.3.3 Kinetics of recrystallization

The kinetics of isothermal static primary recrystallization is usually represented by the phenomenological Johnson-Mehl-Avrami-Kolmogorov (JMAK) equation [Kolmogorov, 1937; Johnson and Mehl, 1939; Avrami, 1939, 1940], which gives the evolution of the volume fraction of recrystallised material X as a function of time:

$$X = 1 - \exp(-Bt^n), \tag{1.13}$$

where B is a constant and n is the Avrami exponent. Comparison with the JMAK model is often carried out by plotting the log-log plot of $\log(1/(1-X))$ as a function of the annealing time, referred to as JMAK plot. This should result in a straight line whose slope is equal to n. However, it is often observed that above a certain volume fraction of recrystallised material the curve deviates from the slope due to microstructure heterogeneity [Rollett et al., 2017] , as visible in Fig. 1.9.

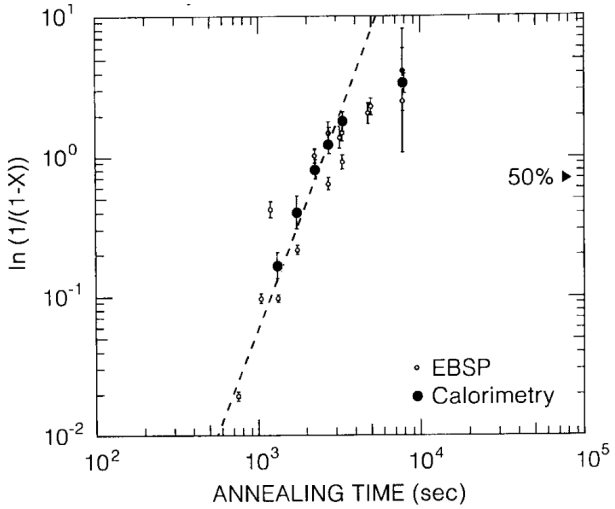

Figure 1.9: *JMAK plot of 99.96% Cu cold-rolled at 92% total deformation and annealed at 121° C [Woldt and Jensen, 1995].*

I.4 Mean field models

Microstructure descriptors such as grain size or recrystallised fraction can be described by mean-field models, which are based on an implicit and reduced representation of the material. These simplifying assumptions allow these types of model to be much faster than full-field models. However, they do not take into account the grain topology and the interactions between grains, so the local variations in properties

are generally neglected. The work of Burke and Turnbull [1952] can be considered as one of the earliest examples of a mean-field model for grain growth.
An extended description of the microstructure was proposed by Hillert [Anand et al., 2015], in which N classes of spherical grains are considered and each class is represented by a grain radius. This makes the model more versatile than that of Burke and Turnbull [Cruz-Fabiano et al., 2014].
More complex models have been proposed by adding more descriptors such as dislocation density to model nucleation and growth in discontinuous dynamic recrystallization [Montheillet et al., 2009; Cram et al., 2009; Bernard et al., 2011; Beltran et al., 2015; Maire et al., 2018].
Most mean field models are based on the SIBM nucleation mechanism, where a critical nucleus radius arises when the driving force due to stored energy becomes greater than the boundary curvature [Bailey and Hirsch, 1962]. Based on the simple Bailey-Hirsch model, approaches describing nucleation as the unstable growth of cells have been proposed by Humphreys [1997]; Hurley and Humphreys [2003], Zurob et al. [2006] and more recently Després et al. [2020] who was able to account for the subgrain boundary properties dependence on misorientation.

I.5 Full-field modelling of grain growth and recrystallization at the mesoscopic scale

I.5.1 Monte-Carlo Potts models

First introduced in a series of papers by Anderson et al. [1984], Monte Carlo Potts models discretise the microstructure into a lattice of N sites. Each site is then assigned an orientation number s_i. A grain is defined as one or more blocks of the same orientation, while grain boundaries are implicitly defined as the boundary between two blocks of different orientations (cf Fig. 1.10). The total energy of the system accounts for grain

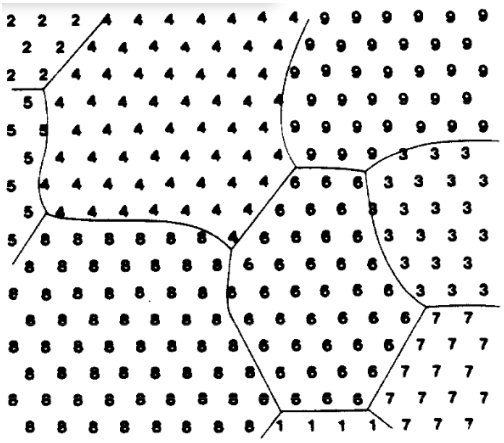

Figure 1.10: *Discretized microstructure in the Monte Carlo Potts model [Anderson et al., 1984]*

boundary and stored energy contributions of lattice site i with n nearest neighbours. A Monte Carlo sampling of the different orientations is then performed to model microstructure evolution. A site is selected at random and given a new orientation, inducing an energy change ΔE. A transition probability p is associated with this new orientation, which favours the changes that lead to a decrease in the energy. When all lattice sites have undergone this orientation change, a 'Monte Carlo step' (MCS) has been completed. One of the main drawbacks of the Monte-Carlo Potts model is the lack of physical time and length scales, although several remedies have been proposed to relate the MCS to real time, see for example [Gao and Thompson, 1996], [Raabe, 2000], [Liu and Lusk, 2002]. Another disadvantage of this type of model is the unsatisfactory non-linear relationship between grain boundary velocity and stored energy driving force, as pointed out by [Rollett and Raabe, 2001]. Finally, the use of a lattice in the Monte Carlo model introduces an inherent anisotropy that cannot be neglected if quantitative results are to be obtained [Mason et al., 2015]. However,

the simplicity of its implementation, computational efficiency and straightforward extension to 3D make it a widely used model to date, for example in additive manufacturing simulations [Wei et al., 2019].

I.5.2 Cellular automata

Similar to Monte Carlo Potts models, cellular automata are based on a discretisation of the microstructure into a grid of cells. A cellular automaton is then characterised by the geometry, neighbourhood and state of the cell, and the transition/switching rules that determine the state of the cell at the next time step. Note that the entire lattice is updated simultaneously.
Applications of cellular automata to recrystallization date back to [Hesselbarth and Göbel, 1991], where only two states were possible: either recrystallised or not. The definition of the states of the cells and the associated transformation rules make the cellular automaton approach very flexible and versatile. For example, in [Liu et al., 1996] the states of the cell account for grain orientations to simulate normal grain growth, and in [Raabe, 1998] probabilistic transformation rules are used. Another advantage of this method is that it can be efficiently parallelized with great scalability, resulting in fast simulations [Sitko et al., 2020]. However, it has been reported that the type of neighbourhood can influence the shape of grains [Janssens et al., 2007], and although stored energy driven migration is well accounted for, curvature driven migration is often neglected due to difficulties in evaluating the local curvature [Mason, 2015].

I.5.3 Level-set models

The use of level-set functions to describe grain growth and recrystallization has been extensively studied by Bernacki and colleagues since [Bernacki et al., 2008]. In this framework grain boundaries are defined as the zero isovalues of a signed distance function ϕ. The temporal evolution of ϕ is given by a transport equation

$$\frac{\partial \phi}{\partial t} + \underline{v} \cdot \nabla \phi = 0, \tag{1.14}$$

where $\underline{v}$ is the grain boundary velocity, which can be split into curvature and stored energy contributions. Grain boundary properties such as mobility and energy are well controlled and go directly into the expression for velocity. The framework allows to account for anisotropy of the grain boundary energy both in 2D and 3D [Hallberg, 2014; Hallberg and Bulatov, 2019]
When considering polycrystals, each grain is given an independent level set function ϕ_i and nucleation is treated by adding new level set functions. A recolouring scheme [Scholtes et al., 2016] can be used to reduce the total number of level set functions. A disadvantage of this approach is the loss of the distance properties of the level sets after transport, which requires a reinitialisation of these functions [Shakoor et al., 2015]. Interface reconstruction may also be needed for the localisation of triple junctions [Hallberg, 2013]. It is a rather algorithmically complex method associated with high computational cost, as remeshing operations may be required to correctly capture the isovalues of the level set functions or when a core is introduced [Sarrazola et al., 2020b]. Furthermore, this type of model is not formulated in a thermodynamic framework. However, despite the high computational cost and numerical difficulties, this approach has been coupled with crystal plasticity to simulate dynamic recrystallization in 3D [Sarrazola et al., 2020b,a].

I.5.4 Phase-field models

In phase-field models, microstructures are described by a set of continuous field variables. Sharp interfaces are made diffuse, allowing continuous variation of physical properties over a narrow region, as illustrated in Figure 1.11 [Moelans et al., 2008; Steinbach, 2009; Finel et al., 2010].

In this paradigm there is no need to explicitly trace the location of the interfaces as they are implicitly described by regions of large gradients of field variables, allowing complex morphologies to be taken into account [Moelans et al., 2008]. Another consequence of the diffuseness of the grain boundaries is the mitigation of the lattice anisotropy effect [Fan et al., 1997] that occurs in Monte Carlo Potts models. Based

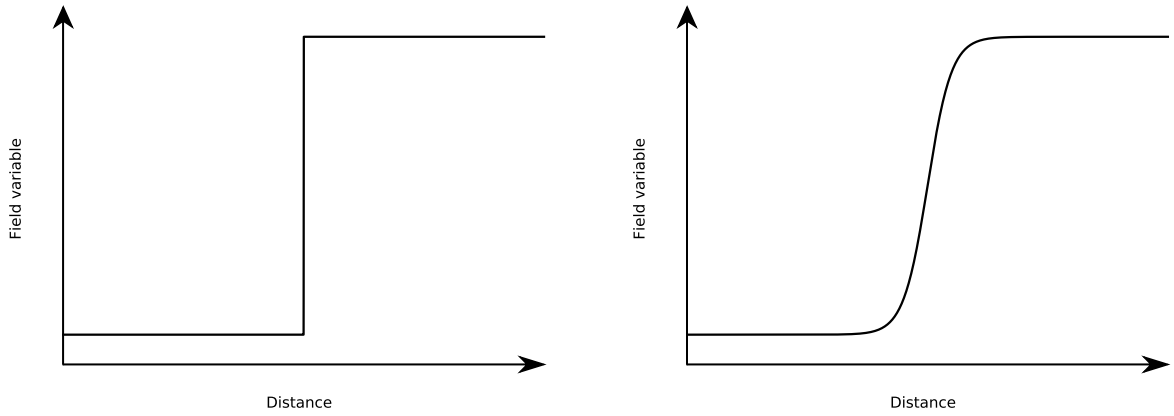

(a) *Sharp interface: discontinous properties* (b) *Diffuse interface: continous properties*

Figure 1.11: *Comparison between the sharp and diffuse interface approaches*

on a mathematical asymptotic analysis, it is possible to derive a "sharp interface limit" of phase field models which recovers the sharp interface behaviour [Elder et al., 2001]. These models are based on thermodynamic principles and include phenomenological parameters to account for material properties, which are derived from experimental and theoretical data [Moelans et al., 2008]. This is not always a trivial task, as will be shown later in the Kobayashi-Warren-Carter model [Kobayashi et al., 2000].
Two types of field variables are distinguished: conserved (e.g. concentration) and non-conserved (e.g. lattice orientation). The main components of phase field models are a free energy potential, which is a function of the field variables and their gradients, and a set of evolution equations describing the time evolution of these field variables. For grain growth applications, the earliest model, proposed by [Chen and Yang, 1994], was based on the following free energy:

$$\mathscr{F}_{CY} = \int_V \sum_{i=1}^{P} \frac{-\alpha}{2}\phi_i^2 + \frac{\beta}{4}\phi_i^4 + \gamma \sum_{i=1}^{P}\sum_{j>1}^{P} \phi_i^2\phi_j^2 + \sum_{i=1}^{P} \frac{\kappa_i}{2}(\nabla\phi_i)^2\, dV,$$

where ϕ_i are the nonconserved order parameters describing the grain orientations and α, β, γ, κ_i are coefficients. In this model the orientation in the grain is constant and equal to 1, while all other ϕ_i vanish. Consequently, there are as many ϕ_i as there are grains. Figure 1.12 shows a schematic microstructure and grain boundary obtained with the Chen-Yang model.

The evolution of the phase field variables is then given by the time-dependent Ginzburg-Landau or Allen-Cahn equation:

$$\frac{\partial\phi_i}{\partial t} = -M_i\frac{\delta\mathscr{F}_{CY}}{\delta\phi_i} = -M_i\left(\frac{\partial\mathscr{F}_{CY}}{\partial\phi_i} - \nabla\cdot\frac{\partial\mathscr{F}_{CY}}{\partial\nabla\phi_i}\right), \tag{1.15}$$

where M_i are kinetic coefficients.

I.5.4.1 Multi-phase-field model

In a similar approach proposed by Steinbach and colleagues [Steinbach and Pezzolla, 1999; Steinbach, 2009], called the Multi-Phase-Field (MPF) model, the interfacial energy γ_{ij} and width ℓ_{ij} enter directly into the free energy functional:

$$\mathscr{F}_{MPF} = \int_V \sum_{i,j=1,\, i\neq j}^{N} 4\frac{\gamma_{ij}}{\ell_{ij}}\left[-\frac{\ell_{ij}^2}{\pi^2}\nabla\phi_i\cdot\nabla\phi_j + \phi_i\phi_j\right] dV. \tag{1.16}$$

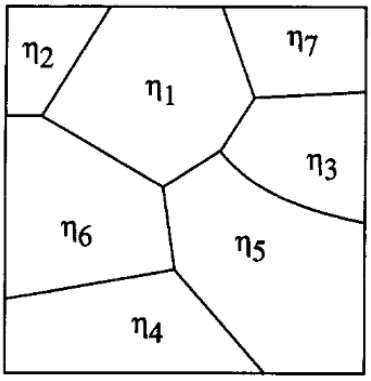

(a) *Schematic microstructure*

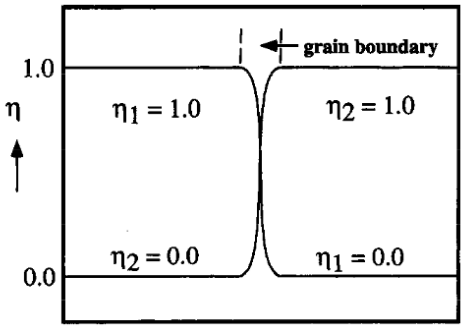

(b) *Schematic profiles of two phase-field variables across the flat grain boundary between grain 1 and grain 2*

Figure 1.12: *Schematic representations of a microstructure and the orientation fields across the grain boundary between grains 1 and 2, after [Chen and Yang, 1994]*

The phase field variables are assumed to represent volume fractions of grains of different orientations, and are therefore bounded by

$$\sum_{i=1}^{N} \phi_i = 1 \tag{1.17}$$

which is the main difference with the Chen-Yang model [Chen, 2002]. Another discrepancy lies in the evolution equations of the phase field variables, which take into account the influence of the other interfaces:

$$\frac{\partial \phi_i}{\partial t} = - \sum_{j=1,\ j\neq i}^{N} \frac{\pi^2}{8\ell_{ij}N} M_{ij} \left(\frac{\delta \mathscr{F}_{MPF}}{\delta \phi_i} - \frac{\delta \mathscr{F}_{MPF}}{\delta \phi_j} \right). \tag{1.18}$$

Both models suffer from the fact that grains are defined as regions of constant orientation and thus may not account for intragranular lattice reorientation due to simultaneous viscoplastic deformation and grain boundary migration. Furthermore, the computational cost is very high as the interfaces have to be discretised with sufficient resolution. Recent work in this area has led to the so-called Sharp Phase Field Method [Finel et al., 2018], which, based on an inherently discrete Chen-Yang type free energy functional, allows the interface width to be reduced to a single lattice point while retaining the grain growth kinetics of the classical phase field model [Dimokrati et al., 2020].

Due to their thermodynamic framework, phase field models can easily be extended to multiphysics. Indeed, other physical contributions, such as elastic strain or stored energy, can be taken into account by adding them to the free energy functional [Steinbach and Apel, 2006]. The MPF model has been coupled with mechanics in a staggered scheme to simulate static and dynamic recrystallization [Takaki et al., 2008a; Takaki and Tomita, 2010] with extension to 3D [Chen et al., 2015].

I.5.4.2 Kobayashi-Warren-Carter model

Unlike the MPF-type models, another phase field approach proposed in [Kobayashi et al., 2000] describes grain boundaries by relying on only two phase fields for the whole system: θ the lattice orientation and ϕ the crystal order, which is a coarse-grained measure of crystallinity. A schematic illustration of the phase-fields is given in Fig. 1.13, where it can be seen that the interface widths are different for both fields. It is however possible to decrease the interface thickness for ϕ by adopting a Modica-Mortola functional [Giga et al., 2023].

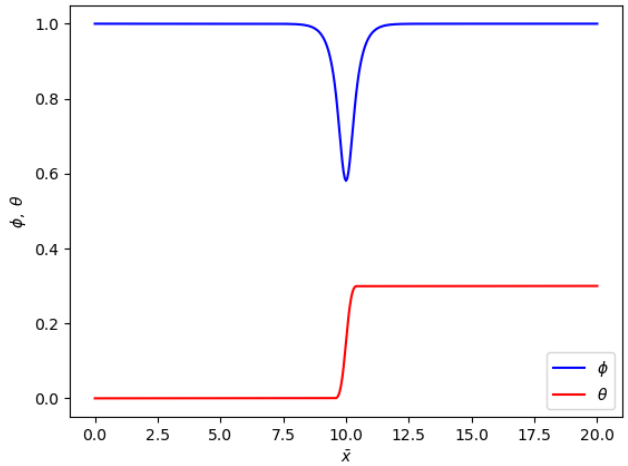

Figure 1.13: *Typical phase-field profiles in the KWC model*

This type of formulation allows for the occurrence of intragranular orientation gradients, thus making this model a strong candidate for the natural modelling of (sub)grain nucleation due to large intra/inter gradients. The frame-invariant free energy of the Kobayashi-Warren-Carter (KWC) model is given by

$$\mathscr{F}_{KWC} = \int_V f(\phi) + \frac{\alpha^2}{2}|\nabla\phi|^2 + sg(\phi)|\nabla\theta| + \frac{\varepsilon^2}{2}|h(\phi)\nabla\theta|^2 dV, \tag{1.19}$$

where $f(\phi)$ is a single well potential with minimum value at $\phi = 1$, $g(\phi)$ and $h(\phi)$ are coupling functions required to be positive definite, and α, s, ε are coefficients. The term $|\nabla\theta|$ allows to localise grain boundaries of finite width, while the term $|\nabla\theta|^2$ tends to smear the interfaces and is required to account for grain boundary motion. The time evolution of the phase fields is then given by the following gradient flow equations:

$$Q(\phi, \nabla\theta)\tau_\phi \frac{\partial\phi}{\partial t} = -\frac{\delta\mathscr{F}_{KWC}}{\delta\phi}, \tag{1.20}$$

$$P(\phi, \nabla\theta)\tau_\theta \frac{\partial\theta}{\partial t} = -\frac{\delta\mathscr{F}_{KWC}}{\delta\theta}, \tag{1.21}$$

where τ_ϕ, τ_θ are kinetic scaling factors and Q, P are inverse mobility functions.
A major drawback of this model is the non-trivial link between the model parameters and the grain boundary properties. In fact, the grain boundary energy and the mobility for curvature driven migration are obtained using a mathematically involved matched asymptotic expansion [Lobkovsky and Warren, 2001]. Coupled with crystal plasticity in a staggered scheme, the KWC model has been used to model recrystallization in [Takaki et al., 2008b], [Abrivard et al., 2012a] and more recently in [Luan et al., 2020].
Monolithic models coupling mechanics and microstructure evolution based on KWC have been proposed in [Admal et al., 2018] and [Ask et al., 2018b] by resorting to generalised continua. They provide a unified and thermodynamically consistent framework for modelling microstructure evolution, capable of accounting for concomitant deformation and grain boundary motion. The common feature of these models is the identification of the lattice orientation gradient in the KWC free energy with a generalised strain gauge: the geometrically necessary dislocation density tensor in Admal's model and the Cosserat curvature in Ask's model. However, the introduction of additional degrees of freedom and stiff equations to solve greatly increases the already high computational cost associated with the KWC model.

A wide variety of approaches have been proposed to simulate recrystallization and grain growth, notably Monte Carlo Potts, cellular automata, level-sets and phase-field methods. The advantages and drawbacks of

the models described above are summarized in table 1.3. Other less common approaches to simulate grain growth such as geometrical [Mahin et al., 1980; Jensen, 1992], tessellation updating method [Telley et al., 1992; Sakout et al., 2020], moving finite element [Kuprat, 2000; Kuprat et al., 2003; Gruber et al., 2005] and vertex models [Kawasaki et al., 1989; Piękoś et al., 2008; Mellbin et al., 2015] are not discussed here for the sake of brevity.

Model	Advantages	Drawbacks
Monte Carlo Potts	Easy implementation Computationaly efficient Straightforward extension to 3D	Complex link between Monte-Carlo step and physical time/length scales Inherent anisotropy due to the lattice Stored energy driven migration not satisfactory
Cellular automata	Very flexible and versatile Great scalability when parallelized	Definition of the cell's neighbourhood influences the shape of the grains Curvature is hard to handle
Level sets	Good control of GB properties Complex morphologies and shape changes	High computational cost Complex to implement No thermodynamic framework
Multiple phase fields (MPF & Yang-Chen)	Thermodynamically consistent Easy extension to multiphysics Complex morphologies and shape changes Good control of the GB properties	High computational cost No intragranular orientation gradients
KWC	Thermodynamically consistent Easy extension to multiphysics Accounts for intragranular orientation gradients Complex morphologies and shape changes	High computational cost No trivial relation between the parameters and the GB properties Two different interface widths

Table 1.3: *Main approaches to simulating recrystallization and grain growth*

I.5.5 Modelling grain nucleation

A major issue in the modelling of recrystallization is the treatment of nucleation. In fact, in numerical simulations it is not treated "naturally" by the models mentioned above, but rather - in an additional step in the model - by introducing spherical/circular nuclei based on a critical stored energy, dislocation density or strain criterion. It is also often restricted to grain boundaries, see for example [Scholtes et al., 2016; Sarrazola et al., 2020b] for necklace-type nucleation in the context of a crystal plasticity level set, or [Takaki et al., 2009; Luan et al., 2020] for nucleation at grain boundaries using a coupled crystal plasticity and MPF or KWC model. This nucleation step can also have a probabilistic character, as in [Li et al., 2020], where the probability of a nucleus appearing in the material follows a Weibull distribution involving dislocation densities. Takaki and Tomita [2010] simulated nucleation by subgrain growth with the MPF model. However, the subgrain structure was obtained by simulation of normal grain growth of circular seeds whose position and radius was predetermined. It cannot be termed as fully spontaneous. Within the context of cellular automaton modelling of recrystallization, a more spontaneous treatment of nucleation has been proposed by Hallberg and Ristinmaa [2013]. In this work, dislocation density concentrates at the grain boundaries and triple junctions, naturally providing the nucleation sites. The nuclei are then initiated where the dislocation density reaches a critical value and are assigned a random orientation from a uniform distribution. Therefore, this approach may be limited in modelling nucleation induced by intragranular lattice orientation gradients.

A promising model for simulating grain nucleation is that of Ask and colleagues [Ask et al., 2018b], as in a recent article [Ask et al., 2020] simulations showed nucleation of subgrain boundaries in conjunction with plastic strain/curvature localisation. In addition, these newly formed boundaries can exhibit spots of different orientation associated with a local decrease in dislocation density, which could be interpreted as nuclei.

I.6 Summary

The microstructural evolution that occurs during thermomechanical processing of crystalline materials is of paramount importance in predicting macroscopic properties. Static primary recrystallization, i.e. the formation and migration of high-angle grain boundaries that reduce the energy stored in the material, is a restoration process that has been studied for decades but is still not fully understood. However, there is experimental evidence that the nucleation stage of recrystallization occurs mainly in regions of large lattice orientation gradients such as grain boundaries, triple junctions or transition and shear bands. It has been shown that it can result from the migration of pre-existing high angle grain boundaries (SIBM) or from the rearrangement of subgrains into grains with high angle grain boundaries relative to their neighbours (subgrain coarsening and subgrain coalescence).

In order to deepen our understanding of the phenomenon and to achieve quantitative predictions of microstructures and properties, many approaches to full-field modelling of recrystallization have been developed, notably Monte Carlo Potts, cellular automata, level-sets and phase-field models. The latter is particularly promising due to their thermodynamic framework, which favours full coupling with continuum mechanics, as well as the implicit tracing of grain boundaries, which allows complex grain shapes and transformations to be taken into account. Among these, the KWC model appears to be a strong candidate for addressing a key issue in the modelling of recrystallization: the nucleation stage. In fact, up to now nuclei have been introduced as an additional step in the simulation, based on criteria such as the critical density of stored energy. However, the KWC model is thought to be able to naturally account for nucleation due to lattice orientation gradients. This will be demonstrated in the present work.

Chapter II

Mechanics of elastoplastic Cosserat continua

Résumé en français

Ce deuxième chapitre aborde la mécanique des milieux continus de Cosserat, l'objectif étant de présenter et illustrer cette formulation sur des exemples simples. Dans un premier temps, les équations de champs sont rappelées dans le cas de matériaux élastiques linéaires isotropes. Deux exemples sont étudiés de façon analytique et numériques tout au long de ce chapitre: la torsion d'un cylindre à section circulaire et le glissement simple d'une bande de matériau pour lequel le champ de microrotation est imposé nul aux bords. Dans le cas du glissement simple, différentes formulations du potentiel d'énergie libre vis-à-vis du tenseur de courbure sont envisagées: une contribution quadratique et une contribution de rang 1. Ce dernier cas étant non régulier pour une courbure nulle, le champ de microrotation est discontinu aux bords du domaine. Une tentative a également été faite de combiner à la fois un potentiel quadratique et un potentiel en norme pour se rapprocher du modèle à champ de phase de Kobayashi-Warren-Carter.

La seconde partie du chapitre est dédiée à l'étude de la torsion du cylindre dans le cas où la loi de comportement est elastoplastique isotrope. Une solution analytique est trouvée dans le cas simplifié où seule la partie symmétrique du déviatorique des contraintes intervient dans la contrainte équivalente, ce qui correspond à un critère de von Mises appliqué à la théorie de Cosserat. Une analyse limite permet de mettre en évidence un effet de taille proportionnel à l'inverse du rayon du cylindre. Des solutions pour des critères plus complexes faisant intervenir la partie antisymmetrique du tenseur des contraintes et le tenseur de couple-contrainte sont également obtenues numériquement par la méthode des éléments finis.

Enfin, la troisième partie de ce chapitre traite de la plasticité cristalline. Après avoir rappelé le cadre théorique du modèle, le cas du monocristal soumis un chargement de glissement simple est à nouveau étudié pour deux potentiels d'énergie libre différents. Une fois de plus, lorsque l'énergie libre dépend de la norme du tenseur de courbure à la puissance 1, le champ de microrotation présente une discontinuité aux bords du domaine.

Contents

II.1 Introduction

The thermodynamic framework of the KWC phase field model is well suited for coupling to mechanics via the free energy potential. Remarkably, it bears similarity to the formulation of Cosserat continuum mechanics [Cosserat and Cosserat, 1909], making it a strong candidate for a fully coupled model that accounts for simultaneous viscoplastic deformation and microstructure evolution. This chapter introduces Cosserat mechanics and proposes new analytical solutions to two academic problems: the torsion of an elastic-plastic cylinder adapted from Ghiglione and Forest [2022] and the shearing of a single crystal based on Forest and Ghiglione [2023]. The first part of this chapter deals with the formulation of Cosserat mechanics in elasticity, while the second and third parts focus respectively on generalised von Mises plasticity and crystal plasticity at small deformations.

II.2 Isotropic elastic behavior

II.2.1 Field equations

The theory of Cosserat/micropolar media was established by the Cosserat brothers [Cosserat and Cosserat, 1909] and was later extended to the general finite deformation setting by Kafadar and Eringen [1971]; Eringen [1976] and finally reported in the book [Eringen, 1999]. Eringen and Kafadar applied their theory to hyperelasticity of Cosserat media. The extension of this model to finite deformation elasto-viscoplasticity was proposed much later in [Dluzewski, 1992; Sievert, 1995; Sansour, 1998; Forest and Sievert, 2003]. The present work however concentrates on small deformations, rotations and curvatures because this theoretical framework is more easily amenable to analytical solutions in elasticity and even plasticity.

Cosserat material points are characterized by their displacement, $\underline{u}$, and microrotation degrees of freedom [Nowacki, 1986; Eringen, 1999]. The inclusion of microrotations makes Cosserat theory particularly amenable to model heterogeneous materials such as granular or particles-containing materials, since the size effects and the relative rotations between grains/particles are captured. It also allows, due to the presence of internal lengths, to address strain localization and, contrary to a Cauchy continuum, the width of the localisation zone is independent of the mesh size [Mühlhaus and Vardoulakis, 1987; Stefanou et al., 2017]. These internal lengths are thought to be scale parameters connected with long range interactions or geometry and thus are indicative of some nonlocality [Kunin, 1968, 1982, 1983]. The approach is not limited to metals, but can also be applied to block and masonry structures [Masiani and Trovalusci, 1996; Trovalusci and Masiani, 2003; Trovalusci and Pau, 2014; Sulem and Mühlhaus, 1997; Stefanou et al., 2008; Godio et al., 2014], random composites [Trovalusci et al., 2015], and geomaterials [Sulem et al., 2011; Stefanou et al., 2017; Rattez et al., 2018].
Early considerations of the incorporation of moments and oriented particles within a theory of elasticity include the molecular model of Voigt [1887, 1900, 1910] in which particles interact through forces and couples.

In the remainder of this work, the microrotation is represented by the axial vector $\underline{\theta}$. Within the small strain, small rotation and small curvature assumption, the Cosserat deformation measures are the relative deformation and curvature tensors defined as

$$\underline{e} = \underline{u} \otimes \nabla + \underline{\underline{\epsilon}} \cdot \underline{\theta}, \quad e_{ij} = u_{i,j} + \epsilon_{ijk}\, \theta_k, \tag{2.1}$$

$$\underline{\underline{\kappa}} = \underline{\theta} \otimes \nabla, \quad \kappa_{ij} = \theta_{i,j}, \tag{2.2}$$

in an orthonormal basis. The work-conjugate variables of the strain measures respectively are the force stress and couple-stress tensors, which, for an isotropic elastic medium, are given by:

$$\underline{\underline{\sigma}} = \lambda\, \mathrm{Tr}\big(\underline{\underline{e}}\big)\underline{\underline{I}} + 2\mu \underline{\underline{e}}^{\mathrm{sym}} + 2\mu_c \underline{\underline{e}}^{\mathrm{skew}}, \quad \sigma_{ij} = \lambda e_{kk}\delta_{ij} + 2\mu e_{ij}^{\mathrm{sym}} + 2\mu_c e_{ij}^{\mathrm{skew}} \tag{2.3}$$

$$\underset{\sim}{m} = \alpha\,\mathrm{Tr}\left(\underset{\sim}{\kappa}\right)\underset{\sim}{I} + 2\beta\underset{\sim}{\kappa}^{\mathrm{sym}} + 2\gamma\underset{\sim}{\kappa}^{\mathrm{skew}}, \quad \alpha\kappa_{kk}\delta_{ij} + 2\beta\,\kappa_{ij}^{\mathrm{sym}} + 2\gamma\kappa_{ij}^{\mathrm{skew}} \tag{2.4}$$

where λ and μ are the classical Lamé coefficients, μ_c is the Cosserat coupling modulus and α, β, γ are Cosserat bending-torsion moduli with force units. The quantities described above fulfil the static balance laws for momentum and moment of momentum

$$\underset{\sim}{\sigma} \cdot \nabla = 0, \quad \sigma_{ij,j} = 0, \tag{2.5}$$

$$\underset{\sim}{m} \cdot \nabla - \underset{\sim}{\epsilon} : \underset{\sim}{\sigma} = 0, \quad m_{ij,j} - \epsilon_{ijk}\,\sigma_{jk} = 0, \tag{2.6}$$

in the absence of body forces and couples. These field equations are accompanied by appropriate Neumann boundary conditions in the form

$$\underline{t} = \underset{\sim}{\sigma}.\underline{n}, \quad t_i = \sigma_{ij}n_j, \quad \underline{m} = \underset{\sim}{m}.\underline{n}, \quad m_i = m_{ij}n_j, \tag{2.7}$$

where $\underline{t}$ and $\underline{m}$ are surface traction and couple stress vectors.

II.2.2 Torsion of a cylinder with circular cross-section

Solutions of many boundary value problems in Cosserat elasticity have been made available in the literature since more than 50 years. Kim and Eringen [1973] solved the problem of the stress concentration at a hole in a micropolar plate. The general Saint-Venant problem was extended to elastic micropolar media in the case of circular cylinders by Reddy and Venkatasubramanian [1976]. The torsion problem is a particular case of the Saint-Venant problem and is the subject of the present work.

The analytical solution of an isotropic Cosserat bar subjected to torsional loading has been known since the work of Ieşan [1971] and Gauthier and Jahsman [1975]. It has been shown that the Cosserat formulation gives rise to characteristic lengths related to the microstructure. This effect has been studied numerically for anisotropic Cosserat bars in Taliercio and Veber [2016]. Torsional loading of elastoplastic materials leads to size effects which are not captured by classical continuum mechanics and require the use of enriched models. In this work, an analytical solution for the torsion of isotropic perfectly plastic Cosserat cylindrical bars with circular cross–section is derived in the case of generalized von Mises plasticity accounting solely for the symmetric part of the deviatoric stress tensor. The influence of the characteristic length on the microrotation, stress and strain profiles as well as torsional size effects are then investigated. In particular, a size effect proportional to the inverse of the radius of the cylinder is found for the normalized torque. A similar analysis for an extended plasticity criterion accounting for both the couple-stress tensor and the skew-symmetric part of the stress tensor is performed by means of systematic finite element simulations. These numerical experiments provide results regarding size effects which are similar to those predicted by the analytical solution. Saturation effects and limit loads are found when the couple stress tensor enters the yield function.

Note that the torsion problem has been solved for several other generalized continua like strain gradient elastic media [Lazopoulos and Lazopoulos, 2012; Iesan, 2013; Beheshti, 2018], and recently elastic stress gradient media [Kaiser et al., 2021]. The torsion of Cosserat bars is of physical relevance for the identification of Cosserat elasticity moduli and associated internal length scales [Gauthier and Jahsman, 1975]. This test was applied to several materials with highly heterogeneous microstructures like bones [Yang and Lakes, 1981] and other foam materials [Lakes, 1987; Onck, 2002]. Early solutions of the torsion problem for elastic Cosserat bars were provided by Smith [1967]; Ieşan [1971]. In the present work, the solution given by Taliercio and Veber [2016]; Drugan and Lakes [2018] will be recalled and used as a starting point for tackling the elastoplastic case.

II.2.2.1 Problem setting

Consider a solid cylinder of radius R and height L subjected to an angle of torsion $\pm\vartheta$ at the top and bottom surfaces respectively (figure 2.1). The difference between the angle of torsion at the top and that at the bottom is denoted $\Delta\vartheta$. The angle of torsion per unit length is written as

$$a = \frac{\Delta\vartheta}{L}. \tag{2.8}$$

The Cartesian coordinate $(\underline{e}_x, \underline{e}_y, \underline{e}_z)$ and the cylindrical coordinate $(\underline{e}_r, \underline{e}_\theta, \underline{e}_z)$ systems are shown in figure 2.1. The lateral sides of the cylinder are traction-free, namely:

$$\underset{\sim}{\boldsymbol{\sigma}}(r=R)\cdot\underline{e}_r = \underline{0}\,, \quad \underset{\sim}{\boldsymbol{m}}(r=R)\cdot\underline{e}_r = \underline{0}\,, \tag{2.9}$$

where $\underset{\sim}{\boldsymbol{\sigma}}$ and $\underset{\sim}{\boldsymbol{m}}$ are the (generally non-symmetric) Cosserat force and couple stress tensors.

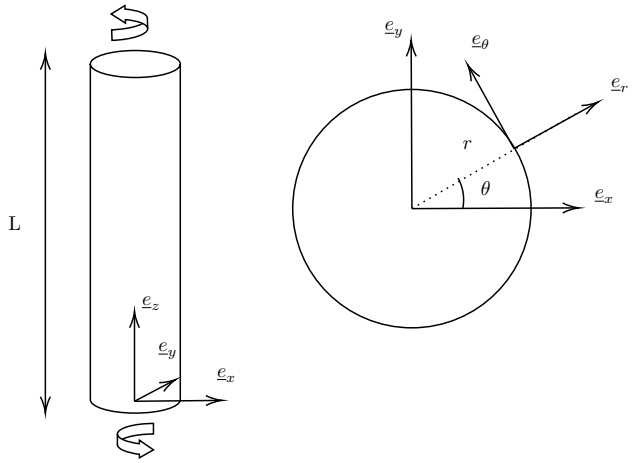

Figure 2.1: *Torsion of a cylindrical bar and coordinates systems.*

II.2.2.2 Problem solution

The analytical solution for an isotropic elastic Cosserat bar is recalled here in cylindrical coordinates. The displacement and micro-rotation fields are of the form:

$$\underline{u} = \begin{pmatrix} 0 \\ arz \\ 0 \end{pmatrix}, \quad \underline{\theta} = \begin{pmatrix} \theta(r) \\ 0 \\ az \end{pmatrix}. \tag{2.10}$$

The displacement vector is exactly the same as for a classical continuum. The micro-rotation field keeps the classical component $\theta_z = az$. However, the r component of the rotation is the unknown function $\theta_r = \theta(r)$ which, for symmetry reasons, can be assumed to only depend on r. The strain and curvature tensors are calculated using equations (2.1) and (2.2) respectively:

$$\underset{\sim}{\boldsymbol{e}} = \begin{pmatrix} 0 & 0 & 0 \\ 0 & 0 & ar+\theta \\ 0 & -\theta & 0 \end{pmatrix}, \quad \underset{\sim}{\boldsymbol{\kappa}} = \begin{pmatrix} \theta' & 0 & 0 \\ 0 & \dfrac{\theta}{r} & 0 \\ 0 & 0 & a \end{pmatrix}, \tag{2.11}$$

where $'$ denotes a derivation with respect to r. The stress and couple-stress tensors then follow from equations (2.3) and (2.4):

$$\underset{\sim}{\sigma} = \begin{pmatrix} 0 & 0 & 0 \\ 0 & 0 & (\mu+\mu_c)ar+2\mu_c\theta \\ 0 & (\mu-\mu_c)ar-2\mu_c\theta & 0 \end{pmatrix}, \tag{2.12}$$

$$\underset{\sim}{m} = \begin{pmatrix} (\alpha+2\beta)\theta'+\alpha\left(\dfrac{\theta}{r}+a\right) & 0 & 0 \\ 0 & (\alpha+2\beta)\dfrac{\theta}{r}+\alpha\left(\theta'+a\right) & 0 \\ 0 & 0 & (\alpha+2\beta)a+\alpha\left(\theta'+\dfrac{\theta}{r}\right) \end{pmatrix}. \tag{2.13}$$

The balance equation (2.6) gives:

$$m'_{rr}+\frac{m_{rr}-m_{\theta\theta}}{r}-(\sigma_{\theta z}-\sigma_{z\theta})=0. \tag{2.14}$$

Replacing the force stresses by their expressions one gets:

$$m'_{rr}+\frac{m_{rr}-m_{\theta\theta}}{r}-2\mu_c(ar+2\theta)=0, \tag{2.15}$$

which can finally be expressed as an ODE for the unknown function $\theta(r)$:

$$\theta''+\frac{\theta'}{r}-\left(\frac{4\mu_c}{\alpha+2\beta}+\frac{1}{r^2}\right)\theta=2\frac{\mu_c}{\alpha+2\beta}ar. \tag{2.16}$$

This differential equation is a modified Bessel equation with a non-zero right-hand side. The regular solution takes the form:

$$\theta(r)=AI_1\left(r/\ell\right)-\frac{a}{2}r, \quad \text{with} \quad \ell=\sqrt{\frac{\alpha+2\beta}{4\mu_c}}, \tag{2.17}$$

where I_1 is the modified Bessel function of the first kind, A is an integration constant and ℓ is the characteristic length, which only depends of the new moduli introduced by the Cosserat formulation. Note that $-\frac{a}{2}r$ is exactly the r component of the material rotation of a classical continuum subjected to torsion. The integration constant A can be determined from the traction-free boundary condition on the lateral sides of the cylinder:

$$\underset{\sim}{m}(r=R)\cdot\underline{e}_r=\underline{0} \Longrightarrow m_{rr}(r=R)=0 \Longrightarrow A=\frac{\beta aR}{4\mu_c\ell RI_0(R/\ell)-2\beta I_1(R/\ell)}. \tag{2.18}$$

The final expression for θ finally is:

$$\theta(r)=\frac{\beta aR}{4\mu_c\ell RI_0(R/\ell)-2\beta I_1(R/\ell)}I_1\left(r/\ell\right)-\frac{a}{2}r. \tag{2.19}$$

This analytical solution is now illustrated and used to validate the finite element implementation of the Cosserat model in Zset software [Besson and Foerch, 1997; Z-set, 2022]. More details regarding the implementation of the Cosserat element are given in reference Forest et al. [2000]. The radius and height of the cylinder are respectively $R=1$ mm and $L=10$ mm. The chosen material parameters are given in table 2.1, with for all cases $E=70000$ MPa, $\nu=0.3$, and $\mu_c=50000$ MPa. The simplification $\gamma=\beta$ is used throughout. The characteristic length of the medium will be varied in the analysis.

Figure 2.2 shows the influence of ℓ on the profiles of θ normalized by aR. Note that in classical Cauchy elasticity, the material rotation along axis $\underline{e}_r$ is $-ar/2$. It can be seen that as ℓ increases, so does θ. For the case $\ell\to 0$ the classical solution is retrieved.

ℓ [mm]	α [N]	β [N]
0.05	300	100
0.1	1000	500
0.2	4000	2000
0.9	62000	50000

Table 2.1: *Material parameters used for the calculations.*

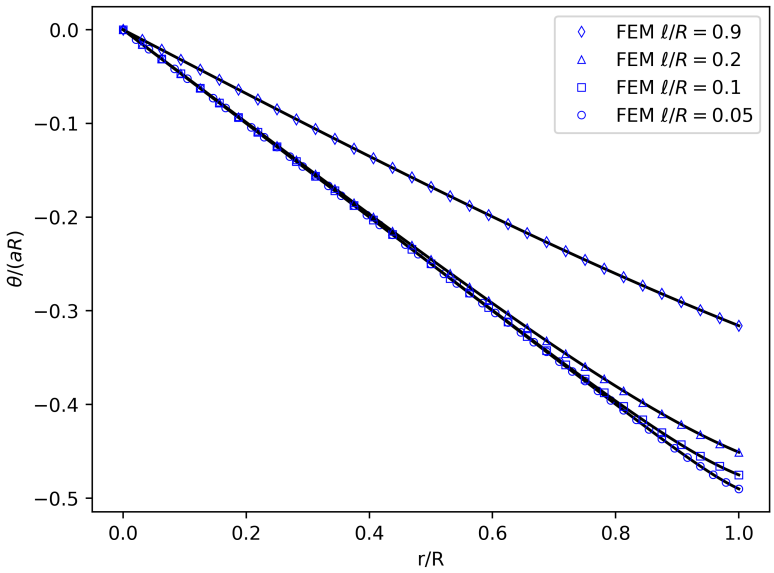

Figure 2.2: *Profiles of θ along a radius for various internal lengths for torsion in linear isotropic Cosserat elasticity. Analytical solutions are in black solid lines. Symbols denote finite element predictions.*

Figure 2.3 shows the influence of ℓ on the stress profiles of $\sigma_{\theta z}$ and $\sigma_{z\theta}$, normalized by the shear at the outer radius for a classical continuum, i.e. μaR. The curves are roughly symmetric with respect to the line $y = r/R$, $\sigma_{\theta z}$ and $\sigma_{z\theta}$ being respectively above and below that line. They tend to coincide with that line for decreasing length scale $\ell \to 0$, where the stress tensor becomes symmetric as expected in the classical case. Strong asymmetry is observed for large values of ℓ.

Finally, the sensitivity of the components of the couple-stress tensor to the characteristic length is illustrated in figure 2.4. The components $m_{rr}, m_{\theta\theta}$ and m_{zz} are normalized by the classical torque divided by the area of a subsection of the cylinder. The components of the couple-stress tensor are fairly uniform for low internal lengths. An increase in ℓ leads to nonlinear profiles as well as an increase of the maximum absolute value attained by the solution. Decreasing ℓ to zero leads to vanishing couple stress values, as it should be for a classical continuum. The boundary condition $m_{rr}(r = R) = 0$ is clearly satisfied, as can be seen on the profile of m_{rr}.

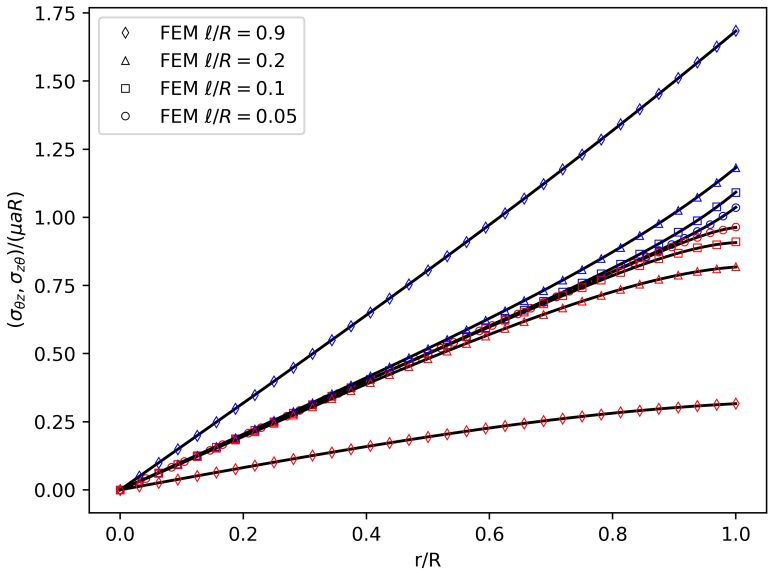

Figure 2.3: *Profiles of $\sigma_{\theta z}$ (in blue) and $\sigma_{z\theta}$ (in red) along a radius for various internal lengths, for torsion in linear isotropic Cosserat elasticity. Analytical solutions are in black solid lines. Symbols denote Finite Element predictions.*

II.2.2.3 Size effect

For a Cosserat continuum, the resulting torque on a given cross-section of the cylindrical bar involves two contributions: one from the stress tensor (moment of forces), as for classical media, and one from the couple-stress tensor (intrinsic surface couple), as follows:

$$\underline{M} = \int_0^{2\pi}\int_0^R \left(\underline{OM} \wedge \left(\underset{\sim}{\sigma}\cdot\underline{e}_z\right) + \underset{\sim}{m}\cdot\underline{e}_z\right) r dr d\theta. \tag{2.20}$$

The torque $\mathscr{C}$ is then simply the component of $\underline{M}$ with respect to axis z, given by:

$$\mathscr{C} = 2\pi\int_0^R (r\sigma_{\theta z} + m_{zz})\, r dr d\theta, \tag{2.21}$$

which in turn gives, in the linear isotropic elastic case:

$$\mathscr{C}^e = \mathscr{C}^e_{class}\left(1 + \frac{4\beta}{\mu R^2}\left(1 + \frac{\mu_c \ell R I_0(R/\ell) - \beta I_1(R/\ell)}{2\mu_c \ell R I_0(R/\ell) - \beta I_1(R/\ell)}\right)\right), \tag{2.22}$$

where the torque for a classical continuum reads:

$$\mathscr{C}^e_{class} = \pi\frac{\mu a R^4}{2}. \tag{2.23}$$

An alternative and useful expression has been derived by Taliercio and Veber [2016]:

$$\frac{\mathscr{C}^e}{\mathscr{C}^e_{class}} = 1 + \frac{4\beta}{\mu R^2}\left(2 - \left(2 - \frac{\beta I_1(R/\ell)}{\mu_c \ell R I_0(R/\ell)}\right)^{-1}\right). \tag{2.24}$$

Using this expression, various limit cases can be studied. Let us start with the case $R/\ell \to 0$. For fixed R, this limit behaviour can be obtained by taking $\ell \to +\infty$. According to formula (2.17), this situation

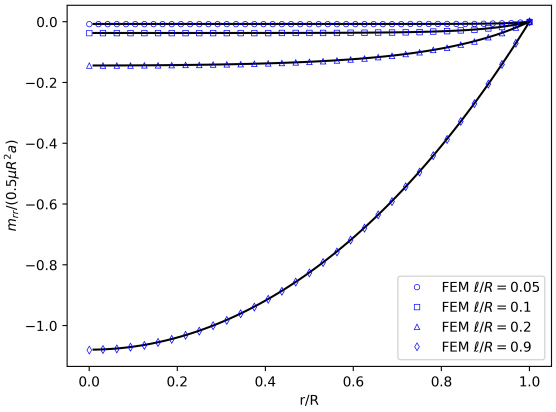

(a) *Profiles of* m_{rr}.

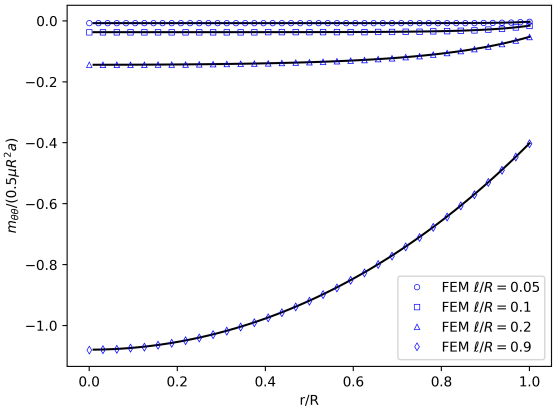

(b) *Profiles of* $m_{\theta\theta}$.

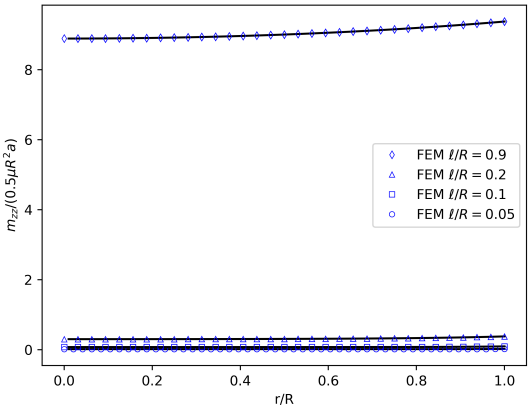

(c) *Profiles of* m_{zz}.

Figure 2.4: *Profiles of* m_{rr} *,* $m_{\theta\theta}$ *and* m_{zz} *along a i radius for various internal lengths in the case of linear isotropic Cosserat elasticity. Analytical solutions are in black solid lines. Symbols denote finite element predictions.*

can equivalently be studied either by taking $\mu_c \to 0$ keeping other parameter constants (which uncouples the micro-rotation and displacement fields but keeps the contribution of intrinsic couples to the resulting torque) or for both $\alpha, \beta \to +\infty$.
Using the equivalents

$$I_n(x) \sim \frac{(x/2)^n}{\Gamma(n+1)} \quad \text{for } x \to 0, \tag{2.25}$$

one gets:

$$I_0(R/\ell) \underset{\ell\to+\infty}{\to} 1, \quad I_1(R/\ell) \underset{\ell\to+\infty}{\to} \frac{R}{4\ell}, \tag{2.26}$$

and finally

$$\frac{\mathscr{C}^e}{\mathscr{C}^e_{class}} \underset{\ell\to+\infty}{\to} 1 + \frac{4\beta}{\mu R^2}\frac{3\alpha+4\beta}{2\alpha+3\beta}. \tag{2.27}$$

In this expression, a size effect proportional to R^{-2} clearly appears. This can be verified in figure 2.5, which illustrates in a log-log plot the ratio of torques as a function of the normalized radius. A fit is also plotted to verify the R^{-2} scaling. It can be seen that as $\frac{R}{\ell} \to +\infty$ the classical torque is retrieved, whereas for $\frac{R}{\ell} \to 0$ the ratio of torques increases. Thus, the smaller the radius of the cylinder, the stiffer the response. Note

that this result seems to also hold true for more general prismatic bars, as investigated by Drugan and Lakes [2018].
Another interesting limit case arises when $\mu_c \to +\infty$ and other parameters are fixed, which leads to:

$$\frac{\mathscr{C}^e}{\mathscr{C}^e_{class}} \underset{\ell \to +0}{\to} 1 + \frac{6\beta}{\mu R^2}. \tag{2.28}$$

This corresponds to the solution obtained for Koiter's couple stress theory, which constrains the micro-rotation to be equal to the material rotation.

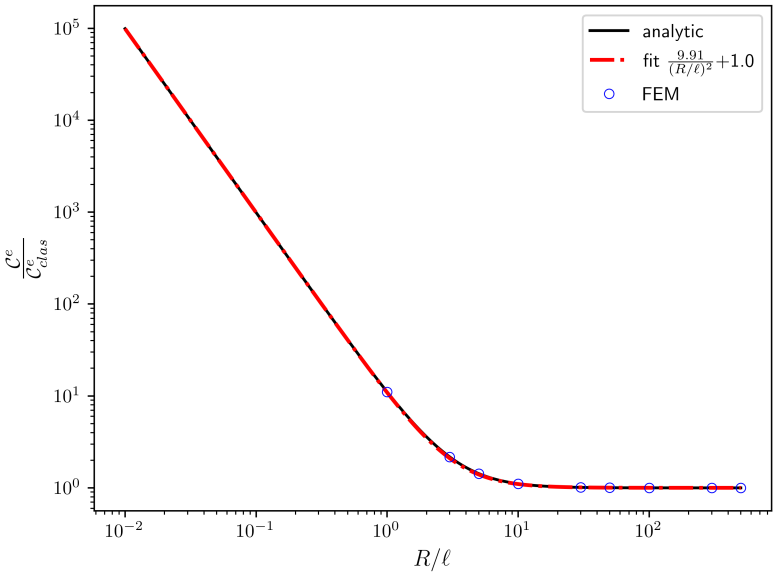

Figure 2.5: *Cosserat torque normalized by that of a Cauchy continuum as a function of the bar's normalized radius for* $\ell = 0.1$ *mm.*

II.2.3 Simple glide

The size-dependent response of a Cosserat continuum is also evaluated in the case of a simple one-dimensional shear test involving one single slip system and vanishing microrotation prescribed at the boundaries of a material strip of width $2L$. The inhomogeneous distribution of slip in the channel mimics the piling-up of dislocations against the boundaries. The free energy density function depends on the elastic strain and Cosserat curvature tensors. Two types of potentials are examined with respect to the curvature tensor, namely a quadratic function of its norm, on the one hand, and the norm itself, on the second hand. The first model is very often used but turns out to be non-physical since, according to physical metallurgy, the stored energy is proportional to the dislocation density (here the density of geometrically necessary dislocations) rather than its square. Analytical solutions are derived first considering pure elasticity in the present section, and crystal plasticity in section II.4.2. The scaling laws predicted by these models are shown to be L^{-2} or L^{-1}, respectively. The latter scaling is reminiscent of Orowan's law of yielding [Hirth and Lothe, 1982]. Finally, a third type of potential involving both quadratic and rank-one contributions of the norm of the curvature tensor, similar to the KWC model for grain boundaries, is assessed in pure elasticity for the sake of simplicity.

II.2.3.1 Studied boundary value problem

The one-dimensional simple shear problem of Fig. 2.6 is considered successively for several choices of the free energy potential and Schmid law. It involves a single slip system $(\underline{\ell}, \underline{n})$ respectively parallel to the two first vectors of the orthonormal basis $(\underline{e}_1, \underline{e}_2, \underline{e}_3)$. The origin is located at the centre of the strip of width $2L$ and height H. The height H is regarded as infinite so that the solution is invariant along the $y-$direction.

The unknown displacement and microrotation fields take the following simple form:

$$\underline{u} = \bar{\gamma} y \underline{e}_1 + u(x)\underline{e}_2, \quad \underline{\theta} = \theta(x)\underline{e}_3, \tag{2.29}$$

where the mean shear amount $\bar{\gamma}$ is prescribed to the strip. The total deformation and curvature tensors follow

$$\underset{\sim}{e} = (\bar{\gamma} + \theta)\underline{e}_1 \otimes \underline{e}_2 + (u' - \theta)\underline{e}_2 \otimes e_1, \quad \underset{\sim}{\kappa} = \theta' \underline{e}_3 \otimes \underline{e}_1, \tag{2.30}$$

where $u(x)$ and $\theta(x)$ are the main unknowns of the problem. The notation u' is set for the derivative of $u(x)$ with respect to x.

The following boundary conditions are enforced:

$$u(0) = 0, \quad u(-L) = u(L), \quad \theta(-L) = \theta(L) = 0. \tag{2.31}$$

The first condition sets the rigid body translation and the second set of conditions correspond to periodicity requirement of the fluctuation $u(x)$. Finally, the micro-clamping conditions for the Cosserat rotation mimic the piling-up of dislocations at the left and right boundaries.

II.2.3.2 Simple glide in isotropic elasticity

The boundary value problem of section II.2.3.1 is first solved in the case of linear isotropic elasticity, i.e. in the absence of plasticity. The isotropic elasticity laws are given by equations 2.6 and 2.5 In the particular case of simple shear, the non-vanishing components of the stress tensors are

$$\sigma_{12} = (\mu + \mu_c)\bar{\gamma} + (\mu - \mu_c)u' + 2\mu_c\theta, \tag{2.32}$$

$$\sigma_{21} = (\mu - \mu_c)\bar{\gamma} + (\mu + \mu_c)u' - 2\mu_c\theta, \tag{2.33}$$

$$m_{31} = 2\beta\theta'. \tag{2.34}$$

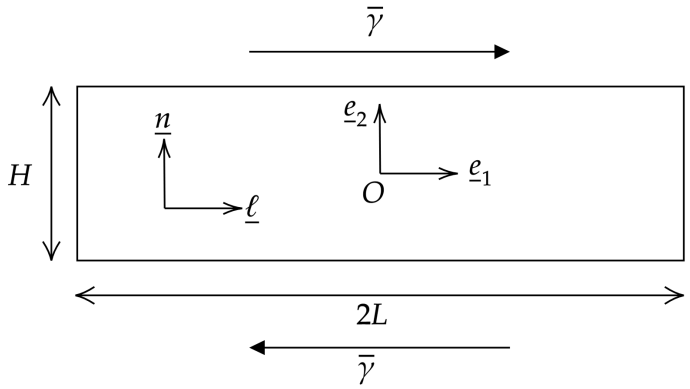

Figure 2.6: *Geometry of the simple shear boundary value problem in crystal plasticity involving a single slip system.*

The force stress balance tells that $\sigma_{12,2} = \sigma_{21,1} = 0$ so that σ_{21} is uniform. This provides a first differential equation

$$(\mu + \mu_c)u'' - 2\mu_c\theta' = 0 \quad \Longrightarrow \quad u'' = \frac{2\mu_c}{\mu + \mu_c}\theta'. \tag{2.35}$$

On the other hand, the couple stress balance equation yields

$$m_{31,1} - (\sigma_{12} - \sigma_{21}) = 0, \tag{2.36}$$

$$\beta\theta'' - \mu_c(\bar{\gamma} - u' + 2\theta) = 0. \tag{2.37}$$

The combination of the previous equations leads to the following differential equation for θ

$$\theta''' = \omega^2\theta', \quad \text{with} \quad \omega = \sqrt{\frac{2\mu\mu_c}{\beta(\mu + \mu_c)}}, \tag{2.38}$$

from which the microrotation function is deduced, after consideration of the boundary conditions $(2.31)_3$,

$$\theta(x) = a(\cosh(\omega x) - \cosh(\omega L)). \tag{2.39}$$

The displacement function then follows from Eq. (2.35):

$$u(x) = \frac{2\mu_c}{\mu + \mu_c}\frac{a}{\omega}\sinh(\omega x) + bx + c. \tag{2.40}$$

The boundary conditions $(2.31)_{1,2}$ are used to determine the constants b and c:

$$u(x) = \frac{2\mu_c}{\mu + \mu_c}\frac{a}{\omega}(\sinh(\omega x) - \frac{x}{L}\sinh(\omega L)). \tag{2.41}$$

The integration constant a is finally determined by inserting the found functions in Eq. (2.37):

$$a = \frac{\bar{\gamma}}{2(\cosh(\omega L) - \frac{\mu_c}{\mu + \mu_c}\frac{\sinh(\omega L)}{\omega L})}. \tag{2.42}$$

The parameters given in table 2.2 are used throughout this work, unless explicitly specified otherwise. Comparisons of the analytical and FEM solutions for the displacement and microrotation fields are plotted in figure 2.7, which shows a perfect agreement between the solutions.

Parameter	value
2L [mm]	20
H [mm]	1
E [MPa]	70000
ν	0.3
μ_c [MPa]	10000
α [N]	0
β [N]	26923.8

Table 2.2: *Parameters used for computing analytical and numerical solutions.*

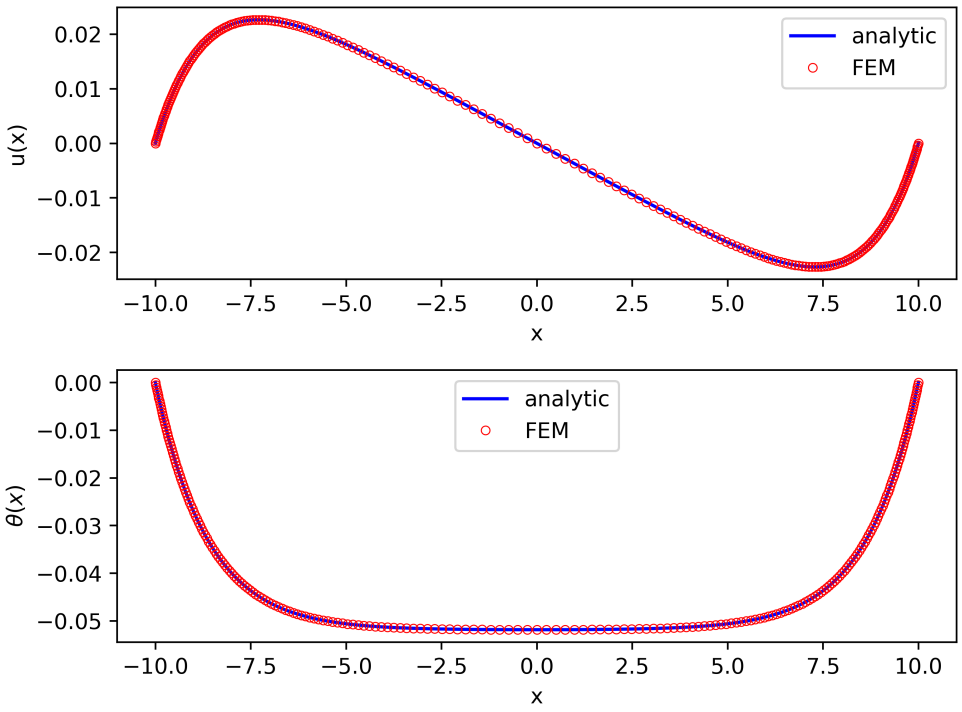

Figure 2.7: *Cosserat elasticity, displacement and microrotation fields. finite element simulations are compared to the analytical solution, based on the parameters of table 2.2.*

II.2.3.3 Rank one energy potential

In this section, a non-quadratic free energy potential is adopted

$$\psi(\underset{\sim}{e}^e, \underset{\sim}{\kappa}) = \frac{1}{2}\underset{\sim}{e}^e : \underset{\approx}{\Lambda} : \underset{\sim}{e}^e + A\|\underset{\sim}{\kappa}\|, \quad \text{with} \quad \|\underset{\sim}{\kappa}\| = \sqrt{\underset{\sim}{\kappa} : \underset{\sim}{\kappa}}, \tag{2.43}$$

involving the norm of the curvature tensor. The force and couple stress tensors are then given by

$$\underset{\sim}{\sigma} = \frac{\partial \psi}{\partial \underset{\sim}{e}^e} = \underset{\approx}{\Lambda} : \underset{\sim}{e}^e, \tag{2.44}$$

$$\underset{\sim}{m} = \frac{\partial \psi}{\partial \underset{\sim}{\kappa}} = A\frac{\underset{\sim}{\kappa}}{\|\underset{\sim}{\kappa}\|}. \tag{2.45}$$

It is apparent that the couple stress tensor is singular in the case of vanishing curvature.

In the one-dimensional shear problem studied here, the single non-vanishing component of the couple stress tensor is

$$m_{31} = A\frac{\theta'}{|\theta'|}. \tag{2.46}$$

In the elastic case, $\underset{\sim}{e}^e \equiv \underset{\sim}{e}$. The microrotation profile is searched for in the following form:

$$\theta(x) = \bar{\theta}(H(x+L) - H(x-L)), \tag{2.47}$$
$$\theta'(x) = \bar{\theta}(\delta(x+L) - \delta(x-L)), \tag{2.48}$$

which means that the microrotation takes the unknown uniform value $\bar{\theta}$ in $]-L:L[$ and is indeterminate at the ends of the interval. The expression involves the Heaviside function and the Dirac distribution such that

$$H'(x-a) = \delta(x-a). \tag{2.49}$$

The uniform rotation field corresponds to the classical solution in the absence of curvature. The difference in the Cosserat case is that curvature energy is now concentrated at the boundaries.

It follows that the couple stress component is indeterminate due to the vanishing of θ'. The total work balance equation is therefore used for a suitable treatment of the distribution functions:

$$\int_V \underset{\sim}{\sigma} : (\underline{u} \otimes \nabla + \underset{\approx}{\epsilon} \cdot \underline{\theta}) + \underset{\sim}{m} : \underset{\sim}{\kappa}\, dV = \int_{\partial V} \underline{t} \cdot \underline{u} + \underline{m} \cdot \underline{\theta}\, dS. \tag{2.50}$$

The volume V is the infinite ribbon $[-L:L] \times \mathbb{R}$ and invariance along y is assumed. The application of the divergence theorem and the Neumann condition $\underline{t} = \underset{\sim}{\sigma} \cdot \underline{n}$ are used to eliminate the $\underline{u} \otimes \nabla$ and $\underline{t} \cdot \underline{u}$ terms (Eq. 2.50), while the last term vanishes due to the vanishing microrotation boundary conditions. It remains

$$\int_V \underset{\sim}{\sigma} : \underset{\approx}{\epsilon} \cdot \underline{\theta} + \underset{\sim}{m} : (\underline{\theta} \otimes \nabla)\, dV = 0. \tag{2.51}$$

Keeping only the non-vanishing components, the latter becomes

$$\int_{-L}^{L} (\sigma_{12} - \sigma_{21})\theta + m_{31}\theta'\, dx = \int_{-L}^{L} (\sigma_{12} - \sigma_{21})\theta + A|\theta'|\, dx = 0, \tag{2.52}$$

where $m_{31}\theta' = A\theta'^2/|\theta'|$ has been used. After considering Eq. (2.48), the last integral is evaluated as

$$\int_{-L}^{L} A|\theta'|dx = A|\bar{\theta}| \int |(\delta(x+L) - \delta(x-L))|dx = 2A|\bar{\theta}|. \tag{2.53}$$

The first contribution in Eq. (2.52) is then evaluated as

$$\int_{-L}^{L} (\sigma_{12} - \sigma_{21})\theta\, dx = \int_{-L}^{L} 2\mu_c(\bar{\gamma} - u' + 2\theta)\theta\, dx = 4\mu_c\bar{\theta}L(\bar{\gamma} + 2\bar{\theta}), \tag{2.54}$$

taking the periodicity of u into account. Finally, the combination of the two found relations provides the value

$$\bar{\theta} = -\frac{\bar{\gamma}}{2} - \frac{A}{4\mu_c L}\text{sign}\bar{\theta} = -\frac{\bar{\gamma}}{2} + \frac{A}{4\mu_c L}\text{sign}\bar{\gamma}, \tag{2.55}$$

where $\bar{\theta}$ and $\bar{\gamma}$ have opposite signs for sufficiently high values of μ_c. The limit case $\mu_c \to +\infty$ constrains $\bar{\theta}$ to coincide with the material rotation $-\bar{\gamma}/2$. Fig. 2.8 shows the profiles of θ for potentials that are quadratic and a rank 1 with respect to the curvature tensor. Physically, the resulting rotation field is interpreted as corresponding to dislocation pile-up at the boundaries in the case of the quadratic potential and the formation of dislocation walls for the rank 1 potential.

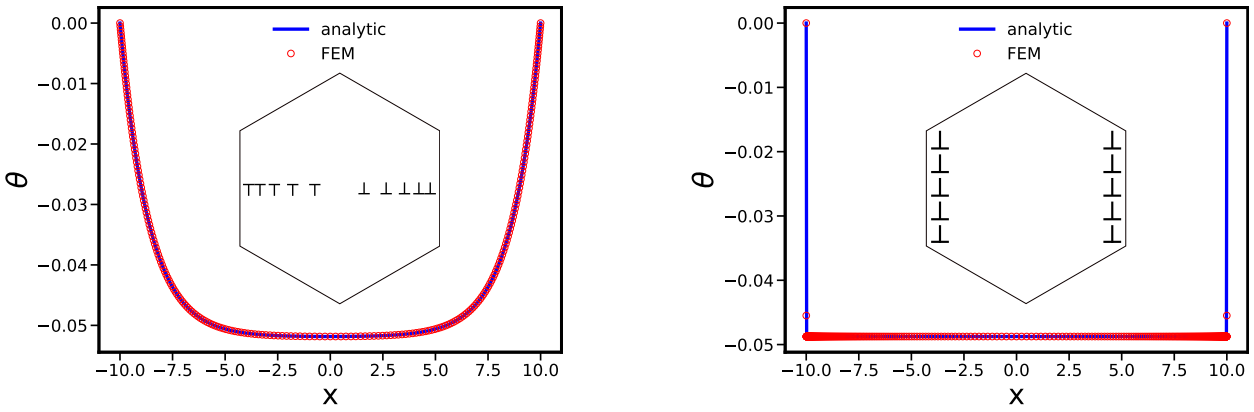

(a) *Quadratic potential* (b) *Rank 1 potential*

Figure 2.8: *Comparison of the rotation field obtained with a quadratic (left) and rank 1 (right) potential in the problem of simple glide*

Finally, the displacement field is obtained from the shear stress component

$$\sigma_{21} = (\mu + \mu_c)u' + (\mu - \mu_c)\bar{\gamma} - 2\mu_c\theta. \tag{2.56}$$

According to equilibrium, this component is uniform from which we deduce that $u'' = 0$ so that $u(x)$ is linear.

The couple stress component m_{31} is indeterminate in the interval $]-L:L[$ where θ' vanishes. Let us assume that it is uniform in this interval. This, combined with the balance of moment of momentum equation, implies that the skew symmetric part of the stress tensor also vanishes. Finally,

$$u = (\bar{\gamma} + 2\theta)x = \frac{A}{2\mu_c L} x \operatorname{sign}\bar{\gamma}, \quad \forall x \in]-L:L[. \tag{2.57}$$

This fluctuation vanishes for $\mu_c \to \infty$ or vanishing length scale.

II.2.3.4 Combined potential

In this section, a free energy involving both quadratic and norm potentials is considered

$$\psi(\underset{\sim}{e}^e, \underset{\sim}{\kappa}) = \frac{1}{2}\underset{\sim}{e}^e : \underset{\approx}{\Lambda} : \underset{\sim}{e}^e + \frac{1}{2}\underset{\sim}{\kappa} : \underset{\approx}{C} : \underset{\sim}{\kappa} + A\|\underset{\sim}{\kappa}\|, \quad \text{with} \quad \|\underset{\sim}{\kappa}\| = \sqrt{\underset{\sim}{\kappa} : \underset{\sim}{\kappa}}. \tag{2.58}$$

The simple and couple stress tensors are then given by

$$\underset{\sim}{\sigma} = \frac{\partial \psi}{\partial e^e} = \underset{\approx}{\Lambda} : \underset{\sim}{e}^e, \tag{2.59}$$

$$\underset{\sim}{m} = \frac{\partial \psi}{\partial \underset{\sim}{\kappa}} = \underset{\approx}{C} : \underset{\sim}{\kappa} + A\frac{\underset{\sim}{\kappa}}{\|\underset{\sim}{\kappa}\|}. \tag{2.60}$$

In the problem considered in this work, the only non-vanishing component of the couple-stress tensor is

$$m_{31} = 2\beta\theta' + A\frac{\theta'}{|\theta'|}. \tag{2.61}$$

More precisely,

$$m_{31}(x) = 2\beta\theta - A, \quad \text{if} \quad x < 0, \tag{2.62}$$

$$= 2\beta\theta + A, \quad \text{if} \quad x > 0, \tag{2.63}$$

considering the situation where $\theta(x)$ is decreasing (resp. increasing) on $[-L,0]$ (resp. $[0,L]$). In that case, the curvature is indeterminate only at $x=0$. The field equations (2.36) to (2.38) from section II.2.3.2 are valid in the present context. The solution has cosh form but there is a jump of sign θ' at zero. The micro-rotation field is therefore assumed to be of the following form:

$$\theta(x) = a^+\cosh(\omega x)+b^+\sinh(\omega x)+c^+, \quad \text{if} \quad x>0, \tag{2.64}$$
$$= a^-\cosh(\omega x)+b^-\sinh(\omega x)+c^-, \quad \text{if} \quad x<0. \tag{2.65}$$

The microtation field is an even function, $\theta(x)=\theta(-x)$, which results in

$$a^+=a^-=a, \quad b^+=-b^-=b, \quad c^+=c^-. \tag{2.66}$$

The boundary conditions, $\theta(-L)=\theta(L)=0$, give

$$c=-(a\cosh(\omega L)+b\sinh(\omega L)). \tag{2.67}$$

The integration constant b can be found by ensuring the continuity of the couple stress at $x=0$, $m_{31}(0^-)=m_{31}(0^+)$, due to the unhindered transmission of the couple stress vector,

$$2\beta\omega b+A=-2\beta\omega b-A \quad \Longrightarrow \quad b=\frac{-A}{2\beta\omega}. \tag{2.68}$$

According to Eq. (2.62) and (2.63), the continuity of m_{31} results in a jump of θ' at $x=0$. Finally, the last integration constant a is obtained after integrating the equilibrium equation for the couple-stress

$$\int_{-L}^{L} m_{31,1}dx=\int_{-L}^{L}\sigma_{12}-\sigma_{21}dx. \tag{2.69}$$

The couple stress $m_{31}(x)$ being an odd function, the left hand-side of the above equation is evaluated as

$$\int_{-L}^{L} m_{31,1}dx \quad =2\lim_{\epsilon\to 0}\int_{\epsilon}^{L} m^+_{31,1}dx, \tag{2.70}$$

$$\int_{-L}^{L} m_{31,1}dx=4\beta\omega\left(a\sinh(\omega L)+b\cosh(\omega L)\right)+2A, \tag{2.71}$$

whereas the second integral to be evaluated gives

$$\int_{-L}^{L}\sigma_{12}-\sigma_{21}dx=\int_{-L}^{L}2\mu_c\left(\bar{\gamma}-u'+2\theta\right)dx, \tag{2.72}$$

$$\int_{-L}^{L}\sigma_{12}-\sigma_{21}dx=4\mu_c\left[\bar{\gamma}L+2\left(\frac{a}{\omega}\sinh(\omega L)+\frac{b}{\omega}\left(\cosh(\omega L)-1\right)+cL\right)\right], \tag{2.73}$$

where the periodicity of u and θ has been accounted for. Eq. (2.69) now becomes

$$4\beta\omega\left(a\sinh(\omega L)+b\cosh(\omega L)\right)+2A=4\mu_c\left[\bar{\gamma}L+2\left(\frac{a}{\omega}\sinh(\omega L)+\frac{b}{\omega}\left(\cosh(\omega L)-1\right)+cL\right)\right]. \tag{2.74}$$

After replacing the constants b and c by their found values one gets

$$a=\frac{2\mu\mu_c L\bar{\gamma}+A(L\omega(\mu+\mu_c)\sinh(\omega L)+\mu_c(1-\cosh(\omega L))}{4\mu\mu_c L\cosh(\omega L)-2\mu_c\beta\omega\sinh(\omega L)}. \tag{2.75}$$

The microrotation field is continuous at $x=0$ but its first derivative experiences a jump at this location.

II.3 Isotropic elastoplastic structures

II.3.1 Formulation of rate-independent Cosserat plasticity

The framework of Cosserat rate-independent plasticity in a general case is briefly introduced here. Extensions of the von Mises plasticity criterion to Cosserat media go back to pioneering contributions by Neuber [1966, 1968]; Lippmann [1969]; Besdo [1974]; Sawczuk [1967]. First applications to the plasticity of metals were proposed by Diepolder et al. [1991]; Lippmann [1995]. A single, extended von Mises equivalent stress measure incorporating both the stress and couple-stress tensors, adapted from [Besdo, 1974; Diepolder et al., 1991], is given in the following form:

$$\sigma_{eq}(\underset{\sim}{\sigma},\underset{\sim}{m}) = \sqrt{\frac{3}{2}\left(\underset{\sim}{\sigma}'^{\,\mathrm{sym}} : \underset{\sim}{\sigma}'^{\,\mathrm{sym}} + b\underset{\sim}{\sigma}^{\mathrm{skew}} : \underset{\sim}{\sigma}^{\mathrm{skew}} + c_1\underset{\sim}{m}^{\mathrm{sym}} : \underset{\sim}{m}^{\mathrm{sym}} + c_2\underset{\sim}{m}^{\mathrm{skew}} : \underset{\sim}{m}^{\mathrm{skew}}\right)}. \tag{2.76}$$

The proposed extended von Mises yield function for the Cosserat continuum is given by:

$$f(\underset{\sim}{\sigma},\underset{\sim}{m}) = \sigma_{eq}(\underset{\sim}{\sigma},\underset{\sim}{m}) - \sigma_Y, \tag{2.77}$$

where σ_Y is the current value of the yield stress.

The total deformation and curvature tensors are split into elastic and plastic parts:

$$\underset{\sim}{e} = \underset{\sim}{e}^e + \underset{\sim}{e}^p, \quad \underset{\sim}{\kappa} = \underset{\sim}{\kappa}^e + \underset{\sim}{\kappa}^p. \tag{2.78}$$

The plastic strain and curvature rates are then derived from a generalized normality rule in the form:

$$\dot{\underset{\sim}{e}}^p = \dot{p}\frac{\partial f}{\partial \underset{\sim}{\sigma}}, \quad \dot{\underset{\sim}{\kappa}}^p = \dot{p}\frac{\partial f}{\partial \underset{\sim}{m}}, \tag{2.79}$$

where $\dot{p}$ is a single plastic multiplier. Time integration of the plastic multiplier provides the path-dependent cumulative plastic slip variable p. In the case of the present extended von Mises yield criterion, this gives

$$\dot{\underset{\sim}{e}}^p = \dot{p}\frac{3}{2}\frac{\underset{\sim}{\sigma}'^{\mathrm{sym}} + b\underset{\sim}{\sigma}^{\mathrm{skew}}}{\sigma_{eq}(\underset{\sim}{\sigma},\underset{\sim}{m})}, \quad \dot{\underset{\sim}{\kappa}}^p = \dot{p}\frac{3}{2}\frac{c_1\underset{\sim}{m}^{\mathrm{sym}} + c_2\underset{\sim}{m}^{\mathrm{skew}}}{\sigma_{eq}(\underset{\sim}{\sigma},\underset{\sim}{m})}. \tag{2.80}$$

The plastic multiplier can be expressed as the following norm of the plastic strain and curvature rates:

$$\dot{p} = \sqrt{\frac{2}{3}\left(\dot{\underset{\sim}{e}}^{p\ \mathrm{sym}} : \dot{\underset{\sim}{e}}^{p\ \mathrm{sym}} + \frac{1}{b}\dot{\underset{\sim}{e}}^{p\ \mathrm{skew}} : \dot{\underset{\sim}{e}}^{p\ \mathrm{skew}} + \frac{1}{c_1}\dot{\underset{\sim}{\kappa}}^{p\ \mathrm{sym}} : \dot{\underset{\sim}{\kappa}}^{p\ \mathrm{sym}} + \frac{1}{c_2}\dot{\underset{\sim}{\kappa}}^{p\ \mathrm{skew}} : \dot{\underset{\sim}{\kappa}}^{p\ \mathrm{skew}}\right)}. \tag{2.81}$$

It is such that $\underset{\sim}{\sigma} : \dot{\underset{\sim}{e}}^p + \underset{\sim}{m} : \dot{\underset{\sim}{\kappa}}^p = \sigma_{eq}\dot{p}$. The yield stress can be a function $\sigma_Y(p)$ to describe isotropic hardening of the material. In the present work, hardening is not considered for simplicity and σ_Y is a constant value, the initial yield threshold, corresponding to perfect plasticity.

II.3.2 Torsion of a cylinder

Kaplunov and Lippmann [1995] provided the first asymptotic solution for the elastic-plastic Cosserat continuum in the case of torsion of circular cylinders. More recently, torsion in Cosserat plasticity was considered from the computational perspective by Grammenoudis and Tsakmakis [2005, 2009] which allows for the consideration of isotropic and kinematic hardening.

The objective of the present work is to provide a fully explicit analytical solution of the torsion problem for elastic perfectly plastic Cosserat bars with circular cross-section. This is made possible by the use of a simplified version of the general extension of the von Mises yield function to Cosserat media. The reduced form includes an equivalent stress measure that depends solely on the symmetric part of the force–

stress tensor. The proposed solution is then compared to finite element results in the case of more general formulations involving the skew–symmetric part of the force–stress tensor and the full couple–stress tensor. The analytical solution is shown to be sufficient to exhibit the main features of the elastic–plastic response of Cosserat bars including stress-strain distributions in the cross–subsection. In particular it predicts size effects depending on the ratio between the bar radius and the intrinsic length arising in the elasticity solution.

II.3.2.1 Analytical solution in a simplified case

An analytical solution is derived in the following particular case of formula (2.76):

$$b = 0, \quad c_1 = c_2 = 0. \tag{2.82}$$

The yield function reduces in that case formally to the classical von Mises criterion involving the quadratic norm of the symmetric deviatoric stress tensor:

$$\sigma_{eq}(\underset{\sim}{\sigma}) = \sqrt{\frac{3}{2}\underset{\sim}{\sigma}'^{\mathrm{sym}} : \underset{\sim}{\sigma}'^{\mathrm{sym}}}. \tag{2.83}$$

Plasticity occurs when $f(\underset{\sim}{\sigma}) = 0$. In the torsion case, this gives

$$\frac{3}{4}(\sigma_{\theta z} + \sigma_{z\theta})^2 = \sigma_Y^2. \tag{2.84}$$

Making use of equation (2.84), $\sigma_{\theta z}$ and $\sigma_{z\theta}$ can be related by the following formula:

$$\sigma_{z\theta} = \frac{2\sigma_Y}{\sqrt{3}} - \sigma_{\theta z}, \tag{2.85}$$

assuming that the loading is such that $\sigma_{\theta z} + \sigma_{z\theta} \geq 0$.

Starting from the elasticity solution exhibited in the previous subsection, the yield criterion will be reached at the outer boundary $r = R$ for a critical value of the loading a_l computed as

$$a_l = \frac{\sigma_Y}{\mu R\sqrt{3}}. \tag{2.86}$$

For increasing torsion loading, the bar cross-section will be split into a central disc of radius r_l where the yield stress has not been reached yet (elastic core), and an annulus $r_l \leq r \leq R$ in which plastic yielding takes place (plastic zone):

$$r_l = \frac{\sigma_Y}{\mu a\sqrt{3}}. \tag{2.87}$$

For the yield criterion presented in equation (2.83), the expressions of r_l and a_l are the same as for a classical continuum.

Figure 2.9 shows the cumulative plastic strain at two different steps of the torsional loading of the Cosserat elastoplastic bar. The elastic core is shrinking with increasing load.

The total deformation induced by torsion is still given by equation (2.11). It is now decomposed into elastic and plastic contributions:

$$\begin{cases} e^e_{\theta z} + e^p_{\theta z} = ar + \theta, \\ e^e_{z\theta} + e^p_{z\theta} = -\theta. \end{cases} \tag{2.88}$$

The elastic strain tensor is obtained by inverting the isotropic elasticity law, equation (2.3). For monotonic loading, the plastic strain tensor is derived directly from equation (2.80):

$$\underset{\sim}{e}^e = \frac{1}{4\mu\mu_c}\left((\mu+\mu_c)\underset{\sim}{\sigma} + (\mu_c-\mu)\underset{\sim}{\sigma}^T\right), \quad \underset{\sim}{e}^p = p\frac{3}{4\sigma_Y}(\underset{\sim}{\sigma} + \underset{\sim}{\sigma}^T) \tag{2.89}$$

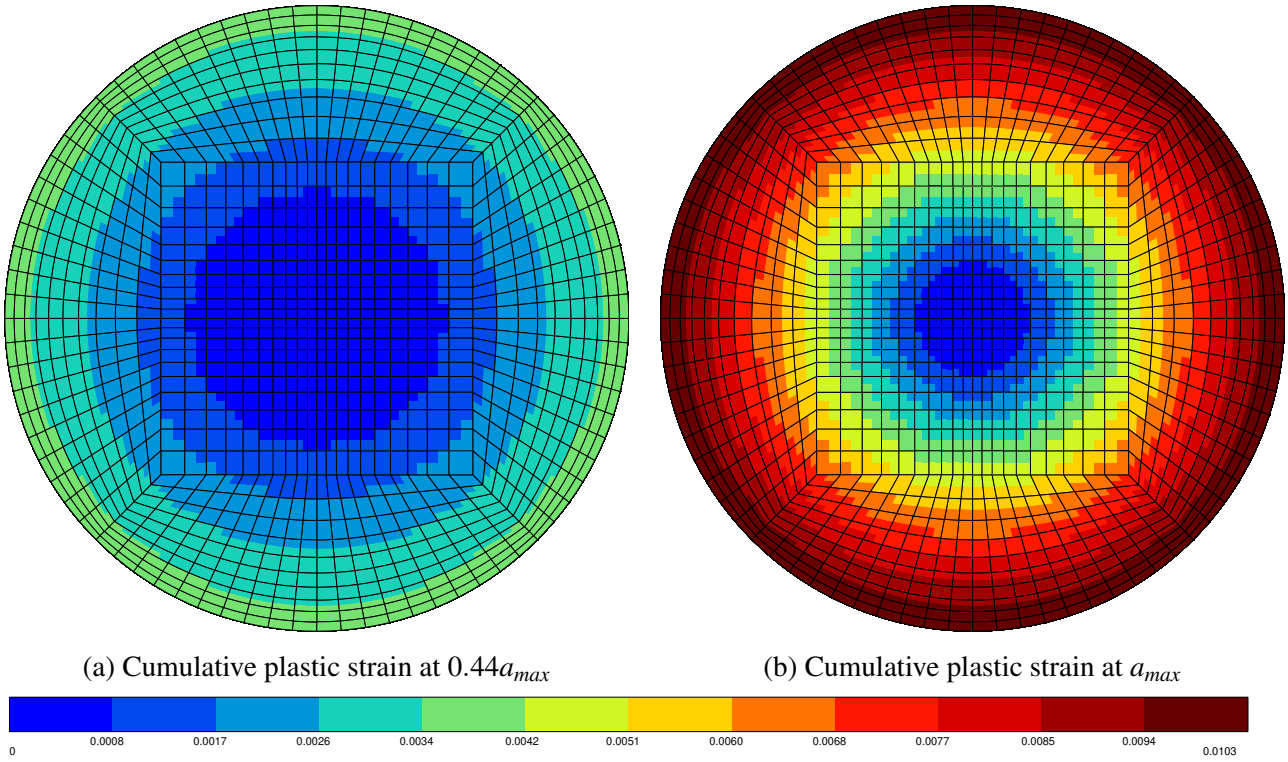

(a) Cumulative plastic strain at $0.44a_{max}$ (b) Cumulative plastic strain at a_{max}

Figure 2.9: *Evolution of the cumulative plastic strain represented on the reference configuration for an imposed maximum angle of torsion* $a_{max} = 0.02$ *rad/mm and* $\ell/R = 0.2$. *The reduced yield function (2.83) is used.*

Substituting the strains given in equation (2.89) into the system of equations (2.88) allows to derive an analytical expression for the plastic strain p:

$$p = \frac{\sigma_Y}{\frac{3}{4}(\sigma_{\theta z} + \sigma_{z\theta})} \left(-\theta - \frac{1}{4\mu\mu_c} \left(\sigma_{z\theta}(\mu + \mu_c) + \sigma_{\theta z}(\mu_c - \mu) \right) \right). \tag{2.90}$$

Finally, substituting this expression of p in the system of equation (2.88) and using equation (2.84), the stress components are fully determined as

$$\begin{cases} \sigma_{\theta z} = \mu_c(ar + 2\theta) + \frac{\sigma_Y}{\sqrt{3}}, \\ \sigma_{z\theta} = -\mu_c(ar + 2\theta) + \frac{\sigma_Y}{\sqrt{3}}. \end{cases} \tag{2.91}$$

Contrary to the classical case, the stress tensor is not uniform in the plastic zone, even though no hardening is present. Moreover, this stress tensor is not symmetric.
Using equation (2.91), equation (2.90) simply reduces to the following expression, which is the same as for a Cauchy continuum:

$$p = \begin{cases} 0 & \text{for } r \leq r_l, \\ \frac{a}{\sqrt{3}}(r - r_l) & \text{else.} \end{cases} \tag{2.92}$$

The profile of p along a normalized radius is shown in figure 2.10 where it can be seen that it is null for $r \leq r_l$ and increases linearly for $r > r_l$.

The obtained stress tensor must also satisfy the moment of momentum balance equation:

$$m'_{rr} + \frac{m_{rr} - m_{\theta\theta}}{r} - (\sigma_{\theta z} - \sigma_{z\theta}) = 0. \tag{2.93}$$

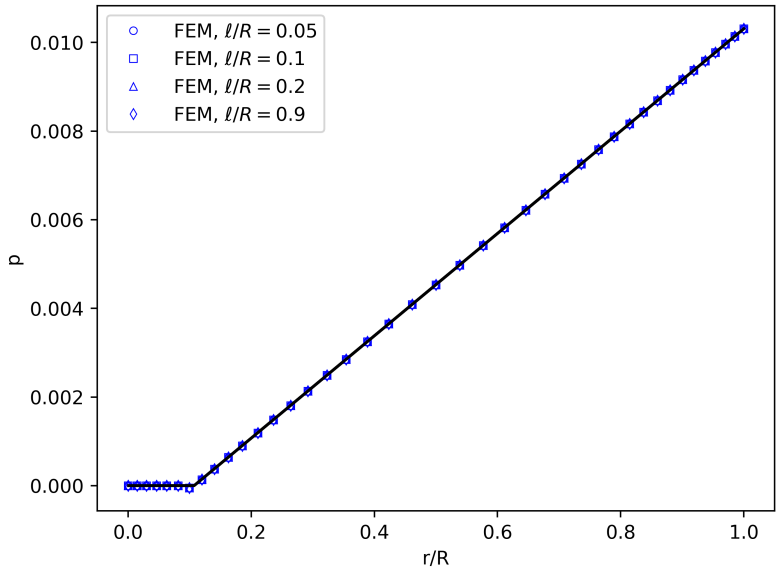

Figure 2.10: *Profiles of cumulative plastic strain p along a radius for various internal lengths and* $a = 0.02$ *rad/mm. Analytical solutions are in black solid lines. Symbols denote finite element predictions. The reduced yield function (2.83) is used.*

Replacing $\sigma_{\theta z}$ and $\sigma_{z\theta}$ by their expression given in equation (2.91), the balance equation becomes:

$$m'_{rr} + \frac{m_{rr} - m_{\theta\theta}}{r} - \left(\mu_c(ar + 2\theta) + \frac{\sigma_Y}{2\sqrt{a_1}} - \left(-\mu_c(ar + 2\theta) + \frac{\sigma_Y}{2\sqrt{a_1}}\right)\right) = 0, \tag{2.94}$$

which reduces to:

$$m'_{rr} + \frac{m_{rr} - m_{\theta\theta}}{r} - 2\mu_c(ar + 2\theta) = 0. \tag{2.95}$$

This equation is exactly the same as equation (2.15) derived in the purely elastic case. Since the simplified criterion (2.83) does not involve the couple-stress tensor, $\underset{\sim}{m}$ keeps its purely elastic form. The ODE governing θ therefore is necessarily the same as for the elastic case and given by equation (2.16). The final expression of θ (2.19) is still valid.

The stress fields can be visualized in figure 2.11. As expected from equation (2.91) $\sigma_{\theta z}$ has greater values than $\sigma_{z\theta}$. Figure 2.12 shows the profiles of these stresses normalized by the shear stress value at the outer radius for a classical continuum μaR, as functions of the normalized radial coordinate. Just like in the elastic case presented in subsection II.2.2.2, the stresses symmetrically deviate from the classical solution and the point at which this deviation occurs decreases with increasing internal length. For a large characteristic length the elastic response ($r \leq r_l$) differs from the Cauchy one and the stresses distributions are not really symmetric with respect to that of a classical continuum.

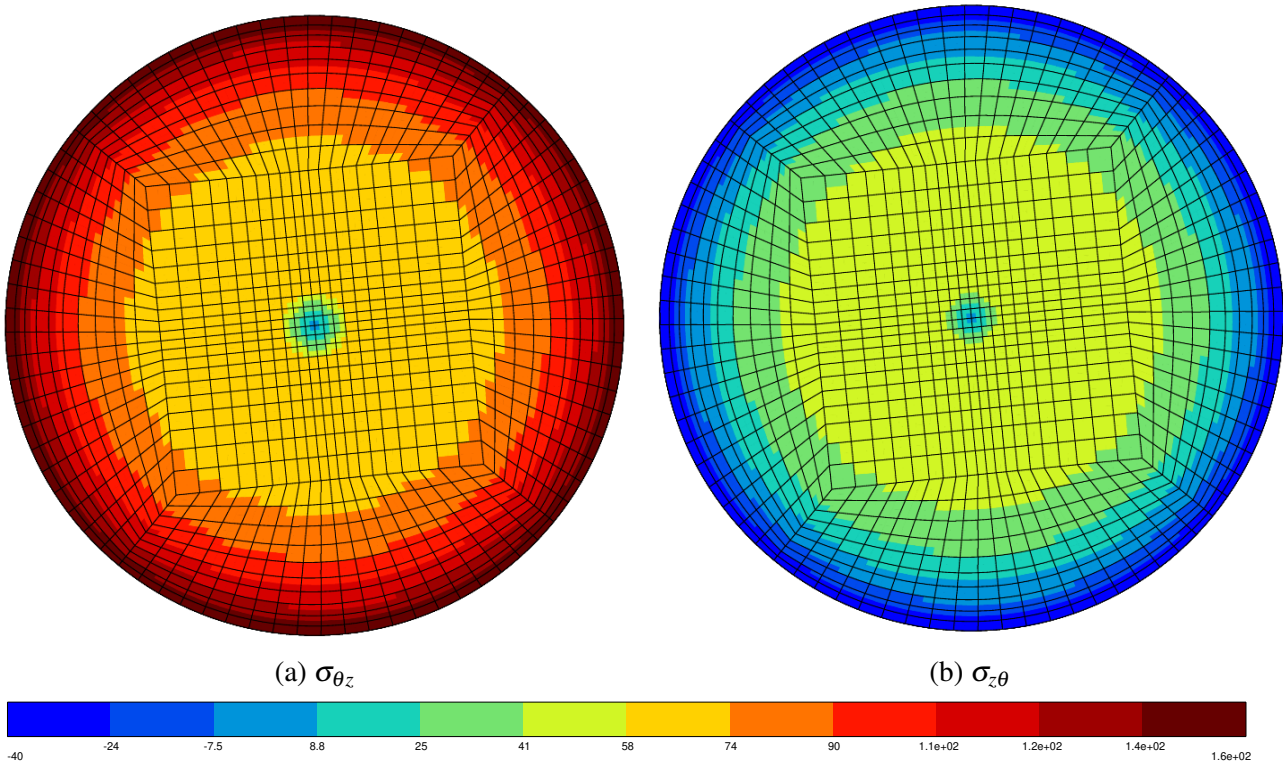

Figure 2.11: *Fields of the $\sigma_{\theta z}$ and $\sigma_{z\theta}$ stress components represented on the deformed configuration for an imposed twist angle $a = 0.02$ rad/mm and $\ell/R = 0.2$. The reduced equivalent stress (2.83) is used in the yield function.*

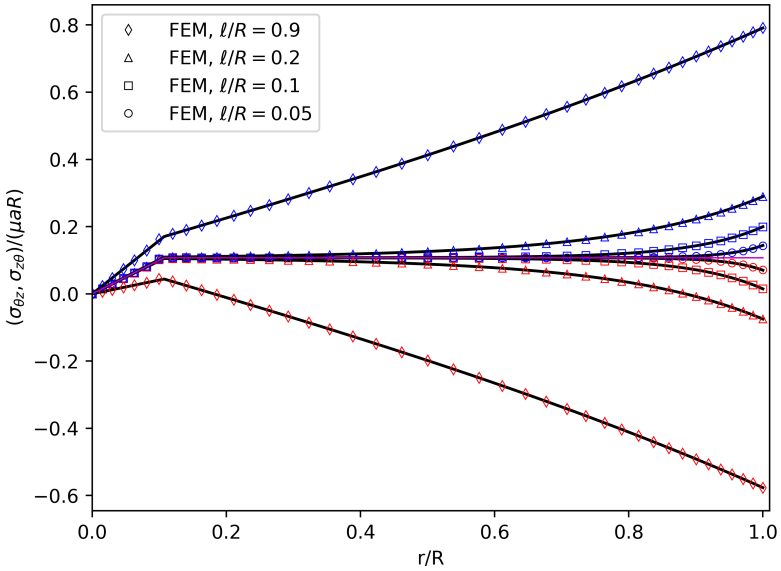

Figure 2.12: *Profiles of $\sigma_{\theta z}$ (in blue) and $\sigma_{z\theta}$ (in red) along a radius for several values of the internal length and loading $a = 0.02$ rad/mm. Analytical solutions are in black solid lines. Symbols denote finite element predictions. The reference solution for a classical continuum is in purple solid line. The reduced equivalent stress (2.83) is used in the yield function.*

II.3.2.2 Size effect

As plasticity does not occur for $a \leq a_l$, the torque must be separated into two parts: the torque produced for a purely elastic bar and the one corresponding to elastoplastic deformation of the bar. For the elastoplastic part, an elastic core zone exists for $r \leq r_l$. The contribution of the stress tensor to the total torque can be split into elastic (for $r \leq r_l$) and plastic (for $r \geq r_l$) parts. In the end, the moment takes the following form:

$$\mathscr{C} = \begin{cases} 2\pi \int_0^R r\sigma_{\theta z}^{\text{elastic zone}} + m_{zz} r dr d\theta, & \text{for } a \leq a_l, \\ 2\pi \int_0^{r_l} r\sigma_{\theta z}^{\text{elastic zone}} r dr d\theta + \int_{r_l}^R r\sigma_{\theta z}^{\text{plastic zone}} r dr d\theta + \int_0^R m_{zz} dr d\theta, & \text{for } a \geq a_l. \end{cases} \tag{2.96}$$

After integration, the expressions of the torque are:

$$\mathscr{C} = \pi \frac{\mu a R^4}{2} \left(1 + \frac{4\beta}{\mu R^2} \left(1 + \frac{\mu_c l R I_0(R/\ell) - \beta I_1(R/\ell)}{2\mu_c l R I_0(R/\ell) - \beta I_1(R/\ell)} \right) \right), \quad \text{for } a \leq a_l, \tag{2.97}$$

$$\begin{aligned} \mathscr{C} &= 2\pi \left[\frac{\mu a r_l^4}{4} + \frac{\sigma_Y}{3\sqrt{3}} \left(R^3 - r_l^3 \right) + 2\mu_c A \ell^3 \left(\left(\frac{R}{\ell} \right)^2 I_0(R/\ell) - 2\frac{R}{\ell} I_1(R/\ell) \right) \right. \\ &+ \left. \beta R^2 a + \alpha A R I_1(R/\ell) \right], \quad \text{for} \quad a \geq a_l. \end{aligned} \tag{2.98}$$

The second expression can be expanded by inserting the value (2.9) of the integration constant A (the same value as in the purely elastic case as discussed earlier), for $a \geq a_l$:

$$\begin{aligned} \mathscr{C} = 2\pi \left[\frac{\mu a r_l^4}{4} + \frac{\sigma_Y}{3\sqrt{3}} \left(R^3 - r_l^3 \right) + \beta R^2 a \right. \\ \left. + \frac{\beta a R}{4\mu_c \ell R I_0(R/\ell) - 2\beta I_1(R/\ell)} \left(2\mu_c \ell^3 \left(\left(\frac{R}{\ell} \right)^2 I_0(R/\ell) - 2\frac{R}{\ell} I_1(R/\ell) \right) + \alpha R I_1(R/\ell) \right) \right]. \end{aligned} \tag{2.99}$$

In the latter expression, the torque for a classical elastoplastic material $\mathscr{C}_{class}^p$ appears:

$$\mathscr{C}_{class}^p = 2\pi \left[\frac{\mu a r_l^4}{4} + \frac{\sigma_Y}{3\sqrt{3}} \left(R^3 - r_l^3 \right) \right]. \tag{2.100}$$

For a Cauchy continuum the torque-twist angle curve exhibits a plateau as $a \to \infty$, which corresponds to the case where the plastic zone invades the whole cylinder, i.e $r_l \to 0$. This limit value of the torque is given by:

$$\mathscr{C}_{class}^{\infty} = \lim_{a \to \infty} \mathscr{C}_{class}^p = \frac{2\pi\sigma_Y}{3\sqrt{3}} R^3. \tag{2.101}$$

However, for a Cosserat continuum with the yield criterion involving the reduced invariant (2.83), such a saturation of the torque does not occur. This is illustrated in figure 2.13. This figure shows the total torque as well as its different contributions normalized by R^3 as functions of the shear strain at the outer radius, as classically done in other works [Fleck et al., 1994; Grammenoudis and Tsakmakis, 2009] for both analytical and FEM solutions. Although no hardening is present in the model, an apparent hardening is visible on this curve. This is due to the last term proportional to the twist angle a in the equation (2.99). This term has two contributions. One is related to the fact that there is no limit for the couple stress component m_{zz} since it does not enter the reduced yield criterion. The second contribution stems from the fact that the sum $\sigma_{\theta z} + \sigma_{z\theta}$ is bounded due to the yield condition, but not the individual components. An excellent agreement is found between the analytical and finite element solutions, as it should.

As for the elastic case, a size effect occurs with the elastoplastic model studied in this subsection. Consider $\ell \to +\infty$, combining the equivalents given in equation (2.26) with the expression of the torque in

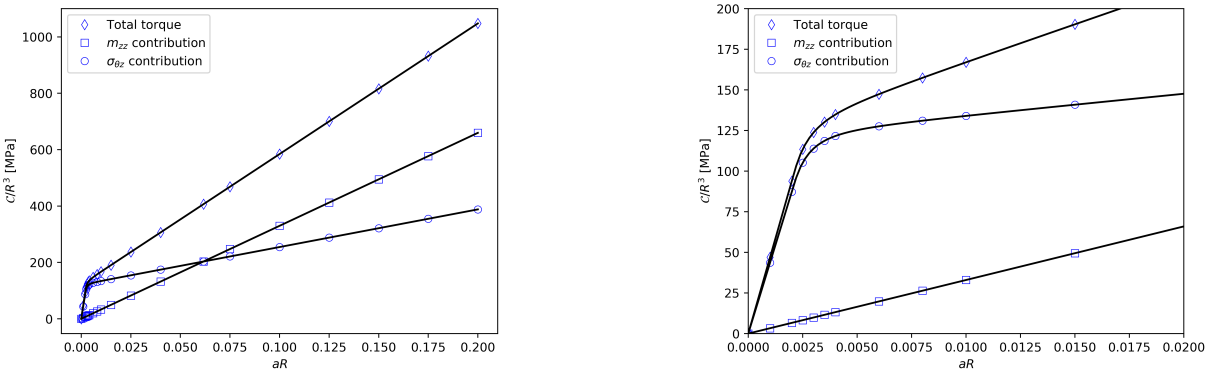

(a) *Normalized torque as a function of the classical shear strain.*

(b) *Normalized torque as a function of the classical shear strain, zoom on the beginning of the curve.*

Figure 2.13: *Normalized torque as a function of the classical shear strain with* $\ell/R = 0.1$. *Analytical solutions are in black solid lines. The reduced equivalent stress (2.83) is used in the yield function.*

the plastic zone equation (2.99) one gets:

$$\mathscr{C} \sim \mathscr{C}_{class} + 2\pi\beta R^2 a \left(1 + \frac{\alpha+\beta}{2\alpha+3\beta}\right), \tag{2.102}$$

and the expression of the normalized torque is then:

$$\frac{\mathscr{C}}{\mathscr{C}^{\infty}_{class}} \sim \frac{\mathscr{C}_{class}}{\mathscr{C}^{\infty}_{class}} + \frac{3\sqrt{3}\beta}{\sigma_Y}\left(1 + \frac{\alpha+\beta}{2\alpha+3\beta}\right)\frac{a}{R}. \tag{2.103}$$

Agreement between the expression of the torque (2.99) and its equivalent (2.103) has been studied numerically and holds true for $\alpha \gg \beta$. Moreover, though a slight accuracy loss occurs, equation (2.103) can be further simplified :

$$\frac{\mathscr{C}}{\mathscr{C}^{\infty}_{class}} \sim 1 + \frac{3\sqrt{3}\beta}{\sigma_Y}\left(1 + \frac{\alpha+\beta}{2\alpha+3\beta}\right)\frac{a}{R}. \tag{2.104}$$

From this expression, a size effect clearly appears. In contrast to the elastic case, the normalized torque is proportional to R^{-1}, instead of R^{-2}, and depends on a. This is due to the fact that the normalization C^{∞}_{class} is proportional to R^3 (instead of R^4 for C^e_{class}) and does not depend on a, contrary to C^e_{class}. This size effect is illustrated in figure 2.14. These figures show, in the case $a \geq a_l$ (i.e. $R \geq \frac{\sigma_Y}{\mu a\sqrt{3}}$), the torque (2.99) normalized by the limit torque of a classical continuum as a function of the relative coordinate R/ℓ, for two different values of a. The fitted curves confirm that the size effect is indeed proportional to R^{-1}. As mentioned above, the size effect is sensitive to the twist angle a, leading to a straighter curve for higher values of a. Once again, a good agreement is found between the analytical and FEM solutions.

II.3.2.3 FEM analysis in a more general case: Effect of $\underset{\sim}{\sigma}^{\text{skew}}$

In this subsection, the influence of the skew-symmetric part of the stress tensor in the yield criterion is numerically investigated. The following equivalent stress measure is considered:

$$\sigma_{eq} = \sqrt{\frac{3}{2}\left(\underset{\sim}{\sigma}'^{\text{sym}} : \underset{\sim}{\sigma}'^{\text{sym}} + \underset{\sim}{\sigma}^{\text{skew}} : \underset{\sim}{\sigma}^{\text{skew}}\right)}, \tag{2.105}$$

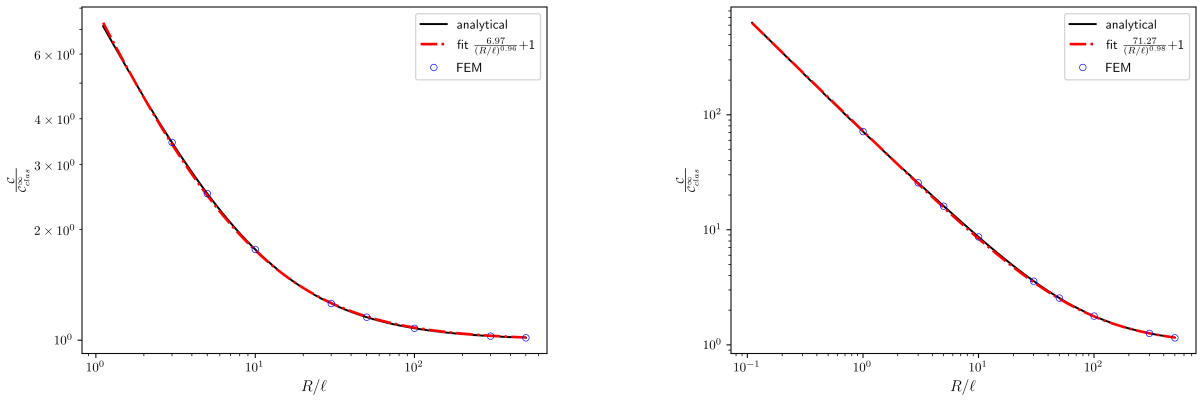

(a) *Normalized torque as a function of the normalized radius for $\ell = 0.1mm$ and $a = 0.02$ rad/mm.*

(b) *Normalized torque as a function of the normalized radius for $\ell = 0.1mm$ and $a = 0.2$ rad/mm.*

Figure 2.14: *Torque normalized by the limit torque of a classical continuum as a function of the normalized radius for $\ell = 0.1$ mm and different values for a. Cylinder radius R is such that $R > \frac{\sigma_Y}{\mu a\sqrt{3}}$ thus ensuring plastic yielding. The reduced equivalent stress (2.83) is used in the yield function.*

which is equivalent to:

$$\sigma_{eq}(\underset{\sim}{\sigma}) = \sqrt{\frac{3}{2}\left(\underset{\sim}{\sigma}' : \underset{\sim}{\sigma}'\right)}. \tag{2.106}$$

This corresponds to the following values of parameters in the general equivalent stress measure (2.76):

$$b = 1, \quad c_1 = c_2 = 0. \tag{2.107}$$

With these parameter values, the yield function is still given by equation (2.77).

The profiles of θ normalized by aR along a normalized radius are shown in figure 2.15 for several internal length values.

The stress profiles are completely different from what was obtained with the reduced criterion (2.83), as illustrated in figure 2.16. The values are much lower and for large internal lengths, $\sigma_{z\theta}$ is no longer the symmetric image of $\sigma_{\theta z}$ with respect to the curve obtained for a classical continuum.

Finally, the normalized profiles of $m_{rr}, m_{\theta\theta}$ and m_{zz} are shown in figure 2.17. Compared to the profiles obtained with criterion (2.83), the values are lower and the curves are straighter and more spread, though it does not seem to be the case for m_{zz}.

The normalized torque-twist angle curve is plotted in figure 2.18 for criterion (2.106). Contrary to the curve obtained with criterion (2.83), the contribution due to $\sigma_{\theta z}$ seems to reach a plateau. The one due to m_{zz} keeps increasing as it does not enter the yield criterion, just like with yield function (2.83). The values are of the same order of magnitude for both yield functions, although those for the contribution due to m_{zz} are slightly higher.

A size effect is also predicted by criterion (2.106), as shown in figure 2.19. The normalized torque is still proportional to R^{-1} and sensitive to the twist angle, just like with criterion (2.83).

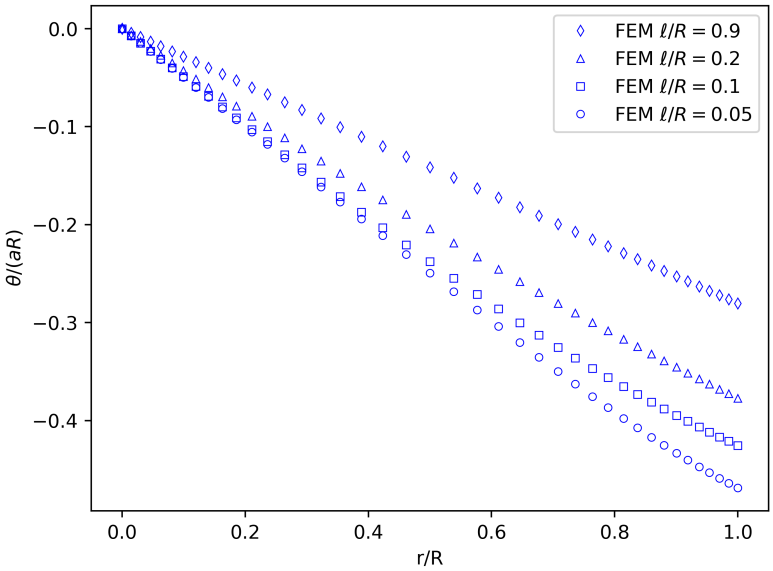

Figure 2.15: *Profiles of θ along a radius for various internal lengths and $a = 0.02$ rad/mm. The equivalent stress used in the yield function is given by equation (2.106).*

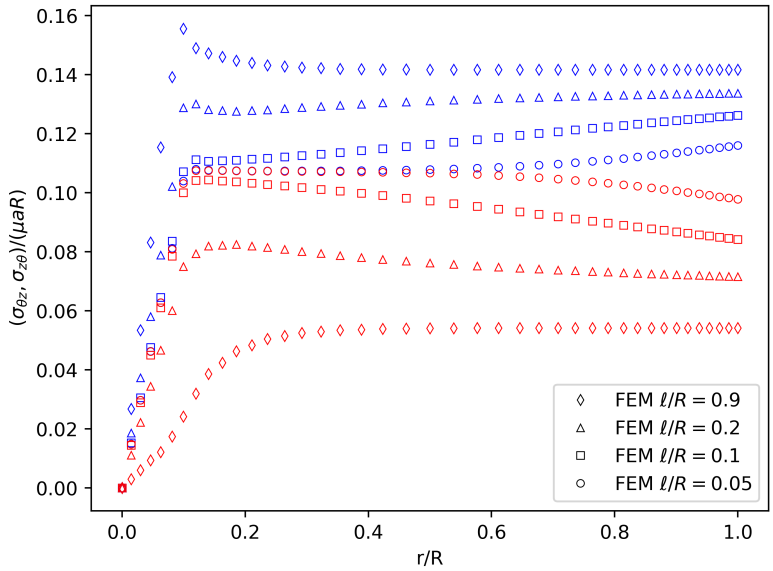

Figure 2.16: *Profiles of $\sigma_{\theta z}$ (in red) and $\sigma_{z\theta}$ (in blue) along a radius for various internal lengths and $a = 0.02$ rad/mm. The equivalent stress used in the yield function is given by equation (2.106).*

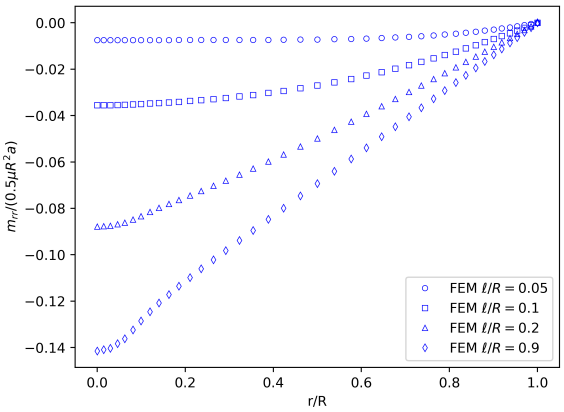

(a) *Profiles of* m_{rr}.

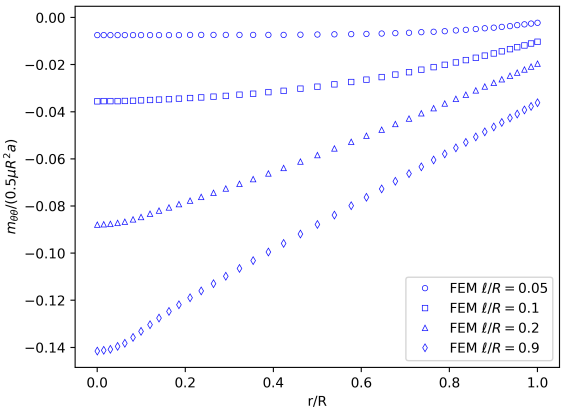

(b) *Profiles of* $m_{\theta\theta}$.

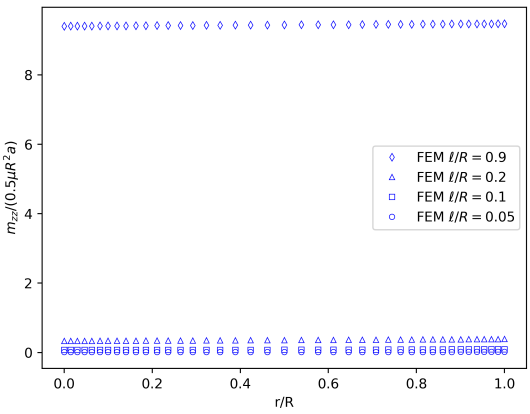

(c) *Profiles of* m_{zz}.

Figure 2.17: *Profiles of* m_{rr} , $m_{\theta\theta}$ *and* m_{zz} *along a radius for various internal lengths and* $a = 0.02$ *rad/mm. The equivalent stress used in the yield function is given by equation (2.106).*

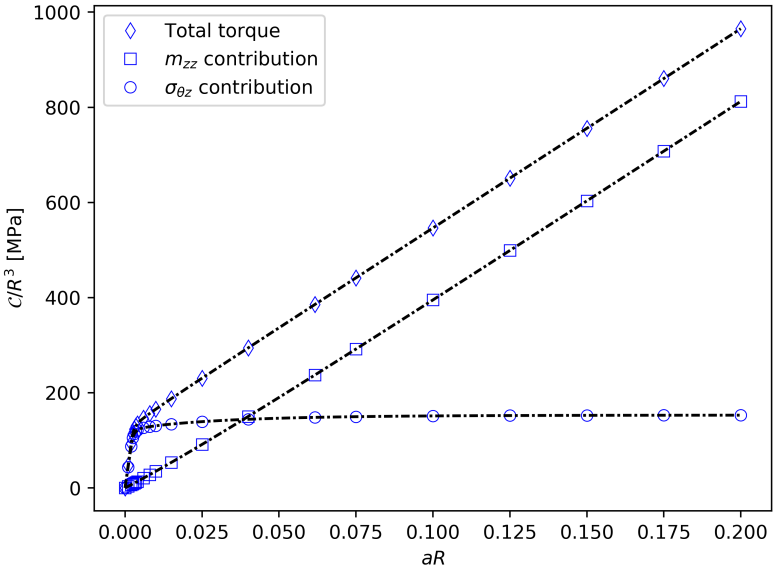

Figure 2.18: *Normalized torque as a function of the shear with $\ell/R = 0.1$. Interpolated solutions are in black dash-dotted lines. The equivalent stress used in the yield function is given by equation (2.106).*

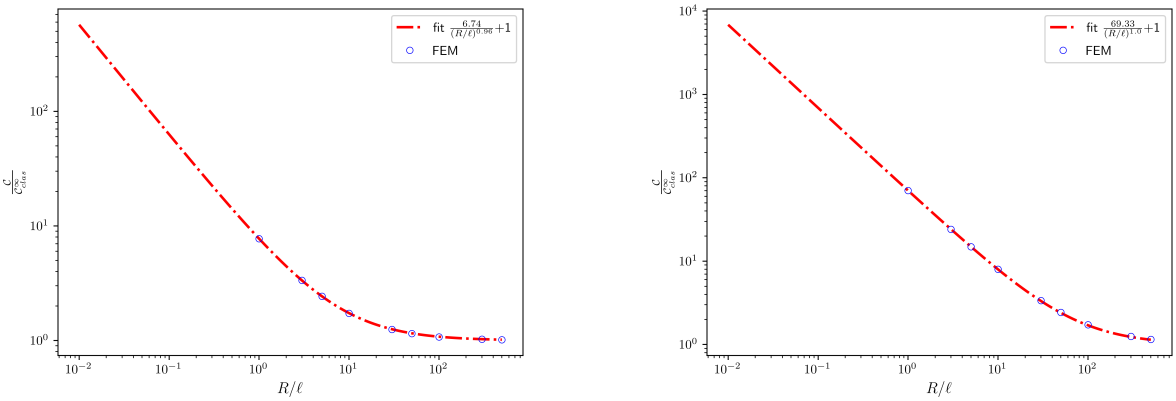

(a) *Normalized torque as a function of the normalized radius for $\ell = 0.1mm$ and $a = 0.02$ rad/mm.*

(b) *Normalized torque as a function of the normalized radius for $\ell = 0.1mm$ and $a = 0.2$ rad/mm.*

Figure 2.19: *Torque normalized by the limit torque of a classical continuum as a function of the normalized radius for $\ell = 0.1mm$ and several values of a. The equivalent stress used in the yield function is given by equation (2.106).*

II.3.2.4 FEM analysis in a more general case: Effect of $\underset{\sim}{\sigma}^{\text{skew}}$ and $\underset{\sim}{m}$

In this subsection, the yield criterion considered takes into account both the couple-stress tensor and the skew-symmetric part of the stress tensor. The chosen equivalent stress measure is taken as

$$\sigma_{eq}(\underset{\sim}{\sigma},\underset{\sim}{m}) = \sqrt{\frac{3}{2}\left(\underset{\sim}{\sigma}'^{\text{sym}} : \underset{\sim}{\sigma}'^{\text{sym}} + \underset{\sim}{\sigma}^{\text{skew}} : \underset{\sim}{\sigma}^{\text{skew}} + \underset{\sim}{m}^{\text{sym}} : \underset{\sim}{m}^{\text{sym}} + \underset{\sim}{m}^{\text{skew}} : \underset{\sim}{m}^{\text{skew}}\right)}, \tag{2.108}$$

which reduces to:

$$\sigma_{eq}(\underset{\sim}{\sigma},\underset{\sim}{m}) = \sqrt{\frac{3}{2}\left(\underset{\sim}{\sigma}' : \underset{\sim}{\sigma}' + \underset{\sim}{m} : \underset{\sim}{m}\right)}. \tag{2.109}$$

This corresponds to the following values of the parameters of the general equivalent stress (2.76):

$$b = 1, \quad c_1 = c_2 = 1 \text{ mm}^{-2}. \tag{2.110}$$

The yield function is still defined by equation (2.77) using the definition (2.109) of the equivalent stress.

The normalized profiles of θ for several internal length values are plotted in figure 2.20. The results are fairly close to those obtained with yield function (2.106) except for large length scales, for which the curves are less straight and the range of values is smaller. As for the stress profiles shown in figure 2.21, for low characteristic lengths the results are similar to those obtained with yield function (2.106) in terms of order of magnitude and shape of the curves. However, the behavior is totally different for large internal length values, the linear elastic part of the curves becomes smaller and the stresses become lower.

Figure 2.22 shows the normalized profiles of the couple stress tensor components. Contrary to the results obtained with the previous yield functions, the yield function (2.109) predicts a saturation of the size effect: The profiles for $\ell/R = 0.2$ and $\ell/R = 0.9$ do not differ much. Another difference is that the m_{zz} component is much lower.

The normalized torque-twist angle curves obtained with yield function (2.109) are shown in figure 2.23. It can be seen that both contributions from the couple-stress and stress tensors display a saturation. Contrary to the curves obtained using the other criteria, the contribution due to the couple stress is not monotonically increasing and exhibits a decrease after an initial increase, before it reaches a plateau.

Finally, the size effect evidenced for the normalized torque in figure 2.24 is still proportional to R^{-1} and sensitive to the the twist angle, just like the other yield criteria studied in this work.

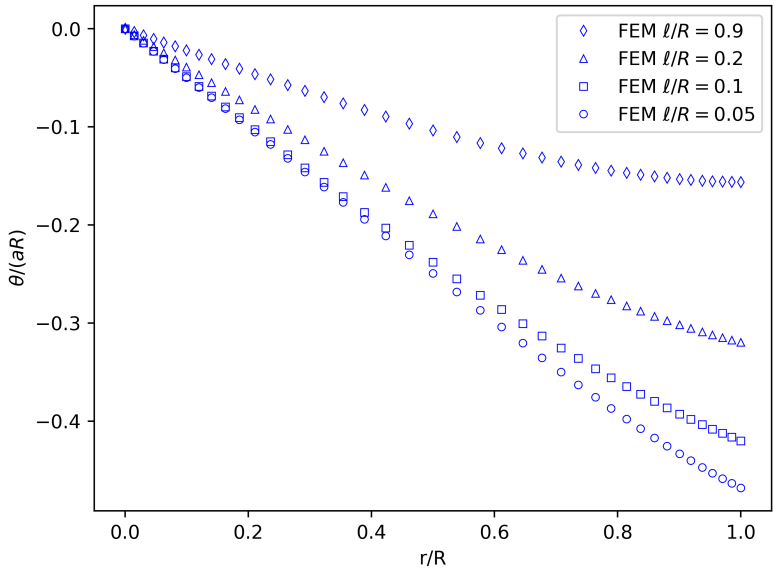

Figure 2.20: *Profiles of θ along a radius for several internal length values and $a = 0.02$ rad/mm. The equivalent stress used in the yield function is given by equation (2.109).*

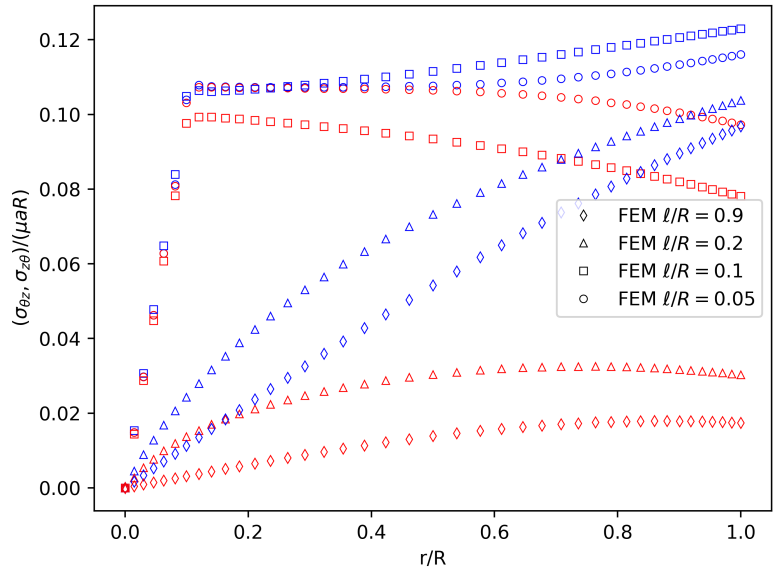

Figure 2.21: *Profiles of $\sigma_{\theta z}$ (in red) and $\sigma_{z\theta}$ (in blue) along a radius for several internal length values and $a = 0.02$ rad/mm.The equivalent stress used in the yield function is given by equation (2.109).*

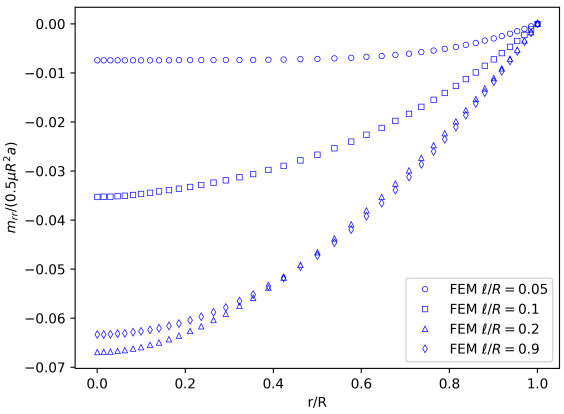

(a)*Profiles of* m_{rr}.

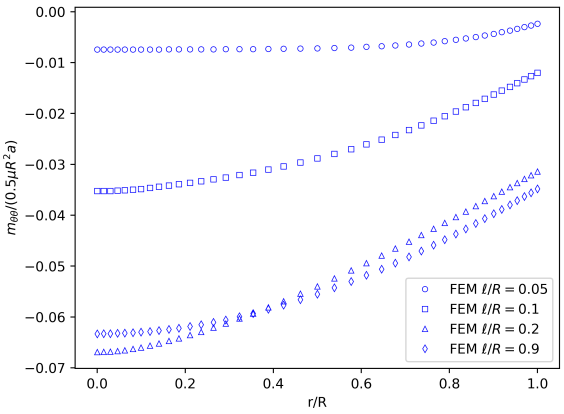

(b)*Profiles of* $m_{\theta\theta}$.

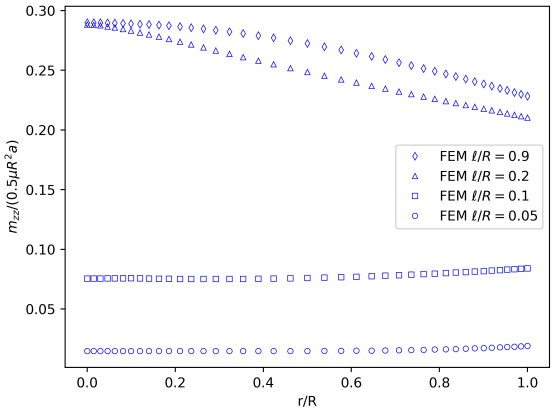

(c)*Profiles of* m_{zz}.

Figure 2.22: *Profiles of* m_{rr} , $m_{\theta\theta}$ *and* m_{zz} *along a radius for various internal length values and* $a = 0.02$ *rad/mm. The equivalent stress used in the yield function is given by equation (2.109).*

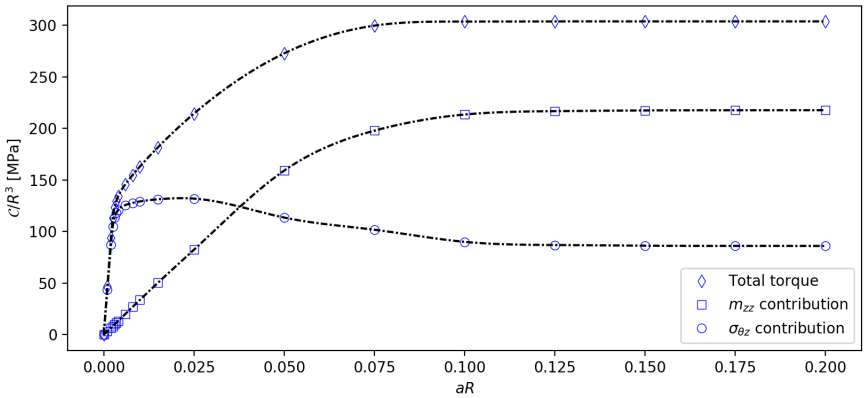

Figure 2.23: *Normalized torque as a function of the shear with* $\ell/R = 0.1$. *Interpolated solutions are in black dash-dotted lines. The equivalent stress used in the yield function is given by equation (2.109).*

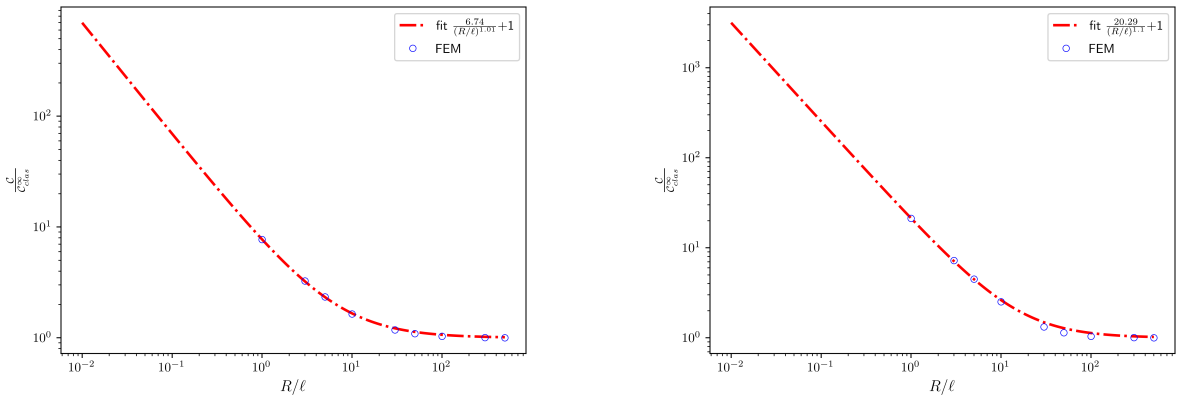

(a) *Normalized torque as a function of the normalized radius for $\ell = 0.1$ mm and $a = 0.02$ rad/mm.*

(b) *Normalized torque as a function of the normalized radius for $\ell = 0.1$ mm and $a = 0.2$ rad/mm.*

Figure 2.24: *Torque normalized by the limit torque of a classical continuum as a function of the normalized radius for $\ell = 0.1$ mm and different values for a. The equivalent stress used in the yield function is given by equation (2.109).*

II.4 Crystal plasticity

Cosserat modelling has been recognized as a good candidate for continuum modelling of plasticity in crystals containing dislocations [Günther, 1958; Schaefer, 1967] due to the relation between inhomogeneous dislocation distributions and lattice curvature [McClintock et al., 1958; Kröner, 1963]. Alternative generalized continuum theories to the Cosserat approach are gradient or micromorphic plasticity, as discussed in [Mayeur et al., 2018; Forest et al., 2018].

Cosserat crystal plasticity constitutive equations involve elastic contributions, a generalized Schmid law and size–dependent hardening induced by the curvature development, as exposed in the formulations presented in the references [Forest et al., 1997, 2000; Mayeur et al., 2011; Mayeur and McDowell, 2014; Rys et al., 2022]. A critical ingredient of the model is the choice of the dependence of the Helmholtz free energy potential on the curvature tensor. Quadratic dependence has been classically used, especially in strain gradient plasticity models [Gurtin, 2003; Gurtin and Anand, 2009]. The quadratic choice was questioned in several contributions like Ohno and Okumura [2007]; Forest [2013], because it predicts unrealistic scaling laws. Alternative potentials include energy functions proportional to the norm of the curvature or dislocation density tensor or its logarithm [Forest and Guéninchault, 2013; Wulfinghoff et al., 2015]. Both rank one and logarithmic potentials are non-differentiable at zero curvature which leads to difficulties in implementing these models and requires the consideration of discontinuities in analytical solutions.

One single slip system is considered for simplicity and the usual Schmid law is extended to the Cosserat case. In particular the scaling laws with respect to the system size are derived and solutions are compared to existing ones in strain gradient plasticity models involving the dislocation density tensor [Cordero et al., 2010; Wulfinghoff et al., 2015].

II.4.1 Constitutive equations

The Cosserat deformation tensor is decomposed into elastic and plastic contributions

$$\underset{\sim}{e} = \underset{\sim}{e}^e + \underset{\sim}{e}^p. \tag{2.111}$$

In the present work, no such decomposition is introduced for curvature, for the sake of simplicity following Russo et al. [2020]; Ghiglione and Forest [2022].

The Helmholtz free energy density function $\psi(\underset{\sim}{e}^e, \underset{\sim}{\kappa})$ is here assumed to depend on elastic deformation and total curvature. Stress–deformation relations are derived from this free energy potential in the form

$$\underset{\sim}{\sigma} = \frac{\partial \psi}{\partial \underset{\sim}{e}^e}, \quad \underset{\sim}{m} = \frac{\partial \psi}{\partial \underset{\sim}{\kappa}}. \tag{2.112}$$

Special forms of the free energy function will be considered in the proposed analysis, including a quadratic potential and more general power law potentials.

Crystal plasticity is based on Schmid's yield function, written here for a single slip system

$$f(\underset{\sim}{\sigma}, \underline{l}, \underline{n}) = |\tau| - \tau_c, \quad \text{with} \quad \tau = \underset{\sim}{\sigma} : (\underline{l} \otimes \underline{n}), \tag{2.113}$$

where τ is the resolved shear stress and τ_c the critical resolved shear stress. The plastic slip system is characterized by the slip direction $\underline{l}$ and the normal to the slip plane $\underline{n}$. Normality is a property of the crystal plasticity flow rule

$$\underset{\sim}{\dot{e}}^p = \dot{\gamma} \frac{\partial f}{\partial \underset{\sim}{\sigma}} = \dot{\gamma} (\operatorname{sign} \tau) \underline{l} \otimes \underline{n}, \tag{2.114}$$

where $\dot{\gamma}$ is the plastic multiplier.

The Schmid law is generalized here for Cosserat media accounting for generally non-symmetric stress tensor Forest et al. [1997]; Mayeur et al. [2018]; Forest et al. [2018]; Rys et al. [2022]. A special case limiting the Schmid law to the symmetric part of the stress tensor will also be considered in the following analysis.

II.4.2 Simple glide

II.4.2.1 Cosserat elastoplasticity based on a quadratic potential

In this section, the Helmholtz free energy potential is assumed to be a quadratic function of the deformation measures

$$\psi(\underset{\sim}{e}^e, \underset{\sim}{\kappa}) = \frac{1}{2} \underset{\sim}{e}^e : \underset{\approx}{\Lambda} : \underset{\sim}{e}^e + \frac{1}{2} \underset{\sim}{\kappa} : \underset{\approx}{C} : \underset{\sim}{\kappa}, \tag{2.115}$$

where $\underset{\approx}{\Lambda}$ and $\underset{\approx}{C}$ are the fourth order tensors of Cosserat elastic moduli. Point symmetry was assumed, thus excluding coupling terms between elastic deformation and curvature. The Cosserat elastic laws follow from Eq. (2.112)

$$\underset{\sim}{\sigma} = \underset{\approx}{\Lambda} : \underset{\sim}{e}^e, \quad \underset{\sim}{m} = \underset{\approx}{C} : \underset{\sim}{\kappa}. \tag{2.116}$$

Crystal plasticity based on the full stress tensor

The resolved shear stress is computed as

$$\tau = \underset{\sim}{\sigma} : (\underline{l} \otimes \underline{n}) = \underset{\sim}{\sigma} : (\underline{e}_1 \otimes \underline{e}_2) = \sigma_{12}. \tag{2.117}$$

In the plastic regime, assuming positive shear, $\tau = \tau_c$, the critical resolved shear stress is taken as a constant parameter (no hardening). Assuming that this plasticity threshold is reached in the whole specimen, the stress components σ_{12} and σ_{21} are therefore uniform during further straining. Space derivation of Eq. (2.36) implies that

$$m_{31}'' = 0 \quad \Longrightarrow \quad \theta''' = 0. \tag{2.118}$$

It follows that the microrotation distribution in the strip is parabolic:

$$\theta(x) = a(x^2 - L^2), \tag{2.119}$$

with the integration constant a. The plastic and elastic deformation tensors take the form

$$\underset{\sim}{e}^p = \gamma \underline{l} \otimes \underline{n} = \gamma \underline{e}_1 \otimes \underline{e}_2, \tag{2.120}$$

$$\underset{\sim}{e}^e = \underset{\sim}{e} - \underset{\sim}{e}^p = (\bar{\gamma} + \theta - \gamma)\underline{e}_1 \otimes \underline{e}_2 + (u' - \theta)\underline{e}_2 \otimes \underline{e}_1, \tag{2.121}$$

where $\gamma(x)$ is the plastic slip distribution to be determined. In the presence of plasticity, the equations (2.32) and (2.33) are replaced by

$$\sigma_{12} = (\mu + \mu_c)(\bar{\gamma} - \gamma) + (\mu - \mu_c)u' + 2\mu_c\theta = \tau_c, \tag{2.122}$$

$$\sigma_{21} = (\mu - \mu_c)(\bar{\gamma} - \gamma) + (\mu + \mu_c)u' - 2\mu_c\theta. \tag{2.123}$$

Elimination of γ in the previous equation and recalling that $\sigma'_{21} = 0$ due to equilibrium leads to the following relation

$$u'' = \theta' \quad \Longrightarrow \quad u(x) = a\frac{x}{3}(x^2 - L^2), \tag{2.124}$$

where the displacement boundary conditions have been taken into account. The slip distribution is obtained from (2.122) and the found expressions for microrotation and displacement are:

$$\gamma(x) = \bar{\gamma} - \frac{\tau_c}{\mu + \mu_c} + a\left(x^2 - \frac{\mu + 5\mu_c}{\mu + \mu_c}\frac{L^2}{3}\right). \tag{2.125}$$

The coefficient a is determined after insertion of $u(x)$ and $\theta(x)$ in the moment of momentum equation Eq. (2.36) which can be worked out as

$$(\mu + \mu_c)\beta\theta'' - \tau_c\mu_c + 2\mu\mu_c(u' - \theta) = 0. \tag{2.126}$$

Finally

$$a = \frac{\tau_c}{2\beta(1 + \mu/\mu_c) + 4\mu L^2/3} = \frac{\tau_c/2\mu}{\beta(1/\mu + 1/\mu_c) + 2L^2/3}. \tag{2.127}$$

To highlight the size effect induced by the Cosserat model, the stress component σ_{21} is computed as a function of the parameter β and structural length L:

$$\sigma_{21} = \frac{\mu - \mu_c}{\mu + \mu_c}\tau_c + \frac{4\mu\mu_c}{\mu + \mu_c}(u' - \theta) \tag{2.128}$$

$$= \frac{\mu - \mu_c}{\mu + \mu_c}\tau_c + \frac{8}{3}\frac{\mu\mu_c}{\mu + \mu_c}aL^2 \tag{2.129}$$

$$= \tau_c\left(\frac{\mu - \mu_c}{\mu + \mu_c} + \frac{4\mu\mu_c}{\mu + \mu_c}\frac{L^2}{3\beta(1 + \mu/\mu_c) + 2\mu L^2}\right). \tag{2.130}$$

The limit case $\mu_c \to \infty$ can be more easily interpreted:

$$\lim_{\mu_c \to \infty} \sigma_{21}/\tau_c = -1 + \frac{4\mu L^2}{3\beta + 2\mu L^2} = \tau_c\frac{1 - 3\beta/2\mu L^2}{1 + 3\beta/2\mu L^2}. \tag{2.131}$$

where $\beta \to 0$, the classical limit $\sigma_{21} = \sigma_{12} = \tau_c$ with a symmetric stress tensor, is retrieved. For vanishing system size $L \to 0$, $\sigma_{21} = -\sigma_{12} = -\tau_c$ and the stress tensor is skew-symmetric.

Schmid law limited to the symmetric part of the stress tensor

A variant of the previous analysis is the consideration of a modification of the generalized Schmid law (2.113):

$$f(\underset{\sim}{\sigma}, \underline{l}, \underline{n}) = |\tau| - \tau_c, \quad \text{with} \quad \tau = \mathrm{sym}(\underset{\sim}{\sigma}) : (\underline{l} \otimes \underline{n}). \tag{2.132}$$

According to this variant, the resolved shear stress is computed from the projection of the symmetric part of the stress tensor instead of the full stress tensor.

The analysis of the one-dimensional shear layer problem is modified as follows.

$$\tau = (\sigma_{12} + \sigma_{21})/2 = \tau_c, \tag{2.133}$$

assuming positive shear loading. This yield condition combined with balance of momentum implies that both σ_{12} and σ_{21} are uniform as in the previous section. It follows that the microrotation profile (2.119) is unchanged in the analysis. This holds true for Eq. (2.120) and (2.121).

A difference arises in the evaluation of the resolved shear stress

$$\sigma_{12} + \sigma_{21} = 2\mu(\bar{\gamma} - \gamma) + 2\mu u' = 2\tau_c, \tag{2.134}$$

but the same relation $u'' = \theta'$ is finally obtained, implying the same displacement profile (2.124). The constant a is determined from Eq. (2.126) which is modified here as

$$\beta\theta'' - \frac{\mu_c}{\mu}\tau_c + 2\mu_c(u' - \theta) = 0 \tag{2.135}$$

and finally

$$a = \frac{\tau_c/2\mu}{\beta/\mu_c + 2L^2/3} \tag{2.136}$$

$$\gamma(x) = \bar{\gamma} - \frac{\tau_c}{\mu} + a(x^2 - L^2/3) \tag{2.137}$$

which are slightly different from (2.127) and (2.125).

The stress components are then computed as

$$\sigma_{12} = \tau_c(1 + \frac{\mu_c}{\mu}) - \frac{4}{3}\mu_c a L^2, \tag{2.138}$$

$$\sigma_{21} = \tau_c(1 - \frac{\mu_c}{\mu}) + \frac{4}{3}\mu_c a L^2. \tag{2.139}$$

The first equation yields the following scaling with the size L of the system

$$\sigma_{12}/\tau_c = 1 + \frac{\beta/\mu}{\beta/\mu_c + 2L^2/3}. \tag{2.140}$$

In the limit case,

$$\lim_{\mu_c \to \infty} \sigma_{12}/\tau_c = 1 + \frac{3\beta}{2\mu L^2}, \tag{2.141}$$

making the $1/L^2$ scaling clearly visible. This scaling is rather questionable according to physical metallurgy which rather predicts $1/L$ (Orowan) or $1/\sqrt{L}$ (Hall-Petch) scaling laws in plasticity [Hirth and Lothe, 1982; Forest, 2013].

Comparison with the Curl H^p model

According to the theory developed in [Wulfinghoff et al., 2015], the displacement gradient is split into elastic and plastic contributions:

$$\underset{\sim}{\boldsymbol{H}} = \operatorname{grad} \underline{u} = \underset{\sim}{\boldsymbol{H}}^e + \underset{\sim}{\boldsymbol{H}}^p. \tag{2.142}$$

The free energy density of the Curl H^p model is taken as a quadratic form

$$\psi(\underset{\sim}{\varepsilon}^e, \operatorname{curl} \underset{\sim}{\boldsymbol{H}}^p) = \frac{1}{2}\underset{\sim}{\varepsilon}^e : \underset{\approx}{\boldsymbol{\Lambda}} : \underset{\sim}{\varepsilon}^e + A\|\operatorname{curl} \underset{\sim}{\boldsymbol{H}}^p\|^2, \tag{2.143}$$

where the elastic strain $\underset{\sim}{\varepsilon}^e$ is the symmetric part of $\underset{\sim}{\boldsymbol{H}}^e$ and A the higher order modulus. The curlH^p model involves a size-dependent back-stress

$$x = -A(\operatorname{curl}\operatorname{curl} H^p) : (\underline{l} \otimes \underline{n}). \tag{2.144}$$

The Schmid law is generalized into

$$f(\underset{\sim}{\boldsymbol{\sigma}}, x, \underline{l}, \underline{n}) = |\tau - x| - \tau_c, \tag{2.145}$$

and

$$\dot{\underset{\sim}{H}}^p = \dot{\gamma}\underline{l} \otimes \underline{n} \operatorname{sign}(\tau - x) \quad \text{with} \quad \tau = \underset{\sim}{\boldsymbol{\sigma}} : (\underline{l} \otimes \underline{n}). \tag{2.146}$$

When applied to the studied boundary value problem, the CurlH^p model predicts the following:

$$\underset{\sim}{\boldsymbol{H}} = \bar{\gamma}\underline{e}_1 \otimes \underline{e}_2 + u'\underline{e}_2 \otimes \underline{e}_1, \quad \underset{\sim}{\boldsymbol{H}}^p = \gamma \underline{e}_1 \otimes \underline{e}_2, \tag{2.147}$$

$$\operatorname{curl} \underset{\sim}{\boldsymbol{H}}^p = -\gamma' \underline{e}_1 \otimes \underline{e}_3, \quad \operatorname{curl}\operatorname{curl} H^p = -\gamma'' \underline{e}_1 \otimes \underline{e}_2, \quad x = -A\gamma'' \tag{2.148}$$

The single non-vanishing component of the stress tensor is

$$\sigma_{12} = \sigma_{21} = \mu(\bar{\gamma} - \gamma + u'). \tag{2.149}$$

The Schmid law then stipulates that

$$\sigma_{12} + A\gamma'' = \tau_c. \tag{2.150}$$

Equilibrium $\sigma_{21,1} = 0$ requires that the shear stress is uniform. The previous equations then imply that $\gamma''' = 0$ so that the slip distribution is parabolic as in the Cosserat case. Boundary conditions must be chosen to represent the fact that no plasticity occurs at the boundaries:

$$\gamma(\pm L) = 0 \quad \Longrightarrow \quad \gamma(x) = a(L^2 - x_2). \tag{2.151}$$

Note that these conditions are only approximately equivalent to those chosen for the Cosserat medium, namely vanishing lattice rotation $\theta(\pm L) = 0$.

The stress is then related to coefficient a by

$$\sigma_{12} = \tau_c - Aa. \tag{2.152}$$

The displacement is derived from Eq. (2.149):

$$\begin{aligned} u' &= \frac{\sigma_{12}}{\mu} - \bar{\gamma} + \gamma, \\ u &= (\frac{\tau_c - Aa}{\mu} - \bar{\gamma} + aL^2)x - a\frac{x^3}{3} + Cste. \end{aligned} \tag{2.153}$$

The constant vanishes since $u(0) = 0$. The condition $u(-L) = u(L)$ is used to determine the remaining constant a:

$$a = \frac{3}{2L^2}\left(\frac{\tau_c}{\mu} - \bar{\gamma}\right), \tag{2.154}$$

and finally, the shear stress value

$$\sigma_{12} = \tau_c - \frac{3A}{2L^2}\left(\frac{\tau_c}{\mu} - \bar{\gamma}\right). \tag{2.155}$$

The $1/L^2$ scaling is clearly observed and is in agreement with the Cosserat solutions Cordero et al. [2010]. Quadratic potentials in Cosserat or strain gradient plasticity therefore suffer from the same limitations compared to common knowledge in mechanical metallurgy.

II.4.2.2 Rank one energy potential

In the crystal plasticity case, the shear stress component σ_{12} is equal to the critical resolved shear stress value. Eq. (2.52) is still valid and now provides the relation

$$(\tau_c - \sigma_{21})\bar{\theta} 2L + 2A|\bar{\theta}| = 0. \tag{2.156}$$

Equilibrium still implies that σ_{21} is uniform. Its value follows

$$\sigma_{21} = \tau_c + \frac{A}{L}\text{sign}\bar{\theta}. \tag{2.157}$$

The scaling in $1/L$ is clearly visible and is distinct from the $1/L^2$ scaling law found for the quadratic potential.

On the other hand, the elasticity law tells us that

$$\sigma_{12} - \sigma_{21} = 2\mu_c(\bar{\gamma} - \gamma(x) - u'(x)) + 4\mu_c\theta. \tag{2.158}$$

Averaging this relation over the interval $[-L : L]$ and assuming periodicity of displacement give

$$\tau_c - \sigma_{21} = 2\mu_c < \bar{\gamma} - \gamma > +4\mu_c\bar{\theta}. \tag{2.159}$$

The average $< \bar{\gamma} - \gamma >$ is deduced from Eq. (2.122) as

$$< \bar{\gamma} - \gamma >= (\tau_c - 2\mu_c\bar{\theta})/(\mu + \mu_c), \tag{2.160}$$

and finally

$$\frac{2\mu_c}{\mu + \mu_c}(\tau_c + 2\mu\bar{\theta}) = -\frac{A}{L}\text{sign}\bar{\theta}, \tag{2.161}$$

from which the constant $\bar{\theta}$ is derived:

$$\bar{\theta} = -\frac{\tau_c}{2\mu} - \frac{A}{L}\frac{\mu + \mu_c}{4\mu\mu_c}\text{sign}\bar{\theta}. \tag{2.162}$$

Comparison with the $\text{Curl}\, H^p$ model

A rank one potential was also considered in Wulfinghoff et al. [2015]; Mesarovic et al. [2019]:

$$\psi(\underset{\sim}{\varepsilon}^e, \text{curl}\, \underset{\sim}{\boldsymbol{H}}^p) = \frac{1}{2}\underset{\sim}{\varepsilon}^e : \underset{\approx}{\boldsymbol{\Lambda}} : \underset{\sim}{\varepsilon}^e + A\|\text{curl}\, \underset{\sim}{\boldsymbol{H}}^p\|, \tag{2.163}$$

involving the norm of the dislocation density $\underset{\sim}{\text{curl}}\, H^p$. The symmetric stress tensor and the higher order stress are then computed as

$$\underset{\sim}{\boldsymbol{\sigma}} = \underset{\approx}{\boldsymbol{\Lambda}} : \underset{\sim}{\varepsilon}^e, \quad \underset{\sim}{\boldsymbol{m}} = A\frac{\text{curl}\, \underset{\sim}{\boldsymbol{H}}^p}{\|\text{curl}\, \underset{\sim}{\boldsymbol{H}}^p\|}. \tag{2.164}$$

In the studied problem,

$$\text{curl}\, \underset{\sim}{\boldsymbol{H}}^p = -\gamma' \underline{e}_1 \otimes \underline{e}_3, \quad \underset{\sim}{\boldsymbol{m}} = -A\text{sign}\,\gamma'. \tag{2.165}$$

It was shown in Wulfinghoff et al. [2015]; Mesarovic et al. [2019] that the total work balance reduces to the integral

$$\int_V \underset{\sim}{\boldsymbol{s}} : \underset{\sim}{\boldsymbol{H}}^p + \underset{\sim}{\boldsymbol{m}} : \text{curl}\, H^p\, dV = 0, \tag{2.166}$$

where the involved generalized stress tensors fulfill the balance law, $\underset{\sim}{\boldsymbol{s}} + \text{curl}\, \underset{\sim}{\boldsymbol{m}} = 0$. For the studied problem, this amounts to

$$\int_{-L}^{L} s_{12}\gamma + A|\gamma'|\, dx = 0. \tag{2.167}$$

According to the Schmid law,

$$\sigma_{12} + s_{12} = \tau_c, \tag{2.168}$$

where both σ_{12} and s_{12} are uniform.
The plastic slip distribution is uniform in $]-L:L[$:

$$\gamma(x) = \bar{\gamma}(H(x+L) - H(x-L)), \tag{2.169}$$
$$\gamma'(x) = \bar{\gamma}(\delta(x+L) - \delta(x-L)). \tag{2.170}$$

Finally, the previous integral is calculated as

$$(\tau_c - \sigma_{12})2L\bar{\gamma} + 2A\bar{\gamma} = 0, \tag{2.171}$$

so that the stress value

$$\sigma_{12} = \tau_c + \frac{A}{L}, \tag{2.172}$$

exhibits a $1/L$ size dependence, in the same way as the previous Cosserat model.

II.5 Summary

In this chapter, the framework of Cosserat mechanics with elastic, generalized von Mises elastoplasticity and crystal plasticity behaviours are presented. The torsion of isotropic, perfectly plastic Cosserat bars is investigated both analytically and numerically. Notably, an analytical solution was derived in the case of a reduced form of the extended von Mises yield criterion only accounting for the symmetric part of the deviatoric stress tensor, though the stress tensor itself is non-symmetric in general. The torsional characteristic length given by equation (2.17) and derived in the elastic case, plays a major role on the resulting profiles of micro-rotation, stresses and couple-stresses. A size effect of the normalized torque proportional to R^{-1} and dependent on the twist angle naturally arises in the torsional response of this model. Comparison with solutions obtained via the finite element method by means of the software Zset shows perfect agreement. Details regarding the implementation of the implicit integration of constitutive equations are given in appendix A.
A numerical investigation accounting for more general extended von Mises yield criteria shows comparable size effects, though the influence of the internal length on the resulting profiles can be very different. Depending on the yield criterion used, the different contributions to the total torque can display a saturation with respect to the twist angle.

The case of a single crystal subjected to shear loading is also addressed. Several Helmholtz free energy potentials with different dependencies on the curvature tensor are considered, namely quadratic, rank one and combined quadratic-rank one. Analytical solutions are presented in both elasticity and crystal plasticity and comparisons are made with strain gradient plasticity based on the dislocation density tensor $\mathrm{Curl}\,(H^p)$. In crystal plasticity these solutions show a clear size effect proportional to L^{-2} and L^{-1} depending on whether the dependence of the free energy on the curvature tensor is quadratic or rank one. These potentials will be used in the following chapters of the manuscript.

Chapter III

Orientation phase-field models for grain boundaries

Résumé en français

Ce chapitre est consacré aux modèles à champs de phase de type Kobayashi-Warren-Carter (KWC) pour l'évolution de microstructures. Dans la première partie, le modèle KWC est rappelé et l'influence des paramètres sur le joint de grain statique (épaisseurs des interfaces, courbe énergie-désorientation) et mobile (vitesse de migration) est étudiée. En particulier, des simulations par la méthode des éléments finis montrent que pour obtenir un profil de ϕ étroit avec un minimum profond la relation $\bar{\alpha} < \bar{s}$ doit être respectée lors du choix de ces paramètres. Également, on observe une vitesse de migration constante pour un joint de grain plat soumis à une différence d'énergie stockée (ici par les dislocations) de part et d'autre de l'interface, celle-ci dépendant principalement du paramètre $\bar{\eta}_\phi$ et peu du paramètre $\bar{\eta}_\theta$ tant que $\bar{\eta}_\theta < \bar{\eta}_\phi$. Dans le cas d'un grain circulaire rétrécissant sous l'effet de sa courbure et de l'énergie di joint de grain, les contributions de chaque paramètre sont moins évidentes et les simulations montrent l'importance du produit $\bar{\eta}_\theta \bar{\mu}_p / \bar{\varepsilon}$ pour empêcher la réorientation du grain durant le rétrécissement. Enfin, Des éléments de choix des paramètres du modèle sont également donnés.

La deuxième partie du chapitre porte sur le modèle KWC-Cosserat et l'influence de la mécanique sur le joint de grain. Une des particularités de ce modèle est l'inclusion d'une orientation de référence, nécessaire à l'établissement d'un état initial sans contrainte. Son évolution suit une loi visqueuse de relaxation des contraintes antisymétriques aux joints de grain, qui a fait l'objet d'une étude particulière. Notamment, on observe, pour un bicristal, des profils de contraintes similaires à ceux obtenus par la théorie élastoplastique des dislocations et disclinaisons de Taupin et al. [2013]. La contribution majeure de ce chapitre réside dans l'ajout d'une contrainte seuil pour cette relaxation, dont la présence induit des contraintes résiduelles au sein du joint de grain. Des simulations numériques montrent que selon la magnitude de ce seuil, un ralentissement voire un ancrage du joint de grain est possible.
Enfin, nous présentons une formulation éléments finis du modèle en trois dimensions qui a fait l'objet d'une implémentation dans le logiciel Zset. Des comparaisons avec le modèle bidimensionnel sur des cas simples tels que la formation et le cisaillement d'un joint de grain ont montré un accord suffisant pour utiliser le modèle sur des simulations 3D plus complexes.

Contents

III.1 Introduction

A wide variety of techniques have been developed to model grain boundary migration and recrystallization in full-field simulations, including Monte-Carlo Potts [Anderson et al., 1984; Gao and Thompson, 1996; Raabe, 2000; Liu and Lusk, 2002; Mason et al., 2015], cellular automata [Hesselbarth and Göbel, 1991; Liu et al., 1996; Raabe, 1998; Sitko et al., 2020], level sets [Bernacki et al., 2008; Scholtes et al., 2016; Sarrazola et al., 2020a,b] and phase-field methods [Chen and Yang, 1994; Steinbach and Pezzolla, 1999; Kobayashi et al., 2000]. Phase field models offer the advantage of being developed in a thermodynamic framework, making them easily extendable to multiphysics coupling via the free energy density [Steinbach and Apel, 2006]. Chapter I outlines two primary strategies for modelling crystal microstructure evolution: multi-phase-field approaches utilising a singular phase-field per grain [Chen and Yang, 1994; Steinbach and Pezzolla, 1999] or the Kobayashi-Warren-Carter (KWC) phase-field model [Kobayashi et al., 2000; Warren et al., 2003], which requires only two phase-fields to simulate the entire microstructure. However, microstructure evolution models lack the ability to account for material deformation by themselves. Hence, they are generally combined with continuum mechanics and crystal plasticity laws in staggered schemes. The framework of generalised continua crystal plasticity, mentioned in Chapter II, has been successfully used in conjunction with phase-field models to simulate deformation-induced microstructure evolution. Strain gradient crystal plasticity [Fleck et al., 1994] for instance has been integrated with a multi phase-field model by Takaki and Tomita [2010] and the KWC model by Takaki et al. [2008b] in staggered schemes. Meanwhile, Admal et al. [2018]; He and Admal [2021] and Ask et al. [2018b, 2020] proposed unified frameworks that respectively combine strain gradient and Cosserat crystal plasticity with the KWC model.

This chapter focuses on the KWC [Kobayashi et al., 2000] and KWC-Cosserat [Ask et al., 2018b] models. The objective is to present fundamental aspects of the orientation phase-field models for both static and mobile grain boundaries. First, the influence of phase-field and mobility parameters on the resulting grain boundary properties (such as energy and mobility) is shown through numerical simulations on bicrystals with the original KWC model. The simulations are performed using finite difference (FD) or finite element (FE) schemes to ensure consistency of the implementations. No original contribution arises from these studies, the goal is mainly to get a better understanding of this model. In a second part, the coupling with Cosserat mechanics is presented. Special attention is drawn to the inelastic grain boundary relaxation behaviour. The main contribution from this chapter is the introduction of a stress threshold that leads to the emergence of residual stresses within the grain boundaries. It will be shown that the inclusion of a critical stress may impede grain boundary motion.

The chapter is structured as follows. Section III.2.1 presents the original KWC model and its formulation, with emphasis on interface width definition. Section III.2.2 pertains to static grain boundaries. In particular, we compare the diffuse model with analytical results based on interfaces with sharp orientation fields [Kobayashi and Giga, 1999; Kobayashi et al., 2000] and matched asymptotics expansions [Lobkovsky and Warren, 2001]. Furthermore, we evaluate the effect of phase-field parameters on grain boundary width and energy. Migration induced by curvature and stored energy is examined in Section III.2.3. The importance of preventing rotation during shrinkage is highlighted. A qualitative analysis of the effect of mobility parameters on grain boundary migration rate is conducted.The second part of this chapter discusses the coupling with Cosserat mechanics presented by Ask et al. [2018b]. The model is summarised in section III.3.1. The influence of mechanics on grain boundaries is assessed without considering crystal plasticity, but accounting for the viscoelastic or viscoplastic behaviour of the grain boundaries. We analyse the mathematical formulation used to relax the skew-symmetric stresses at the grain boundaries and illustrate this with numerical simulations on both stationary and moving grain boundaries in sections III.3.2-III.3.3. Additionally, we explore the formulation and validation of a three-dimensional implementation of the model using the finite element method in section III.3.4.

III.2 Kobayashi-Warren-Carter model

III.2.1 Free energy and interface widths

The two-dimensional phase-field model proposed by Kobayashi et al. [2000]; Warren et al. [2003] is based on two scalar order parameters: the crystal lattice orientation θ and the crystal order parameter ϕ. The latter varies between zero for a fully disordered phase and one for a perfect crystal. The presence of grain boundaries contribute to lower the value of ϕ. Extensions have been made to include the contributions of defects, such as dislocations, that also decrease the value of the crystal order [Takaki et al., 2008b; Abrivard et al., 2012a].The dimensionless free energy $\bar{\mathscr{F}}_{\mathrm{KWC}}$ of the KWC model is given by

$$\bar{\mathscr{F}}_{\mathrm{KWC}} = \frac{\mathscr{F}_{\mathrm{KWC}}}{f_0 \Lambda^3} = \int_{\bar{\Omega}} \bar{\psi}(\bar{\nabla}\theta, \phi, \bar{\nabla}\phi) + \phi \bar{E} d\bar{\Omega} \tag{3.1}$$

where f_0 [J/m^3] is a scaling factor for the magnitude of the free energy density and Λ [m] is a length scale, $\bar{\nabla} = \Lambda\nabla$ is the dimensionless gradient operator and $\bar{E} = E/f_0$ is the dimensionless stored energy due to storage of dislocations. The last term in Eq. (3.1) representing the stored energy contribution, was introduced in the original KWC potential by Abrivard et al. [2012a]. An alternative formulation of the stored energy potential in the context of KWC modeling can be found in Takaki et al. [2008b]. The dimensionless free energy density $\bar{\psi}(\bar{\nabla}\theta, \phi, \bar{\nabla}\phi)$ is independent of the lattice orientation due to the frame invariance requirement, and has the following form:

$$\bar{\psi}(\bar{\nabla}\theta, \phi, \bar{\nabla}\phi) = \psi(\nabla\theta, \phi, \nabla\phi)/f_0 = f(\phi) + \frac{\bar{\alpha}^2}{2}\left|\bar{\nabla}\phi\right|^2 + \bar{s}g(\phi)\left|\bar{\nabla}\theta\right| + \frac{\bar{\varepsilon}^2}{2}h(\phi)\left|\bar{\nabla}\theta\right|^2 \tag{3.2}$$

where the model parameters $\bar{\alpha} = \dfrac{\alpha}{\sqrt{f_0}\Lambda}, \bar{s} = \dfrac{s}{f_0\Lambda}, \bar{\varepsilon} = \dfrac{\varepsilon}{\sqrt{f_0}\Lambda}$ are dimensionless. In addition to regular quadratic terms with respect to the gradient of the phase-field variables, the singular term $|\bar{\nabla}\theta|$, not differentiable at 0, is required to localize grain boundaries of finite width. The term $|\bar{\nabla}\theta|^2$ is needed for grain boundary motion according to [Warren et al., 2003]. The functions f, g, h are dimensionless by construction and have the following form:

$$f(\phi) = \frac{1}{2}(1-\phi)^2 \tag{3.3}$$

$$g(\phi) = \phi^2 \quad \text{or} \quad g(\phi) = -2\left(\log(1-\phi) + \phi\right) \tag{3.4}$$

$$h(\phi) = \phi^2 \tag{3.5}$$

Using $g(\phi)$ as a logarithmic function, the Read-Shockley form of the grain boundary energy can be obtained [Kobayashi et al., 2000]. For $\phi = 1$ the function $g(\phi)$ diverges, so a regularisation is needed for the numerical implementation of the model. This is achieved by adding a small positive constant $\gamma_g \ll 1$ to the argument of the logarithm.

A feature of the model is the presence of two interface widths, one for each phase field variable, as sketched in Fig. 3.1. The interface widths ℓ_ϕ and ℓ_θ of the phase fields ϕ and θ depend in a non-trivial way on the parameters $\bar{\alpha}$, $\bar{s}$, and $\bar{\varepsilon}$. With the usual parameters used in the literature, l_ϕ can be almost one order of magnitude larger than l_θ. In the matched asymptotics analysis performed by Lobkovsky and Warren [2001], the interface width ℓ_θ is defined as the region of non-zero orientation gradient in a bicrystal. Rather than adopting the usual definition $\ell_\phi = 2\bar{\alpha}$, we have chosen to take ℓ_θ and ℓ_ϕ as the distance between two points corresponding to 10% of the maximum value of the phase field gradients:

$$\ell_\theta = 2\bar{x} \mid \bar{x} > 0 \text{ and } \bar{\nabla}\theta(\bar{x}) = 0.1\max(|\bar{\nabla}\theta|) \tag{3.6}$$

$$\ell_\phi = 2\bar{x} \mid \bar{x} > 0 \text{ and } \bar{\nabla}\phi(\bar{x}) = 0.1\max(|\bar{\nabla}\phi|) \tag{3.7}$$

This definition has the advantage to better account for the large tails of the exponential profiles of the phase

field (Fig. 3.1). The interface widths also depend on the misorientation angle, as shown in Fig. 3.2. At the mesoscale of a few micrometers, a typical interface width ℓ_θ can be selected down to a few hundred nanometers to remain in acceptable computational time. The difference between the interface widths can be mitigated somewhat by changing the magnitude of the contributions in the free energy density. This can be achieved by using a Modica-Mortola formulation of $f(\phi)$, such that $f(\phi) = (1-\phi)^2/\bar{\alpha}$, as in [Giga et al., 2023]. A finite element simulation using such a formulation of the KWC free energy was performed for a grain boundary energy comparable to that of the regular KWC model, and the resulting interface widths are plotted as well in Fig. 3.2. It can be seen that the ratio ℓ_ϕ/ℓ_θ decreases from approximately 6 in the classical formulation to 4 in this modified version of the free energy.

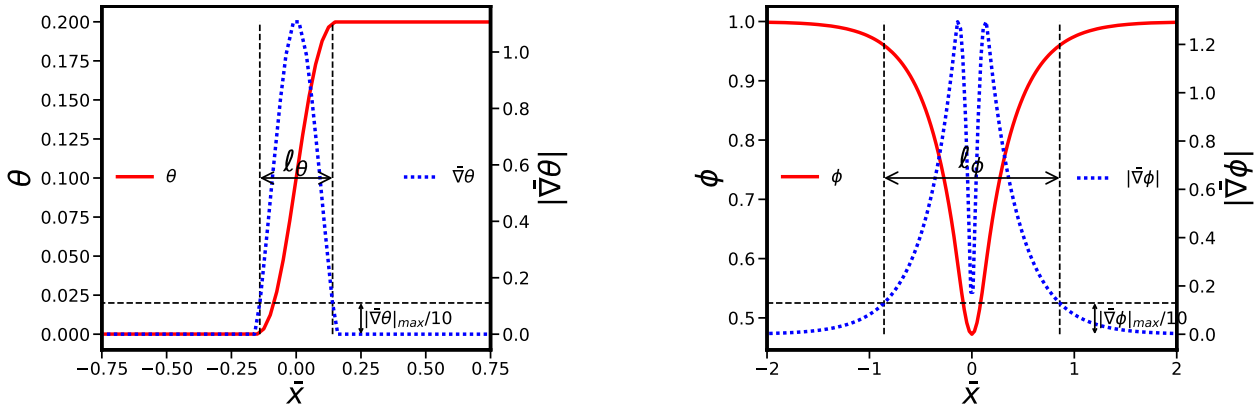

Figure 3.1: *Definition of the lengths ℓ_ϕ and ℓ_θ characterizing the width of the grain boundary zone.*

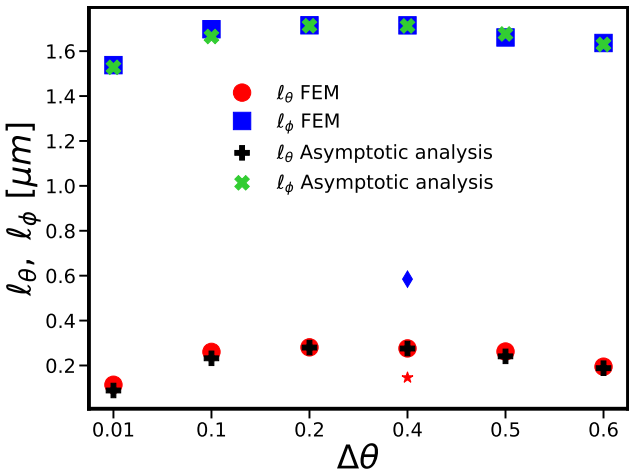

Figure 3.2: *Interface widths ℓ_ϕ and ℓ_θ as functions of misorientation $\Delta\theta$ for the logarithmic function $g(\phi)$.These widths refer to the distance between two points where the phase-field gradient reaches 10% of its maximum. In addition, measurements with a modified KWC free energy functional following Giga et al. [2023] are represented by a star and diamond symbol for ℓ_θ and ℓ_ϕ respectively.*

Contrary to the multi-phase-field method, the KWC model does not readily allow for the introduction of physical quantities such as grain boundary energy and mobility. The non-dimensional grain boundary energy of a flat interface is obtained by integrating the non-dimensional free energy without the stored energy term along a line passing through the grain boundary, denoted by $\partial^2\bar{\Omega}$:

$$\bar{\gamma}_{GB} = \int_{\partial^2\bar{\Omega}} f(\phi) + \frac{\bar{\alpha}^2}{2}\left|\bar{\nabla}\phi\right|^2 + \bar{s}g(\phi)\left|\bar{\nabla}\theta\right| + \frac{\bar{\varepsilon}^2}{2}h(\phi)\left|\bar{\nabla}\theta\right|^2 d\bar{x} \tag{3.8}$$

III.2.2 Static grain boundaries

In this section the static behaviour of grain boundaries is analysed. Firstly, we compare the phase-field equilibrium profiles with analytical solutions for sharp orientation field interfaces and semi-analytical solutions in the asymptotic expansion of Lobkovsky and Warren [2001]. We then assess the impact of static parameters $\bar{\alpha}$, $\bar{s}$ and $\bar{\varepsilon}$ on the equilibrium profiles and grain boundary energy. Note that up to section III.2.4, calculations are performed with $\mathbf{g}(\phi) = \phi^2$ unless explicitly stated otherwise.

III.2.2.1 Interface with sharp orientation field

Consider a one-dimensional bicrystal whose grain boundary is at $\bar{x} = 0$. The orientation at $\bar{x} = +\infty$ is θ^+, that at $\bar{x} = -\infty$ is θ^-. The misorientation angle is given by $\Delta\theta = |\theta^+ - \theta^-|$. The crystal order field takes the value 1 at $\bar{x} = \pm\infty$. It was proved by Kobayashi and Giga [1999] that if ϕ has only one minimum and $\bar{\varepsilon} = 0$, then θ is a step function located at the minimum of ϕ. The resulting equilibrium profiles are then given by Kobayashi et al. [2000] :

$$\theta(x) = \begin{cases} \theta^-, \ x < 0 \\ \theta^+, \ x > 0 \end{cases} \tag{3.9}$$

$$\phi(x) = 1 - (1 - \phi_{min}) \exp\left(-\frac{1}{\bar{\alpha}}|\bar{x}|\right) \tag{3.10}$$

where

$$\phi_{min} = \min(\phi) = \frac{1}{1 + \frac{\bar{s}\Delta\theta}{\bar{\alpha}}} \tag{3.11}$$

The grain boundary energy can be shown to be equal to:

$$\bar{\gamma}_{GB} = \frac{\bar{\alpha}\bar{s}\Delta\theta}{\bar{\alpha} + \bar{s}\Delta\theta} \tag{3.12}$$

The solutions are compared with those from the KWC model, solved using a finite difference (FD) scheme described in [Warren et al., 2003], with $\bar{\varepsilon} = 0$. The results are shown in Fig. 3.3 and indicate good agreement between the two solutions for the profiles of θ, ϕ, ϕ_{min}, and the dimensionless grain boundary energy. Furthermore, it is observed that with increasing misorientation the minimum value of ϕ decreases and the grain boundary energy increases, as expected from Eqs. 3.12 and 3.11.

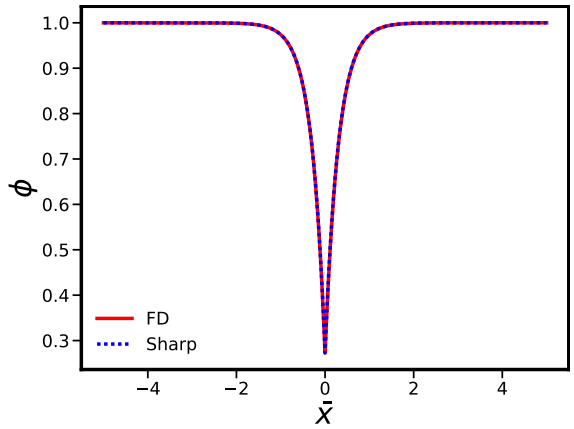

(a) *Profile of* ϕ.

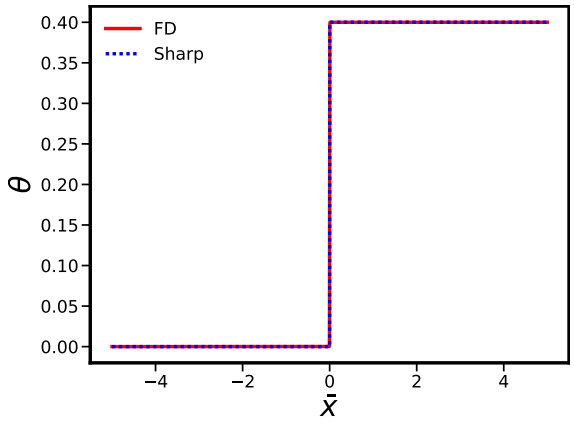

(b) *Profile of* θ.

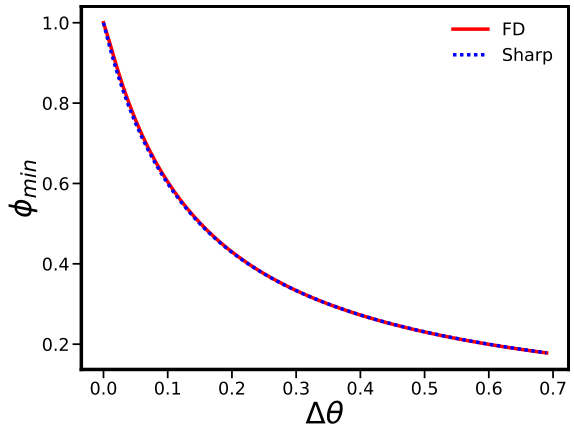

(c) *Minimum value of* ϕ (ϕ_{min}) *as a function of misorientation* $\Delta\theta$.

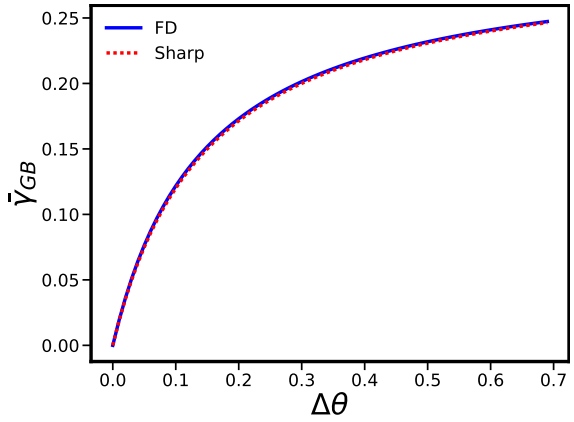

(d) *Dimensionless grain boundary energy* $\bar{\gamma}_{GB}$ *as a function of misorientation* $\Delta\theta$.

Figure 3.3: *Comparison of the profiles of* ϕ *(top left),* θ *(top right) along a bicrystal as well as* ϕ_{min} *(bottom left) and* $\bar{\gamma}_{GB}$ *as functions of the misorientation* $\Delta\theta$ *for the KWC model solved with a finite difference (FD) scheme and analytical solutions for interfaces with sharp orientation field (*$\bar{\alpha} = 0.3, \bar{s} = 2, \bar{\varepsilon} = 0$*).*

III.2.2.2 Matched asymptotics analysis

In the original KWC model, explicit semi-analytical solutions for the profiles of ϕ and θ, grain boundary energy, and mobility can be obtained through a formal asymptotic expansion, as demonstrated by Lobkovsky and Warren [2001]. The key concept is to define the grain boundary as the strip S between two non-intersecting smooth curves Γ^- and Γ^+ where $\bar{\nabla}\theta \neq 0$. A curvilinear coordinate system $\{\bar{r}(\bar{x},\bar{y},\bar{t}), \bar{s}(\bar{x},\bar{y},\bar{t})\}$ is adopted with $\bar{r}(\bar{x},\bar{y},\bar{t})$ representing the distance from $\Gamma-$ to a point $(\bar{x},\bar{y})$ in the inner domain and $\bar{s}(\bar{x},\bar{y},\bar{t})$ is the arc length on $\Gamma-$. In addition, a stretched coordinate $z = \bar{r}/\bar{\varepsilon}$ is introduced. Figure 3.4 depicts a flat, static interface with three distinct regions. Firstly, the phase-fields remain constant far from the interface, with $\bar{\nabla}\phi = 0$ and $\bar{\nabla}\theta = 0$. Secondly, at the interface for $z > \delta z$, $\bar{\nabla}\phi \neq 0$ while $\bar{\nabla}\theta = 0$. Lastly, for $z < \delta z$, $\bar{\nabla}\phi \neq 0$ and $\bar{\nabla}\theta \neq 0$.

The phase-fields are expanded into power series of $\bar{\varepsilon}$:

$$\begin{cases} \phi = \phi^0 + \bar{\varepsilon}\phi^1 + ... \\ \theta = \theta^0 + \bar{\varepsilon}\theta^1 + ... \end{cases}$$

The parameters $\bar{\alpha}$ and $\bar{s}$ are scaled with respect to $\bar{\varepsilon}$:

$$\widetilde{\alpha} = \bar{\alpha}/\bar{\varepsilon},\ \widetilde{s} = \bar{s}/\bar{\varepsilon},\ \widetilde{\eta}_\phi = \bar{\eta}_\phi/\bar{\varepsilon}^2,\ \widetilde{\eta}_\theta = \bar{\eta}_\theta/\bar{\varepsilon}^2$$

The solutions are identified within each region and then matched at the interface between them. The interface width, energy, and stationary profiles are obtained through the 0^{th} order expansion in $\bar{\varepsilon}$, while the interface mobility and velocity are obtained through the 1^{st} order expansion in $\bar{\varepsilon}$. It should be noted that this analysis does not apply to migration driven by stored energy.

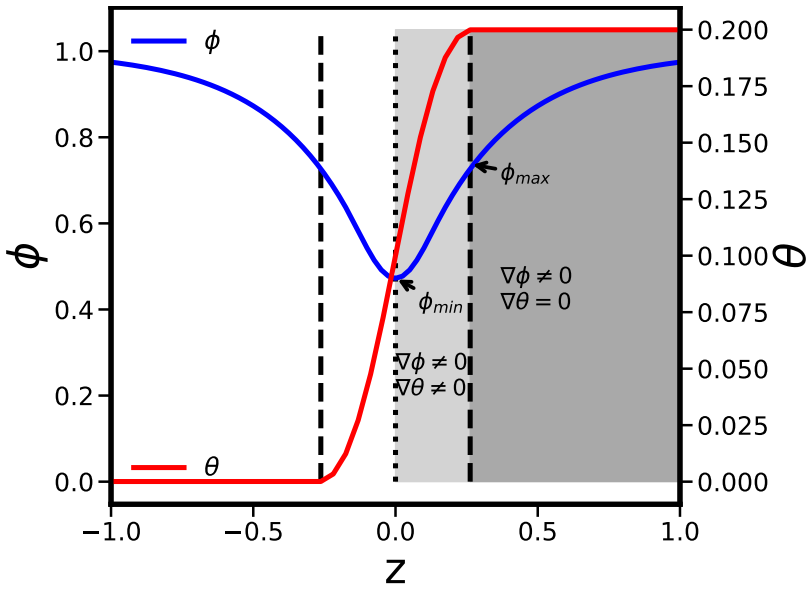

Figure 3.4: *Schematic representation of the solution for a flat static interface between two grains.*

The profiles of ϕ^0 and θ^0 are obtained by integrating

$$\frac{\partial \phi^0}{\partial z} = \begin{cases} \frac{1}{\widetilde{\alpha}} \sqrt{2f^0 - \frac{\widetilde{s}^2}{h^0}\left(g^0(\phi^0_{max}) - g^0\right)}, & \phi^0_{min} \leq \phi^0 \leq \phi^0_{max} \\ \frac{1}{\widetilde{\alpha}} \sqrt{2f^0}, & \phi^0_{max} < \phi^0 \leq 1 \end{cases} \tag{3.13}$$

$$\frac{\partial \theta_0}{\partial z} = \widetilde{s} \frac{g^0(\phi^0_{max}) - g(\phi^0)}{h^0(\phi^0)}, \quad 0 \leq z \leq \delta z \tag{3.14}$$

The values of ϕ^0_{min} (at $z = 0$) and ϕ^0_{max} (at the limit between the two regions of the grain boundary) are obtained from

$$\frac{\widetilde{s}}{2} \frac{\left(g^0(\phi^0_{max}) - g^0(\phi^0_{min})\right)^2}{h^0(\phi^0_{min})} - f^0(\phi^0_{min}) = 0 \tag{3.15}$$

$$\frac{\Delta\theta}{2} = \int_{\phi^0_{min}}^{\phi^0_{max}} \frac{\partial \theta^0}{\partial z} \frac{\partial z}{\partial \phi^0} d\phi^0 \tag{3.16}$$

The half interface width $\ell_\theta/2$ is given by

$$\ell_\theta/2 = \delta z = \widetilde{\alpha} \int_{\phi^0_{min}}^{\phi^0_{max}} \frac{1}{2f^0 - \frac{\widetilde{s}^2}{h^0}\left(g^0(\phi^0_{max}) - g^0\right)} d\phi^0 \tag{3.17}$$

Finally, the grain boundary energy is found to be

$$\bar{\gamma}_{GB} = 2\widetilde{\alpha}^2 \int_{\phi^0_{min}}^{1} \frac{\partial \phi^0}{\partial z} d\phi^0 + \widetilde{s} g^0(\phi^0_{max}) \Delta\theta \tag{3.18}$$

The profiles from the asymptotic analysis are compared to those from the formulas for an interface with sharp orientation field and a KWC model solved through a finite difference scheme for $\bar{\varepsilon} \in \{0, 2\}$ in Fig.

3.5. It is evident that when a fixed set of parameters, $\bar{\alpha}$ and $\bar{s}$ is utilized, the addition of the term $\bar{\varepsilon}^2|\bar{\nabla}\theta|^2$ to the KWC free energy results in a more diffuse grain boundary, a reduced crystal order field and increased grain boundary energy. The increase in grain boundary energy is expected from the positivity of the term $\varepsilon^2 h(\phi)\left|\bar{\nabla}\theta\right|^2$ that is added to the free energy density.

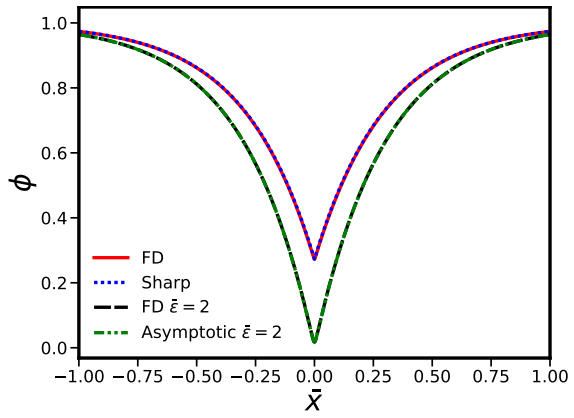

(a) *Profile of* ϕ.

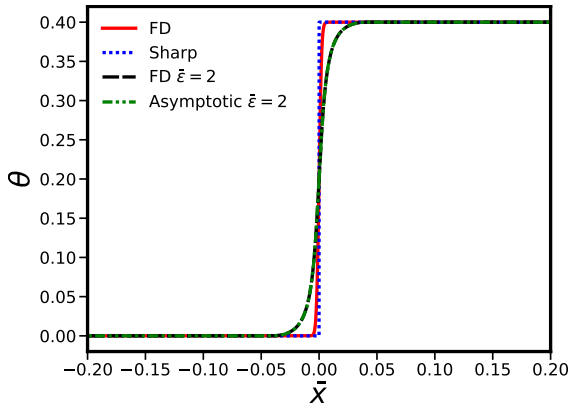

(b) *Profile of* θ.

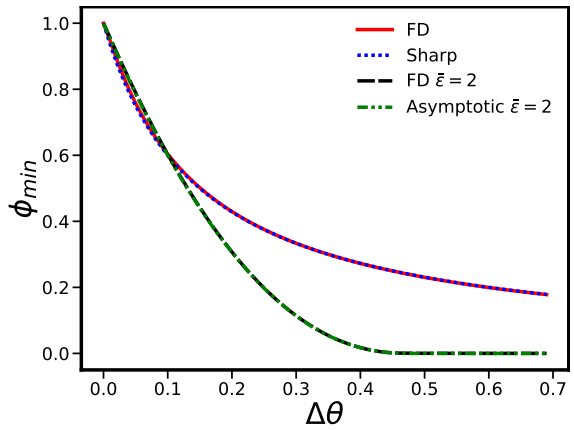

(c) *Minimum value of* ϕ (ϕ_{min}) *as a function of misorientation* $\Delta\theta$.

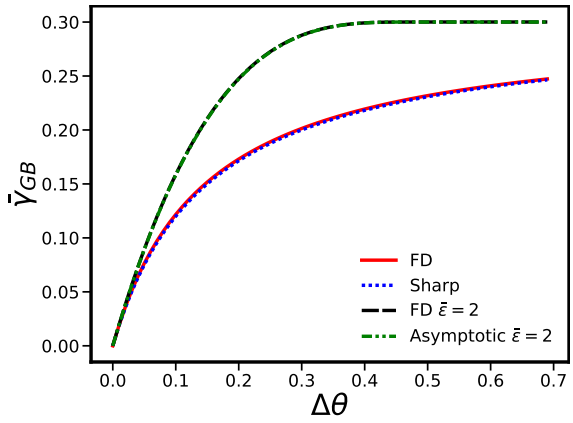

(d) *Dimensionless grain boundary energy* $\bar{\gamma}_{GB}$ *as a function of misorientation* $\Delta\theta$.

Figure 3.5: *Comparison of the profiles of* ϕ *(top left),* θ *(top right) along a bicrystal as well as* ϕ_{min} *(bottom left) and* $\bar{\gamma}_{GB}$ *as a function of the misorientation* $\Delta\theta$ *for the KWC model solved with a finite difference scheme, matched asymptotic analysis* $(\bar{\varepsilon} \neq 0)$ *and analytical solution for interfaces with sharp orientation field* $(\bar{\varepsilon} = 0)$.

III.2.2.3 Influence of phase-field parameters

Interface widths

The choice of parameters $\bar{\alpha}$, $\bar{s}$, $\bar{\varepsilon}$ influences the phase-field profiles and the grain boundary energy. The impact of parameter $\bar{s}$ is illustrated for the case $\bar{\varepsilon} = 0$ in Fig. 3.6 where it can be seen that for a fixed $\bar{\alpha}$ the larger $\bar{s}$ the deeper the profile of ϕ and the thinner the profile of θ. The decrease of ϕ_{min} to 0 as $\bar{\alpha}/\bar{s}$ decreases is a predictable result of Eq. 3.12.

Now accounting for $\bar{\varepsilon} \neq 0$, figures 3.7a and 3.7b show the ϕ and θ profiles respectively for different values of $\bar{s}$, while keeping fixed values of $\bar{\alpha}$ and $\bar{\varepsilon}$. As anticipated, similarly to $\bar{\varepsilon} = 0$, it is clear that if $\bar{s} > \bar{\alpha}$, the minimum value of ϕ is lower, and the θ profile is narrower. However, when $\bar{\alpha} \approx \bar{s}$, the finite element method (FEM) solution does not identify a grain boundary, whereas the matched asymptotic analysis identifies a grain boundary with a misorientation of $\Delta\theta = 0.4$ instead of $\Delta\theta = 0.3$. This implies that certain combinations of $\bar{s}$ and $\bar{\alpha}$ are not allowed for this particular set of initial and boundary conditions.

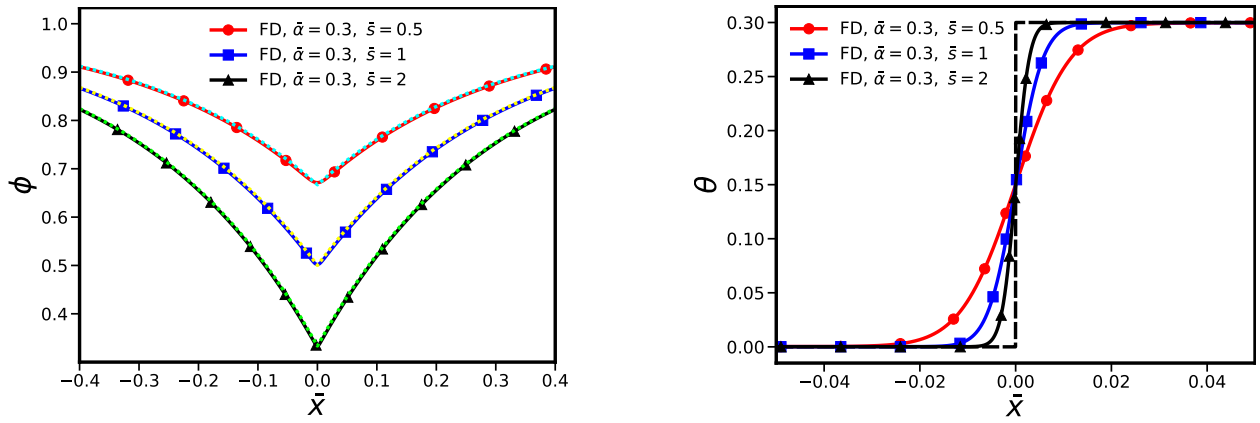

Figure 3.6: *Comparison of the profiles of ϕ (left) and θ (right) along a bicrystal for the KWC model solved with a finite difference scheme and analytical sharp interface solutions for several values of $\bar{s}$ ($\bar{\alpha} = 0.3, \bar{\varepsilon} = 0$). Dashed/dotted lines correspond to the analytical solutions for interfaces with sharp orientation field.*

To investigate this further, several FEM calculations were performed for $\bar{s}$ and $\bar{\alpha}$ values ranging from 0 to 2, with $\bar{\varepsilon}$ fixed at 0.5. The results are displayed in Fig. 3.8, and the θ-width ℓ_θ (the region where $\nabla\theta \neq 0$) was capped at 1. As shown in this figure, deep and thin grain boundaries can only be achieved if $\bar{s} > \bar{\alpha}$, thus limiting the parameter space.

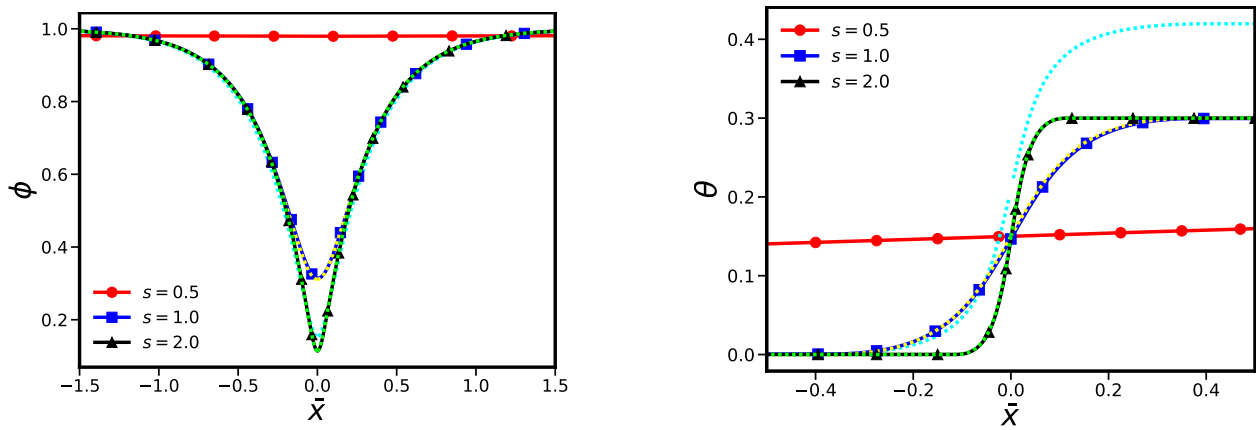

(a) *Profiles of ϕ for $\bar{\alpha} = 0.3$, $\bar{\varepsilon} = 2$ for different $\bar{s}$*

(b) *Profiles of θ for $\bar{\alpha} = 0.3$, $\bar{\varepsilon} = 2$ for different $\bar{s}$*

Figure 3.7: *Influence of the parameter $\bar{s}$ on the phase-field profiles (ϕ on the left, θ on the right). FEM solutions are denoted by solid lines, while dashed lines depict matched asymptotic analysis solutions.*

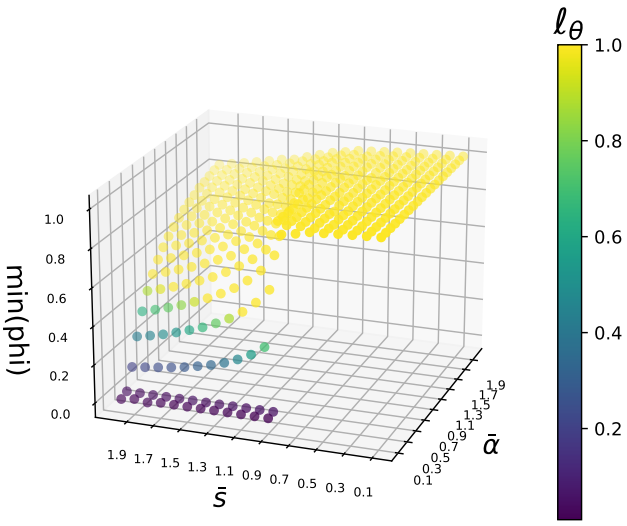

Figure 3.8: *Influence of the parameters $\bar{\alpha}$ and $\bar{s}$ on the GB width ℓ_θ and the value of ϕ_{min} for $\bar{\varepsilon} = 0.5$, $\Delta\theta = 0.3$.*

Grain boundary energy

The grain boundary energy is also affected by the choice of phase-field parameters. Figure 3.9a illustrates a grain boundary energy-misorientation curve with different values of $\bar{s}$, while holding fixed values of $\bar{\alpha} = 0.3$ and $\bar{\varepsilon} = 2$. It is evident that with increased $\bar{s}$, the grain boundary energy for the same misorientation also increases, owing to the augmented contribution of $\bar{s}g(\phi)|\bar{\nabla}\theta|$ to the free energy density.

The energy of low-angle grain boundaries is often expressed as a function of misorientation through the normalized Read-Shockley equation [Read and Shockley, 1950] recalled below:

$$\gamma_{GB} = \begin{cases} \dfrac{\gamma_m \Delta\theta}{\Delta\theta_m}\left(1 - \ln\left(\dfrac{\Delta\theta}{\Delta\theta_m}\right)\right) & \text{for } \Delta\theta < \Delta\theta_m \\ \gamma_m \quad \text{for } \Delta\theta \geq \Delta\theta_m \end{cases}$$

where $\Delta\theta_m$ represents the transition misorientation that distinguishes low angle from high angle grain boundaries and γ_m the associated grain boundary energy. To facilitate comparison with the KWC model, we introduce the dimensionless Read-Shockley grain boundary energy: $\bar{\gamma}_{GB} = \gamma_{GB}/\gamma_m$. Figure 3.9b shows a comparison of the grain boundary energy misorientation curves using the Read-Shockley formula and asymptotic analysis for different $\bar{s}$ and $g(\phi)$. The energies are scaled such that $\max(\bar{\gamma}_{GB}) = 1$. The use of a logarithmic $g(\phi)$ allows to obtain a grain boundary energy of the Read-Shockley type. It will be demonstrated in section III.2.4 that the parameters $\bar{\alpha}$ and $\bar{s}$ can be calibrated to fit the low angle grain boundary energy to data obtained from experiments or molecular dynamics simulations.

III.2.3 Mobile grain boundaries

The present section evaluates the dynamic behaviour of grain boundaries in the original KWC model. Firstly, the case of curvature-driven migration is examined, with attention given to the separation of bulk and boundary behaviours through the inverse mobility function P (see Eq. 3.21). Secondly, stored energy-driven migration, formulated by Abrivard et al. [2012a], is illustrated via numerical simulations. Finally, the influence of mobility parameters is discussed for both mechanisms.

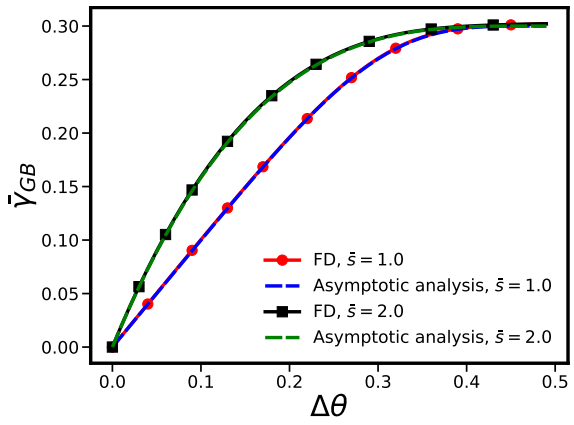

(a) *Grain boundary energy as a function of misorientation using Finite difference and asymptotic analysis.*

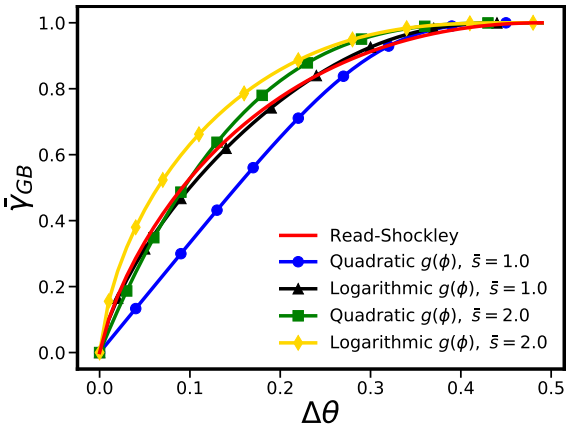

(b) *Influence of $g(\phi)$ on the grain boundary energy as a function of misorientation using asymptotic analysis. The grain boundary energies are scaled so that* $\max(\bar{\gamma}_{GB})=1$.

Figure 3.9: *Grain boundary-misorientation curves for different values of $\bar{s}$ and $\bar{\alpha}=0.3, \bar{\varepsilon}=2$.*

III.2.3.1 Evolution equations

Assuming relaxational dynamics for both phase-fields, the evolution equations of the phase-fields are given by

$$\bar{\eta}_\phi \dot{\phi} = \left(\frac{\partial \bar{\psi}}{\partial \bar{\nabla}\phi}\right)\cdot\bar{\nabla} - \frac{\partial \bar{\psi}}{\partial \phi} = \bar{\alpha}^2\bar{\nabla}^2\phi - f_{,\phi} - \bar{s}g_{,\phi}|\bar{\nabla}\theta| - \frac{\bar{\varepsilon}^2}{2}h_{,\phi}|\bar{\nabla}\theta|^2 - \bar{E} \tag{3.19}$$

$$P\bar{\eta}_\theta\phi^2\dot{\theta} = \left(\frac{\partial \bar{\psi}}{\partial \bar{\nabla}\theta}\right)\cdot\bar{\nabla} - \frac{\partial \bar{\psi}}{\partial \theta} = \bar{\nabla}\cdot\left(\bar{\varepsilon}^2 h\bar{\nabla}\theta + \bar{s}g\frac{\bar{\nabla}\theta}{|\bar{\nabla}\theta|}\right) \tag{3.20}$$

with $\dot{x}=\partial x/\partial\bar{t}$, $\bar{t}=t/\tau_0$ where τ_0 is a time scale. P is a dimensionless inverse mobility function assumed to depend on ϕ and/or $\bar{\nabla}\theta$ and $\bar{\eta}_\phi$, $\bar{\eta}_\theta$ are constant kinetic factors. The choice $P=1$ results in a spatially uniform mobility. Alternatively, the function P can be different in the bulk of the grain and in the diffuse grain boundary region to avoid simultaneous shrinkage and non-physical rotation during curvature driven migration by depending on $\bar{\nabla}\theta$:

$$P=1 \text{ or } P(\bar{\nabla}\theta) = 1 + \left(\frac{\bar{\mu}_p}{\bar{\varepsilon}} - 1\right)\exp\left(-\beta_p\bar{\varepsilon}|\bar{\nabla}\theta|\right) \tag{3.21}$$

A microforce formalism *à la* Gurtin [1996] provides a variational framework that allows to recover the evolution equations for the phase-fields. For this purpose, internal microforces and microstress vectors $\bar{\pi}_\phi, \bar{\pi}_\theta, \underline{\bar{\xi}}_\phi, \underline{\bar{\xi}}_\theta$ are associated with $\phi, \theta, \bar{\nabla}\phi$ and $\bar{\nabla}\theta$ respectively. The application of the principle of virtual power and thermodynamics gives the following balance equations in the body $\bar{\Omega}$ and boundary conditions on $\partial\bar{\Omega}$, here written in the absence of external and surface or volume densities of microforces:

$$\underline{\bar{\xi}}_\phi\cdot\bar{\nabla} + \bar{\pi}_\phi^{sto} + \bar{\pi}_\phi^{dis} = 0 \quad \text{in } \bar{\Omega} \tag{3.22}$$

$$\underline{\bar{\xi}}_\theta\cdot\bar{\nabla} + \bar{\pi}_\theta^{sto} + \bar{\pi}_\theta^{dis} = 0 \quad \text{in } \bar{\Omega} \tag{3.23}$$

$$\bar{\xi}_\phi\cdot\underline{n} = 0, \quad \bar{\xi}_\theta\cdot\underline{n} = 0 \quad \text{on } \partial\bar{\Omega} \tag{3.24}$$

with

$$\underline{\bar{\xi}}_{\phi} = \frac{\partial \psi}{\partial \bar{\nabla}\phi}, \quad \underline{\bar{\xi}}_{\theta} = \frac{\partial \psi}{\partial \bar{\nabla}\theta} \tag{3.25}$$

$$\bar{\pi}_{\phi}^{sto} = -\frac{\partial \psi}{\partial \phi}, \quad \bar{\pi}_{\phi}^{dis} = -\bar{\eta}_{\phi}\dot{\phi} \tag{3.26}$$

$$\bar{\pi}_{\theta}^{sto} = -\frac{\partial \psi}{\partial \theta}, \quad \bar{\pi}_{\theta}^{dis} = -\phi^2 P \bar{\eta}_{\theta}\dot{\theta} \tag{3.27}$$

so that the evolution equations (3.19)-(3.20) are retrieved.
An additional evolution equation for the stored energy must be added to account for recovery in the wake of the moving grain boundary. Following Abrivard et al. [2012a] the time evolution of the stored energy is given by:

$$\dot{\bar{E}} = \begin{cases} -C_D \bar{E} \tanh\left(\bar{C}_A |\bar{\nabla}\theta|^2\right)\dot{\phi}, & \dot{\phi} > 0 \\ 0, & \dot{\phi} \leq 0 \end{cases} \tag{3.28}$$

The singular term $1/|\bar{\nabla}\theta|$ in Eq. 3.20 requires regularization in the numerical treatment. In [Warren et al., 2003] this is achieved by replacing the term $|\bar{\nabla}\theta|$ in the free energy with a quadratic potential for orientation gradients below a numerical threshold $1/\bar{\gamma}$:

$$|\bar{\nabla}\theta| \sim A_{\gamma}(|\bar{\nabla}\theta|) = \begin{cases} \frac{\bar{\gamma}}{2}|\bar{\nabla}\theta|^2 \text{ for } 0 \leq |\bar{\nabla}\theta| \leq 1/\bar{\gamma} \\ |\bar{\nabla}\theta| - \frac{1}{2\bar{\gamma}} \text{ for } |\bar{\nabla}\theta| > 1/\bar{\gamma} \end{cases} \tag{3.29}$$

From Eq. 3.19, it is apparent that the presence of stored energy will tend to decrease the value of the phase-field ϕ. As this stored energy is related to the buildup of crystal defects (dislocations) that occurs during plastic deformation, it is physically motivated that the crystal order should decrease. It should be noted that in this work, grain boundary motion results from both the grain boundary energy/curvature and/or a stored energy difference. To tackle the first issue, we investigate the shrinkage of a circular grain embedded in a larger grain, which is the subject of section III.2.3.2. The second driving force is examined in subsection III.2.3.3, where a difference in stored energy is imposed on a bicrystal.

III.2.3.2 Curvature driven migration

Spurious grain lattice rotation

In the absence of stored energy, subgrains may reduce their total energy by shrinking or rotating [Rollett et al., 2017]. The KWC model can simulate these phenomena by considering a circular grain embedded in a larger square grain (periodic boundary conditions for ϕ are applied at the boundaries of the larger grain). However, rotation is only present in ultra-fine materials with sub-micron grains. Therefore, this is an undesirable mechanism for engineering materials, which usually contain grains of several micrometres. The KWC model includes both mechanisms, but this spurious rotation can be avoided by careful parameter selection for the inverse mobility function, which limits reorientation to a small region around the interface:

$$P(\bar{\nabla}\theta) = 1 + \left(\frac{\bar{\mu}_p}{\bar{\varepsilon}} - 1\right)\exp\left(-\beta_p \bar{\varepsilon}|\bar{\nabla}\theta|\right) \tag{3.30}$$

where β_p is the size of the localisation zone and $\bar{\mu}_p$ is the magnitude of the inverse mobility function in the bulk of the grain, where it must be large. If $P(\bar{\nabla}\theta)$ is too small in the bulk, rotation without shrinkage may occur. To illustrate this, finite element computations were carried out on a 10×10 mesh of 25600 elements

with reduced integration and quadratic shape functions. The initial conditions were given by

$$\phi(\bar{x},\bar{y},\bar{t}=0) = 1 - \frac{1-\phi_{min}}{\left[\cosh\left(\ell_{\phi_0}[\bar{x}^2+\bar{y}^2-\bar{R}_0^2]\right)\right]^2} \tag{3.31}$$

$$\theta(\bar{x},\bar{y},\bar{t}=0) = \begin{cases} \Delta\theta, & \sqrt{x^2+y^2} < \bar{R}_0 \\ 0, & \text{else} \end{cases} \tag{3.32}$$

with $\Delta\theta = 0.3$, $\phi_{min} = 0.05$, $\ell_{\phi_0} = 0.5$, $\bar{R}_0 = 6$. The parameters used in the FEM computations of this section are given in table 3.1. At the moment they do not correspond to any precise material.

Parameter	$\bar{\alpha}$	$\bar{s}$	$\bar{\varepsilon}$	$\bar{\eta}_\phi$	$\bar{\eta}^\star$	$\bar{\mu}_p$	β_p	C_D	$\bar{C}_A$	$\bar{\gamma}$
Value	0.3	2	2	50	0.5	10^6	10^3	100	1	10^4

Table 3.1: *Parameters used in the FEM computations of curvature and stored energy driven migration of grain boundaries.*

Figure 3.10, which depicts the evolution of the θ (top) and ϕ (bottom) phase-fields at several times, shows reorientation without shrinkage. We can see that both the circular and the larger grains reorient to form a single crystal, thereby reducing the total energy of the system.

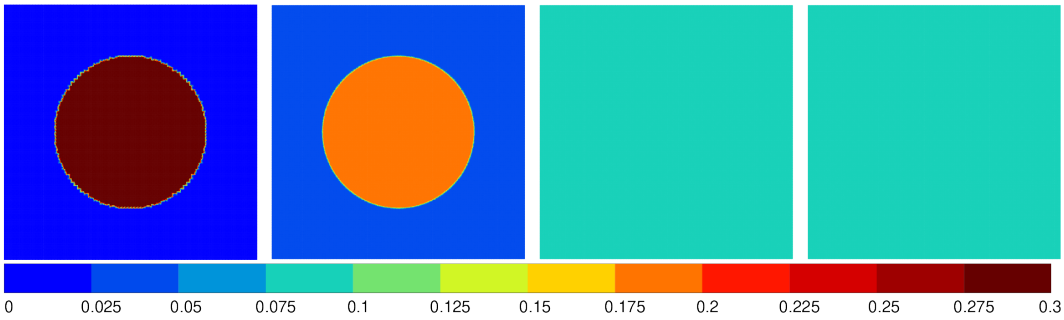

(a) *Lattice orientation* θ *at* $\bar{t}=0$, $\bar{t}=3$, $\bar{t}=7$, $\bar{t}=10$

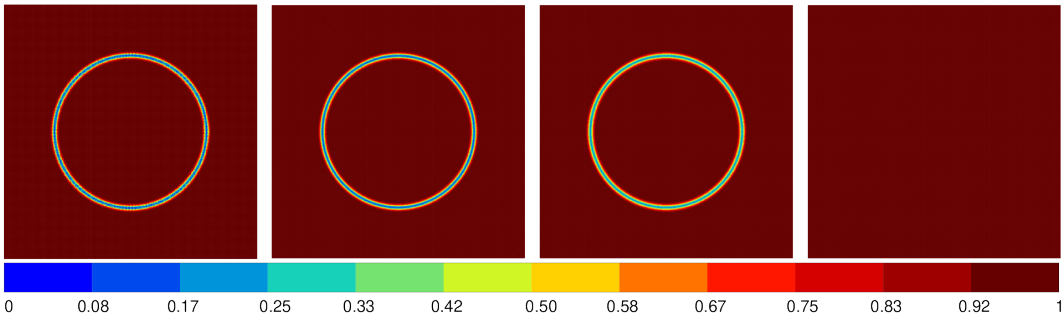

(b) *Crystal order* ϕ *at* $\bar{t}=0$, $\bar{t}=3$, $\bar{t}=7$, $\bar{t}=10$

Figure 3.10: *Snapshots of* θ *(top) and* ϕ *(bottom) fields during spurious rotation of a grain embedded in a matrix. Parameters are* $\bar{\alpha}=0.3, \bar{s}=2, \bar{\varepsilon}=2, \bar{\mu}_p=2$, $\bar{\eta}_\phi=1$, $\bar{\eta}_\theta=1$ *at* $\bar{t}=0$, $\bar{t}=3$, $\bar{t}=7$, $\bar{t}=10$.

Grain shrinkage without reorientation

By selecting the appropriate parameters of the inverse mobility function $P(\bar{\nabla}\theta)$, the KWC model can successfully model grain shrinkage without concurrent rotation. This is demonstrated in Fig. 3.11, which shows that the grain shrinks without rotating until it vanishes, resulting in a single crystal with 0 misorientation.

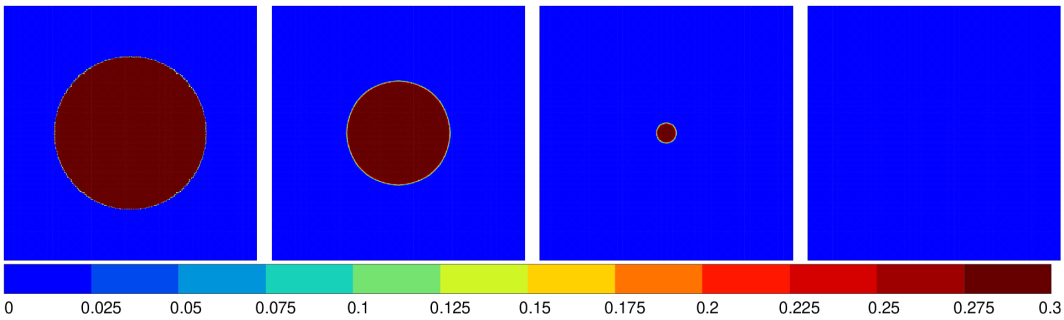

(a) *Lattice orientation* θ *at* $\bar{t}=0$, $\bar{t}=4000$, $\bar{t}=7100$, $\bar{t}=7500$

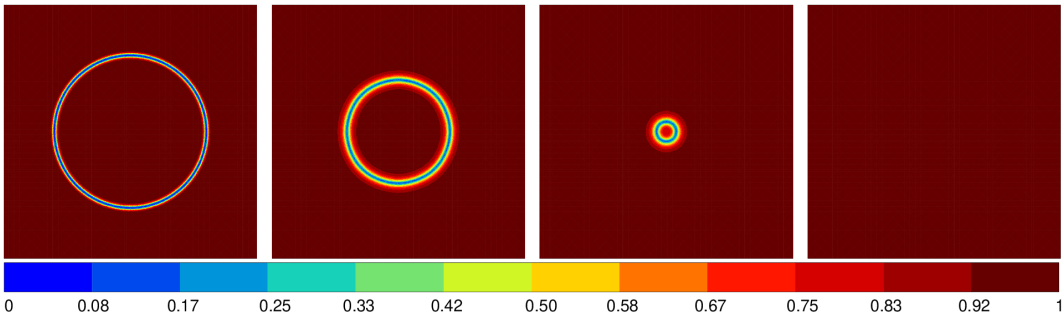

(b) *Crystal order* ϕ *at* $\bar{t}=0$, $\bar{t}=4000$, $\bar{t}=7100$, $\bar{t}=7500$

Figure 3.11: *Snapshots of* θ *(top) and* ϕ *(bottom) fields during shrinkage of a circular grain embedded in a matrix at* $\bar{t}=0$, $\bar{t}=4000$, $\bar{t}=7100$, $\bar{t}=7500$. *The parameters are* $\bar{\alpha}=0.3, \bar{s}=2, \bar{\varepsilon}=2, \bar{\eta}_\phi=50, \bar{\eta}_\theta=0.5, \mu_P=10^6, \beta_P=1000$.

This simulation is further investigated below. Figure 3.12a depicts the time evolution of the total dimensionless energy, which shows a significant decrease at the beginning. This indicates the balancing of the system, as the initial state is far from equilibrium. Alternatively, a preliminary KWC simulation could have been run to find the correct ϕ and θ fields, which could then be used as initial conditions. The time evolution of the radius of the circular grain is shown in figure 3.12b. As in Kobayashi et al. [2000], the radius is marked by the minimum value of ϕ. The curve displays the characteristic shape of the shrinkage of a circular grain as described in Kobayashi et al. [2000]. The serrated aspect of the curve is probably due to the spatial discretisation.

The rate of grain boundary migration v is generally accepted to be proportional to the driving force F responsible for this movement, according to the following relationship:

$$v = MF \tag{3.33}$$

where M is the grain boundary mobility. The dimensionless grain boundary migration rate, mobility and driving force are respectively $\bar{v}=v\tau_0/\Lambda$, $\bar{M}=M\tau_0 f_0/\Lambda$ and $\bar{F}=F/f_0$. In the case of interest in this section, this boils down to:

$$\dot{\bar{R}}_{GB} = \bar{M}\frac{\bar{\gamma}_{GB}}{\bar{R}_{GB}} \tag{3.34}$$

where γ_{GB} is the grain boundary energy and $1/R_{GB}$ is the curvature of the grain boundary. According to Kobayashi et al. [2000] the grain boundary energy is computed from the total energy of the KWC model $\bar{\mathscr{F}}_{KWC}$ and the grain radius $\bar{R}_{GB}$ as

$$\bar{\gamma}_{GB} = \frac{\bar{\mathscr{F}}_{KWC}}{2\pi\bar{R}_{GB}} \tag{3.35}$$

Equation 3.34 is valid for $\bar{t}\in[165,7150]$ approximately as shown in Fig. 3.12c, where the relationship between $\dot{\bar{R}}_{GB}$ and $1/\bar{R}_{GB}$ is linear. The grain boundary energy, calculated using Equation 3.35, is plotted as a function of time in Fig. 3.12d and remains approximately constant throughout this range.

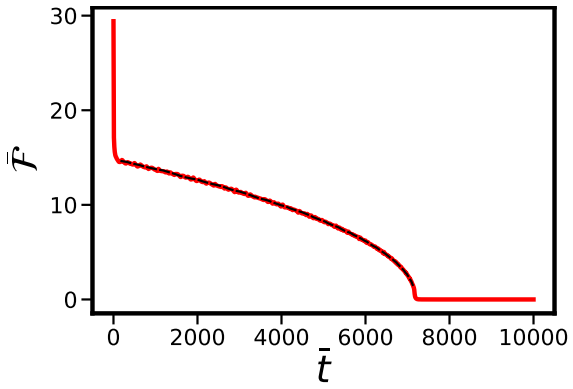

(a) *Total dimensionless energy as a function of time.*

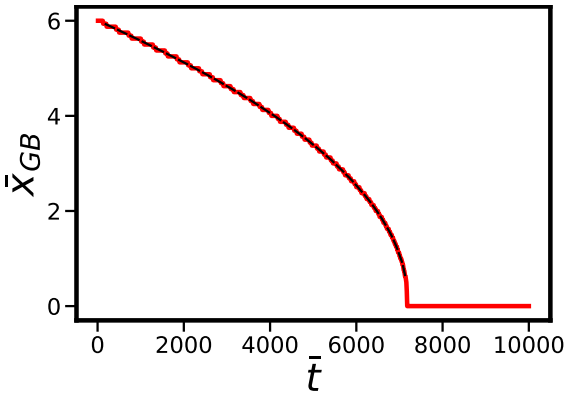

(b) *Dimensionless grain radius as a function of time.*

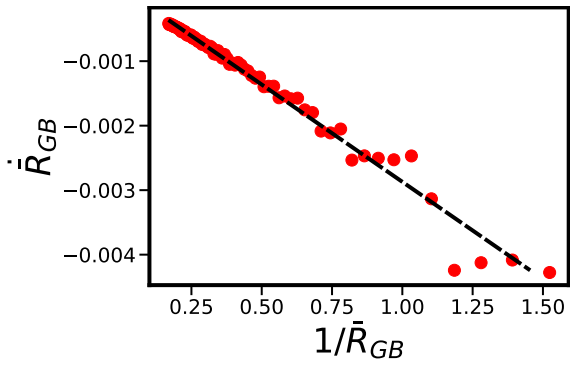

(c) *Dimensionless grain boundary migration rate as a function of grain curvature. The dashed black line indicates a linear fit.*

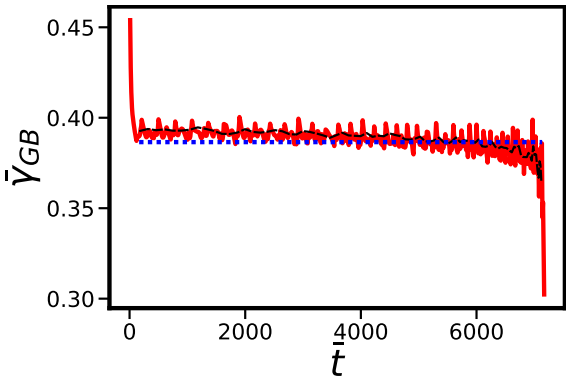

(d) *Dimensionless grain boundary energy as a function of time. The dashed blue line is the mean value.*

Figure 3.12: *Total dimensionless energy as a function of time (top left), dimensionless grain radius as a function of time (top right), dimensionless grain boundary migration rate as a function of the curvature (bottom left) and dimensionless grain boundary energy as a function of time (bottom right) during shrinkage of a circular grain. Black lines correspond to the smoothed curve for which there is a linear relationship between* $\dot{\bar{R}}_{GB}$ *and* $1/\bar{R}_{GB}$ $(\bar{t} \in [165, 7150])$.

III.2.3.3 Stored energy driven migration

The subject of this section is the second driving force of interest, which relates to a dislocation based stored energy difference. We recall that in the dimensionless KWC model the contribution of dislocation storage is included in the free energy density through the term $\phi\bar{E}$ where $\bar{E} = E/f_0$. Let's consider a bicrystal with an initial dimensionless stored energy content of $\bar{E} = 0.1$ on the left side of the grain boundary and $\bar{E} = 0.4$ on the right side. As the interface is flat, there is no curvature and reducing the stored energy content on the right side of the interface is the only way to decrease the total energy. For simplicity, it is assumed that complete recovery occurs behind the region swept by the grain boundary during its migration. As stated in section III.2.3.1, it is anticipated that the presence of stored energy will decrease the value of ϕ. A value for the crystal order far from the interface, where $\nabla\theta = \nabla\phi = 0$, can be analytically derived from the equilibrium evolution equation for ϕ [Abrivard et al., 2012a]:

$$0 = \bar{\alpha}^2\bar{\nabla}^2\phi - f_{,\phi} - \bar{s}g_{,\phi}|\bar{\nabla}\theta| - \frac{\bar{\varepsilon}^2}{2}h_{,\phi}|\bar{\nabla}\theta|^2 - \bar{E} \tag{3.36}$$

$$0 = -f_{,\phi} - \bar{E} \tag{3.37}$$

$$\phi = 1 - \bar{E} \tag{3.38}$$

As $0 \leq \phi \leq 1$, Eq. 3.38 gives an upper bound for $\bar{E} = E/f_0$:

$$\bar{E} \leq 1 \tag{3.39}$$

For the simulations, the bicrystal has a total length $2\bar{L} = 20$ and the following initial and boundary conditions are applied:

$$\text{IC} \begin{cases} \theta(\bar{x}, \bar{t}=0) = \dfrac{\Delta\theta}{2}\left(\tanh(a\bar{x}) + 1\right) \\ \bar{E}(\bar{x}, \bar{t}=0) = \bar{E}_l + \dfrac{\Delta\bar{E}}{2}\left(\tanh(a\bar{x}) + 1\right) \\ \phi(\bar{x}, \bar{t}=0) = \begin{cases} 1 - \bar{E}_l - \dfrac{1 - \bar{E}_l - \min(\phi)}{\left[\cosh(b\bar{x})\right]^2}, & \bar{x} \leq 0, \\ 1 - \bar{E}_r - \dfrac{1 - \bar{E}_r - \min(\phi)}{\left[\cosh(b\bar{x})\right]^2}, & x \geq 0 \end{cases} \end{cases} \tag{3.40}$$

$$\text{BC} \begin{cases} \theta = 0 \text{ rad @ left} \\ \theta = \Delta\theta \text{ rad @ right} \\ \theta \ \& \ \phi \text{ periodic at the top and bottom edges} \end{cases} \tag{3.41}$$

With $\bar{E}_l$ and $\bar{E}_r$ the dimensionless stored energies on the left and right sides of the interface, $\Delta\bar{E} = \bar{E}_r - \bar{E}_l$ the stored energy difference and parameters a, b control the spread of the tanh and cosh functions respectively. The parameters for the initial and boundary conditions are as follows: $\bar{E}_l = 0.1$, $\bar{E}_r = 0.4$, $\Delta\theta = 0.3$, $a = 10$, $b = 5$. Note that in the case studied here the phase-fields are not at equilibrium at $\bar{t} = 0$. Doing so would require the results of an extremely low mobility simulation to find the equilibrium profiles of ϕ and θ without migration. The parameters given in table 3.1 are still used.
Figure 3.13 displays the profiles of θ (top left), ϕ (top right), and $\bar{E}$ (bottom left) along the bicrystal at various dimensionless times. They clearly illustrate that the grain boundary moves to the right side of the domain, which has a higher dislocation content, in order to reduce the total energy. It can be seen that in the wake of the moving grain boundary the stored energy goes to 0 and ϕ goes to 1, indicating full recovery. It is recalled that the recovery rate is controlled by the recovery parameter C_D in Eq. 3.28. Furthermore, when plotting the position of the grain boundary (assumed to be at the minimum value of ϕ) against dimensionless time (see Fig. 3.13 bottom right), a straight line is obtained, suggesting a steady migration rate.

Finally, Eq. 3.33 still holds. In this case it reduces to:

$$\bar{v} = \bar{M}\Delta\bar{E} \tag{3.42}$$

where $\Delta\bar{E}$ is the stored energy difference. Plotting the migration rate as a function of the stored energy difference gives a straight line whose slope is the grain boundary mobility, as can be seen in Fig. 3.14.

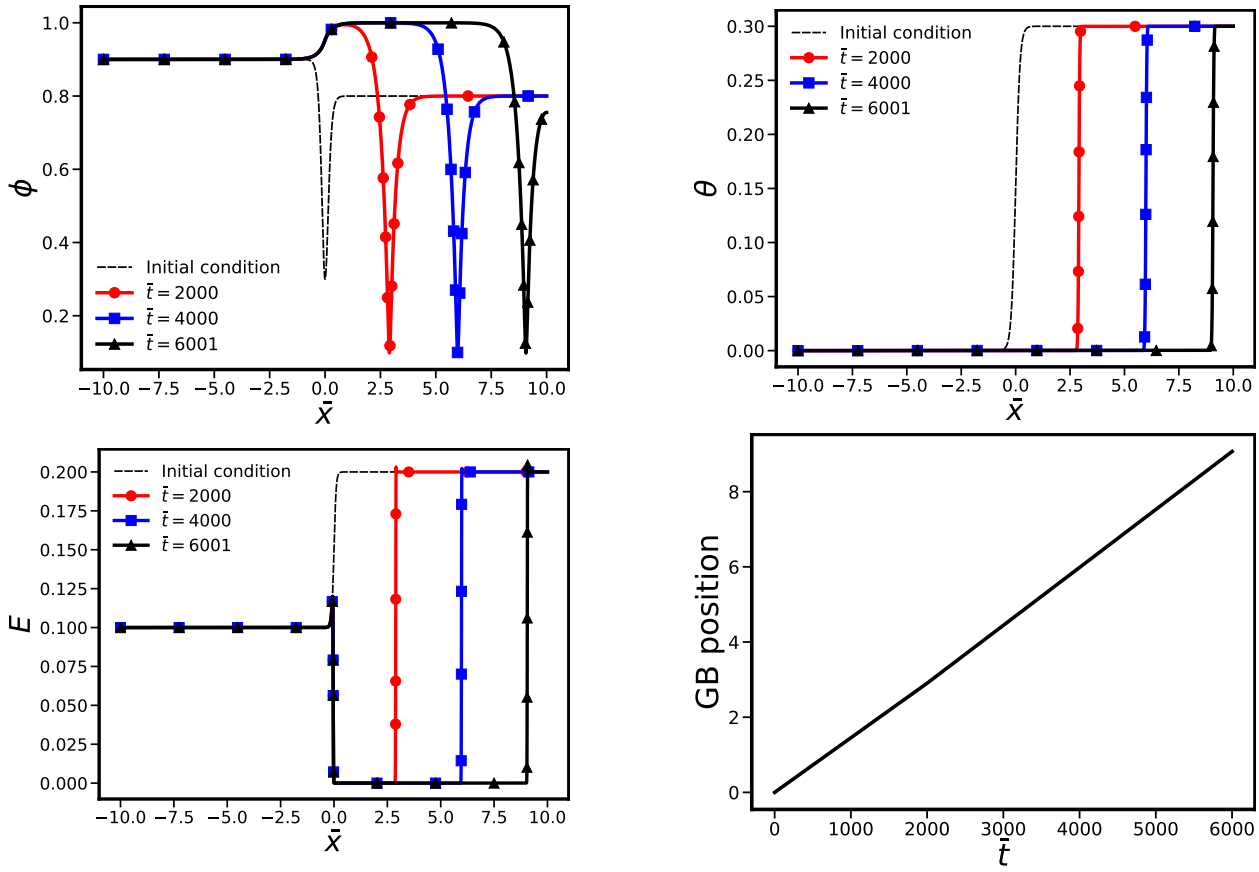

Figure 3.13: *Profiles of ϕ (top left), θ (top right), $\bar{E}$ (bottom left) and position of the grain boundary (bottom right) during stored energy driven migration of a flat interface. The parameters are* $\bar{\alpha} = 0.3, \bar{s} = 2, \bar{\varepsilon} = 2, \bar{\eta}_\phi = 50, \bar{\eta}_\theta = 0.5, \mu_P = 10^6, \beta_P = 1000, C_D = 100, C_A = 1$.

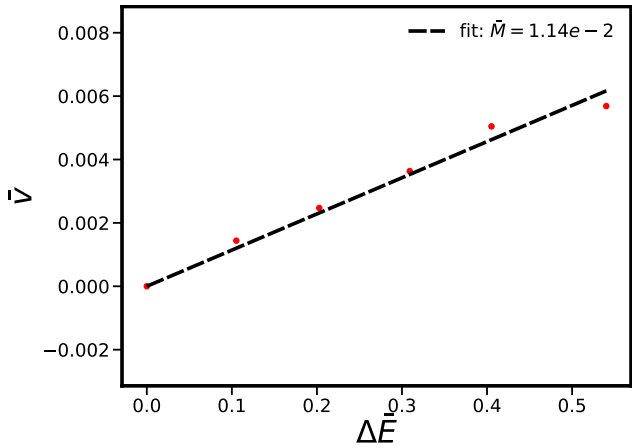

Figure 3.14: *Dimensionless grain boundary migration rate as a function of the stored energy difference during stored energy migration of a flat grain boundary. The parameters are* $\bar{\alpha} = 0.3, \bar{s} = 2, \bar{\varepsilon} = 2, \bar{\eta}_\phi = 50, \bar{\eta}_\theta = 0.5, \bar{\mu}_p = 10^6, \beta_P = 1000, C_D = 100, C_A = 1$.

III.2.3.4 Influence of mobility parameters

The influence of several mobility parameters is studied in this section by running multiple finite element simulations for a fixed set of parameters, given in table 3.1 with $\beta_p = 100$, while varying one parameter. This investigation is conducted for both stored energy and curvature driven migration.

Stored energy driven migration

The impact of the mobility parameters $\bar{\eta}_\phi$ and $\bar{\eta}_\theta$ is examined on a bicrystal. The bicrystal is subject to a dimensionless stored energy jump of 0.3. The dimensionless velocity of the interface remains constant and is determined by the slope of the function representing the position of the grain boundary over time. Figure 3.15a presents the dimensionless migration rate plotted against the value of the parameter $\bar{\eta}_\phi$. With an increase in $\bar{\eta}_\phi$ the grain boundary migration rate decreases by several orders of magnitude and tends exponentially towards 0. A similar assessment was performed to determine the influence of the mobility parameter $\bar{\eta}_\theta$ with a fixed $\bar{\eta}_\phi$ of 50. The obtained curve $\bar{v} - \bar{\eta}_\theta$ is shown in Fig. 3.15b. This curve indicates that the rate of grain boundary migration remains relatively constant when $\bar{\eta}_\theta \leq \bar{\eta}_\phi$. For $\bar{\eta}_\theta \geq \bar{\eta}_\phi$, the migration rate decreases as $\bar{\eta}_\theta$ increases. It appears that the influence of $\bar{\eta}_\theta$ on the resulting migration rate is much less significant: changing $\bar{\eta}_\phi$ can change the migration rate (and thus mobility) by several orders of magnitude, while varying $\bar{\eta}_\theta$ changes the migration rate by only a factor of 2. This observation is expected since the stored energy term only appears in the evolution equation for ϕ, whose kinetic constant is $\bar{\eta}_\phi$.

The effect of parameters $\bar{\mu}_p$ and β_p entering the inverse mobility function P on the migration rate is then assessed. For a flat interface, the parameter $\bar{\mu}_p$ appears to have little influence on the kinetics, as can be seen in Fig. 3.16a. Finally, this study examines the impact of the parameter β_p on the outcomes, as displayed in Fig. 3.16b. It is observed that the migration rate increases with increasing β_p, reaching a threshold limit.

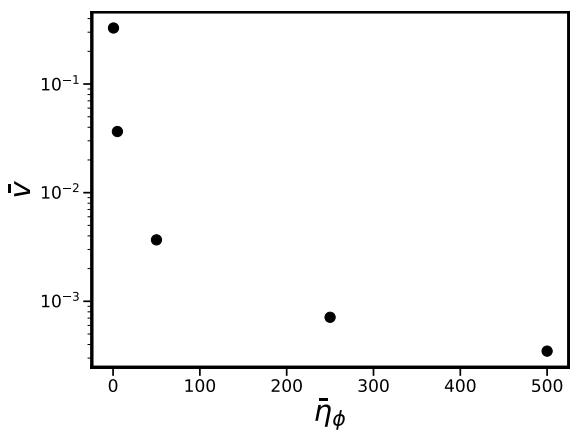

(a) *Influence of parameter* $\bar{\eta}_\phi$.

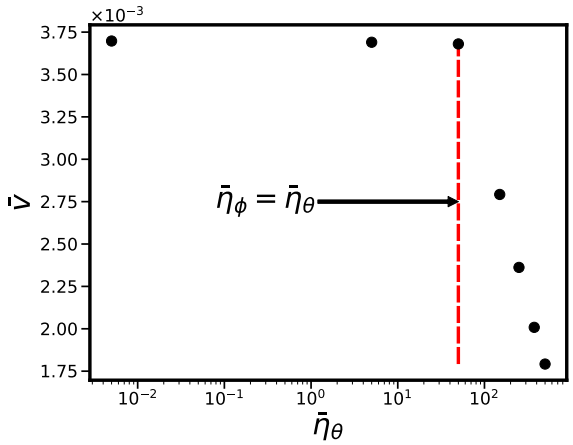

(b) *Influence of parameter* $\bar{\eta}_\theta$.

Figure 3.15: *Influence of parameters* $\bar{\eta}_\theta$ *and* $\bar{\eta}_\phi$ *on the resulting dimensionless migration rate for stored energy driven migration.*

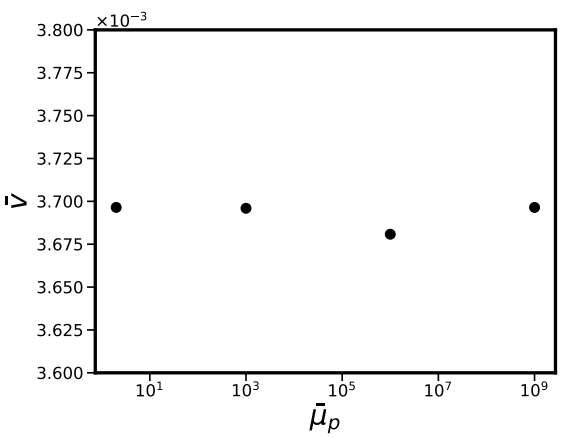

(a) *Influence of parameter* $\bar{\mu}_p$.

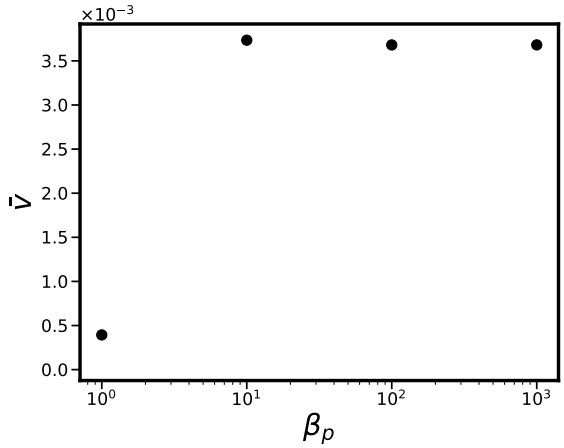

(b) *Influence of parameter* $\bar{\beta}_p$.

Figure 3.16: *Influence of parameters* $\bar{\mu}_p$ *and* β_p *on the resulting dimensionless migration rate for stored energy driven migration.*

Curvature driven grain shrinkage

We now examine the case of a circular grain embedded in a larger matrix to simulate curvature driven migration. Influence of parameters $\bar{\eta}_\phi$ and $\bar{\eta}_\theta$ on grain size, as a function of time, is depicted in Fig. 3.17. It is evident that the grain size decreases more quickly as the inverse mobility parameters decrease. The migration rate in this case appears to depend on parameters $\bar{\eta}_\theta$ and $\bar{\eta}_\phi$ in a more complex manner than for migration driven by stored energy, but features can still be extracted. It is apparent in this figure that for $\bar{\eta}_\theta \in [0.05, 5]$ the kinetics is rather similar. Indeed, variations of about 30% for the time required to reach a null radius are observed, despite the fact that $\bar{\eta}_\theta$ varies over two orders of magnitude. However, if $\bar{\eta}_\theta$ is too low compared to $\bar{\mu}_p/\bar{\varepsilon}$, there may be a reorientation of the inclusion and matrix, as the product of $\bar{\eta}_\theta$ and the inverse mobility function P may not be high enough in the bulk to prevent spurious reorientations. That is the case for $\bar{\eta}_\theta = 0.005$ and explains why the radius suddenly goes to 0.

Figure 3.18 illustrates the time evolution of the grain radius for various values of $\bar{\mu}_p$ and β_p. Clearly, as $\bar{\mu}_p$ approaches infinity, the velocity approaches 0. When $\bar{\mu}_p/\bar{\varepsilon} = 1$, which occurs at $\bar{\mu}_p = 2$, the inverse mobility function P always equals 1 regardless of the orientation gradient. This makes it impossible to distinguish between bulk and grain boundary behaviours. For some larger values such as $\bar{\mu}_p = 10^3$, one would expect the localisation to be active. However, the value of $\bar{\mu}_p$ alone is not what determines the mobility, but that of $\bar{\eta}_\theta \bar{\mu}_p/\bar{\varepsilon}$. In this case, it is not high enough to prevent reorientation. It is therefore necessary to increase the magnitude of parameter $\bar{\mu}_p$ for the behaviours to be really distinct in the bulk and in the grain boundary. A value of $\bar{\mu}_p = 10^6$ for instance, appears to be effective in halting grain rotation during shrinkage.
For parameter β_p, the choice $\beta_p = 0$ yields a constant value of $P = \bar{\mu}_p/\bar{\varepsilon}$, which does not prevent concomitant reorientation and shrinkage. As $\bar{\mu}_p = 10^6$ the time evolution of the radius is very slow due to the low mobility. For larger values of β_p, like in the case of migration driven by stored energy, the velocity remains constant once a threshold value is reached. It is expected that this value depends on the interface width ℓ_θ.

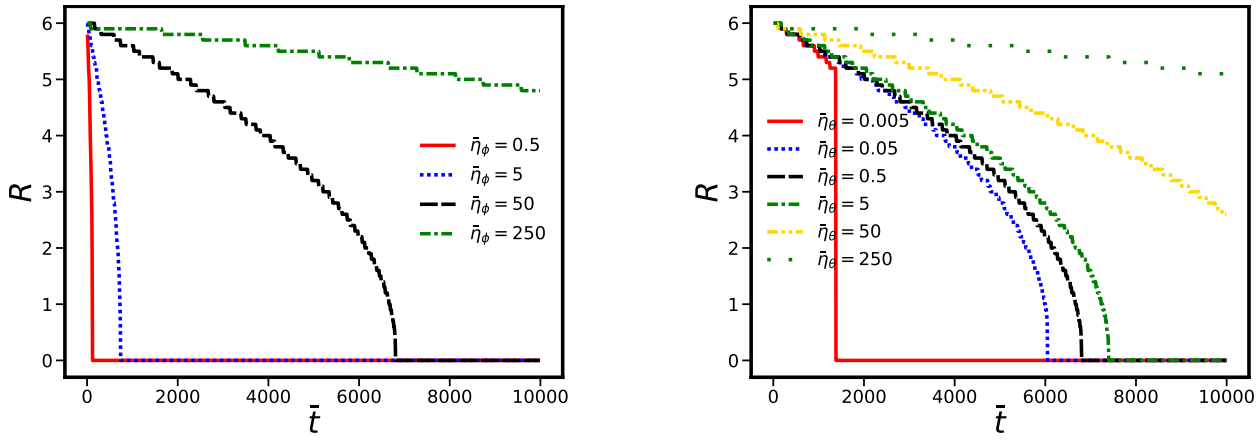

(a) *Influence of parameter* $\bar{\eta}_\phi$. (b) *Influence of parameter* $\bar{\eta}_\theta$.

Figure 3.17: *Influence of parameters* $\bar{\eta}_\theta$ *and* $\bar{\eta}_\phi$ *on the resulting grain size for curvature driven migration.*

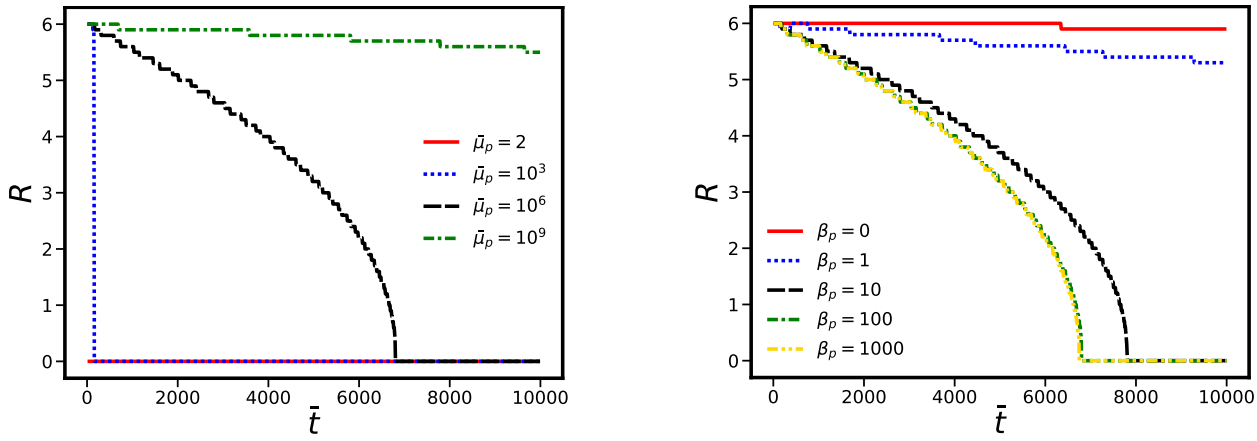

(a) *Influence of parameter* $\bar{\mu}_p$. (b) *Influence of parameter* $\bar{\beta}_p$.

Figure 3.18: *Influence of parameters* $\bar{\mu}_p$ *and* β_p *on the resulting grain size for curvature driven migration.*

III.2.4 Calibration of phase-field and mobility parameters

The studies conducted so far did not incorporate parameters with physical relevance. In this section, we describe a simple calibration procedure to retrieve more physically meaningful phase-field and mobility parameters.

The phase-field parameters $\bar{\alpha}$ and $\bar{s}$ in the free enery density can be calibrated using the asymptotic analysis of Lobkovsky and Warren [2001] to fit a zero-temperature grain boundary energy misorientation curve found in the literature (see Fig. 1 in Ask et al. [2020]). The misorientation is capped at $\Delta\theta = 30^\circ$ to include only the Read-Shockley part of the curve and discard the local GB energy cusps. A grain boundary energy magnification factor fac can be defined such that

$$fac = \frac{\gamma_{ref}(\Delta\theta = 30^\circ)}{\widetilde{\gamma}(\Delta\theta = 30^\circ)} = f_0 \Lambda \bar{\varepsilon}, \quad \gamma(\Delta\theta) = \widetilde{\gamma}(\Delta\theta) \times fac \tag{3.43}$$

where $\gamma_{ref}(\Delta\theta = 30^\circ)$ and $\widetilde{\gamma}(\Delta\theta = 30^\circ)$ are the reference (used to calibrate the parameters) and asymptotic grain boundary energies, respectively, for a misorientation of 30°. The parameter $\bar{\varepsilon}$ in the free energy density, which controls the grain boundary diffusivity, can be chosen freely. The parameters are calibrated for pure copper with $g(\phi) = -2(\log(1-\phi)+\phi)$. At the mesoscale, appropriate length scale Λ and time scale τ_0 are respectively $\Lambda = 1\mu m$ and $\tau_0 = 1s$. This calibration method gives $\bar{s} = 0.75$ and $\bar{\alpha} = 0.31$ for $\bar{\varepsilon} = 1$.

The grain boundary energy is fitted against that of a $< 100 >$ Cu tilt boundary obtained from atomistic simulations [Wolf, 1990], see Fig. 3.19a. The grain boundary energy scale factor is $fac = 2300\ mJ/m^2$, which corresponds to a grain boundary energy scale parameter $f_0 = \dfrac{fac}{\Lambda\bar{\varepsilon}} = 2.3\ MPa$.

The various parameters of the model are summarised in table 3.2. Note that the grain boundary width can

Parameter/quantity	dimensionless expression	calibration
Energy magnitude f_0 [Jm^{-3}]	NA	Fit of the GB energy
Time scale τ_0 [s]	NA	Choice or ratio of mobilities
Length scale Λ [m]	NA	Choice
Length x [m]	$\bar{x} = \dfrac{x}{\Lambda}$	NA
Free energy $\mathscr{F}$ [J]	$\bar{\mathscr{F}} = \dfrac{\mathscr{F}}{f_0\Lambda^3}$	NA
Stored energy density $\bar{E}$ [Jm^{-3}]	$\bar{E} = \dfrac{E}{f_0}$	Choice or computation
α [$\sqrt{\mathrm{J/m}}$]	$\bar{\alpha} = \dfrac{\alpha}{\sqrt{f_0}\Lambda}$	Fit of the GB energy
ε [$\sqrt{\mathrm{J/m}}$]	$\bar{\varepsilon} = \dfrac{\varepsilon}{\sqrt{f_0}\Lambda}$	Choice
$\bar{s}$ [$\mathrm{J/m}^2$]	$\bar{s} = \dfrac{s}{f_0\Lambda}$	Fit of the GB energy
grain boundary energy γ [Jm^{-3}]	$\bar{\gamma} = \dfrac{\gamma}{f_0\Lambda}$	Asymptotic analysis/FD/FE computation
grain boundary mobility $\mathscr{M}$ [$\mathrm{m}^4\mathrm{s}^{-1}\mathrm{MJ}^{-1}$]	$\bar{\mathscr{M}} = \mathscr{M}\dfrac{\tau_0 f_0}{\Lambda}$	Numerical experiment
η_ϕ [$\mathrm{Js/m}^3$]	$\bar{\eta}_\phi = \dfrac{\eta_\phi}{f_0\tau_0}$	Numerical experiment
η_θ [$\mathrm{Js/m}^3$]	$\bar{\eta}_\theta = \dfrac{\eta_\theta}{f_0\tau_0}$	Numerical experiment
μ_p [m]	$\bar{\mu}_p = \dfrac{\mu_p}{\Lambda}$	Choice
β_p [-]	NA	Numerical experiment
C_A [m]	$\bar{C}_A = \dfrac{C_A}{\Lambda}$	Choice
C_D [-]	NA	Choice

Table 3.2: *Parameters and material properties of the KWC model.*

be selected with some control by changing the $\bar{\varepsilon}$ parameter and the $\widetilde{\alpha} = \bar{\alpha}/\bar{\varepsilon}, \widetilde{s} = \bar{s}/\bar{\varepsilon}$ parameters accordingly. For example, choosing $\bar{\alpha} = 0.31, \bar{s} = 0.75, \bar{\varepsilon} = 1 \rightarrow \widetilde{\alpha} = 0.31, \widetilde{s} = 0.75$ will give a θ–width $\ell_\theta \sim 0.3$. This width can be halved by dividing the value of the parameter $\bar{\varepsilon}$ by a factor of 2: $\bar{\varepsilon} = 0.5, \bar{\alpha} = 0.31, \bar{s} = 0.75 \Rightarrow \widetilde{\alpha} = 0.155, \widetilde{s} = 0.375$ gives a $\ell_\theta \sim 0.15$. These two parameter sets are energetically equivalent. However, there seems to be a lower limit to the value of $\bar{\varepsilon}$ that can be chosen, as can be seen in Fig. 3.20 where for $\bar{\varepsilon} = 0.1$ the grain boundary is not well defined. This figure shows the θ and ϕ fields zoomed in the interface region for different values of $\bar{\varepsilon}$, which changes the grain boundary width for a given set of $\bar{\alpha}, \bar{s}$.

As there is no published asymptotic analysis that accounts for grain boundary migration due to a stored energy difference, the mobility parameters $\bar{\eta}_\phi, \bar{\eta}_\theta, \bar{\mu}_p, \beta_p$ must be tuned so that the resulting mobility of a 1D boundary subjected to a stored energy difference is comparable to data found in the literature [Gottstein and Shvindlerman, 2009]. Parameter $\bar{\mu}_p$ must be sufficiently high to effectively separate the behaviours in the bulk and in the grain boundary. Parameter β_p must be chosen so that the threshold value for constant

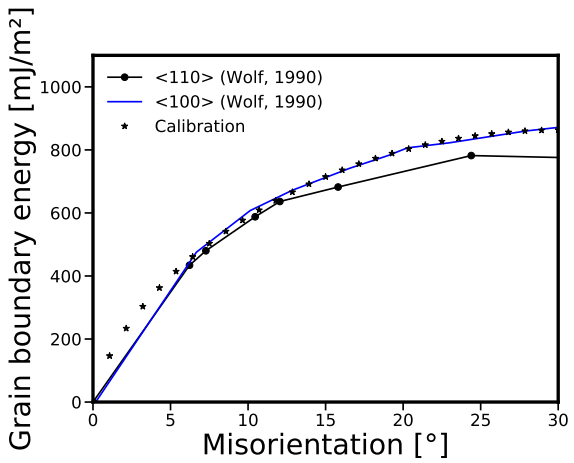

(a) *Calibration of the grain boundary energy - misorientation curve.*

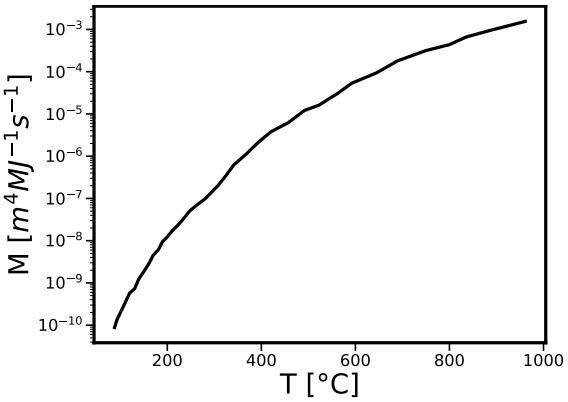

(b) *Pure copper grain boundary mobility as a function of temperature, adapted from Vandermeer et al. [1997].*

Figure 3.19: *Grain boundary energy–misorientation curve (left) and grain boundary mobility as a function of temperature (right).*

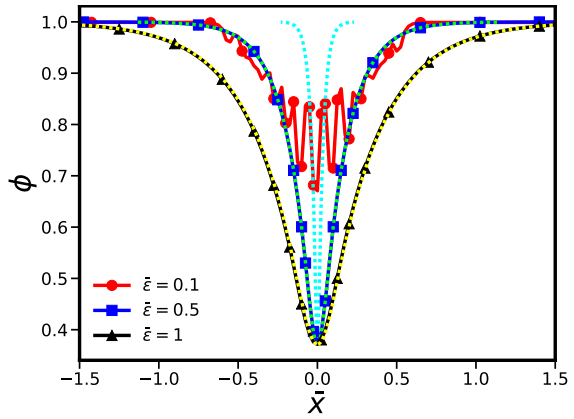

(a) *Profiles of ϕ for different $\bar{\varepsilon}$ and fixed $\bar{\alpha}, \bar{s}$*

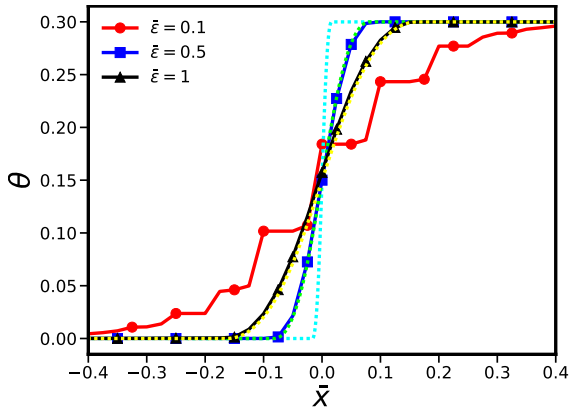

(b) *Profiles of θ for different $\bar{\varepsilon}$ and fixed $\bar{\alpha}, \bar{s}$*

Figure 3.20: *Profiles of ϕ and θ for different values of $\bar{\varepsilon}$ (and thus different values of $\widetilde{\alpha}, \widetilde{s}$). Marked solid lines are FEM solutions whereas dotted lines denote solutions obtained with the matched asymtotic analysis.*

velocity is reached. The recovery parameters $\bar{C}_A, C_D$ are chosen so that full recovery, i.e. annihilation of stored dislocations, occurs behind the moving grain boundary. Data related to the grain boundary mobility of pure copper can be found in the work of Vandermeer et al. [1997], where mobilities for a wide range of temperatures are presented, which can be used as a reference to estimate the temperature in the KWC model. The data used in Fig. 5 of this reference is plotted in Fig. 3.19b. The basic test of a bicrystal with a lattice misorientation of 0.3 subjected to a stored energy difference of 0.09 is carried out to determine sensible values of $\bar{\eta}_\phi$ and $\bar{\eta}_\theta$. The initial state is in equilibrium. To do this, a KWC simulation is first run to find the fields ϕ, θ at equilibrium. The parameters used in this simulation as well as the resulting temperatures and mobilities are listed in table 3.3. Migration of a flat interface driven by a stored energy was chosen due to the linear relationship between boundary migration rate and driving force. Moreover, the stored energy related to dislocations is the predominant driving force in plastically deformed crystals. Alternatively, simulations of curvature driven migration in wedged bicrystals [Gottstein and Shvindlerman, 2009] could be run in order to calibrate the kinetic constants of the model.

Parameter/property	Unit	Value	Comment
τ_0	s	1	time scale
Λ	μm	1	Length scale
f_0	MPa	2.3	GB energy magnitude parameter
$\bar{\alpha}$	-	0.31	Phase-field parameter
$\bar{s}$	-	0.75	Phase-field parameter
$\bar{\varepsilon}$	-	1	Sets the θ-width for fixed $\bar{\alpha}, \bar{s}$
$\bar{\eta}_\phi$	-	10	Viscosity parameter for the evolution of ϕ
$\bar{\eta}_\theta$	-	0.1 or 1	Viscosity parameter for the evolution of θ
$\bar{C}_A$	-	1	Sets the width of the recovery area aroung the GB
$\bar{C}_D$	-	100	Sets the magnitude of the recovery
$\bar{\mu}_p$	-	1×10^6	Specifies the magnitude of $P(\bar{\nabla}\theta)$ in the bulk of the grain
β_p	-	100 or 1000	Sets the rate at which the mobility function goes to 1 in the GB
$\bar{\gamma}$	-	1×10^4	Regularizing term for the singular diffusivity
γ_g	-	1×10^{-4}	Regularizing term for function $g(\phi)$
$\Delta\theta$	$^\circ$	15	Lattice misorientation
$\Delta\bar{E}$	-	0.09	Stored energy difference
γ_{GB}	mJ/m^2	756	GB energy
M	$m^4/MJ/s$	2.4×10^{-8} or 2.2×10^{-8}	GB mobility
T	$^\circ C$	$\simeq$ 230 or 220	Temperature

Table 3.3: *Parameters and properties of a bicrystal used to determine the GB mobility during stored energy driven migration.*

III.3 Coupled KWC-Cosserat crystal plasticity model

III.3.1 Governing equations

The KWC phase-field model seems to be a powerful tool for modelling microstructure evolution in (poly)crystalline materials. However, it does not account for lattice reorientation due to deformation, nor the increase in stored energy due to dislocation buildup. To tackle this problem and consider the interaction between mechanics and grain boundary motion, the KWC model can be extended in a fully coupled formulation with generalised continua such as strain-gradient plasticity Admal et al. [2018] or Cosserat mechanics Ask et al. [2018b].

III.3.1.1 Link between KWC model and Cosserat mechanics

The framework of continuum thermodynamics used for formulating phase-field models as described by Gurtin [1996] allows for a strong coupling between continuum mechanics and phase-field models for microstructure evolution [Steinbach and Apel, 2006]. The model proposed in a series of papers by Ask et al. [2018b,a, 2019, 2020] is based on a modified KWC free energy in which the orientation phase-field is identified with Cosserat microrotational degrees of freedom. The free energy potential therefore has both quadratic and rank-one dependencies on the norm of the curvature. Contributions due to elastic strain and statistically stored dislocation densities are also included in this free energy. Furthermore, the evolution equation of the lattice orientation in the KWC model is interpreted as a balance equation for the couple stress in the framework of Cosserat continuum dynamics with both quadratic and rank-one contributions of the norm of the curvature. In the current work, the hypothesis of isothermal processes at small strains,

rotations and curvatures is assumed, which results in the following equations:

$$P\eta_\theta \phi^2 \dot{\theta} = -\frac{\partial \psi}{\partial \theta} + \nabla \cdot \frac{\partial \psi}{\partial \nabla \theta} = \nabla \cdot \left(\varepsilon^2 h \nabla \theta + sg \frac{\nabla \theta}{|\nabla \theta|} \right) (KWC) \tag{3.44}$$

$$\varrho\, I \ddot{\underline{\theta}} = -\frac{\partial \psi}{\partial \underline{\theta}} + \nabla \cdot \frac{\partial \psi}{\partial \underline{\theta} \otimes \nabla} = -\underline{\underline{\epsilon}} : \left(\underline{\underline{\underline{\underline{\Lambda}}}} : \mathrm{skew}(\nabla \underline{u} + \underline{\underline{\epsilon}} \cdot \underline{\theta}) \right) + \nabla \cdot \left(\underline{\underline{\underline{\underline{C}}}} : \underline{\theta} \otimes \nabla + A \frac{\underline{\theta} \otimes \nabla}{\|\underline{\theta} \otimes \nabla\|} \right) (Cosserat) \tag{3.45}$$

This full-field mesoscopic model is thermodynamically consistent by construction and is able to account for the heterogeneous reorientation produced by plastic slip, as well as that of a material point caused by a migrating front.

III.3.1.2 Free energy, evolution equations & difference with the KWC model

Free energy

In this section we briefly recall the dimensionless coupled KWC-Cosserat model proposed by Ask et al. [2018a,b, 2020]. This model is valid for small strains, rotations and curvatures and only considers the Read-Shockley part of the grain boundary energy-misoriation curve. It is therefore limited to low angle grain boundaries. This formulation couples the KWC phase-field model to Cosserat mechanics via the following free energy potential:

$$\begin{aligned} \psi(\phi, \nabla\phi, \underline{\theta} \otimes \nabla, \underline{\underline{e}}^e, r^\alpha) = & \underbrace{f_0 \left(f(\phi) + \frac{\alpha^2}{2} |\nabla \phi|^2 + sg(\phi) ||\underline{\theta} \otimes \nabla|| + \frac{\varepsilon^2}{2} h(\phi) ||\underline{\theta} \otimes \nabla||^2 \right)}_{\text{KWC GB energy}} \\ & + \underbrace{\frac{1}{2} \mathrm{sym}(\underline{\underline{e}}^e) : \underline{\underline{\underline{\underline{E}}}}^s : \mathrm{sym}(\underline{\underline{e}}^e) + 2\mu_c \mathrm{skew}(\underline{\underline{e}}^e) : \mathrm{skew}(\underline{\underline{e}}^e)}_{\text{Cosserat elasticity}} + \underbrace{\psi_\rho(\phi, r^\alpha)}_{\text{SSD accumulation}} \end{aligned} \tag{3.46}$$

$$\psi_\rho(\phi, r^\alpha) = \phi \frac{1}{2} \chi \mu \sum_{\alpha=1}^{N} r^{\alpha^2}, \quad r^\alpha = b \sqrt{\sum_{\beta=1}^{N} h^{\alpha\beta} \rho^\beta} \tag{3.47}$$

where $\mu, b, \rho^\alpha, h^{\alpha\beta}$ and $\chi \sim 0.3$ are respectively the shear modulus, the magnitude of the Burgers vector, the dislocation density of the slip system α, the slip interaction matrix and a coefficient. The number of slip systems is denoted by N. The generally non symmetric strain tensor $\underline{\underline{e}}$ in the free energy density given by Eq. 3.46 has been split into symmetric and skew-symmetric contributions. For simplicity, the skew-symmetric part will be assumed isotropic, though the symmetric isotropic elasticity tensor $\underline{\underline{\underline{\underline{e}}}}^s$ can be anisotropic.

Principle of virtual power

The balance laws and boundary conditions are derived using the principle of virtual power on the following set of virtual field variables and their gradients:

$$\mathscr{V} = \{\dot{\phi}, \nabla\dot{\phi}, \dot{\underline{u}}, \dot{\underline{u}} \otimes \nabla, \dot{\underline{\theta}}, \dot{\underline{\theta}} \otimes \nabla\} \tag{3.48}$$

The generalised stresses $\{\underline{\underline{\sigma}}, \underline{\underline{m}}, \pi_\phi, \underline{\xi}_\phi\}$ are the work conjugates quantities of the phase-field and deformation variables $\{\underline{\underline{e}}, \underline{\theta} \otimes \nabla, \phi, \nabla\phi\}$. For any region $\mathscr{D}$ with boundary $\partial\mathscr{D}$ of a volume Ω, the principle of virtual power in the absence of inertial (micro) forces states that for all virtual fields $\phi, \dot{\underline{u}}, \dot{\underline{\theta}}$:

$$\int_{\mathscr{D}} p^i dV = \int_{\mathscr{D}} p^e dV + \int_{\mathscr{D}} p^c dV \tag{3.49}$$

where p^i, p^e, p^c are respectively the virtual density of internal, external and contact forces. They are given by:

$$p^i = -\pi_\phi \dot{\phi} + \underline{\xi}_\phi \cdot \nabla\dot{\phi} + \underbrace{\underset{\sim}{\sigma} : \underline{\dot{u}} \otimes \nabla - 2\overset{\times}{\underline{\sigma}} \cdot \underline{\dot{\theta}}}_{\underset{\sim}{\sigma}:\underset{\sim}{\dot{e}}} + \underset{\sim}{m} : \underline{\dot{\theta}} \otimes \nabla \tag{3.50}$$

$$p^e = \pi_\phi^{ext}\dot{\phi} + \underline{f}^{ext} \cdot \underline{\dot{u}} + \underline{c}^{ext} \cdot \underline{\dot{\theta}} \tag{3.51}$$

$$p^c = \pi_\phi^{c}\dot{\phi} + \underline{f}^{c} \cdot \underline{\dot{u}} + \underline{c}^{c} \cdot \underline{\dot{\theta}} \tag{3.52}$$

By integrating by parts and applying the divergence theorem to the principle of virtual power, the balance equations and boundary conditions are obtained $\forall \mathscr{D} \subset \Omega$, $\forall (\phi, \underline{\dot{u}}, \underline{\dot{\theta}})$:

$$\nabla \cdot \underline{\xi}_\phi + \pi_\phi + \pi_\phi^{ext} = 0 \qquad \text{in } \Omega \tag{3.53}$$

$$\underset{\sim}{\sigma} \cdot \nabla + \underline{f}^{ext} = 0 \qquad \text{in } \Omega \tag{3.54}$$

$$\underset{\sim}{m} \cdot \nabla + 2\overset{\times}{\underline{\sigma}} + \underline{c}^{ext} = 0 \qquad \text{in } \Omega \tag{3.55}$$

$$\underline{\xi}_\phi \cdot \underline{n} = \pi_\phi^c \qquad \text{on } \partial\mathscr{D} \tag{3.56}$$

$$\underset{\sim}{\sigma} \cdot \underline{n} = \underline{f}^{c} \qquad \text{on } \partial\mathscr{D} \tag{3.57}$$

$$\underset{\sim}{m} \cdot \underline{n} = \underline{c}^{c} \qquad \text{on } \partial\mathscr{D} \tag{3.58}$$

The constitutive equations derive from the Clausius-Duhem inequality:

$$-\rho\dot{\Psi} + p^i \geq 0 \tag{3.59}$$

with Ψ the Helmholtz free energy density such that:

$$\rho\Psi = \psi(\phi, \nabla\phi, \underline{\theta} \otimes \nabla, \underset{\sim}{e}^e, r^\alpha) \tag{3.60}$$

where r^α are the internal variables associated with the inelastic behavior. Combining Eqs. 3.60 and 3.50, the Clausius-Duhem inequality 3.59 becomes

$$-\dot{\psi} - \pi_\phi\dot{\phi} + \underline{\xi}_\phi \cdot \nabla\phi + \underset{\sim}{\sigma} : \underset{\sim}{e}^e + \underset{\sim}{m} : \underline{\theta} \otimes \nabla + \underset{\sim}{\sigma} : \underset{\sim}{e}^{in} \geq 0 \tag{3.61}$$

Applying the chain rule to the term $\dot{\psi}$ gives the following inequality

$$-\left[\pi_\phi + \frac{\partial\psi}{\partial\phi}\right]\dot{\phi} + \left[\underline{\xi}_\phi - \frac{\partial\psi}{\partial\nabla\phi}\right] \cdot \nabla\dot{\phi} + \left[\underset{\sim}{\sigma} - \frac{\partial\psi}{\partial\underset{\sim}{e}^e}\right] : \underset{\sim}{\dot{e}}^e + \left[\underset{\sim}{m} - \frac{\partial\psi}{\partial\underline{\theta} \otimes \nabla}\right] : \underline{\dot{\theta}} \otimes \nabla$$
$$+ \underset{\sim}{\sigma} : \underset{\sim}{\dot{e}}^{in} - \sum_\alpha \frac{\partial\psi}{\partial r^\alpha}\dot{r}^\alpha \geq 0 \tag{3.62}$$

In accordance with Gurtin [1996] it is assumed that π_ϕ contains energetic and dissipation contributions such that:

$$\pi_\phi = \pi_\phi^{eq} + \pi_\phi^{neq} \tag{3.63}$$

The Clausius-Duhem inequality becomes

$$\underbrace{-\left[\pi_\phi^{eq}+\frac{\partial\psi}{\partial\phi}\right]\dot{\phi}+\left[\underline{\xi}_\phi-\frac{\partial\psi}{\partial\nabla\phi}\right]\cdot\nabla\dot{\phi}+\left[\underset{\sim}{\sigma}-\frac{\partial\psi}{\partial\underset{\sim}{e}^e}\right]:\dot{\underset{\sim}{\varepsilon}}^e+\left[\underset{\sim}{m}-\frac{\partial\psi}{\partial\underline{\theta}\otimes\nabla}\right]:\dot{\underline{\theta}}\otimes\nabla}_{\text{Energetic contribution}}$$

$$\underbrace{-\pi_\phi^{neq}\dot{\phi}+\underset{\sim}{\sigma}:\dot{\underset{\sim}{\varepsilon}}^{in}-\sum_\alpha\frac{\partial\psi}{\partial r^\alpha}\dot{r}^\alpha}_{\text{Dissipative contribution}}\geq 0 \tag{3.64}$$

The following constitutive relations are deduced from the Clausius-Duhem inequality 3.64:

$$\pi_\phi^{eq}=\frac{-\partial\psi}{\partial\phi},\quad \underline{\xi}_\phi=\frac{\partial\psi}{\partial\nabla\phi} \tag{3.65}$$

$$\underset{\sim}{\sigma}=\frac{\partial\psi}{\partial\underset{\sim}{e}^e},\quad \underset{\sim}{m}=\frac{\partial\psi}{\partial\underline{\theta}\otimes\nabla} \tag{3.66}$$

$$R^\alpha=\frac{\partial\psi}{\partial r^\alpha} \tag{3.67}$$

where R^α is the thermodynamic force associated with the internal variable r^α. In this model these internal variables are related to the statistically stored dislocation densities ρ^α such that

$$r^\alpha=b\sqrt{\sum_{\beta=1}^{N}h^{\alpha\beta}\rho^\beta} \tag{3.68}$$

Constitutive and evolution equations

With the free energy given by Eq. 3.46, the constitutive equations are:

$$\mathrm{sym}(\underset{\sim}{\sigma})=\underset{\approx}{E}^s:\underset{\sim}{\varepsilon}^e \tag{3.69}$$

$$\overset{\times}{\underline{\sigma}}=2\mu_c\,\overset{\times}{\underline{\mathbf{e}}}^e \tag{3.70}$$

$$\underset{\sim}{\xi}_\theta=f_0\left[sg(\phi)\frac{1}{||\underline{\theta}\otimes\nabla||}+\varepsilon^2h(\phi)\right]\underline{\theta}\otimes\nabla \tag{3.71}$$

$$\underline{\xi}_\phi=f_0\alpha^2\nabla\phi \tag{3.72}$$

The Cosserat couple stress $\underset{\sim}{m}=\partial\psi/\partial\underline{\theta}\otimes\nabla$ and skew-symmetric stress $\overset{\times}{\underline{\sigma}}$ are identified with $\underline{\xi}_\theta$ and $\pi_\theta/2$ respectively in Gurtin's formulation of the KWC model (Eq. 3.23). The evolution equations of the dissipative contributions are assumed to derive from the following dissipation potential:

$$\Omega=\Omega^{in}(\underset{\sim}{\sigma})+\Omega^\phi(\phi)+\Omega^\alpha(r^\alpha) \tag{3.73}$$

so that

$$\dot{\underset{\sim}{\varepsilon}}^{in}=\frac{\partial\Omega^{in}}{\partial\underset{\sim}{\sigma}},\quad \dot{r}^\alpha=-\frac{\partial\Omega^\alpha}{\partial R^\alpha},\quad \dot{\phi}=-\frac{\partial\Omega^\phi}{\partial\pi_\phi^{neq}} \tag{3.74}$$

The KWC evolution equation for the crystal order can be retrieved by choosing a quadratic dissipation potential for Ω^ϕ:

$$\Omega^\phi=\frac{1}{2}\eta_\phi^{-1}\left(\pi_\phi^{neq}\right)^2 \tag{3.75}$$

The KWC evolution equation for ϕ is retrieved by the equilibrium law for the microstress :

$$\nabla \cdot \underbrace{\underline{\xi}_{\phi}}_{\frac{\partial \psi}{\partial \nabla \phi}} + \underbrace{\pi_{\phi}^{eq}}_{-\frac{\partial \psi}{\partial \phi}} + \underbrace{\pi_{\phi}^{neq}}_{-\eta_{\phi}\dot{\phi}} = 0 \tag{3.76}$$

$$\eta_{\phi}\dot{\phi} = \alpha^2 \nabla^2 \phi - f_{,\phi} - sg_{,\phi}|\nabla\theta| - \frac{\varepsilon^2}{2} h_{,\phi} |\nabla\theta|^2 - \underbrace{\frac{1}{2}\mu b^2 \sum_{\alpha=1}^{N}\sum_{\beta=1}^{N} h^{\alpha\beta}\rho^{\beta}}_{E} \tag{3.77}$$

The inelastic dissipation potential Ω^{in} is assumed to have contributions from crystal plasticity in the bulk of the grain (Ω^{slip}) and viscoelastic/viscoplastic relaxation of the skew symmetric stress at the grain boundary in response to lattice reorientation ($\Omega^{\star}$):

$$\Omega^{in} = \Omega^{slip}(\underset{\sim}{\sigma}) + \Omega^{\star}(\overset{\times}{\underline{\sigma}}; \underline{\theta} \otimes \nabla) \tag{3.78}$$

$$\Omega^{slip} = \sum_{\alpha=1}^{N} \frac{K}{n+1} \left\langle \frac{|\tau^{\alpha}| - R^{\alpha}/\phi - \tau_c}{K} \right\rangle^{n+1} \tag{3.79}$$

$$\tau^{\alpha} = \underset{\sim}{\sigma} : \underline{\ell}^{\alpha} \otimes \underline{n}^{\alpha}, \quad R^{\alpha} = \phi\chi\mu b \sqrt{\sum_{\beta=1}^{N} h^{\alpha\beta}\rho^{\beta}} \tag{3.80}$$

where $\langle \bullet \rangle$ denotes the positive part and K, n are viscoplasticity parameters. The resolved shear stress is denoted by τ^{α} and the hardening value by R^{α}. The initial critical resolved shear stress is represented by τ_c. During grain boundary migration, local lattice reorientation occurs inside the grain boundary and gives rise to skew symmetric stresses. This change of lattice orientation reference for a zero-stress state is represented by $\underline{\theta}^{\star}$, a grain boundary contribution to the skew symmetric part of the plastic deformation $\underset{\sim}{e}^{in}$. In other words, in the bulk of the grain lattice rotation is only due to elastic/plastic deformation, whereas in the grain boundary an orientation change is only prompted by the evolution of $\underline{\theta}^{\star}$, the orientation reference with zero skew-symmetric stress. This inelastic mechanism is associated with a relaxation equation whose driving force is the skew-symmetric stress. This equation is described in detail in section III.3.2, where it is also shown that without this grain boundary relaxation, grain boundary motion would be hindered. The inelastic strain rate is derived from the dissipation potential Ω^{in} such that:

$$\underset{\sim}{\dot{e}}^{in} = \frac{\partial \Omega^{slip}}{\partial \underset{\sim}{\sigma}} - \underline{\underline{\epsilon}} \cdot \frac{\partial \Omega^{\star}}{\partial \overset{\times}{\underline{\sigma}}} = \underset{\sim}{\dot{e}}^{slip} - \underline{\underline{\epsilon}} \cdot \dot{\underline{\theta}}^{\star} \tag{3.81}$$

$$\underset{\sim}{\dot{e}}^{slip} = \sum_{\alpha=1}^{N} \dot{\gamma}^{\alpha} \underline{\ell}^{\alpha} \otimes \underline{n}^{\alpha}, \quad \dot{\gamma}^{\alpha} = \left\langle \frac{|\tau^{\alpha}| - R^{\alpha}/\phi - \tau_c}{K} \right\rangle^{n} \mathrm{sign}(\tau^{\alpha}) \tag{3.82}$$

$$\tag{3.83}$$

where $\underline{\ell}^{\alpha}$ and $\underline{n}^{\alpha}$ are the slip direction and normal to the slip plane for the slip system α, $\dot{\gamma}^{\alpha}$ is the slip rate. The strain tensor is therefore given by

$$\underset{\sim}{e} = \underline{u} \otimes \nabla + \underline{\underline{\epsilon}} \cdot \underline{\theta} = \underset{\sim}{e}^{e} + \underset{\sim}{e}^{slip} - \underline{\underline{\epsilon}} \cdot \underline{\theta}^{\star} \tag{3.84}$$

$$\tag{3.85}$$

The strain tensor is split into symmetric and skew-symmetric contributions

$$\mathrm{sym}(\underset{\sim}{e}) = \underset{\sim}{\varepsilon} = \underset{\sim}{\varepsilon}^{e} + \underset{\sim}{\varepsilon}^{slip} \tag{3.86}$$

$$\mathrm{skew}(\underset{\sim}{e}) = \underset{\sim}{\omega} + \underline{\underline{\epsilon}} \cdot \underline{\theta} = \mathrm{skew}(\underset{\sim}{e}^{e}) + \mathrm{skew}(\underset{\sim}{e}^{slip}) - \underline{\underline{\epsilon}} \cdot \underline{\theta}^{\star} \tag{3.87}$$

The skew-symmetric part of the elastic strain is now

$$\text{skew}(e^e) = \underbrace{\underset{\sim}{\omega} - \text{skew}(\underset{\sim}{e}^{slip})}_{\underset{\sim}{\omega}^e} + \underline{\underline{\epsilon}} \cdot \underline{\theta} + \underline{\underline{\epsilon}} \cdot \underline{\theta}^\star \tag{3.88}$$

$$\overset{\times}{\underline{e}}^e = \overset{\times}{\underline{\omega}}^e - \underline{\theta} - \underline{\theta}^\star \sim \underline{0} \Rightarrow \overset{\times}{\underline{\omega}}^e \sim \underline{\theta} + \underline{\theta}^\star \tag{3.89}$$

As the Cosserat microrotation is associated with the lattice orientation, it is generally non-zero in the initial state. Thus, the reference configuration can only be stress-free if the initial inelastic deformation is also non-zero. Therefore, it is necessary to adopt the following initial condition:

$$\underline{\theta}^\star(t=0) = -\underline{\theta}\,(t=0) \tag{3.90}$$

The inelastic grain boundary behaviour is therefore necessary to accommodate an initial orientation distribution from a stress-free state. It can be as a reference orientation state of the grain, whose evolution law ensures that it is inherited to a region swept by a migrating grain boundary.

From Clausius-Duhem inequality 3.64 and the constitutive equations 3.65-3.66 the residual dissipation reads

$$-\pi_\phi^{neq}\dot{\phi} + \underset{\sim}{\sigma} : \underset{\sim}{\dot{e}}^{in} - \sum_\alpha \frac{\partial \psi}{\partial r^\alpha}\dot{r}^\alpha \geq 0 \tag{3.91}$$

with

$$\underset{\sim}{\sigma} : \underset{\sim}{\dot{e}}^{in} = \underset{\sim}{\sigma} : \underset{\sim}{\dot{e}}^{slip} + 2\overset{\times}{\underline{\sigma}} \cdot \underline{\dot{\theta}}^\star \geq 0 \tag{3.92}$$

A dissipation potential for the internal variables r^α is not explicitly formulated. Instead, a Kocks-Mecking-Teodosiu law is adopted to describe the evolution of the stastically stored dislocations. It is slightly modified to acccount fore static recovery behind a moving grain boundary, in a similar way to Abrivard et al. [2012a], thereby allowing the release of the stored energy via grain boundary motion:

$$\dot{\rho}^\alpha = \begin{cases} \dfrac{1}{b}\left(\dfrac{1}{K_r}\sqrt{\displaystyle\sum_\beta \rho^\beta} - 2d\rho^\alpha\right)|\dot{\gamma}^\alpha| - \rho^\alpha C_D \tanh\left(C_A|\theta \otimes \nabla|\right)\dot{\phi}, & \dot{\phi} > 0 \\ \dfrac{1}{b}\left(\dfrac{1}{K_r}\sqrt{\displaystyle\sum_\beta \rho^\beta} - 2d\rho^\alpha\right)|\dot{\gamma}^\alpha|, & \dot{\phi} \leq 0 \end{cases} \tag{3.93}$$

The finite element implementation of the presented models is based on the weak formulation of the balance laws. The discretization and resolution methods are described in the references [Abrivard et al., 2012a; Ask et al., 2018b] while details on the extension to 3D are given in section III.3.4.1. The implicit finite element solver Z–set is used [Besson and Foerch, 1997; Z-set, 2022]. Global resolution is carried out using a Newton-Raphson method and the nonlinear constitutive laws are time-integrated by means of a Runge-Kutta method with automatic time stepping, see [Besson et al., 2009].

III.3.2 Models for the relaxation of skew-symmetric stresses in the grain boundaries

The inelastic stress relaxation at the grain boundaries can be modelled with several formulations. In addition to viscous rheological laws like the Kelvin-Voigt or Maxwell viscoelasticity models, the Norton law with threshold or time-independent formulation can also be employed. This section focuses on the impact of the selected relaxation model on the static and dynamic behaviour of grain boundaries. In line with Ask et al. [2018b, 2020], the relaxation will be restricted to the grain boundaries via the localization function P (Eq. 3.21), unless explicitly stated otherwise. In the following, physical quantities and parameters are dimensionless, see table 3.6 for more information.

III.3.2.1 Kelvin-Voigt rheological model

The skew-symmetric stress in the initial KWC-Cosserat formulation [Ask et al., 2018b] was based on a Kelvin-Voigt rheological model. In this case, the thermodynamics is slightly different from the one that was presented above as the skew-symmetric stress is also assumed to have stored and dissipative contributions:

$$\overset{\times}{\underline{\sigma}} = \overset{\times}{\underline{\sigma}}^{eq} + \overset{\times}{\underline{\sigma}}^{neq} \tag{3.94}$$

$$\underset{\sim}{\sigma}^{eq} = \frac{\partial \psi}{\partial \underset{\sim}{e}^{e}} \tag{3.95}$$

The Clausius-Duhem inequality 3.62 now becomes

$$\underbrace{-\left[\pi_\phi^{eq} + \frac{\partial \psi}{\partial \phi}\right]\dot{\phi} + \left[\underline{\xi}_\phi - \frac{\partial \psi}{\partial \nabla \phi}\right]\cdot\nabla\dot{\phi} + \left[\underset{\sim}{\sigma}^{eq} - \frac{\partial \psi}{\partial \underset{\sim}{e}^{e}}\right] : \dot{\underset{\sim}{e}}^{e} + \left[\underset{\sim}{m} - \frac{\partial \psi}{\partial \underline{\theta} \otimes \nabla}\right] : \underline{\dot{\theta}} \otimes \nabla}_{\text{Energetic contribution}}$$

$$\underbrace{-\pi_\phi^{neq}\dot{\phi} + 2\overset{\times}{\underline{\sigma}}^{neq}\cdot\dot{\overset{\times}{\underline{e}}}^{e} + 2\overset{\times}{\underline{\sigma}}\cdot\underline{\dot{\theta}}^{\star} + \underset{\sim}{\sigma} : \dot{\underset{\sim}{e}}^{slip} - \sum_\alpha \frac{\partial \psi}{\partial r^\alpha}\dot{r}^\alpha}_{\text{Dissipative contribution}} \geq 0 \tag{3.96}$$

In addition, the following relation still holds

$$\dot{\overset{\times}{\underline{e}}}^{e} = \dot{\overset{\times}{\underline{\omega}}}^{e} - \underline{\dot{\theta}} - \underline{\dot{\theta}}^{\star} \tag{3.97}$$

Combining the above equations therefore allows to retrieve the expression for the residual dissipation:

$$-\pi_\phi^{neq}\dot{\phi} + 2\overset{\times}{\underline{\sigma}}^{neq}\cdot\left[\dot{\overset{\times}{\underline{\omega}}}^{e} - \underline{\dot{\theta}}\right] + 2\overset{\times}{\underline{\sigma}}^{eq}\cdot\underline{\dot{\theta}}^{\star} + \underset{\sim}{\sigma} : \dot{\underset{\sim}{e}}^{slip} - \sum_\alpha \frac{\partial \psi}{\partial r^\alpha}\dot{r}^\alpha \geq 0 \tag{3.98}$$

The inelastic dissipation potential is then given by:

$$\Omega^{in} = \Omega^{slip}(\underset{\sim}{\sigma}) + \Omega^{\star}(\overset{\times}{\underline{\sigma}}^{eq}) + \Omega^{\theta}(\overset{\times}{\underline{\sigma}}^{neq}) \tag{3.99}$$

such that

$$\dot{\overset{\times}{\underline{\omega}}}^{e} - \underline{\dot{\theta}} = \frac{\partial \Omega^{\theta}}{\partial \overset{\times}{\underline{\sigma}}^{neq}}, \quad \underline{\dot{\theta}}^{\star} = \frac{\partial \Omega^{\star}}{\partial \overset{\times}{\underline{\sigma}}^{eq}}, \quad \dot{\underset{\sim}{e}}^{slip} = \frac{\partial \Omega slip}{\partial \underset{\sim}{\sigma}} \tag{3.100}$$

The following quadratic dissipation potentials are chosen, in order to ensure positivity of the dissipation:

$$\Omega^{\theta} = \frac{1}{2}\tau_\theta^{-1}\overset{\times}{\underline{\sigma}}^{neq}\cdot\overset{\times}{\underline{\sigma}}^{neq} \tag{3.101}$$

$$\Omega^{\star} = \frac{1}{2}\tau_\star^{-1}\overset{\times}{\underline{\sigma}}^{eq}\cdot\overset{\times}{\underline{\sigma}}^{eq} \tag{3.102}$$

where $\tau_\star$ and τ_θ are mobility functions. In [Ask et al., 2018b] they are taken such that

$$\tau_\theta(\underline{\theta} \otimes \nabla) = \frac{1}{2}\phi^2\eta^\theta P(\underline{\theta} \otimes \nabla) \tag{3.103}$$

$$\tau_\star(\nabla\phi) = \eta^\star \tanh^{-1}\left(C_\star^2|\nabla\phi|^2\right) \tag{3.104}$$

where $\eta^\star$ and η^θ are kinetic constants and $C_\star$ is a parameter with unit [m]. The contributions to the skew-symmetric stress are therefore

$$\overset{\times}{\underline{\sigma}}^{eq} = 2\mu_c \overset{\times}{\underline{e}}^{e} = \tau_\star \dot{\underline{\theta}}^{\star} \tag{3.105}$$

$$\overset{\times}{\underline{\sigma}}^{neq} = \tau_\theta \left[\dot{\overset{\times}{\underline{\omega}}}^{e} - \dot{\underline{\theta}} \right] \tag{3.106}$$

which can be schematically represented by the rheological element in Fig. 3.21.

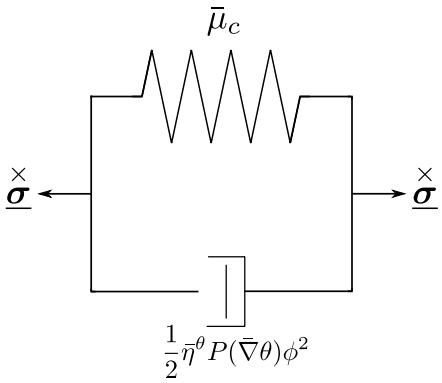

Figure 3.21: *Kelvin-Voigt rheological model for the skew-symmetric stress relaxation at the grain boundary.*

The evolution equation for $\underline{\theta}$, here written in its dimensionless form, is obtained from the balance of moment of momentum and substitution of constitutive laws:

$$\bar{\underset{\sim}{m}} \cdot \bar{\nabla} + 2\overset{\times}{\bar{\underline{\sigma}}} = \underline{0} \tag{3.107}$$

$$\left(\bar{s}g \frac{\underline{\theta} \otimes \bar{\nabla}}{||\underline{\theta} \otimes \bar{\nabla}||} + \frac{\bar{\varepsilon}^2}{2} h ||\underline{\theta} \otimes \bar{\nabla}|| \right) \cdot \bar{\nabla} + 2 \left(2\bar{\mu}_c \overset{\times}{\underline{e}}^{e} + \frac{1}{2}\phi^2 \bar{\eta}^\theta P(\underline{\theta} \otimes \bar{\nabla}) \left[\dot{\overset{\times}{\underline{\omega}}}^{e} - \dot{\underline{\theta}} \right] \right) = 0 \tag{3.108}$$

$$\phi^2 \bar{\eta}^\theta P(\underline{\theta} \otimes \bar{\nabla}) \left[-\dot{\overset{\times}{\underline{\omega}}}^{e} + \dot{\underline{\theta}} \right] = \left(\bar{s}g \frac{\underline{\theta} \otimes \bar{\nabla}}{||\underline{\theta} \otimes \bar{\nabla}||} + \frac{\bar{\varepsilon}^2}{2} h ||\underline{\theta} \otimes \bar{\nabla}|| \right) \cdot \bar{\nabla} + 4\bar{\mu}_c \overset{\times}{\underline{e}}^{e} \tag{3.109}$$

The main difference with the KWC evolution Eq. 3.44 is the addition of the lattice rotation rate $\dot{\overset{\times}{\underline{\omega}}}^{e}$. An additional term related to the skew-symmetric part of the elastic strain is also included, which is not present in the KWC model. As it has been extensively studied in [Ask et al., 2018b], this relaxation model will not be discussed further in the rest of the manuscript.

III.3.2.2 Maxwell rhelogical model

The second viscoelastic law considered is that of a Maxwell rheological model according to Ask et al. [2020] and illustrated in Fig. 3.22. The dissipation potential is given by

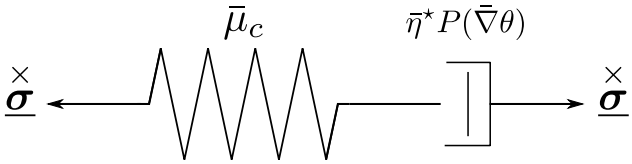

Figure 3.22: *Maxwell rheological model for the skew-symmetric stress relaxation at the grain boundary*

$$\Omega^\star = \frac{1}{2}\tau_\star^{-1} \overset{\times}{\underline{\sigma}} \cdot \overset{\times}{\underline{\sigma}} \tag{3.110}$$

with

$$\tau\star = \eta^\star P(\underline{\theta} \otimes \nabla) \tag{3.111}$$

where $\eta^\star$ is a constant viscosity parameter and $P(\nabla\theta)$ is the same as in Eq. (3.21). The evolution of the reference orientation is then given by the viscous constitutive law

$$\dot{\underline{\theta}}^\star = \frac{1}{\bar{\eta}^\star P(\underline{\theta} \otimes \bar{\nabla})} \overset{\times}{\bar{\underline{\sigma}}} = -\dot{\overset{\times}{\underline{e}}}^e + \dot{\underline{\omega}}^e - \dot{\underline{\theta}} \tag{3.112}$$

Inserting Eq. (3.112) into the momentum balance (eq. (3.55)) gives the following evolution for $\underline{\theta}$:

$$\bar{\eta}^\star P(\underline{\theta} \otimes \bar{\nabla}) \left[\dot{\overset{\times}{\underline{e}}}^e - \dot{\overset{\times}{\underline{\omega}}}^e + \dot{\underline{\theta}} \right] = \left(\bar{s}g \frac{\underline{\theta} \otimes \bar{\nabla}}{||\underline{\theta} \otimes \bar{\nabla}||} + \frac{\bar{\varepsilon}^2}{2} h ||\underline{\theta} \otimes \bar{\nabla}|| \right) \cdot \bar{\nabla} \tag{3.113}$$

The main difference from the original KWC evolution equation (3.20) is the addition of the relative rotation rate $\dot{\overset{\times}{\underline{e}}}^e - \dot{\overset{\times}{\underline{\omega}}}^e$. Note that, similarly to Ask et al. [2020] and unlike [Warren et al., 2003; Ask et al., 2018b], it was decided not to include the phenomenological coupling term ϕ^2 multiplying $P(\bar{\theta})$, as it appeared to significantly increase the computational cost in the coupled model.

III.3.2.3 Norton law with threshold

The third relaxation law considered in this work is based on a viscoplastic Norton formulation with threshold that only concerns the skew-symmetric stress, which gives the following dissipation potential for $\Omega^\star$:

$$\frac{\bar{K}_c}{n_c+1} \frac{1}{\bar{\eta}^\star P(\theta \otimes \bar{\nabla})} \left\langle \frac{|\overset{\times}{\bar{\underline{\sigma}}}| - \bar{\sigma}_c}{\bar{K}_c} \right\rangle^{n_c+1} \tag{3.114}$$

The evolution equation for $\dot{\underline{\theta}}^\star$ is then derived from this potential:

$$\dot{\underline{\theta}}^\star = \frac{1}{\bar{\eta}^\star P(\theta \otimes \bar{\nabla})} \left\langle \frac{|\overset{\times}{\bar{\underline{\sigma}}}| - \bar{\sigma}_c}{\bar{K}_c} \right\rangle^{n_c} \frac{\overset{\times}{\bar{\underline{\sigma}}}}{|\overset{\times}{\bar{\underline{\sigma}}}|} \tag{3.115}$$

where $\bar{\sigma}_c$ is the stress threshold for relaxation and $\bar{K}_c, n_c$ are viscoplasticity type parameters. The momentum balance is once again used to retrieve the evolution law for θ:

$$|\overset{\times}{\bar{\underline{\sigma}}}| \bar{\eta}^\star P(\underline{\theta} \otimes \bar{\nabla}) \left\langle \frac{|\overset{\times}{\bar{\underline{\sigma}}}| - \bar{\sigma}_c}{K_c} \right\rangle^{-n_c} \left[\dot{\overset{\times}{\underline{e}}}^e - \dot{\overset{\times}{\underline{\omega}}}^e + \dot{\underline{\theta}} \right] = \left(\bar{s}g \frac{\underline{\theta} \otimes \bar{\nabla}}{||\underline{\theta} \otimes \bar{\nabla}||} + \frac{\bar{\varepsilon}^2}{2} h ||\underline{\theta} \otimes \bar{\nabla}|| \right) \cdot \nabla \tag{3.116}$$

By setting $\bar{K}_c = n_c = 1$, as illustrated in Fig. 3.23, the only difference with Maxwell's model is the addition of a threshold for the activation of a skew-symmetric stress relaxation.

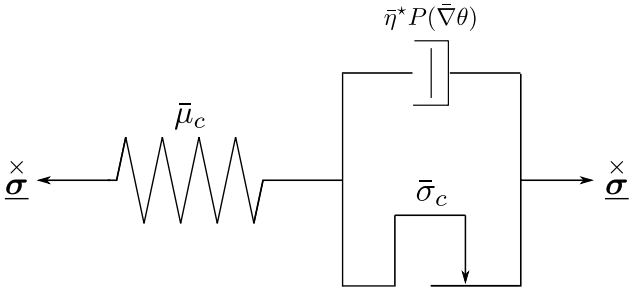

Figure 3.23: *Norton law with threshold for the skew-symmetric stress relaxation at the grain boundary*

In the following the two-dimensional case is considered. The evolution equation for $\theta^\star$ is now

$$\dot{\theta}^\star = \frac{1}{\bar{\eta}^\star P(\bar{\nabla}\theta)} \left\langle |\overset{\times}{\bar{\sigma}}| - \bar{\sigma}_c \right\rangle \mathrm{sgn}(\overset{\times}{\bar{\sigma}}) \tag{3.117}$$

III.3.2.4 Rate-independent relaxation law

Finally, a rate-independent relaxation law is formulated. Inspired by rate-independent isotropic plasticity (see section II.3.1), the following yield function is adopted:

$$f(\overset{\times}{\underline{\sigma}}) = |\overset{\times}{\underline{\sigma}}| - \sigma_c \tag{3.118}$$

The eigen rotation rate is then given by

$$\underline{\dot{\theta}}^\star = \upsilon \underbrace{\frac{\partial f}{\partial \overset{\times}{\underline{\sigma}}}}_{\underline{n}} = \upsilon \frac{\overset{\times}{\underline{\sigma}}}{|\overset{\times}{\underline{\sigma}}|} \tag{3.119}$$

where υ is the cumulated eigen rotation (similar to plastic multiplier in isotropic plasticity) and $\underline{n}$ the normal to the yield surface. The consistency condition $\dot{f} = 0$ is then used to deduce the expression for υ:

$$\dot{f} = 0 \Leftrightarrow \underline{n} \cdot \dot{\overset{\times}{\underline{\sigma}}} = 0 \tag{3.120}$$

Replacing $\dot{\overset{\times}{\underline{\sigma}}}$ with its expression one gets:

$$\underline{n} \cdot (\dot{\overset{\times}{\underline{\omega}}}^e - \underline{\dot{\theta}} - \underline{\dot{\theta}}^\star) 2\mu_c = 0 \tag{3.121}$$

which after inserting Eq. 3.119 becomes:

$$\underline{n} \cdot (\dot{\overset{\times}{\underline{\omega}}}^e - \underline{\dot{\theta}} - \upsilon \underline{n}) = 0 \tag{3.122}$$

The expression for υ is finally retrieved:

$$\upsilon = \frac{\underline{n} \cdot (\dot{\overset{\times}{\underline{\omega}}}^e - \underline{\dot{\theta}})}{\underline{n} \cdot \underline{n}} \tag{3.123}$$

Note that contrary to the other laws explored in this section, the relaxation of skew-symmetric stress occurs in the whole domain due to the absence of a localisation function in this formulation, provided the skew-symmetric stresses are high enough.

III.3.3 Effect of mechanics on grain boundaries in the absence of crystal plasticity

III.3.3.1 Static grain boundaries

In this section the effect of mechanics is evaluated in the absence of crystal plasticity for different formulations of the reference orientation rate $\underline{\dot{\theta}}^\star$. Finite element simulations are performed with the parameters given in table 3.4 on a regular two-dimensional domain of total length $2\bar{L} = 10$ with one element in height and 200 elements in length. Rectangular elements with quadratic shape functions with reduced integration are used. Only the viscoelastic and viscoplastic behavior of grain boundaries is considered in this section, which means that no dislocation slip is activated in the stability analysis. No mechanical loading is applied to the material strip. The function $g(\phi) = -2\log(1-\phi) + \phi$ is used in the remainder of this chapter.

Parameter	$\bar{E}^e$	ν	$\bar{\mu}_c$	$\bar{\alpha}$	$\bar{s}$	$\bar{\varepsilon}$	$\bar{\eta}_\phi$	$\bar{\eta}^\star$	$\bar{\mu}_p$	β_p	$\bar{\gamma}$	γ_g
Value	56×10^3	0.3	10^4	0.31	0.75	1	10	1	10^6	10^3	10^4	10^{-4}

Table 3.4: *Model parameters used in the simulations with the coupled model, without crystal plasticity.*

The following initial and boundary conditions are used to evaluate the effect of relaxation of the skew symmetric stress during grain boundary formation:

$$\text{IC:} \begin{cases} \phi(\bar{t}=0,\bar{x}) = 1 \\ \theta(\bar{t}=0,\bar{x}) = \dfrac{\Delta\theta}{2}(\tanh(15\bar{x})+1) \end{cases} \tag{3.124}$$

$$\text{BC:} \begin{cases} \phi(\bar{t},\bar{x}=-\bar{L}) = \phi(\bar{t},\bar{x}=\bar{L}) = 1 \\ \theta(\bar{t},\bar{x}=-\bar{L}) = 0, \quad \theta(\bar{t},\bar{x}=\bar{L}) = \Delta\theta \\ \bar{u}_x = \bar{u}_y = 0 \text{ at the bottom left corner} \\ \bar{u}_y = 0 \text{ at the top right corner} \end{cases} \tag{3.125}$$

with $\Delta\theta = 0.3$. Multiple point constraints are also imposed on the top and bottom edges to ensure the periodicity of $\phi, \theta, \bar{u}_x, \bar{u}_y$ along the vertical direction y. The objective is to analyze the build-up and relaxation of stresses in the diffuse GB zone during the formation of a grain boundary. The out-of-equilibrium initial conditions lead to instantaneous build-up of stresses in the GB region which then relax according to the viscoelastic law for $\theta^\star$.

Maxwell rheological model for the relaxation of the skew-symmetric stress

The results of the simulation are shown in Fig. 3.24, which shows the element-averaged profiles of $\text{sym}(\bar{\underset{\sim}{\sigma}})_{12}$ and $\overset{\times}{\bar{\sigma}} = \text{skew}(\bar{\underset{\sim}{\sigma}})_{12}$ at different times during grain boundary formation. The stresses $\text{sym}(\bar{\underset{\sim}{\sigma}})_{12}$ and $\text{skew}(\bar{\underset{\sim}{\sigma}})_{12}$ are clearly mirror images of each other with respect to the line $\bar{y}=0$ and the profiles are also antisymmetric with respect to $\bar{x}=0$. The stresses vanish in the region where $|\bar{\nabla}\theta| \neq 0$, as expected from the localisation function $1/P(\bar{\nabla}\theta)$. Numerical residual stresses of the order of 10^{-2} are present after full relaxation.

The existence of internal stresses in the grain boundary region is a physically relevant feature due to strong elastic strains induced by change of atomic order. Such nanoscale residual stresses can be computed by molecular dynamics but also continuum theories. Interestingly, the profile of $\text{sym}(\bar{\underset{\sim}{\sigma}})_{12}$ resembles that of the elasto-plastic theory of dislocation and disclination fields by Taupin et al. [2013], as shown in Fig. 3.25, probably because they both share the same generalized balance equation for the moment of momentum and associated couple stress tensor. It can be seen that they show similar trends, such as sharp variation in a narrow region and anti-symmetric profile. However, a major difference is that in the nanoscale model of Taupin et al. [2013] a residual stress still remains *within* the grain boundary at equilibrium, whereas in the micron-scale model of Ask et al. [2020] relaxed grain boundaries are assumed to be stress-free after relaxation. However these residual stresses can play some role in the GB formation and migration. That is why a viscoplastic formulation of the GB behavior is introduced in the next section.

Introduction of a threshold: residual skew-symmetric stresses

The influence of the value of the stress threshold $\bar{\sigma}_c$ on the profiles of ϕ and θ during grain boundary formation is shown in Fig. 3.26. As $\bar{\sigma}_c \to 0$ the behavior of the Maxwell relaxation model is recovered and the profiles are identical to the original KWC model. However, increasing the threshold leads to a delay in the development of the equilibrium profiles.

The effect of the threshold on the stress profile of $\text{skew}(\bar{\underset{\sim}{\sigma}})_{12}$ is illustrated in Fig. 3.27. Fluctuations of

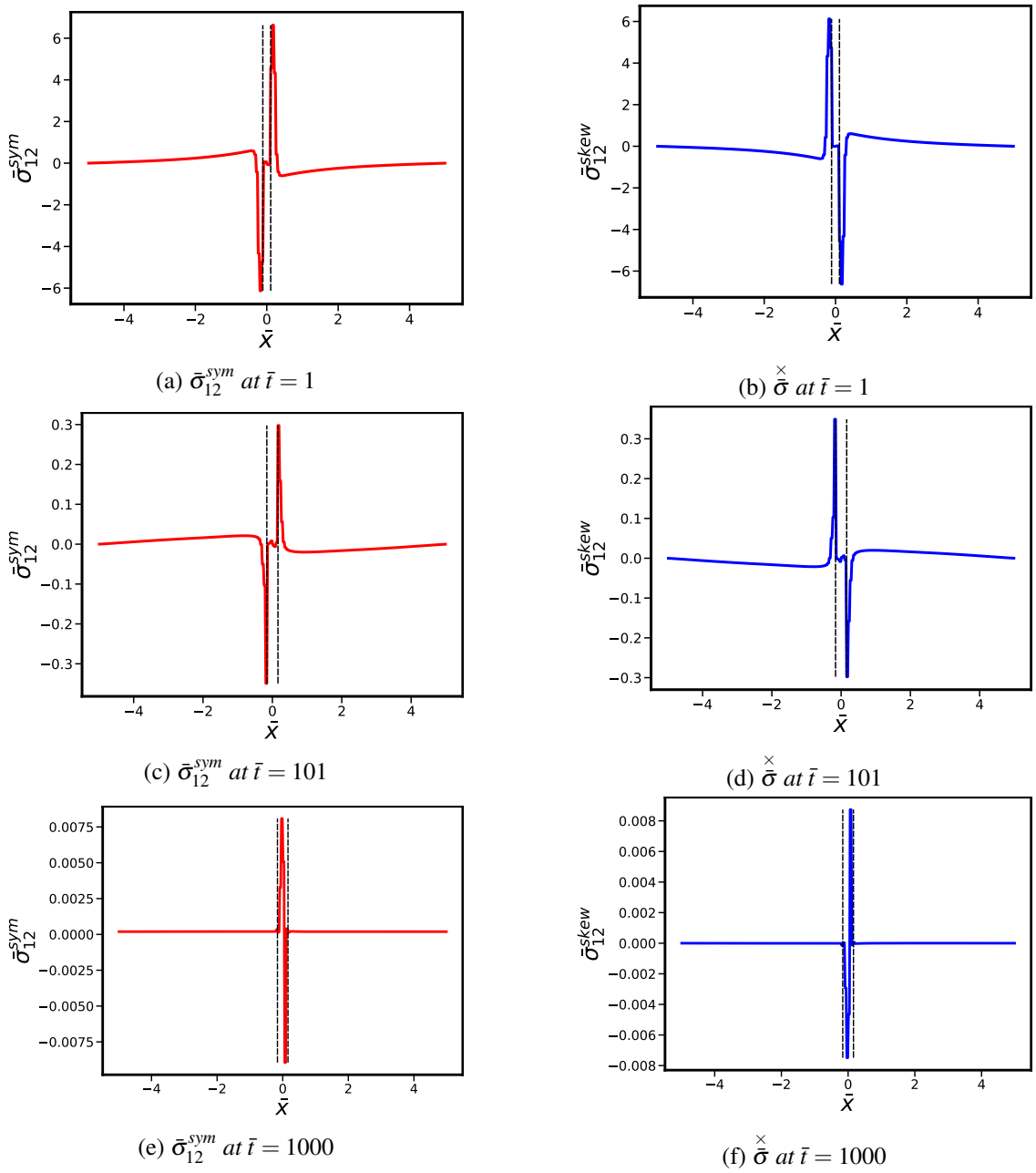

(a) $\bar{\sigma}_{12}^{sym}$ *at* $\bar{t} = 1$

(b) $\overset{\times}{\bar{\sigma}}$ *at* $\bar{t} = 1$

(c) $\bar{\sigma}_{12}^{sym}$ *at* $\bar{t} = 101$

(d) $\overset{\times}{\bar{\sigma}}$ *at* $\bar{t} = 101$

(e) $\bar{\sigma}_{12}^{sym}$ *at* $\bar{t} = 1000$

(f) $\overset{\times}{\bar{\sigma}}$ *at* $\bar{t} = 1000$

Figure 3.24: *Relaxation of the element averaged symmetric shear stress component* $\bar{\sigma}_{12}^{sym}$ *(in red on the left) and skew-symmetric shear stress* $\overset{\times}{\bar{\sigma}}$ *(in blue on the right) for the KWC-Cosserat model with Maxwell type relaxation during grain boundary formation. The vertical dashed lines mark the region where* $|\bar{\nabla}\theta| \neq 0$.

stresses are observed in the GB zone at the initial stress due to the strong out-of-equilibrium initial conditions. At the point of maximum relaxation ($\bar{t} = 1000$) all stresses above the threshold have decreased to the value of $\bar{\sigma}_c$, forming plateau-like regions. The stresses below this value are not relaxed, which explains why some oscillations below $\bar{\sigma}_c$ still remain. The introduction of a viscoplastic GB law with threshold therefore enables the existence of residual stresses in the GB region.

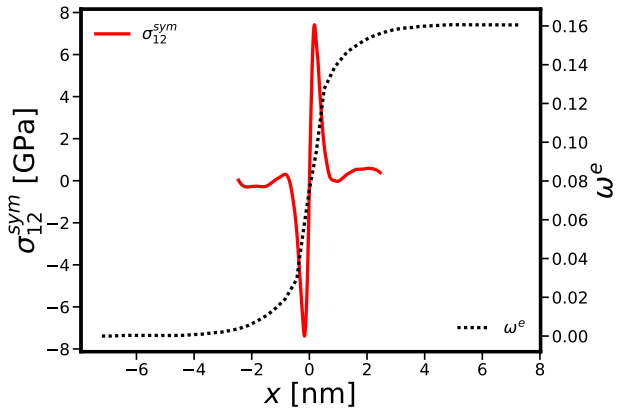

(a) *Stress profile of* σ_{12}^{sym} *and compatible lattice rotation* ω^e *(relative to* 36.87°*) along a relaxed* $<001>\Sigma29(520)$ *tilt boundary of misorientation* 46.40° *after Taupin et al. [2013].*

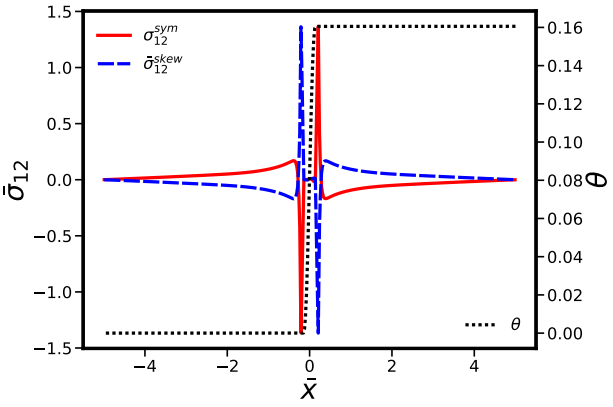

(b) *Stress profiles of* σ_{12}^{sym}, σ_{12}^{skew} *and lattice orientation* θ *at* $\bar{t} = 31$ *along a bicrystal of misorientation* 9.2°*. The stresses are not fully relaxed.*

Figure 3.25: *Superimposed stress and rotation profiles for a grain boundary according to Taupin et al. [2013] (left) and using the KWC-Cosserat model of Ask et al. [2020] (right).*

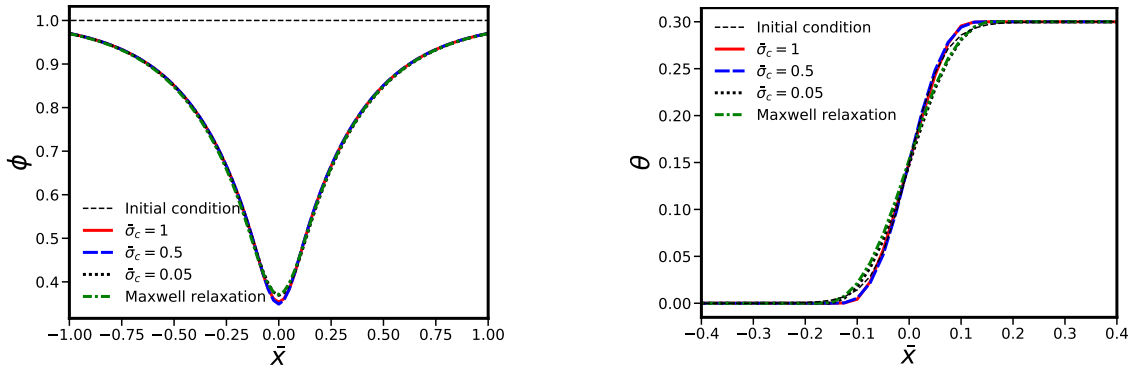

Figure 3.26: *Influence of the magnitude of the critical skew-symmetric stress in the KWC-Cosserat model with Norton law with threshold on the profiles of* ϕ *and* θ *at* $\bar{t} = 200$ *during grain boundary formation.*

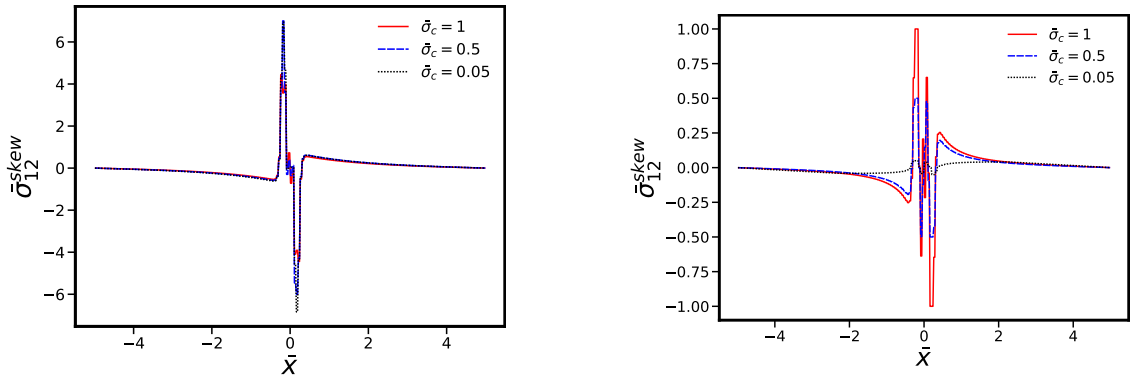

(a) $\bar{t} = 1$

(b) $\bar{t} = 1000$

Figure 3.27: *Relaxation of the skew-symmetric stress for the KWC-Cosserat model with Norton relaxation law with threshold during grain boundary formation.*

Time-independent relaxation

Finally, the stress profiles in Fig. 3.28 are obtained with the time-independent model (equations 3.119-3.123). Close to the grain boundary, similar profiles to those obtained with the Norton law with threshold

are visible, except that the relaxation is now quasi-instantaneous as the maximum skew-symmetric stress is equal to $\bar{\sigma}_c$ from the beginning. However, the absence of a localisation function restricting the relaxation to the grain boundary leads to non-zero stresses away from the interface.

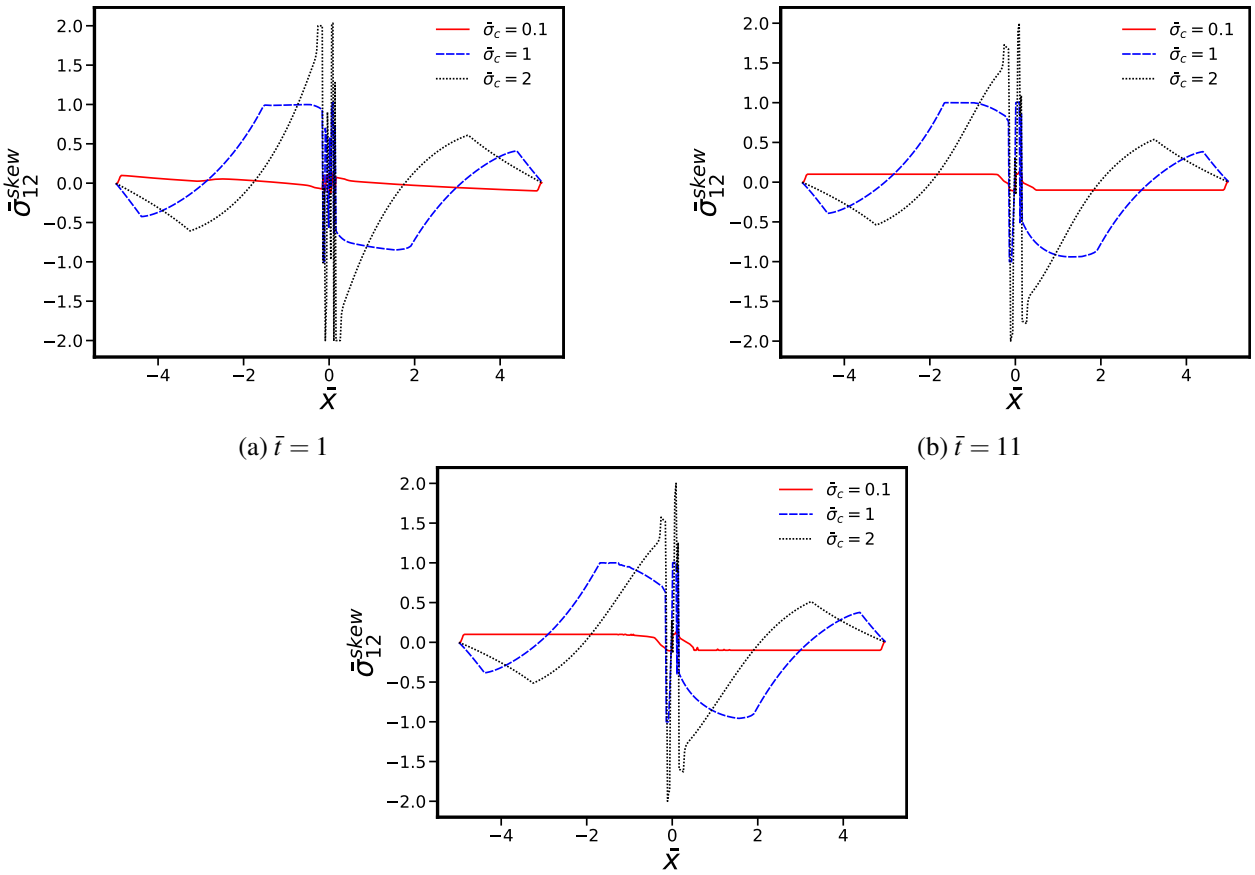

(a) $\bar{t} = 1$ (b) $\bar{t} = 11$

(c) $\bar{t} = 1000$

Figure 3.28: *Relaxation of the skew-symmetric stress for the KWC-Cosserat model with time-independent relaxation law during grain boundary formation.*

III.3.3.2 Mobile grain boundaries

Stored energy driven migration in a bicrystal

Simulations of stored energy driven migration are performed in a bicrystal by prescribing an initial heterogeneous stored energy distribution ($\bar{E} = 0.01$ on the left side of the interface and $\bar{E} = 0.1$ on the right side). A first preliminary computation is run with the KWC model to find the equilibrium profiles of ϕ and θ. In a second time, the symmetric and skew-symmetric stresses are relaxed by the KWC-Cosserat model with Maxwell relaxation. The resulting ϕ, θ and $\bar{E}$ fields then serve as initial conditions for the simulation of stored energy-driven migration in a bicrystal. The parameters given in table 3.4 are used in all simulations with $C_D = 100$ and $\bar{C}_A = 1$ to account for full recovery behind the moving grain boundary. Figure 3.29 shows ϕ and θ at $\bar{t} = 400$ for the original KWC model and the two versions of the KWC-Cosserat model presented above. Comparing the KWC-Cosserat model with Maxwell relaxation law and the original KWC model, the differences in the observed kinetics are due to the dissimilar evolution equations for θ, Eq. (3.20) and (3.113). For the KWC-Cosserat model with threshold, increasing the magnitude of $\bar{\sigma}_c$ slows down the grain boundary and can even pin it if it is high enough. Pinning of the grain boundary is observed here for $\bar{\sigma}_c = 0.5$ but this property will depend in general on the ratio between the values of the stored energy jump and GB yielding threshold. As shown in Fig. 3.30, a similar behaviour is observed for the time-independent model.

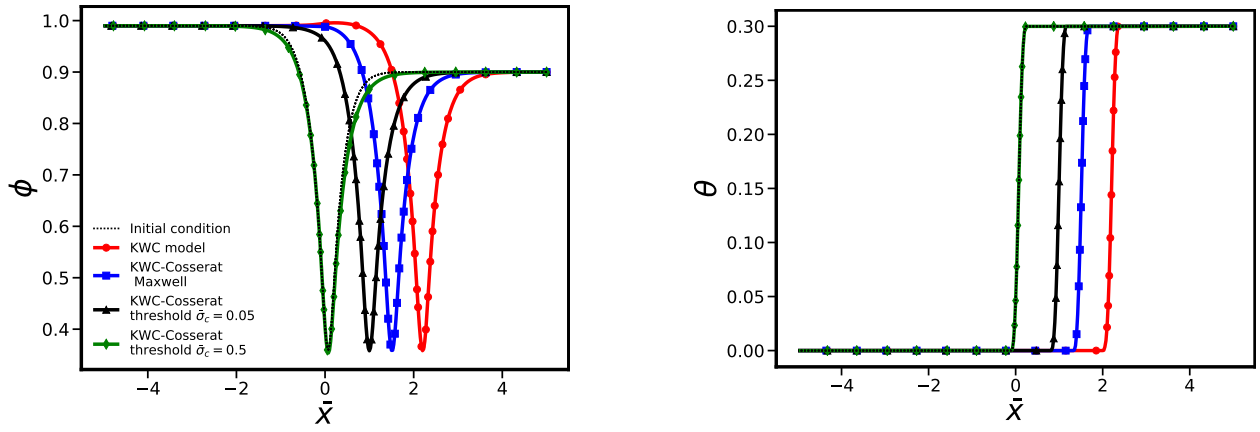

Figure 3.29: *Comparison of the KWC and KWC-Cosserat model with different relaxation laws for the stored energy driven migration of a flat interface. The profiles of ϕ (on the left) and θ (on the right) are plotted at $\bar{t} = 400$.*

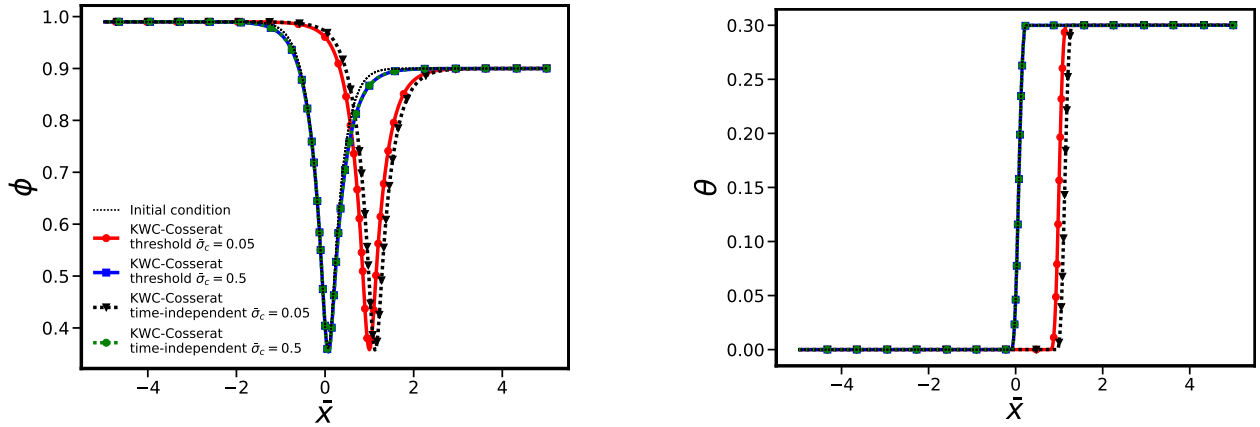

Figure 3.30: *Comparison of the Norton law with threshold and time-independent relaxation for the KWC-Cosserat model during stored energy driven migration of a flat interface. The profiles of ϕ (on the left) and θ (on the right) are plotted at $\bar{t} = 400$.*

Curvature driven migration

Finally, the last case considered is that of a circular grain embedded in a larger matrix. For this calculation, the grain has an initial dimensionless radius of about 2.4 with a misorientation of $\Delta\theta = 0.3$. The time evolution of the radius is shown in Fig. 3.31. As with the stored energy driven migration, the relaxation threshold can slow down or pin the grain boundaries as its value increases. In the case of $\bar{\sigma}_c \to 0$ the kinetics of the KWC Cosserat model with Maxwell relaxation is recovered.

III.3.4 Implementation and validation of a 3D finite element model

III.3.4.1 Finite element formulation

While the KWC-Cosserat model was developed in a three-dimensional framework in Ask et al. [2018b, 2020], its implementation has only been performed in a two-dimensional finite element formulation so far. In this section, we provide details on its application in 3D. The framework remains that of small deformations, rotations, and curvatures. The isotropic grain boundary energy is still assumed. The weak form of the balance equations, as shown in equations 3.53–3.55, is derived by multiplying with a virtual

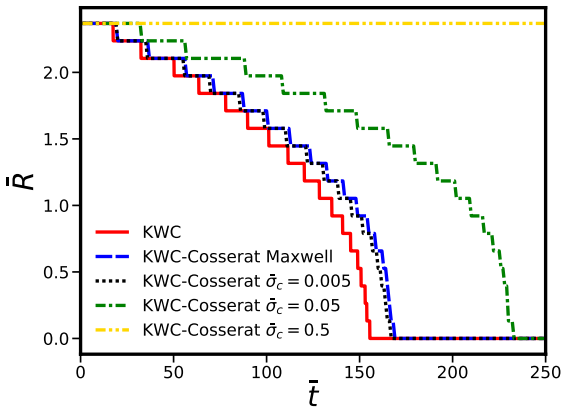

Figure 3.31: *Radius as a function of time during grain shrinkage of a circular grain.*

field, integrating across the entire domain and employing the divergence theorem.

$$-\int_V \underset{\sim}{\sigma}^s : \underline{u} \otimes \nabla^s + \underline{\pi}_\theta \cdot \overset{\times}{\underline{\omega}}\, dV + \int_{\partial V} \underline{u} \cdot \underline{t}\, dS = 0 \tag{3.126}$$

$$\int_V -\underset{\sim}{\xi}_\theta : \underline{\theta} \otimes \nabla + \underline{\theta} \cdot \underline{\pi}_\theta dV + \int_{\partial V} \underline{\theta} \cdot \underset{\sim}{\xi}_\theta \cdot \underline{n}\, dS = 0 \tag{3.127}$$

$$\int_V -\underline{\xi}_\phi \cdot \nabla\phi + \phi \cdot \pi_\phi dV + \int_{\partial V} \phi \cdot \underline{\xi}_\phi \cdot \underline{n}\, dS = 0 \tag{3.128}$$

with $\underline{\pi}_\theta = 2\,\overset{\times}{\underline{\sigma}}$, $\underline{t} = \underset{\sim}{\sigma} \cdot \underline{n}$, $\underline{M} = \underset{\sim}{\xi}_\theta \cdot \underline{n}$. The displacement, lattice orientation and crystal order fields are interpolated at the n nodes of the elements such that

$$\underline{u}(\underline{x},t) = \sum_{i=1}^{n} N_{ij}^{e^u}(\underline{x})\underline{u}_j^e(t), \quad \underline{\theta}(\underline{x},t) = \sum_{i=1}^{n} N_{ij}^{e^\theta}(\underline{x})\underline{\theta}_j^e(t), \quad \underline{\phi}(\underline{x},t) = \sum_{i=1}^{n} N_i^e(\underline{x})\underline{\phi}_i^e(t) \tag{3.129}$$

with the nodal values arranged as follows:

$$\phi^e(t) = \begin{pmatrix} \phi^1 & \phi^2 & \phi^3 & \dots & \phi^n \end{pmatrix}^T \tag{3.130}$$

$$\underline{u}^e(t) = \begin{pmatrix} u_1^1 & u_2^1 & u_3^1 & u_1^2 & u_2^2 & u_3^2 & \dots & u_1^n & u_2^n & u_3^n \end{pmatrix}^T \tag{3.131}$$

$$\underline{\theta}^e(t) = \begin{pmatrix} \theta_1^1 & \theta_1^2 & \dots & \theta_1^n & \theta_2^1 & \theta_2^2 & \dots & \theta_2^n & \theta_3^1 & \theta_3^2 & \dots & \theta_3^n \end{pmatrix}^T \tag{3.132}$$

The shape functions are thus:

$$N_i^e = \begin{bmatrix} N_1 & N_2 & N_3 & \dots & N_n \end{bmatrix} \tag{3.133}$$

$$N_{ij}^{e^u} = \begin{bmatrix} N_1 & 0 & 0 & N_2 & 0 & 0 & \dots & N_n & 0 & 0 \\ 0 & N_1 & 0 & 0 & N_2 & 0 & \dots & 0 & N_n & 0 \\ 0 & 0 & N_1 & 0 & 0 & N_2 & \dots & 0 & 0 & N_n \end{bmatrix} \tag{3.134}$$

$$N_{ij}^{e^\theta} = \begin{bmatrix} N_1 & N_2 & \dots & N_n & 0 & 0 & \dots & 0 & 0 & 0 & \dots & 0 \\ 0 & 0 & \dots & 0 & N_1 & N_2 & \dots & N_n & 0 & 0 & \dots & 0 \\ 0 & 0 & \dots & 0 & 0 & 0 & \dots & 0 & N_1 & N_2 & \dots & N_n \end{bmatrix} \tag{3.135}$$

The discrete gradients of the degrees of freedom in the element are given by

$$\nabla\phi(\underline{x},t) = \sum_{i=1}^{n} \underset{\sim}{B}_{ij}^{e\phi}\,\phi_j^e(t), \quad \underline{\theta}\,(\underline{x},t)\otimes\nabla = \sum_{i=1}^{n} \underset{\sim}{\boldsymbol{B}}_{ij}^{e\theta}(\underline{x})\underline{\theta}_j^{\,e}(t) \tag{3.136}$$

$$\underline{u}\,(\underline{x},t)\otimes\nabla^s = \sum_{i=1}^{n} \underset{\sim}{\boldsymbol{B}}_{s_{ij}}^{eu}(\underline{x})\underline{u}_j^{\,e}(t), \quad \overset{\times}{\underline{\omega}}\,(\underline{x},t) = \sum_{i=1}^{n} \underset{\sim}{\boldsymbol{B}}_{\omega_{ij}}^{eu}(\underline{x})\underline{u}_j^{\,e}(t) \tag{3.137}$$

such that

$$\begin{bmatrix} u_{1,1} \\ u_{2,2} \\ u_{3,3} \\ \sqrt{2}u_{1,2} \\ \sqrt{2}u_{2,3} \\ \sqrt{2}u_{3,1} \end{bmatrix} = \underbrace{\begin{bmatrix} \frac{\partial N_1}{\partial x} & 0 & 0 & \frac{\partial N_2}{\partial x} & 0 & 0 & \dots & \frac{\partial N_n}{\partial x} & 0 & 0 \\ 0 & \frac{\partial N_1}{\partial y} & 0 & 0 & \frac{\partial N_2}{\partial y} & 0 & \dots & 0 & \frac{\partial N_n}{\partial y} & 0 \\ 0 & 0 & \frac{\partial N_1}{\partial z} & 0 & 0 & \frac{\partial N_2}{\partial z} & \dots & 0 & 0 & \frac{\partial N_1}{\partial z} \\ \frac{1}{\sqrt{2}}\frac{\partial N_1}{\partial y} & \frac{1}{\sqrt{2}}\frac{\partial N_1}{\partial x} & 0 & \frac{1}{\sqrt{2}}\frac{\partial N_2}{\partial y} & \frac{1}{\sqrt{2}}\frac{\partial N_2}{\partial x} & 0 & \dots & \frac{1}{\sqrt{2}}\frac{\partial N_n}{\partial y} & \frac{1}{\sqrt{2}}\frac{\partial N_n}{\partial x} & 0 \\ 0 & \frac{1}{\sqrt{2}}\frac{\partial N_1}{\partial z} & \frac{1}{\sqrt{2}}\frac{\partial N_1}{\partial y} & 0 & \frac{1}{\sqrt{2}}\frac{\partial N_2}{\partial z} & \frac{1}{\sqrt{2}}\frac{\partial N_2}{\partial y} & \dots & 0 & \frac{1}{\sqrt{2}}\frac{\partial N_n}{\partial z} & \frac{1}{\sqrt{2}}\frac{\partial N_n}{\partial y} \\ \frac{1}{\sqrt{2}}\frac{\partial N_1}{\partial z} & 0 & \frac{\partial N_1}{\partial x} & \frac{1}{\sqrt{2}}\frac{\partial N_2}{\partial z} & 0 & \frac{\partial N_2}{\partial x} & \dots & \frac{1}{\sqrt{2}}\frac{\partial N_n}{\partial z} & 0 & \frac{\partial N_1}{\partial x} \end{bmatrix}}_{[\underset{\sim}{\boldsymbol{B}}_s^{eu}]} \cdot \begin{pmatrix} u_1^1 \\ u_2^1 \\ u_3^1 \\ u_1^2 \\ u_2^2 \\ u_3^2 \\ \vdots \\ u_1^n \\ u_2^n \\ u_3^n \end{pmatrix} \tag{3.138}$$

$$\begin{bmatrix} \omega_1 \\ \omega_2 \\ \omega_3 \end{bmatrix} = \underbrace{\begin{bmatrix} 0 & -\frac{1}{2}\frac{\partial N_1}{\partial z} & \frac{1}{2}\frac{\partial N_1}{\partial y} & 0 & -\frac{1}{2}\frac{\partial N_2}{\partial z} & \frac{1}{2}\frac{\partial N_2}{\partial y} & \dots & 0 & -\frac{1}{2}\frac{\partial N_n}{\partial z} & \frac{1}{2}\frac{\partial N_n}{\partial y} \\ \frac{1}{2}\frac{\partial N_1}{\partial z} & 0 & -\frac{1}{2}\frac{\partial N_1}{\partial x} & \frac{1}{2}\frac{\partial N_2}{\partial z} & 0 & -\frac{1}{2}\frac{\partial N_2}{\partial x} & \dots & \frac{1}{2}\frac{\partial N_n}{\partial z} & 0 & -\frac{1}{2}\frac{\partial N_1 n}{\partial x} \\ -\frac{1}{2}\frac{\partial N_1}{\partial y} & \frac{1}{2}\frac{\partial N_1}{\partial x} & 0 & -\frac{1}{2}\frac{\partial N_2}{\partial y} & \frac{1}{2}\frac{\partial N_2}{\partial x} & 0 & \dots & -\frac{1}{2}\frac{\partial N_n}{\partial y} & \frac{1}{2}\frac{\partial N_n}{\partial x} & 0 \end{bmatrix}}_{[\underset{\sim}{\boldsymbol{B}}_\omega^{eu}]} \cdot \begin{pmatrix} u_1^1 \\ u_2^1 \\ u_3^1 \\ u_1^2 \\ u_2^2 \\ u_3^2 \\ \vdots \\ u_1^n \\ u_2^n \\ u_3^n \end{pmatrix} \tag{3.139}$$

$$\begin{bmatrix} \theta_{1,1} \\ \theta_{2,2} \\ \theta_{3,3} \\ \theta_{1,2} \\ \theta_{2,3} \\ \theta_{3,1} \\ \theta_{2,1} \\ \theta_{3,2} \\ \theta_{1,3} \end{bmatrix} = \underbrace{\begin{bmatrix} \frac{\partial N_1}{\partial x} & \frac{\partial N_2}{\partial x} & \dots & \frac{\partial N_n}{\partial x} & 0 & 0 & \dots & 0 & 0 & 0 & \dots & 0 \\ 0 & 0 & \dots & 0 & \frac{\partial N_1}{\partial y} & \frac{\partial N_2}{\partial y} & \dots & \frac{\partial N_n}{\partial y} & 0 & 0 & \dots & 0 \\ 0 & 0 & \dots & 0 & 0 & 0 & \dots & 0 & \frac{\partial N_1}{\partial z} & \frac{\partial N_2}{\partial z} & \dots & \frac{\partial N_n}{\partial z} \\ \frac{\partial N_1}{\partial y} & \frac{\partial N_2}{\partial y} & \dots & \frac{\partial N_n}{\partial y} & 0 & 0 & \dots & 0 & 0 & 0 & \dots & 0 \\ 0 & 0 & \dots & 0 & \frac{\partial N_1}{\partial z} & \frac{\partial N_2}{\partial z} & \dots & \frac{\partial N_n}{\partial z} & 0 & 0 & \dots & 0 \\ 0 & 0 & \dots & 0 & 0 & 0 & \dots & 0 & \frac{\partial N_1}{\partial x} & \frac{\partial N_2}{\partial x} & \dots & \frac{\partial N_n}{\partial x} \\ 0 & 0 & \dots & 0 & \frac{\partial N_1}{\partial x} & \frac{\partial N_2}{\partial x} & \dots & \frac{\partial N_n}{\partial x} & 0 & 0 & \dots & 0 \\ 0 & 0 & \dots & 0 & 0 & 0 & \dots & 0 & \frac{\partial N_1}{\partial y} & \frac{\partial N_2}{\partial y} & \dots & \frac{\partial N_n}{\partial y} \\ \frac{\partial N_1}{\partial z} & \frac{\partial N_2}{\partial z} & \dots & \frac{\partial N_n}{\partial z} & 0 & 0 & \dots & 0 & 0 & 0 & \dots & 0 \end{bmatrix}}_{[\underset{\sim}{\boldsymbol{B}}^{e\theta}]} \cdot \begin{pmatrix} \theta_1^1 \\ \theta_1^2 \\ \vdots \\ \theta_1^n \\ \theta_2^1 \\ \theta_2^2 \\ \vdots \\ \theta_2^n \\ \theta_3^1 \\ \theta_3^2 \\ \vdots \\ \theta_3^n \end{pmatrix} \tag{3.140}$$

$$\begin{pmatrix}\phi_{,1}\\ \phi_{,2}\\ \phi_{,3}\end{pmatrix} = \underbrace{\begin{bmatrix}\frac{\partial N_1}{\partial x} & \frac{\partial N_2}{\partial x} & \cdots & \frac{\partial N_1}{\partial n}\\ \frac{\partial N_1}{\partial y} & \frac{\partial N_2}{\partial y} & \cdots & \frac{\partial N_1}{\partial n}\\ \frac{\partial N_1}{\partial z} & \frac{\partial N_2}{\partial z} & \cdots & \frac{\partial N_1}{\partial n}\end{bmatrix}}_{[B_{ij}^{e^\phi}]} \cdot \begin{pmatrix}\phi_1\\ \phi_2\\ \vdots\\ \phi_n\end{pmatrix} \tag{3.141}$$

The element residuals $\mathscr{R}_i^{e^\bullet}$ (where $\bullet$ is the degree of freedom considered) for the variational formulation are then

$$\mathscr{R}_i^{e^u} = -\int_{V^e}\left[\underset{\sim}{B}_s^{e^u}\right]^T\cdot\{\sigma^s\} + \left[\underset{\sim}{B}_\omega^{e^u}\right]^T\cdot\{\pi_\theta\}\,dV + \int_{\partial V}[N^{e^u}]^T\cdot\{t\}\,dS = 0 \tag{3.142}$$

$$\equiv \{{}^uF_i^e\} - \{{}^uF_e^e\} = 0 \tag{3.143}$$

$$\mathscr{R}_i^{e^\theta} = \int_{V^e}\left[N^{e^\theta}\right]^T\cdot\{\pi_\theta\} - \left[\underset{\sim}{B}^{e^\theta}\right]^T\cdot\{\xi_\theta\}\,dV + \int_{\partial V}[N^{e^\theta}]^T\cdot\{M\}dS = 0 \tag{3.144}$$

$$\equiv \{{}^\theta F_i^e\} - \{{}^\theta F_e^e\} = 0 \tag{3.145}$$

$$\mathscr{R}_i^{e^\phi} = \int_{V^e} -[B^{e^\phi}]^T\left\{\xi_\phi\right\} + \pi_\phi[N^{e^\phi}]dV + \int_{\partial V^e}[N^{e^\phi}]\Xi_\phi\,dS = 0 \tag{3.146}$$

$$\equiv \{{}^\phi F_i^e\} - \{{}^\phi F_e^e\} = 0 \tag{3.147}$$

$$\tag{3.148}$$

where $\{{}^\bullet F_i^e\}$ and $\{{}^\bullet F_e^e\}$ are the vector of the internal reaction associated with the degree of freedom $\bullet$ and the vector of the external forces in the element, respectively. The nonlinear system to be solved with Newton's method is then

$$\begin{Bmatrix}\mathscr{A}\left(\{{}^uF_i^e\}\right)\\ \mathscr{A}\left(\{{}^\theta F_i^e\}\right)\\ \mathscr{A}\left(\{{}^\phi F_i^e\}\right)\end{Bmatrix} - \begin{Bmatrix}\mathscr{A}\left(\{{}^uF_e^e\}\right)\\ \mathscr{A}\left(\{{}^\theta F_e^e\}\right)\\ \mathscr{A}\left(\{{}^\phi F_e^e\}\right)\end{Bmatrix} = 0 \tag{3.149}$$

where $\mathscr{A}$ denotes the assembly operator over all the elements. The Jacobian matrix $[K_t^e]$ of the element is obtained by derivation of the internal reactions with respect to the degrees of freedom:

$$[K_t^e] = \frac{\partial\left\{\{{}^uF_i^e\}\quad\{{}^\theta F_i^e\}\quad\{{}^\phi F_i^e\}\right\}^T}{\partial\left\{\{u\}\quad\{\theta\}\quad\{\phi\}\right\}^T} = \begin{bmatrix}[K_{uu}^e] & [K_{u\theta}^e] & [K_{u\phi}^e]\\ [K_{\theta u}^e] & [K_{\theta\theta}^e] & [K_{\theta\phi}^e]\\ [K_{\phi u}^e] & [K_{\phi\theta}^e] & [K_{\phi\phi}^e]\end{bmatrix} \tag{3.150}$$

with

$$[K_{uu}^e] = -\int_{V^e}\left[\underset{\sim}{B}_s^{e^u}\right]^T\cdot\left[\frac{\partial\underset{\sim}{\sigma}^s}{\partial\underline{u}\otimes\nabla^s}\right]\cdot\left[\underset{\sim}{B}_s^{e^u}\right] + \left[\underset{\sim}{B}_\omega^{e^u}\right]^T\cdot\left[\frac{\partial\underline{\pi}_\theta}{\partial\overset{\times}{\underline{\mathbf{e}}}}\right]\cdot\left[\underset{\sim}{B}_\omega^{e^u}\right]dV \tag{3.151}$$

$$[K_{u\theta}^e] = \int_{V^e} -\left[\underset{\sim}{B}_\omega^{e^u}\right]^T\cdot\left[-\frac{\partial\underline{\pi}_\theta}{\partial\overset{\times}{\underline{\mathbf{e}}}}\right]\cdot\left[N^{e^\theta}\right]dV \tag{3.152}$$

$$[K_{u\phi}^e] = \int_{V^e} -\left[\underset{\sim}{B}_\omega^{e^u}\right]^T\cdot\left(\left[\frac{\partial\underline{\pi}_\theta}{\partial\phi}\right]\otimes\left[N^{e^\phi}\right]\right)dV \tag{3.153}$$

$$[K^e_{\theta u}] = \int_{V^e} \left[N^{e^\theta}\right]^T \cdot \left[\frac{\partial \underline{\pi}_\theta}{\partial \overset{\times}{\underline{\mathbf{e}}}}\right] \cdot \left[\underset{\sim}{B}^{e^u}_{\omega}\right] dV \tag{3.154}$$

$$[K^e_{\theta\theta}] = \int_{V^e} \left[N^{e^\theta}\right]^T \cdot \left[-\frac{\partial \underline{\pi}_\theta}{\partial \overset{\times}{\underline{\mathbf{e}}}}\right] \cdot \left[N^{e^\theta}\right] - \left[\underset{\sim}{B}^{e^\theta}\right]^T \cdot \left[\frac{\partial \underset{\sim}{\xi}_\theta}{\partial \underline{\theta} \otimes \nabla}\right] \left[\underset{\sim}{B}^{e^\theta}\right] dV \tag{3.155}$$

$$[K^e_{\theta\phi}] = \int_{V^e} \left[N^{e^\theta}\right]^T \cdot \left(\left[\frac{\partial \underline{\pi}_\theta}{\partial \phi}\right] \otimes \left[N^{e^\phi}\right]\right) - \left[\underset{\sim}{B}^{e^\theta}\right]^T \cdot \left(\left[\frac{\partial \underset{\sim}{\xi}_\theta}{\partial \phi}\right] \otimes \left[N^{e^\phi}\right]\right) dV \tag{3.156}$$

$$[K^e_{\phi u}] = \int_{V^e} [N^{e^\phi}] \otimes \left[\frac{\partial \pi_\phi}{\partial \overset{\times}{\underline{\omega}}}\right] \cdot \left[\underset{\sim}{B}^{e^u}_{\omega}\right] dV \tag{3.157}$$

$$[K^e_{\phi\theta}] = \int_{V^e} [N^{e^\phi}] \otimes \left[\frac{\partial \pi_\phi}{\partial \underline{\theta}}\right] \cdot [N^{e^\theta}] + [N^{e^\phi}] \otimes \left[\frac{\partial \pi_\phi}{\partial \underline{\theta} \otimes \nabla}\right] \cdot \left[\underset{\sim}{B}^{e^\theta}\right] dV \tag{3.158}$$

$$[K^e_{\phi\phi}] = \int_{V^e} -[B^{e^\phi}]^T \cdot \left[\frac{\partial \underline{\xi}_\phi}{\partial \nabla \phi}\right] \cdot [B^{e^\phi}] + \frac{\partial \pi_\phi}{\partial \phi} \left([N^{e^\phi}] \otimes [N^{e^\phi}]\right) dV \tag{3.159}$$

III.3.4.2 Validation tests

The implemented three-dimensional formulation is tested against the two-dimensional one in several cases.

Formation of a bicrystal

The first test case is the formation of a flat grain boundary. The mesh is a cuboid of 200 quadratic elements with reduced integration. The initial conditions are given by Eq. 3.124 and the boundary conditions for the 2D computation are the same as Eq. 3.125. For the 3D computation $\bar{u}_1, \bar{u}_2, \bar{u}_3$ are constrained at the front bottom left corner while $\bar{u}_2, \bar{u}_3$ are constrained at the top right back corner in order to prevent rigid body motion. Multiple point constraints are applied to the bottom-top and front-back surfaces for all DOFs to ensure invariance. The resulting equilibrium profiles are shown in Fig. 3.32, where it can be seen that they coincide.

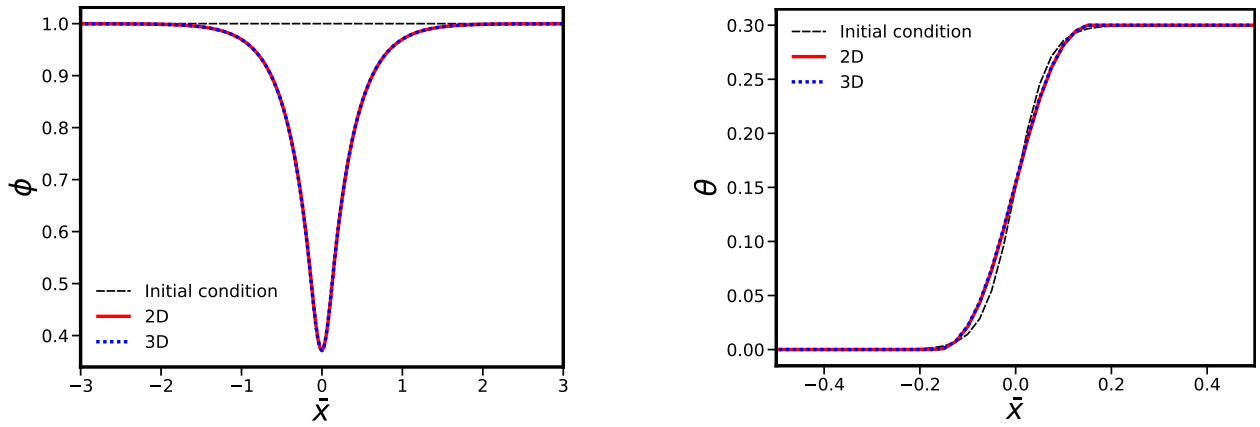

Figure 3.32: *Profiles of ϕ (left) and θ (right) during the formation of a grain boundary for the 2D and 3D FEM implementation of the KWC-Cosserat model with Maxwell relaxation law for the skew-symmetric stress.*

Periodic shear of a periodic bicrystal

The final test involves the periodic shear of a periodic bicrystal. To create the dislocation-free microstructure, a KWC simulation is performed to determine the equilibrium profiles of ϕ and θ. A 5% periodic shear loading is then applied to the periodic bicrystal. In the 3D case, $\bar{u}_3$, θ_1, θ_2 are set to 0 for all nodes, and crystal plasticity is enabled with only the slip system $\underline{\ell} = [100]$, $\underline{n} = [010]$. The mechanical properties parameters are presented in table 3.5. The remaining parameters are identical to those listed in table 3.4.

Parameter	$\bar{C}_{11}$	$\bar{C}_{12}$	$\bar{C}_{44}$	$\bar{K}$	n	$\bar{\tau}_c$	χ	$\bar{\mu}$	K_r	$\bar{d}$	$\bar{b}$
Value	69600	47800	32600	4.35	10	4.35	0.3	21750	10	10^{-3}	0.256

Table 3.5: *Additional parameters for plastic flow and evolution of dislocation density for a periodic bicrystal subjected to periodic shear loading.*

The simulation results are presented in Fig. 3.33. Figure 3.33a demonstrates that the 3D and 2D profiles for ϕ coincide. Changes in the initial profile arise from the production of dislocations due to plasticity activation that produce statistically stored dislocations, i.e stored energy. Likewise, the profiles for θ appear identical, as illustrated in Fig. 3.33b. The mechanical loading induces lattice rotation, which subsequently affects θ. This explains the disparity with the initial condition. The symmetrical and skew-symmetrical stress profiles, as shown in Fig. 3.33c and 3.33d, are comparable, with the primary difference residing near the interfaces. Ultimately, for lattice rotation and cumulative slip (Fig. 3.33e and 3.33f), the 2D and 3D profiles remain constant per grain and agree sufficiently well.

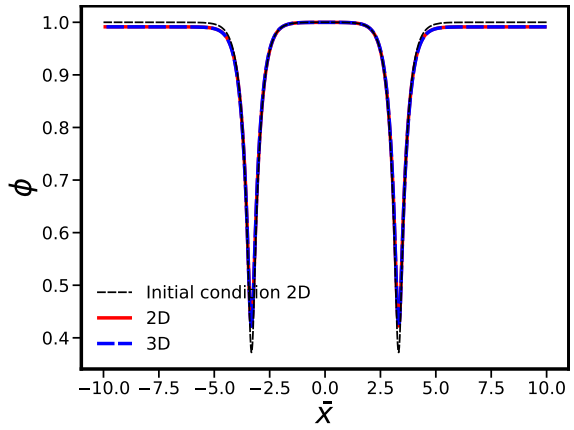

(a) *Crystal order* ϕ.

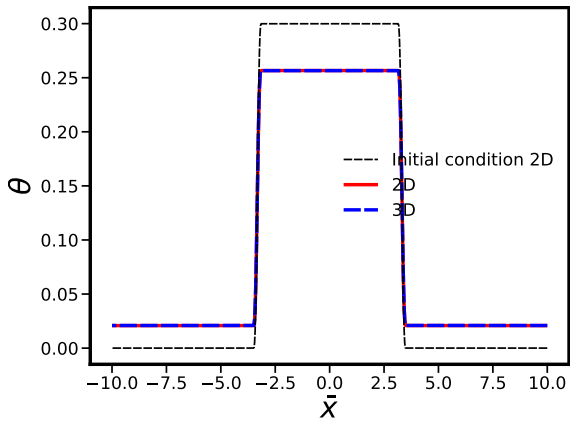

(b) *Lattice orientation* θ.

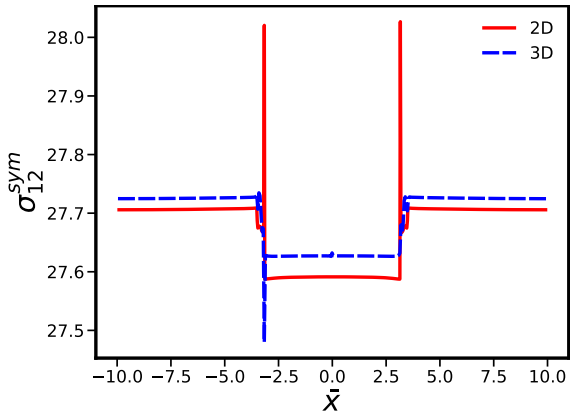

(c) *Symmetric shear stress* $\bar{\sigma}sym_{12}$.

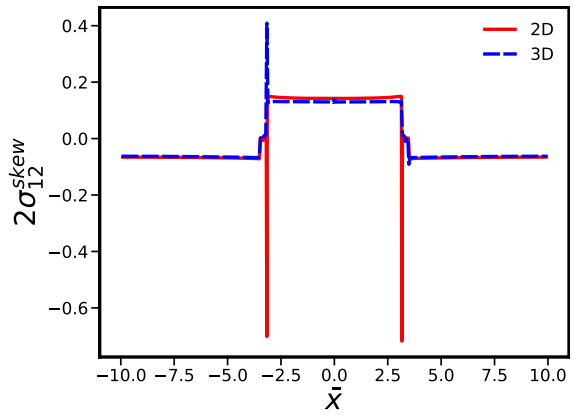

(d) *Skew-symmetric shear stress* $2\bar{\sigma}skew_{12}$.

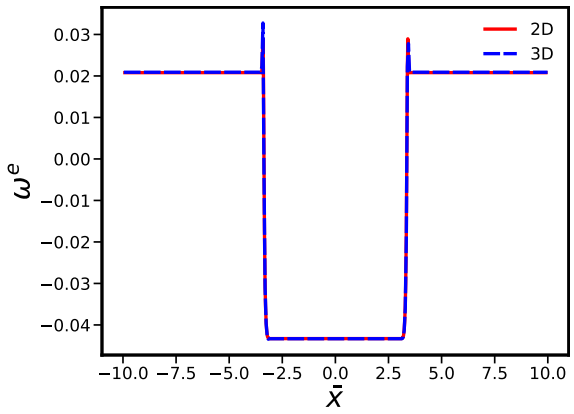

(e) *Lattice rotation* ω^e.

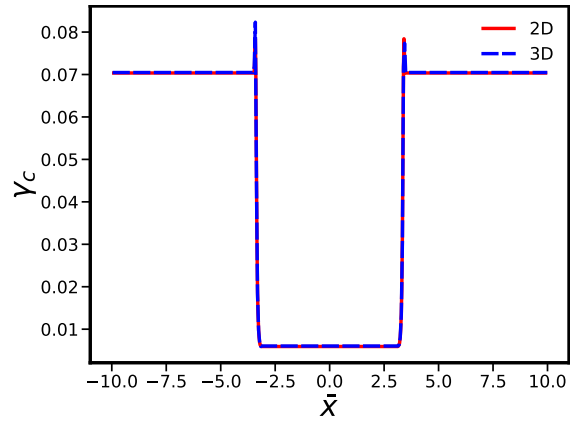

(f) *Cumulative slip* γ^c

Figure 3.33: *Comparison of 3D and 2D simulations of a periodic shear of a periodic bicrystal:* ϕ *(top left),* θ *(top right),* $\bar{\sigma}_{12}^{sym}$ *(middle left) ,* $2\bar{\sigma}_{12}^{skew}$ *(middle right),* ω *(bottom left) and* γ_c *(bottom right).*

III.3.5 Choice of parameters

The determination of the phase-field and mobility parameters follows the procedure outlined in section III.2.4. To ensure effective stress relaxation and unhindered grain boundary motion in the coupled model, it is essential to maintain $\bar{\eta}^{\star} < \bar{\eta}_{\phi}$. It should be noted that currently, the selection of these kinetic parameters is based on stored energy driven migration, which results in a linear relationship between the migration rate and the driving force, as opposed to the shrinkage of a circular grain. To obtain quantitative results comparable to experiments, a more thorough calibration procedure is necessary. This may be accomplished through modelling experiments on curvature-driven migration in bicrystals, as described in Gottstein and Shvindlerman [2009]. Mechanical behavior parameters are adopted from existing literature focused on pure copper, for instance Gérard et al. [2009]; Cheong and Busso [2004]. It is worth repeating that the Cosserat coupling modulus acts as a penalty parameter and forces $\overset{\times}{\underline{e}}^{e} \simeq \underline{0}$. The selected value for $\bar{\mu}_c$ must therefore ensure that this relationship is upheld. To achieve this, two-dimensional FEM simulations with various values of $\bar{\mu}_c$ are performed for grain boundary formation. The L^2 norm of $\overset{\times}{e}^{e}$ is then presented in Fig. 3.34 as a function of time. Choosing $\bar{\mu}_c = 10^4$ results in $\int_{\bar{V}} \overset{\times}{e}^{e^2} d\bar{V} \approx 10^{-14}$. The different parameters/properties involved and their dimensionless versions are summarized in table 3.6.

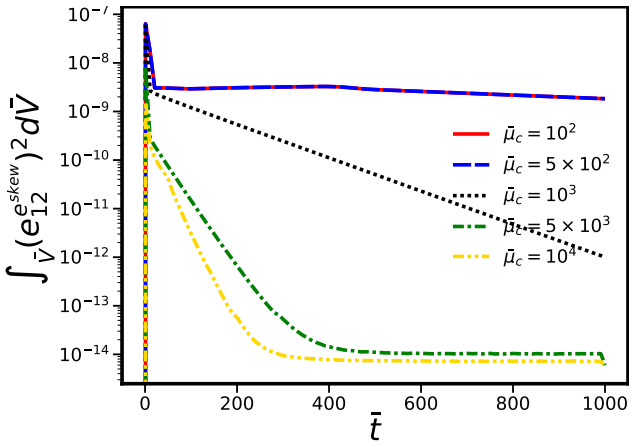

Figure 3.34: *L^2 norm of the skew-symmetric elastic strain $\overset{\times}{e}^{e}$ as a function of time during grain boundary formation for various values of parameter $\bar{\mu}_c$.*

Parameter/ property	Unit	Dimensionless expression	Comment
τ_0	s	-	Time scale
Λ	μm	-	Length scale
f_0	Jm^{-3}	-	Energy magnitude
E	MPa	$\bar{E} = E/f_0$	Stored energy due to dislocation build-up
ρ	m^{-2}	$\bar{\rho} = \rho/\Lambda^2$	SSD density
$\underset{\sim}{\sigma}$	MPa	$\bar{\underset{\sim}{\sigma}} = \underset{\sim}{\sigma}/f_0$	Stress tensor
$\underset{\sim}{\underset{\sim}{m}}$	MPa m	$\bar{\underset{\sim}{\underset{\sim}{m}}} = \underset{\sim}{\underset{\sim}{m}}/(f_0\Lambda)$	Couple stress tensor
α	m	$\bar{\alpha} = \alpha/\Lambda$	Phase field parameters
s	m	$\bar{s} = s/\Lambda$	
ε	m	$\bar{\varepsilon} = \varepsilon/\Lambda$	
η_ϕ	Js/m^3	$\bar{\eta}_\phi = \eta_\phi/(f_0\tau_0)$	Mobility parameter for ϕ
$\eta^\star$	Js/m^3	$\bar{\eta}^\star = \eta^\star/(f_0\tau_0)$	Mobility parameter for $\underline{\theta}^\star$
μ_p	m	$\bar{\mu}_p = \mu_p/\Lambda$	Parameters for the localization function $P(\nabla\theta)$
β_p	-	-	
E^e	MPa	$\bar{E}^e = E/f_0$	Young's modulus
ν	-	-	Poisson's ratio
μ_c	MPa	$\bar{\mu}_c = \mu/f_0$	Cosserat coupling modulus
K	MPa $s^{1/n}$	$\bar{K} = K/f_0$	Viscoplasticity parameters
n	-	-	
τ_c	MPa	$\bar{\tau}_c = \tau_c/f_0$	Critical resolved shear stress
χ	-	-	Coefficient
μ	MPa	$\bar{\mu} = \mu/f_0$	Mean shear modulus
K_r	-	-	Kocks-Mecking parameters
d	m	$\bar{d}_r = d_r/\Lambda$	
b	m	$\bar{b} = b/\Lambda$	Burgers vector
C_A	m^2	$\bar{C}_A = C_A/\Lambda^2$	Parameters for recovery
C_D	-	-	
γ	m	$\bar{\gamma} = \gamma/\Lambda$	Regularization for $\lvert\bar{\nabla}\theta\rvert$
γ_g	-	-	Regularization for $g(\phi) = -2(\log(1-\phi)+\phi)$

Table 3.6: *Parameters in the KWC-Cosserat model.*

III.4 Summary

In this chapter, the primary equations of the KWC model are recalled, and numerical simulations are used to evaluate the impact that parameters have on the static and dynamic behaviour of grain boundaries. Specifically, it is demonstrated that to achieve narrow grain boundaries with significant minima of ϕ, the relation $\bar{\alpha} < \bar{s}$ must be met. It was also shown that in the case of migration driven by stored energy, the grain boundary migration rate is primarily dependent on $\bar{\eta}_\phi$ and independent of $\bar{\eta}_\theta$, as long as $\bar{\eta}_\theta < \bar{\eta}_\phi$. This observation holds true to some extent for curvature-driven migration during the shrinkage of a circular grain, though the contribution of each parameter is less obvious. Simulations demonstrated the significance of the product $\bar{\eta}_\theta \dfrac{\bar{\mu}_p}{\bar{\varepsilon}}$ in preventing spurious grain reorientation during shrinkage. It was shown that low values of this product are not effective for that purpose.

The second section of this chapter concentrates on the KWC-Cosserat model and the influence of mechanics on grain boundaries. Specifically, the development and relaxation of stresses during grain boundary

formation and stored energy driven migration is discussed. The role of the chosen function for the relaxation of skew-symmetric stresses is assessed for both stationary and moving grain boundaries. In addition to the viscoelastic Maxwell and Voigt models for relaxation, which have already been described in Ask et al. [2018b] and Ask et al. [2020] respectively, the inclusion of a stress threshold was taken into account and represents the major original contribution in this chapter. This critical stress was introduced in two distinct models: a viscoplastic Norton law with threshold and a rate-independent law based on isotropic plasticity. The evolution equation for ϕ is identical for all models, but the same cannot be said for θ as outlined in Table 3.7. It was shown that the stress profiles of the bicrystal exhibit similarities with the elasto-plastic theory of dislocations and disclinations [Taupin et al., 2013]. The incorporation of a threshold in the relaxation law results in residual stresses that may impede motion of the grain boundary. As predicted, the limit $\bar{\sigma}_c \to 0$ retrieves the kinetics of a Maxwell model.
Subsequently, a three-dimensional version of the KWC-Cosserat model with Maxwell relaxation was formulated using finite elements and coded in Zset software. The implementation was compared to the two-dimensional version in different test cases, such as grain boundary formation and periodic shear of a periodic bicrystal. The results were considered satisfactory enough to carry out 3D simulations on more complex microstructures and load cases.

Model	**Evolution equation for θ**	**Reference**
KWC	$P(\nabla\theta)\bar{\eta}_\theta\phi^2\dot{\theta} = \bar{\nabla}\cdot\left(\bar{s}g\dfrac{\bar{\nabla}\theta}{\lvert\bar{\nabla}\theta\rvert} + \bar{\varepsilon}^2 h\bar{\nabla}\theta\right)$	Kobayashi et al. [2000]
KWC-Cosserat Kelvin relaxation law	$\phi^2\bar{\eta}^\theta P(\underline{\theta}\otimes\bar{\nabla})\left[-\overset{\times}{\underline{\omega}}^e + \underline{\dot{\theta}}\right] = \left(\bar{s}g\dfrac{\underline{\theta}\otimes\bar{\nabla}}{\lvert\lvert\underline{\theta}\otimes\bar{\nabla}\rvert\rvert} + \dfrac{\bar{\varepsilon}^2}{2}h\lvert\lvert\underline{\theta}\otimes\bar{\nabla}\rvert\rvert\right)\cdot\bar{\nabla} + 4\bar{\mu}_c\overset{\times}{\underline{e}}^e$	Ask et al. [2018b]
KWC-Cosserat Maxwell relaxation law	$\bar{\eta}^\star P(\underline{\theta}\otimes\bar{\nabla})\left[\dot{\underline{e}}^e - \dot{\underline{\omega}}^e + \underline{\dot{\theta}}\right] = \left(\bar{s}g\dfrac{\underline{\theta}\otimes\bar{\nabla}}{\lvert\lvert\underline{\theta}\otimes\bar{\nabla}\rvert\rvert} + \dfrac{\bar{\varepsilon}^2}{2}h\lvert\lvert\underline{\theta}\otimes\bar{\nabla}\rvert\rvert\right)\cdot\bar{\nabla}$	Ask et al. [2020]
KWC-Cosserat Norton law with threshold	$\lvert\overset{\times}{\underline{\sigma}}\rvert\bar{\eta}^\star P(\underline{\theta}\otimes\bar{\nabla})\left\langle\dfrac{\lvert\overset{\times}{\underline{\sigma}}\rvert - \bar{\sigma}_c}{K_c}\right\rangle^{-n_c}\left[\dot{\underline{e}}^e - \dot{\underline{\omega}}^e + \underline{\dot{\theta}}\right] = \left(\bar{s}g\dfrac{\underline{\theta}\otimes\bar{\nabla}}{\lvert\lvert\underline{\theta}\otimes\bar{\nabla}\rvert\rvert} + \dfrac{\bar{\varepsilon}^2}{2}h\lvert\lvert\underline{\theta}\otimes\bar{\nabla}\rvert\rvert\right)\cdot\nabla$	This work

Table 3.7: *Summary of the evolution equations for θ for the orientation phase-field models*

Chapter IV

Phase-field Cosserat modelling of grain nucleation in single crystals

Résumé en français

Dans ce chapitre, les modèle à champs de phase KWC et KWC-Cosserat sont appliqués au problème de la germination de grains en présence de gradients d'orientation du réseau cristallin dans les monocristaux, phénomène que nous interprétons comme l'accommodation d'une configuration instable. Dans un premier temps, une analyse de stabilité linéaire quasi-1D montre qu'un gradient homogène d'orientation présente une zone d'instabilité. Puis, une étude numérique est menée pour différentes configurations initiales du gradient d'orientation. On observe une fragmentation du monocristal initial en une multitude de grains de faible désorientation, qui vont ensuite fusionner pour former des grains plus larges et plus désorientés en raison des interactions entre les interfaces diffuses. Les simulations montrent également qu'une diminution de l'énergie totale est associée à ce phénomène de germination. La présence de gradients d'orientation est nécessaire pour déclencher le processus de germination. En effet, des simulations menées en présence d'un gradient d'énergie stockée par les dislocations de type SSD ne permettent la formation de nouveaux grains. L'effet de la mécanique sur la germination de grains été étudié pour le modèle KWC-Cosserat en l'absence de chargement mécanique pour deux lois d'évolution de l'orientation de référence: un modèle viscoélastique de Maxwell et un modèle de Norton à seuil. La présence du seuil de relaxation conduit à des contraintes résiduelles et peut, selon sa magnitude, retarder voire empêcher le phénomène de germination.

Enfin, nous simulons la torsion d'une barre monocristalline de cuivre à section circulaire dont l'axe est aligné avec la direction [111]. Seuls les systèmes du plan (111) sont pris en compte dans ce calcul. Le chargement mécanique génère un fort gradient d'orientation autour de l'axe du cylindre, ce qui permet la formation de nouveaux grains le long de cet axe, en accord avec les simulations quasi-1D. Les gradients radiaux et circonférentiels d'orientation et d'énergie stockées générés sont en revanche trop faibles pour impacter le champ d'ordre cristallin de façon significative. Les nouveaux grains formés sont donc homogènes dans la section transverse et forment un empilement de grains le long du cylindre. Des expériences de fluage en torsion menées par Kassner [1989] sur des monocristaux d'aluminium montrent également une microstructure en bambou ou les grains sont parallèles aux plans (111). Il ya donc un accord qualitatif entre la simulation et cette expérience.

Contents

IV.1 Introduction

Few attempts have been made towards phase field modelling of spontaneous grain and subgrain nucleation in single phase single component crystalline materials. Amongst the main mechanisms identified in the literature and described in Chapter I, nucleation by subgrain growth/coarsening for instance, has been simulated with a multi phase field model by Suwa et al. [2008, 2021] using the controversial assumption that the subgrain energy/curvature is the main driving force for nucleation Holm et al. [2003]. Another example is the simulation of nucleation by subgrain coalescence and nucleus growth with the KWC model by Muramatsu et al. [2014]. They showed that the model captured the shift in the misorientation distribution towards low-angle grain boundaries after recrystallization. It is worth pointing out that in both instances the effect of mechanical deformation was not considered. The inclusion of continuum mechanics in simulating recrystallization is classically done by coupling phase field models with crystal plasticity in staggered schemes. The nucleation step is handled by placing a circular/spherical nucleus at grain boundaries based on a critical strain, stress or dislocation density criterion. This *ad hoc* step can be deterministic or probabilistic as in Li et al. [2020]. Examples of such coupling in the multiple phase-field approach to simulate static and dynamic recrystallization can be found in [Steinbach and Apel, 2006; Takaki et al., 2008a; Takaki and Tomita, 2010] with extension to 3D by Chen et al. [2015]; as for the KWC model, examples can be found in [Takaki et al., 2008b], [Abrivard et al., 2012a,b] and more recently in [Luan et al., 2020]. It is noteworthy that Takaki and Tomita [2010] proposed an interesting approach to modelling nucleation in this context. The key concept involves substituting the stored energy derived from crystal plasticity computations with a subgrain structure, whose total boundary energy is equivalent to the stored energy. Subgrain radii are derived from the equality of energies and non-overlapping circular subgrain seeds are then placed on the computational domain. A normal grain growth step then occurs to achieve the subgrain structure. With continued grain growth, nucleation as a result of subgrain coarsening is observed. The method was labelled "spontaneous" by the authors, however, a seeding stage is still required for the subgrain structure to form. The highlighted limitations in the simulation of the nucleation of recrystallization call for the development of models that incorporate this phenomenon more spontaneously, i.e without prior seeding of grain/subgrain nuclei. We believe that the orientation phase-field models described in Chapter III could facilitate the resolution of this problem.

The aim of this chapter is to contribute to the mesoscopic and full-field simulation of the nucleation stage of recrystallization in single crystals. We emphasize that we are not proposing a new model for recrystallization, but rather show the capabilities of already existing frameworks to simulate spontaneous nucleation in single crystals. We will show through numerical simulations with the orientation phase-field models [Kobayashi et al., 2000; Ask et al., 2018b] described in details in Chapter III that lattice curvature in single crystals can lead to grain nucleation to accommodate these gradients. The process by which nucleation occurs in these cases is not related to SIBM or subgrain coarsening/coalescence but emerges as a consequence of the unstable development of strong lattice gradients inside grains. To our knowledge, these potentialities of KWC and KWC-Cosserat approaches have not been demonstrated in earlier contributions, although Admal et al. [2018] discussed subgrain nucleation due to plastic distortion within the framework of KWC-strain gradient plasticity.

This chapter is organized as follows. First, an analytic linear stability analysis is carried out and confronted to numerical simulations using the finite element method in section IV.2. In a second time, purely numerical experimentations are performed in section IV.3 in order to have a finer understanding of the model. They pertain to the influence of boundary and initial conditions as well as coupling function $g(\phi)$ and inverse mobility P. Time evolution of the phase-fields and key indicators are also studied. The influence of stored energy on the nucleation process is discussed as well. Finally, three-dimensional simulations of (sub)grain nucleation in a single crystal bar subjected to torsion are presented in section IV.4 and qualitative comparisons to experimental results from the literature are made.

IV.2 Stability of lattice curvature fields: linear stability analysis of the KWC model

The aim of this section is to assess the linear stability of the KWC phase-field model around the configuration $(\phi_0(\bar{x},\bar{t}),\theta_0(\bar{x},\bar{t}))$. To do so, small perturbations of the phase fields (denoted by $\delta\phi(\bar{x},\bar{t})$ and $\delta\theta(\bar{x},\bar{t})$) are introduced such that:

$$\phi(\bar{x},\bar{t}) = \phi_0(\bar{x},\bar{t}) + \delta\phi(\bar{x},\bar{t}), \tag{4.1}$$
$$\theta(\bar{x},\bar{t}) = \theta_0(\bar{x},\bar{t}) + \delta\theta(\bar{x},\bar{t}). \tag{4.2}$$

Let $\psi(a)$ be a scalar function where a is either ϕ or θ. A Taylor series expansion around a_0 at the first order gives:

$$\psi(a) \simeq \psi(a_0) + \left.\frac{\partial\psi}{\partial a}\right|_{a_0}\delta a = \psi_0 + \frac{\partial\psi_0}{\partial a}\delta a. \tag{4.3}$$

Let ψ,χ be functions of θ,ϕ and their derivatives with respect to space. Perturbation of $\psi\chi$ gives:

$$\delta(\psi\chi) = \psi_0\delta\chi + \chi_0\delta\psi. \tag{4.4}$$

We recall that the evolution equations are

$$Q\bar{\eta}_\phi\dot{\phi} = \bar{\alpha}^2\bar{\nabla}^2\phi - f_{,\phi} - \bar{s}g_{,\phi}|\bar{\nabla}\theta| - \frac{\bar{\varepsilon}^2}{2}h_{,\phi}|\bar{\nabla}\theta|^2 - \bar{E}, \tag{4.5}$$
$$P\bar{\eta}_\theta\phi^2\dot{\theta} = \bar{\nabla}\cdot\left(\bar{\varepsilon}^2 h\bar{\nabla}\theta + \bar{s}g\frac{\bar{\nabla}\theta}{|\bar{\nabla}\theta|}\right). \tag{4.6}$$

For the sake of simplicity, the chosen functions are

$$f(\phi) = \frac{1}{2}(1-\phi)^2,\ f_{,\phi}(\phi) = \phi - 1, \tag{4.7}$$
$$g(\phi) = h(\phi) = \phi^2,\ g_{,\phi}(\phi) = h_{,\phi}(\phi) = 2\phi. \tag{4.8}$$

Following the work of Warren et al. [2003] the singular term $sg(\phi)|\bar{\nabla}\theta|$ in the free energy is regularized by the function $sg(\phi)R_\gamma(|\bar{\nabla}\theta|)$ where

$$R_\gamma(|\bar{\nabla}\theta|) = \begin{cases} \dfrac{\gamma}{2}|\bar{\nabla}\theta|^2 \text{ for } 0 \le |\bar{\nabla}\theta| \le \dfrac{1}{\gamma}, \\ |\bar{\nabla}\theta| - \dfrac{1}{2\gamma} \text{ for } |\bar{\nabla}\theta| > \dfrac{1}{\gamma}. \end{cases} \tag{4.9}$$

Derivatives with respect to $\bar{t}$ and $\bar{x}$ are denoted $\dot{}$ and $'$ respectively. For the sake of simplicity, inverse mobility functions P and Q are assumed to be constant and the parameters given in table 4.1 are used throughout this section, unless specified otherwise. It is recalled that $\bar{\alpha},\bar{s},\bar{\varepsilon}$ are phase-field parameters, $\bar{\eta}_\phi,\bar{\eta}_\theta$ are inverse mobility parameters, L is the length of the 1D domain, K is the value of the constant orientation gradient, A,ξ are the amplitude and period of the perturbation, and γ is a regularization parameter.

Parameter	$\bar{\alpha}$	$\bar{s}$	$\bar{\varepsilon}$	P	Q	$\bar{\eta}_\phi$	$\bar{\eta}_\theta$	L	K	A	ξ	γ
Value	0.31	0.75	1	1	1	10	0.1	10	0.03	0.01	1	10000

Table 4.1: *Parameters used for the numerical simulations.*

IV.2.1 Perturbation analysis in the quadratic regime

It is first assumed that $0 \leq |\bar{\nabla}\theta| \leq \dfrac{1}{\gamma}$. The 1D regularized evolutions equation are thus

$$Q\bar{\eta}_\phi \dot{\phi} = \bar{\alpha}^2 \phi'' - (\phi - 1) - 2\phi \left(\bar{s}\frac{\gamma}{2} + \frac{\bar{\varepsilon}^2}{2} \right) (\theta')^2 \tag{4.10}$$

$$P\bar{\eta}_\theta \phi^2 \dot{\theta} = 2\phi'\phi(\bar{\varepsilon}^2 + \bar{s}\gamma)\theta' + \phi^2(\bar{\varepsilon}^2 + \bar{s}\gamma)\theta'' \tag{4.11}$$

Perturbing the above equations around the functions (ϕ_0, θ_0) gives:

$$Q\bar{\eta}_\phi \delta\dot{\phi} = \bar{\alpha}^2 \delta\phi'' - \delta\phi - 2\left(\bar{s}\frac{\gamma}{2} + \frac{\bar{\varepsilon}^2}{2} \right) [(\theta_0')^2 \delta\phi + 2\phi_0\theta_0'\delta\theta'] \tag{4.12}$$

$$\begin{aligned} P\bar{\eta}_\theta(\phi_0^2\delta\dot{\theta} + 2\phi_0\dot{\theta}_0\delta\phi) &= 2(\bar{\varepsilon}^2 + \bar{s}\gamma)(\phi_0\theta_0'\delta\phi' + \phi_0'\theta_0'\delta\phi + \phi_0'\phi_0\delta\theta') \\ &\quad + (\bar{\varepsilon}^2 + \bar{s}\gamma)(\phi_0^2\delta\theta'' + 2\theta_0''\phi_0\delta\phi) \end{aligned} \tag{4.13}$$

The perturbations are taken of the following form:

$$\delta\phi = \widehat{\delta\phi} \exp(ik\bar{x}) \exp\left(\omega_\phi \bar{t}\right) \tag{4.14}$$

$$\delta\theta = \widehat{\delta\theta} \exp(ik\bar{x}) \exp(\omega_\theta \bar{t}) \tag{4.15}$$

where $k = \dfrac{2\pi}{\xi}$ is a dimensionless wavenumber and $\omega_\phi, \omega_\theta$ are dimensionless growth rate of the perturbations. The evolution equations then become:

$$Q\bar{\eta}_\phi \delta\dot{\phi} = -\left[k^2\bar{\alpha}^2 + 1 + \left(\bar{s}\gamma + \bar{\varepsilon}^2\right)(\theta_0')^2\right]\delta\phi - 2\left(\bar{s}\gamma + \bar{\varepsilon}^2\right)\phi_0\theta_0' ik\delta\theta \tag{4.16}$$

$$\begin{aligned} P\bar{\eta}_\theta\phi_0^2\delta\dot{\theta} &= \left[2(\bar{\varepsilon}^2 + \bar{s}\gamma)\left(\phi_0\theta_0' ik + \phi_0'\theta_0' + \theta_0''\phi_0\right) - 2P\bar{\eta}_\theta\phi_0\dot{\theta}_0\right]\delta\phi \\ &\quad + (\bar{\varepsilon}^2 + \bar{s}\gamma)\left(-k^2\phi_0^2 + 2\phi_0'\phi_0 ik\right)\delta\theta \end{aligned} \tag{4.17}$$

This system of first order differential equations can be put in the following matrix form:

$$\begin{pmatrix} \delta\dot{\phi} \\ \delta\dot{\theta} \end{pmatrix} = \underbrace{\begin{pmatrix} -\dfrac{\bar{\alpha}^2k^2 + 1 + \left(\bar{s}\gamma + \bar{\varepsilon}^2\right)(\theta_0')^2}{Q\bar{\eta}_\phi} & \dfrac{-2\phi_0 ik\left(\bar{s}\gamma + \bar{\varepsilon}^2\right)\theta_0'}{Q\bar{\eta}_\phi} \\ \dfrac{2(\bar{\varepsilon}^2 + \bar{s}\gamma)\left(\phi_0\theta_0' ik + \phi_0'\theta_0' + \theta_0''\phi_0\right) - 2P\bar{\eta}_\theta\phi_0\dot{\theta}_0}{P\bar{\eta}_\theta\phi_0^2} & \dfrac{(\bar{\varepsilon}^2 + \bar{s}\gamma)\left(-k^2\phi_0^2 + 2\phi_0'\phi_0 ik\right)}{P\bar{\eta}_\theta\phi_0^2} \end{pmatrix}}_{M} \cdot \begin{pmatrix} \delta\phi \\ \delta\theta \end{pmatrix} \tag{4.18}$$

The solutions of this system of ODEs are:

$$\begin{pmatrix} \delta\phi \\ \delta\theta \end{pmatrix} = A\exp(\lambda_1\bar{t})\underline{V}_1 + B\exp(\lambda_2\bar{t})\underline{V}_2 \tag{4.19}$$

with A, B constants to be determined from the initial conditions, λ_1, λ_2 the complex eigenvalues and $\underline{V}_1, \underline{V}_2$ the associated eigenvectors. The stability of this system of ODEs depends on the sign of the real part of the eigenvalues: if there is at least one positive eigenvalue then the system is unstable. The configuration that is first tested is that of a single crystal subjected to a constant orientation gradient:

$$\phi_0(\bar{x}, \bar{t}) = 1 \tag{4.20}$$

$$\theta_0(\bar{x}, \bar{t}) = K\bar{x} \tag{4.21}$$

It is worth noting that equations (4.20,4.21) do not fulfil the equilibrium condition for ϕ, except for $K = 0$. For $K \neq 0$, the chosen perturbed state is therefore not a stationary solution of the system of equations (4.10,4.11).

The system becomes:

$$\begin{pmatrix} \delta\dot{\phi} \\ \delta\dot{\theta} \end{pmatrix} = \begin{pmatrix} -\dfrac{\bar{\alpha}^2k^2 + 1 + \left(\bar{s}\gamma + \bar{\varepsilon}^2\right)K^2}{Q\bar{\eta}_\phi} & \dfrac{-2ik\left(\bar{s}\gamma + \bar{\varepsilon}^2\right)K}{Q\bar{\eta}_\phi} \\ \dfrac{2ik\left(\bar{s}\gamma + \bar{\varepsilon}^2\right)K}{P\bar{\eta}_\theta} & \dfrac{-k^2(\bar{\varepsilon}^2 + \bar{s}\gamma)}{P\bar{\eta}_\theta} \end{pmatrix} \cdot \begin{pmatrix} \delta\phi \\ \delta\theta \end{pmatrix} \tag{4.22}$$

For $K = 0$ the eigenvalues are given by the diagonal coefficients, which are always negative, hence ensuring the stability:

$$\lambda_1 = -\frac{\bar{\alpha}^2k^2 + 1}{Q\bar{\eta}_\phi} \tag{4.23}$$

$$\lambda_2 = \frac{-k^2(\bar{\varepsilon}^2 + \bar{s}\gamma)}{P\bar{\eta}_\theta} \tag{4.24}$$

This can be explained by the fact that $\theta(\bar{x},\bar{t}) = constant,\ \phi(\bar{x},\bar{t}) = 1$ is a stable equilibrium configuration corresponding to the bulk state of the grain. Finite element simulations are carried out to assess the relevance of this linear stability analysis. The parameters used for these computations are given in table 4.1 with $\gamma = 10$. A low value of γ was chosen to ensure that the regularization is effective for all values of $\nabla\theta$. The initial conditions are periodic fluctuations of period $\xi = 10$ around $\phi(\bar{x},\bar{t}) = 1,\ \theta(\bar{x},\bar{t}) = 0$ and the following boundary conditions are imposed:

$$\phi(\bar{x} = -L,\bar{t}) = \phi(\bar{x} = L,\bar{t}) = 1 \tag{4.25}$$

$$\theta'(\bar{x} = -L,\bar{t}) = \theta'(\bar{x} = L,\bar{t}) = 0 \tag{4.26}$$

The results are shown in figure 4.1 where visibly the profiles of ϕ and θ converge towards $\phi = 1$ and $\theta = 0$, which corroborates the linear stability analysis.

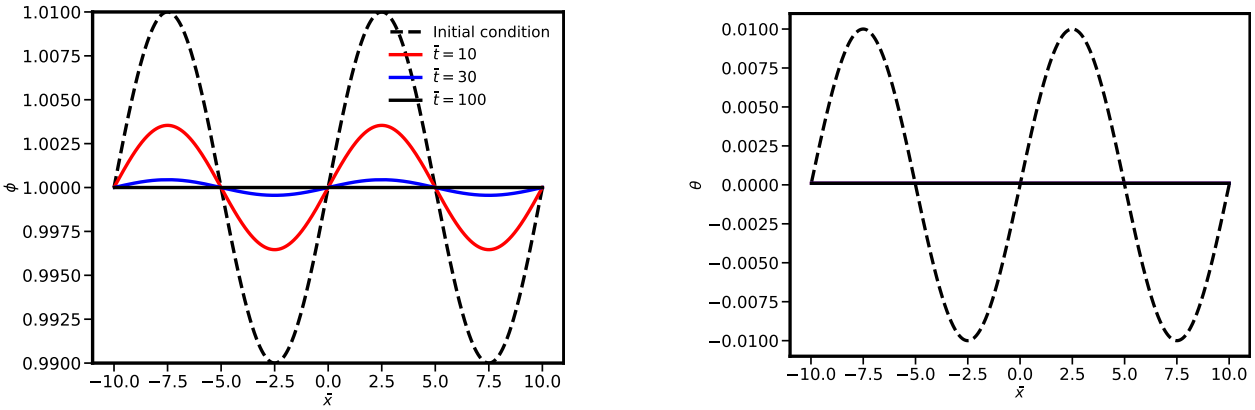

Figure 4.1: *Profiles of ϕ and θ for $\gamma = 10,\ \xi = 10$ in the quadratic regime and $\phi_0 = 1,\ \theta_0 = 0$.*

Now considering $K \neq 0$, the characteristic equation is:

$$(M_{11} - \lambda)(M_{22} - \lambda) - M_{21}M_{12} = 0 \tag{4.27}$$

$$\lambda^2 - \mathrm{Tr}(M)\lambda + \det(M) = 0 \tag{4.28}$$

with

$$\det(M) = M_{11}M_{22} - M_{21}M_{12} \tag{4.29}$$

$$\mathrm{Tr}(M) = M_{11} + M_{22} \tag{4.30}$$

The discriminant of the characteristic equation is then:

$$\Delta = (\mathrm{Tr}(M))^2 - 4\det(M) \tag{4.31}$$

$$\Delta = \left(\frac{\bar{\alpha}^2 k^2 + 1 + \left(\bar{s}\gamma + \bar{\varepsilon}^2\right) K^2}{Q\bar{\eta}_\phi} - \frac{k^2(\bar{\varepsilon}^2 + \bar{s}\gamma)}{P\bar{\eta}_\theta} \right)^2 + 16\frac{k^2\left(\bar{s}\gamma + \bar{\varepsilon}^2\right)^2 K^2}{P\bar{\eta}_\theta Q\bar{\eta}_\phi} \geq 0 \tag{4.32}$$

The eigenvalues are purely real and given by:

$$\lambda = \frac{\mathrm{Tr}(M) \pm \sqrt{\Delta}}{2} \tag{4.33}$$

$$\begin{aligned} 2\lambda = &- \left(\frac{\bar{\alpha}^2 k^2 + 1 + \left(\bar{s}\gamma + \bar{\varepsilon}^2\right) K^2}{Q\bar{\eta}_\phi} + \frac{k^2(\bar{\varepsilon}^2 + \bar{s}\gamma)}{P\bar{\eta}_\theta} \right) \\ &\pm \sqrt{\left(\frac{\bar{\alpha}^2 k^2 + 1 + (\bar{s}\gamma + \bar{\varepsilon}^2) K^2}{Q\bar{\eta}_\phi} - \frac{k^2(\bar{\varepsilon}^2 + \bar{s}\gamma)}{P\bar{\eta}_\theta} \right)^2 + 16\frac{k^2\left(\bar{s}\gamma + \bar{\varepsilon}^2\right)^2 K^2}{P\bar{\eta}_\theta Q\bar{\eta}_\phi}} \end{aligned} \tag{4.34}$$

Let us now study the sign of these eigenvalues. As $\mathrm{Tr}(M) < 0$, $\mathrm{Tr}(M) - \sqrt{\Delta} < 0$. Thus there can be a positive eigenvalue only if $\mathrm{Tr}(M) + \sqrt{\Delta} \geq 0$. We now look for the wave-numbers which fulfill that condition. We obtain:

$$-\sqrt{\frac{3K^2(\bar{s}\gamma + \varepsilon^2) - 1}{\bar{\alpha}^2}} \leq k \leq \sqrt{\frac{3K^2(\bar{s}\gamma + \varepsilon^2) - 1}{\bar{\alpha}^2}} \tag{4.35}$$

By choosing $k \in \mathbb{R}$ the following constraint must be fulfilled:

$$3K_{lim}^2(\bar{s}\gamma + \varepsilon^2) - 1 \geq 0 \tag{4.36}$$

$$|K_{lim}| \geq \sqrt{\frac{1}{3(\bar{s}\gamma + \varepsilon^2)}} \tag{4.37}$$

For $K < K_{lim}$ there is no $k \in \mathbb{R}$ such that $\lambda > 0$, thus no instability occurs. For $K > K_{lim}$ an instability may arise if $k \in \left[-\sqrt{\frac{3K^2(\bar{s}\gamma + \varepsilon^2) - 1}{\bar{\alpha}^2}}, \sqrt{\frac{3K^2(\bar{s}\gamma + \varepsilon^2) - 1}{\bar{\alpha}^2}} \right]$.

The eigenvalues are plotted as a function of k for different values of K in figure 4.2 with the set of parameters given in table 4.1 and $\gamma = 10$ to ensure activation of the quadratic regime.

FEM computations are performed for different values of the orientation gradient K and perturbation period ξ in figure 4.3. With an orientation gradient corresponding to a variation of about 0.6 radians over $2L = 20$ ($K = 0.03$) and a perturbation of period $\xi = 1$, it is predicted that no instability will occur as $K < K_{lim}$. The FEM simulations in figure 4.3a show that, in accordance with this stability analysis, the phase fields do not depart much from the configuration $\theta(\bar{x},\bar{t}) = K\bar{x}$, $\phi(\bar{x},\bar{t}) = 1$. On the contrary with $K = 0.3 > K_{lim}$, $\xi = 10$ it is expected that the instability will grow as for this set of parameters $k \in \left[-\sqrt{\frac{3K^2(\bar{s}\gamma + \varepsilon^2) - 1}{\bar{\alpha}^2}}, \sqrt{\frac{3K^2(\bar{s}\gamma + \varepsilon^2) - 1}{\bar{\alpha}^2}} \right]$. That is what is indeed observed in figure 4.3b) in which FEM simulations show the formation of a grain boundary to accommodate this instability.

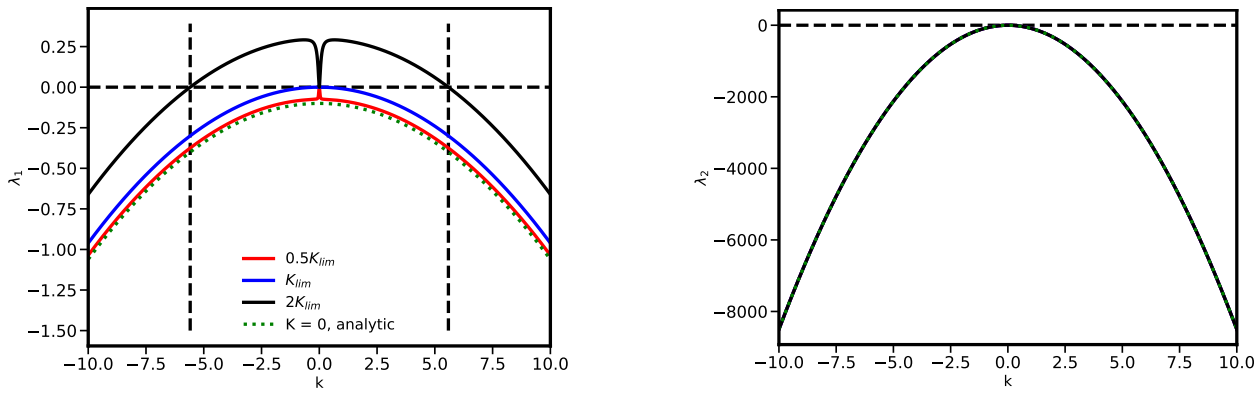

Figure 4.2: *Eigenvalues λ_1 and λ_2 as functions of the wavenumber for $\gamma = 10$ in the quadratic regime and $\phi_0 = 1,\ \theta_0(\bar{x}) = K\bar{x}$.*

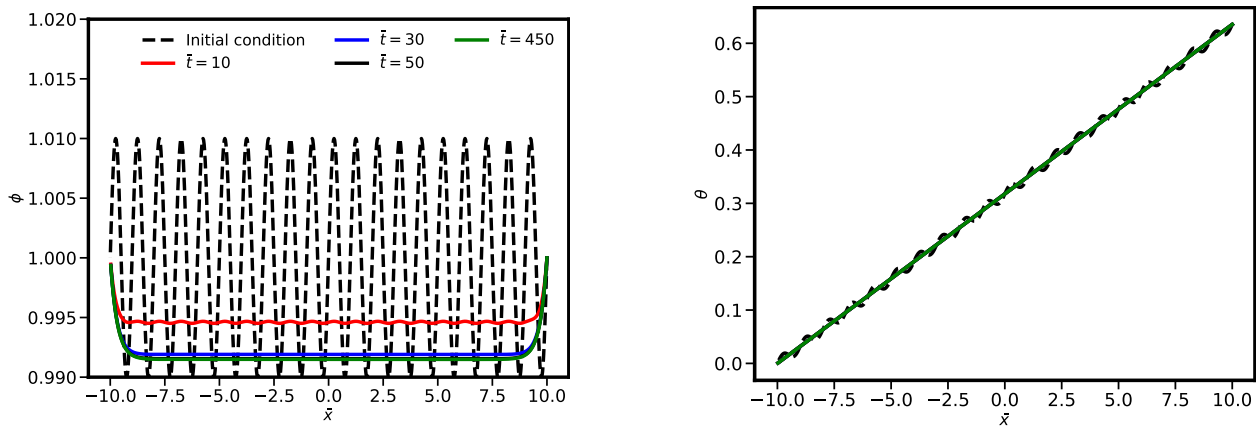

(a) $K = 0.03,\ \xi = 1.$

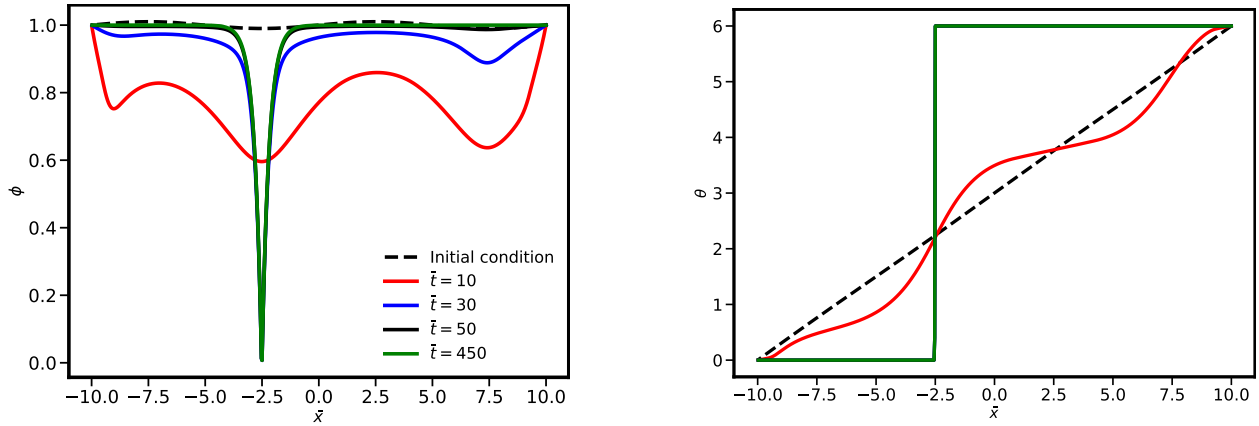

(b) $K = 0.3,\ \xi = 10.$

Figure 4.3: *Profiles of ϕ and θ for $\gamma = 10$ in the quadratic regime and $\phi_0 = 1,\ \theta_0(\bar{x}) = K\bar{x}$.*

IV.2.2 Stability analysis in the non-quadratic regime

It is now assumed that $|\bar{\nabla}\theta| > \dfrac{1}{\gamma}$. The 1D non regularized evolution equations are then:

$$Q\bar{\eta}_\phi\dot{\phi} = \bar{\alpha}^2\phi'' - (\phi - 1) - 2s\phi\ \epsilon\ \theta' - \bar{\varepsilon}^2\phi(\theta')^2 \tag{4.38}$$

$$P\bar{\eta}_\theta\phi^2\dot{\theta} = \bar{\varepsilon}^2\left(2\phi\phi'\theta' + \phi^2\theta''\right) + 2\bar{s}\ \epsilon\ \phi\phi' \tag{4.39}$$

with $\epsilon = \pm 1$.

Perturbation of the above equations gives:

$$\begin{pmatrix} \delta\dot{\phi} \\ \delta\dot{\theta} \end{pmatrix} = \begin{pmatrix} -\dfrac{\bar{\alpha}^2k^2+1+2\bar{s}\,\epsilon\,\theta_0'+\bar{\varepsilon}^2(\theta_0')^2}{Q\bar{\eta}_\phi} & \dfrac{-2\phi_0 ik(\bar{s}\,\epsilon+\bar{\varepsilon}^2\theta_0')}{Q\bar{\eta}_\phi} \\ \dfrac{-2P\bar{\eta}_\theta\phi_0\dot{\theta}_0+2\bar{\varepsilon}^2[\phi_0'\theta_0'+\phi_0\theta_0'']+2\bar{s}\,\epsilon\,\phi_0'+2\phi_0 ik(\bar{s}\,\epsilon+\bar{\varepsilon}^2\theta_0')}{P\bar{\eta}_\theta\phi_0^2} & \dfrac{2\bar{\varepsilon}^2\phi_0\phi_0' ik-\bar{\varepsilon}^2k^2\phi_0^2}{P\bar{\eta}_\theta\phi_0^2} \end{pmatrix} \cdot \begin{pmatrix} \delta\phi \\ \delta\theta \end{pmatrix} \tag{4.40}$$

Considering equations 4.20-4.21, eq. 4.40 now becomes:

$$\begin{pmatrix} \delta\dot{\phi} \\ \delta\dot{\theta} \end{pmatrix} = \underbrace{\begin{pmatrix} -\dfrac{\bar{\alpha}^2k^2+1+2\bar{s}\,\epsilon\,K+\bar{\varepsilon}^2K^2}{Q\bar{\eta}_\phi} & \dfrac{-2ik\phi_0(\bar{s}\,\epsilon+\bar{\varepsilon}^2K)}{Q\bar{\eta}_\phi} \\ \dfrac{2ik\phi_0(\bar{s}\,\epsilon+\bar{\varepsilon}^2K)}{P\bar{\eta}_\theta\phi_0^2} & \dfrac{-\bar{\varepsilon}^2k^2}{P\bar{\eta}_\theta} \end{pmatrix}}_{M} \cdot \begin{pmatrix} \delta\phi \\ \delta\theta \end{pmatrix} \tag{4.41}$$

The discriminant of the characteristic equation is then:

$$\Delta = \left(\frac{\bar{\alpha}^2k^2+1+2\bar{s}\,\epsilon\,K+\bar{\varepsilon}^2K^2}{Q\bar{\eta}_\phi} - \frac{\bar{\varepsilon}^2k^2}{P\bar{\eta}_\theta}\right)^2 + 16\frac{k^2(\bar{s}\,\epsilon+\bar{\varepsilon}^2K)^2}{P\bar{\eta}_\theta Q\bar{\eta}_\phi} \geq 0 \tag{4.42}$$

The eigenvalues are real and given by:

$$\begin{aligned} 2\lambda = &-\left(\frac{\bar{\alpha}^2k^2+1+2\bar{s}\,\epsilon\,K+\bar{\varepsilon}^2K^2}{Q\bar{\eta}_\phi} + \frac{\bar{\varepsilon}^2k^2}{P\bar{\eta}_\theta}\right) \\ &\pm\sqrt{\left(\frac{\bar{\alpha}^2k^2+1+2\bar{s}\,\epsilon\,K+\bar{\varepsilon}^2K^2}{Q\bar{\eta}_\phi} - \frac{\bar{\varepsilon}^2k^2}{P\bar{\eta}_\theta}\right)^2 + 16\frac{k^2(\bar{s}\,\epsilon+\bar{\varepsilon}^2K)^2}{P\bar{\eta}_\theta Q\bar{\eta}_\phi}} \end{aligned} \tag{4.43}$$

We once again look for the wave-numbers k satisfying $\mathrm{Tr}(M)+\sqrt{\Delta} > 0$. The following domain of instability is found:

$$-\sqrt{\frac{3\bar{\varepsilon}^4K^2+6\bar{s}\,\epsilon\,K\bar{\varepsilon}^2-\bar{\varepsilon}^2+4s^2}{\bar{\varepsilon}^2\bar{\alpha}^2}} \leq k \leq \sqrt{\frac{3\bar{\varepsilon}^4K^2+6\bar{s}\,\epsilon\,K\bar{\varepsilon}^2-\bar{\varepsilon}^2+4s^2}{\bar{\varepsilon}^2\bar{\alpha}^2}} \tag{4.44}$$

As $k \in \mathbb{R}$ the following constraint must be fulfilled:

$$3\bar{\varepsilon}^4K^2+6\bar{s}\,\epsilon\,K\bar{\varepsilon}^2-\bar{\varepsilon}^2+4s^2 \geq 0 \tag{4.45}$$

which has solutions in $\mathbb{R}$ only if

$$\Delta_K = 12(\bar{\varepsilon}^6-\bar{\varepsilon}^4\bar{s}^2) \geq 0 \tag{4.46}$$

This is ensured with the parameters given in table 4.1. Finally the condition for K is

$$K \leq \frac{-6\bar{s}\,\epsilon\,\bar{\varepsilon}^2-\sqrt{12(\bar{\varepsilon}^6-\bar{\varepsilon}^4\bar{s}^2)}}{6\bar{\varepsilon}^4} \text{ or } K \geq \frac{-6\bar{s}\,\epsilon\,\bar{\varepsilon}^2+\sqrt{12(\bar{\varepsilon}^6-\bar{\varepsilon}^4\bar{s}^2)}}{6\bar{\varepsilon}^4} \tag{4.47}$$

The eigenvalues are plotted as functions of k for several values of K in figure 4.4 with the set of parameters given in table 4.1. It can be seen that for $\epsilon = 1$ the instability domain increases with K, meaning that larger initial orientation gradients tend to destabilize the system.

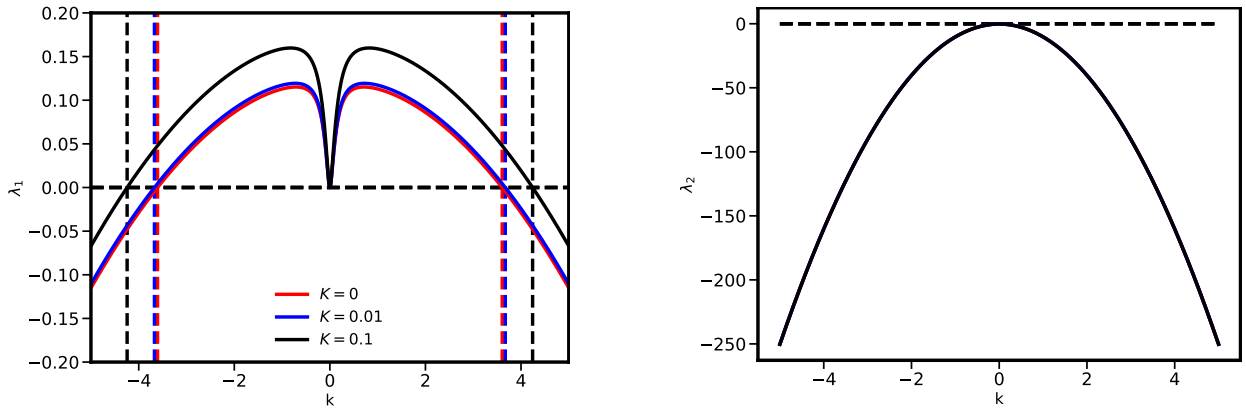

(a) $\epsilon = 1$.

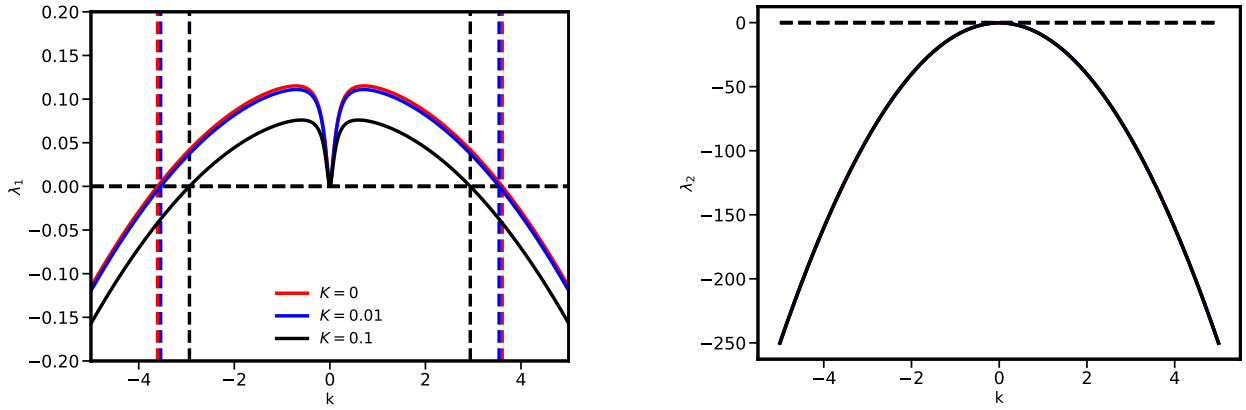

(b) $\epsilon = -1$.

Figure 4.4: *Eigenvalues λ_1 and λ_2 as functions of the wavenumber for the non-quadratic regime and $\phi_0 = 1$, $\theta_0(\bar{x}) = K\bar{x}$.*

Finite element simulations performed for $\xi = 10$ in figure 4.5 show that grain boundaries arise to accommodate the instability predicted by the linear stability analysis. However, for large values of k it is expected that no instability will occur, which is not what is observed by FEA as grain boundaries are still formed. This discrepancy is likely to stem from non-linear effects which are not accounted for in the linear stability analysis that was performed.

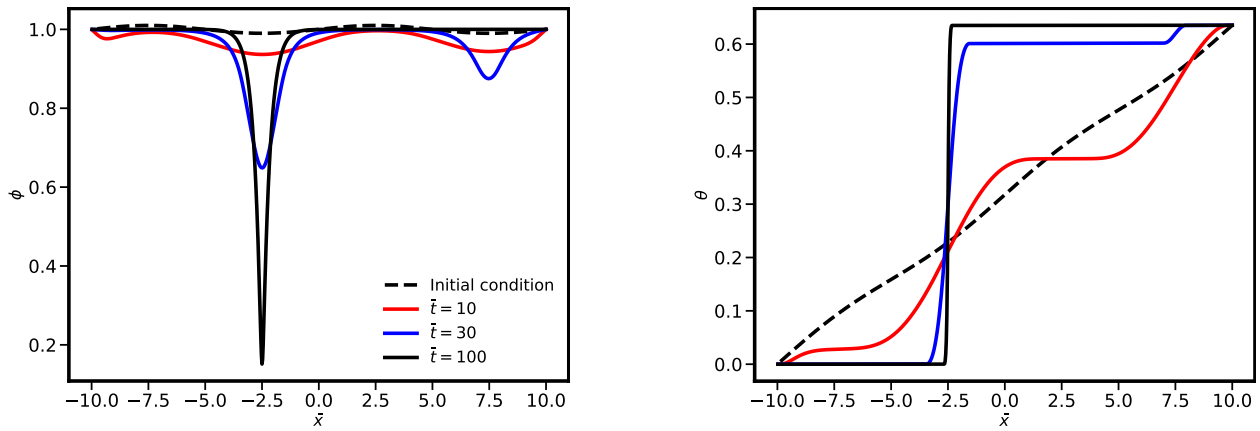

(a) $\lambda = 10$.

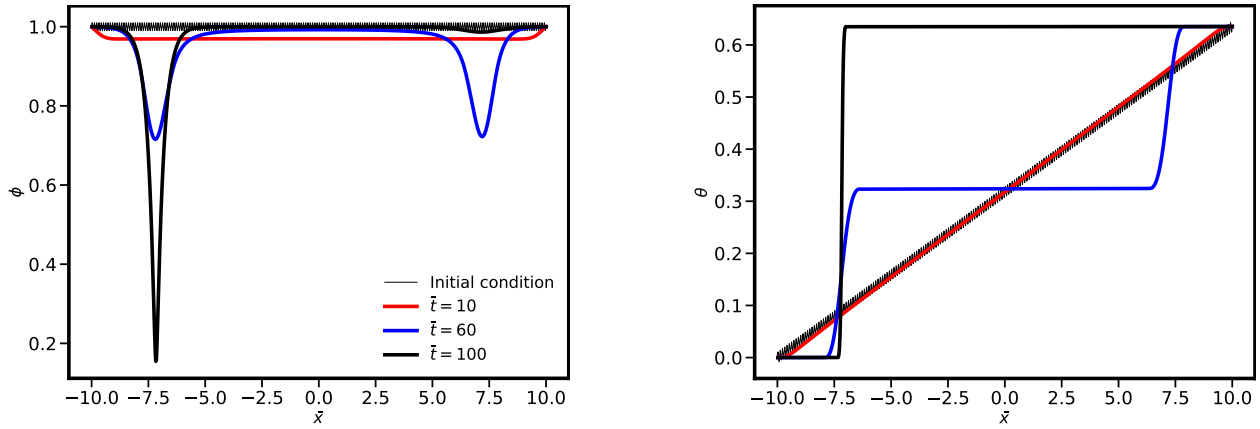

(b) $\lambda = 0.1$.

Figure 4.5: *Profiles of ϕ and θ for the non-quadratic regime and $\phi_0 = 1,\ \theta_0(\bar{x}) = K\bar{x}$.*

IV.2.3 Influence of the equilibrium solution: quadratic regime

We now look for the equilibrium solution of $\phi(\bar{x},\bar{t})$ satisfying $\theta(\bar{x},\bar{t}) = K\bar{x}$ in the quadratic regime:

$$\bar{\alpha}^2\phi'' - (1 + K^2(\bar{s}\gamma + \bar{\varepsilon}^2))\phi + 1 = 0 \tag{4.48}$$

The solution to the homogeneous equation is simply:

$$\phi(x) = A\exp(\nu_1 x) + B\exp(\nu_2 x) \tag{4.49}$$

where ν_1, ν_2 are the solutions to the characteristic equation:

$$\bar{\alpha}^2\nu^2 - (1 + K^2(\bar{s}\gamma + \bar{\varepsilon}^2)) = 0 \tag{4.50}$$

Thus

$$\nu_1 = \frac{\sqrt{1 + K^2(\bar{s}\gamma + \bar{\varepsilon}^2)}}{\bar{\alpha}}, \qquad \nu_2 = -\nu_1 \tag{4.51}$$

We look for a particular solution of the form $\phi = C$ where C is a constant. We find $C = \dfrac{1}{1+K^2(\bar{s}\gamma+\bar{\varepsilon}^2)}$, so that the general solution is:

$$\phi(x) = A\exp(\nu_1 x) + B\exp(-\nu_1 x) + \frac{1}{1+K^2(\bar{s}\gamma+\bar{\varepsilon}^2)} \tag{4.52}$$

The constants A, B are determined by the boundary conditions taken as:

$$\phi(x=L) = \phi(x=-L) = 1 \tag{4.53}$$

The system to be solved is then:

$$A\exp(\nu_1 L) + B\exp(-\nu_1 L) + \frac{1}{1+K^2(\bar{s}\gamma+\bar{\varepsilon}^2)} = 1 \tag{4.54}$$

$$A\exp(-\nu_1 L) + B\exp(\nu_1 L) + \frac{1}{1+K^2(\bar{s}\gamma+\bar{\varepsilon}^2)} = 1 \tag{4.55}$$

which gives:

$$A = \frac{1 - \frac{1}{1+K^2(\bar{s}\gamma+\bar{\varepsilon}^2)} - B\exp(-\nu_1 L)}{\exp(\nu_1 L)} \tag{4.56}$$

$$B = \frac{(\exp(\nu_1 L) - 1)\left(1 - \frac{1}{1+K^2(\bar{s}\gamma+\bar{\varepsilon}^2)}\right)}{2\sinh(2\nu_1 L)} \tag{4.57}$$

Note that $\theta(\bar{x},\bar{t}) = K\bar{x}$ does not fulfil the equilibrium equation for θ. Indeed, at equilibrium ϕ and θ must satisfy

$$\bar{\alpha}^2\phi'' - (\phi - 1) - \phi(\bar{s}\gamma\bar{\varepsilon}^2)(\theta')^2 = 0 \tag{4.58}$$

$$\left(\phi^2(\bar{s}\gamma+\bar{\varepsilon}^2)\theta'\right)' = 0 \tag{4.59}$$

$$\bar{\alpha}^2\phi'' - (\phi - 1) - \phi(\bar{s}\gamma\bar{\varepsilon}^2)(\theta')^2 = 0 \tag{4.60}$$

$$\phi^2(\bar{s}\gamma+\bar{\varepsilon}^2)\theta' = C \tag{4.61}$$

where C is a constant. From equation 4.61 an expression for θ' can be obtained and inserted in equation 4.60:

$$\theta' = \frac{C}{\bar{s}\gamma+\bar{\varepsilon}^2}\phi^{-2} \tag{4.62}$$

$$\bar{\alpha}^2\phi'' - (\phi - 1) - \phi(\bar{s}\gamma+\bar{\varepsilon}^2)\frac{C^2}{(\bar{s}\gamma+\bar{\varepsilon}^2)}\phi^{-4} = 0 \tag{4.63}$$

Analytical solutions to this system of nonlinear differential equations are not readily found.
Finite element simulations with $\gamma = 10$ to ensure the quadratic regime is active give the profiles depicted in figure 4.6. The equilibrium solution found by FEA is close to $\theta(\bar{x},\bar{t}) = K\bar{x}$ and ϕ given by equation 4.52. To assess the difference between the two solutions in a more quantitative way, the relative difference is plotted as a function of $\bar{x}$ in figure 4.7. The maximum relative difference is about 0.005% for ϕ and 1.5% for θ. Thus, $\theta(\bar{x},\bar{t}) = K\bar{x}$ and ϕ given by equation 4.52 can be considered as a near equilibrium configuration.

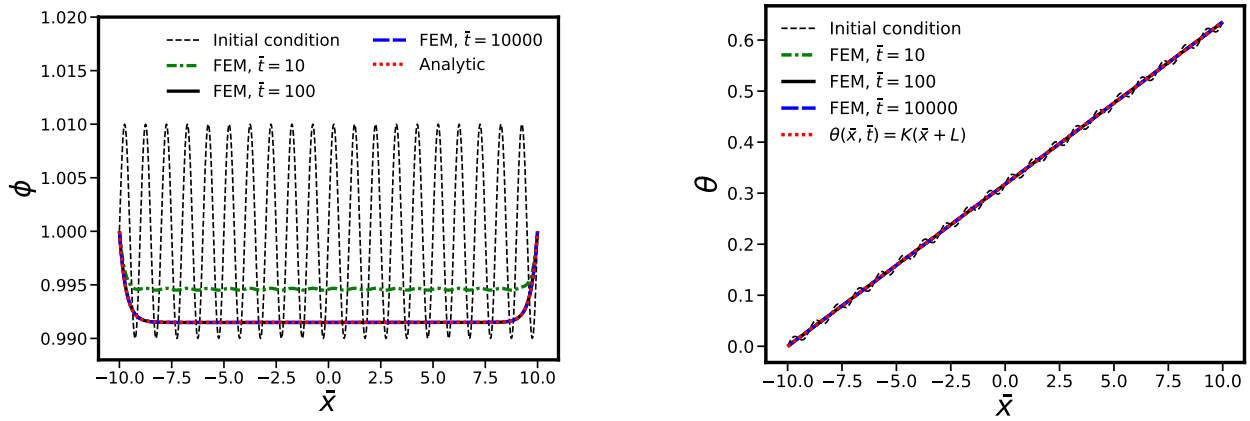

Figure 4.6: *Comparison of the analytical and FEM solutions of the equilibrium profile of ϕ and θ in the quadratic regime.*

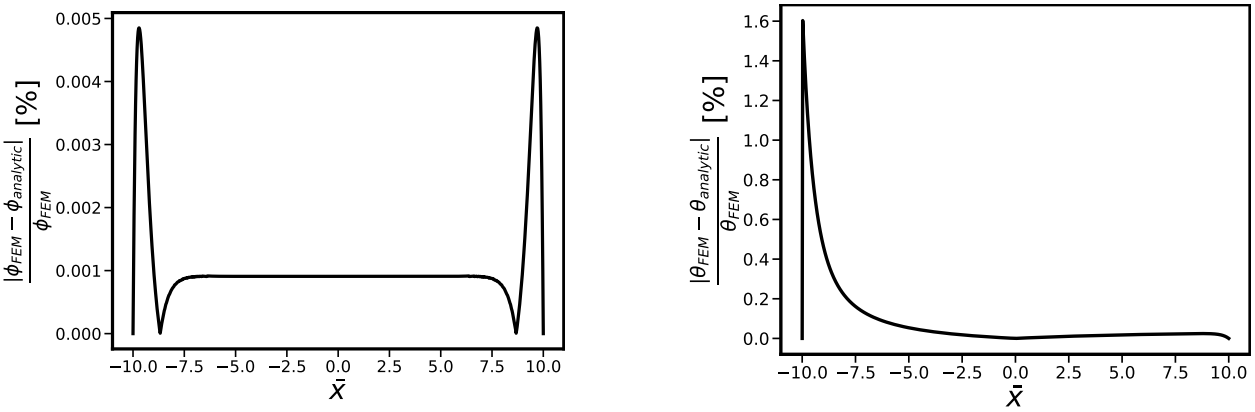

Figure 4.7: *Relative difference between the analytical and FEM solutions of the equilibrium profiles of ϕ and θ in the quadratic regime.*

One can notice in figure 4.6 that

$$|\phi_0'| = \varphi \sim 0 \; \forall x \in \left[-\frac{\ln\left(\frac{\varphi}{B\nu_1}\right)}{\nu_1}, \frac{\ln\left(\frac{\varphi}{A\nu_1}\right)}{\nu_1} \right] \tag{4.64}$$

with $\varphi \ll 1$.
The stability analysis performed in section IV.2.1 found the following system:

$$\begin{pmatrix} \delta\dot{\phi} \\ \delta\dot{\theta} \end{pmatrix} = \underbrace{\begin{pmatrix} -\dfrac{\bar{\alpha}^2k^2+1+\left(\bar{s}\gamma+\bar{\varepsilon}^2\right)(\theta_0')^2}{Q\bar{\eta}_\phi} & \dfrac{-2\phi_0 ik\left(\bar{s}\gamma+\bar{\varepsilon}^2\right)\theta_0'}{Q\bar{\eta}_\phi} \\ \dfrac{2(\bar{\varepsilon}^2+\bar{s}\gamma)(\phi_0\theta_0' ik+\phi_0'\theta_0'+\theta_0''\phi_0)-2P\bar{\eta}_\theta\phi_0\dot{\theta}_0}{P\bar{\eta}_\theta\phi_0^2} & \dfrac{(\bar{\varepsilon}^2+\bar{s}\gamma)\left(-k^2\phi_0^2+2\phi_0'\phi_0 ik\right)}{P\bar{\eta}_\theta\phi_0^2} \end{pmatrix}}_{M} \cdot \begin{pmatrix} \delta\phi \\ \delta\theta \end{pmatrix} \tag{4.65}$$

The interval $[-L,L]$ is split into two parts: $\left[-L, -\frac{\ln\left(\frac{\varphi}{B\nu_1}\right)}{\nu_1}\right] \cup \left[\frac{\ln\left(\frac{\varphi}{A\nu_1}\right)}{\nu_1}, L\right]$ and $\left[-\frac{\ln\left(\frac{\varphi}{B\nu_1}\right)}{\nu_1}, \frac{\ln\left(\frac{\varphi}{A\nu_1}\right)}{\nu_1}\right]$.

Let us first consider $x \in \left[-\frac{\ln\left(\frac{\varphi}{Bv_2}\right)}{v_2}, \frac{\ln\left(\frac{\varphi}{Av_1}\right)}{v_1} \right]$, thus $\phi_0' \sim 0$ and $\phi_0 \sim$ constant. We then have:

$$\begin{pmatrix} \delta\dot{\phi} \\ \delta\dot{\theta} \end{pmatrix} = \begin{pmatrix} -\frac{\bar{\alpha}^2 k^2 + 1 + \left(\bar{s}\gamma + \bar{\varepsilon}^2\right) K^2}{Q\bar{\eta}_\phi} & \frac{-2ik\left(\bar{s}\gamma + \bar{\varepsilon}^2\right) K}{Q\bar{\eta}_\phi} \\ \frac{2ik\left(\bar{s}\gamma + \bar{\varepsilon}^2\right) K}{P\bar{\eta}_\theta} & \frac{-k^2(\bar{\varepsilon}^2 + \bar{s}\gamma)}{P\bar{\eta}_\theta} \end{pmatrix} \cdot \begin{pmatrix} \delta\phi \\ \delta\theta \end{pmatrix} \tag{4.66}$$

which corresponds to the system found in equation 4.22. With the parameters used for the simulations in figure 4.6, it is found that $K < K_{lim}$, meaning that no instability occurs according to this analysis. The FEM solution indeed found no evolution of the equilibrium configuration, which corroborates the linear stability analysis.

Let us now consider $x \in \left[-L, -\frac{\ln\left(\frac{\varphi}{Bv_1}\right)}{v_1} \right] \cup \left[\frac{\ln\left(\frac{\varphi}{Av_1}\right)}{v_1}, L \right]$, such that $\phi_0' = Av_1 \exp(v_1 x) - Bv_1 \exp(-v_1 x)$.

The discriminant being complex, we look for $z \in \mathbb{C}$ such that $z^2 = \Delta$. Let a and b be the real and imaginary parts of z whereas x, y denote those of Δ. We obtain:

$$a^2 - b^2 = x, \quad 2ab = y, \quad a^2 + b^2 = \sqrt{x^2 + y^2} \tag{4.67}$$

We find:

$$a = \pm\sqrt{\frac{x + \sqrt{x^2 + y^2}}{2}}, \quad b = \pm\sqrt{\frac{-x + \sqrt{x^2 + y^2}}{2}} \tag{4.68}$$

The sign of a and b is obtained from the equation $2ab = xy$:

$$\text{if } y \geq 0 : \ a \geq 0,\ b \geq 0, \quad \text{else} \ : \ a \geq 0,\ b \leq 0 \tag{4.69}$$

The eigenvalues are then given by:

$$\lambda = \frac{\mathrm{Tr}(M) \pm z}{2} \tag{4.70}$$

Due to the mathematical cumbersomeness of the expanded form of this solution, the eigenvalues are only computed numerically. The $\lambda - k$ curve is plotted in figure 4.8 at the point $\bar{x} = 9.8$. Similarly to the case studied in section IV.2.1, there seems to be a threshold value of the orientation gradient K required to give rise to a domain of instability. Note that this domain is different from the one found for $x \in \left[-\frac{\ln\left(\frac{\varphi}{Bv_2}\right)}{v_2}, \frac{\ln\left(\frac{\varphi}{Av_1}\right)}{v_1} \right]$.

IV.2.4 Influence of the equilibrium solution: Non-quadratic regime

A similar investigation to the one performed in section IV.2.3 is then carried out for the non-quadratic regime. We look for $\phi(\bar{x})$ such that:

$$\bar{\alpha}^2 \phi'' - (1 + \bar{\varepsilon}^2 K^2 + 2\bar{s}\,\epsilon\, K)\phi + 1 = 0 \tag{4.71}$$

The solution is then

$$\phi(x) = A\exp(v_1 x) + B\exp(-v_1 x) + \frac{1}{1 + \bar{\varepsilon}^2 K^2 + 2\bar{s}\,\epsilon\, K} \tag{4.72}$$

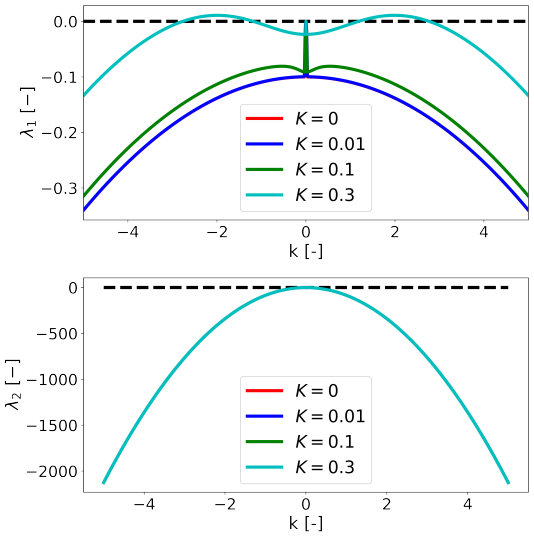

Figure 4.8: *Eigenvalues as a function of the wavenumber for the near equilibrium solution in the quadratic regime.*

with

$$\nu_1 = \frac{\sqrt{1+\bar{\varepsilon}^2K^2+2\bar{s}\,\epsilon\,K}}{\bar{\alpha}} \tag{4.73}$$

$$A = \frac{1-\frac{1}{1+\bar{\varepsilon}^2K^2+2\bar{s}\epsilon K}-B\exp(-\nu_1 L)}{\exp(\nu_1 L)} \tag{4.74}$$

$$B = \frac{(\exp(\nu_1 L)-1)\left(1-\frac{1}{1+\bar{\varepsilon}^2K^2+2\bar{s}\epsilon K}\right)}{2\sinh(2\nu_1 L)} \tag{4.75}$$

This analytical solution is compared to the one obtained with the FEM by imposing $\theta = K\bar{x}\ \forall x \in [-L, L]$ (figure 4.9). The two solutions match fairly well with each other.

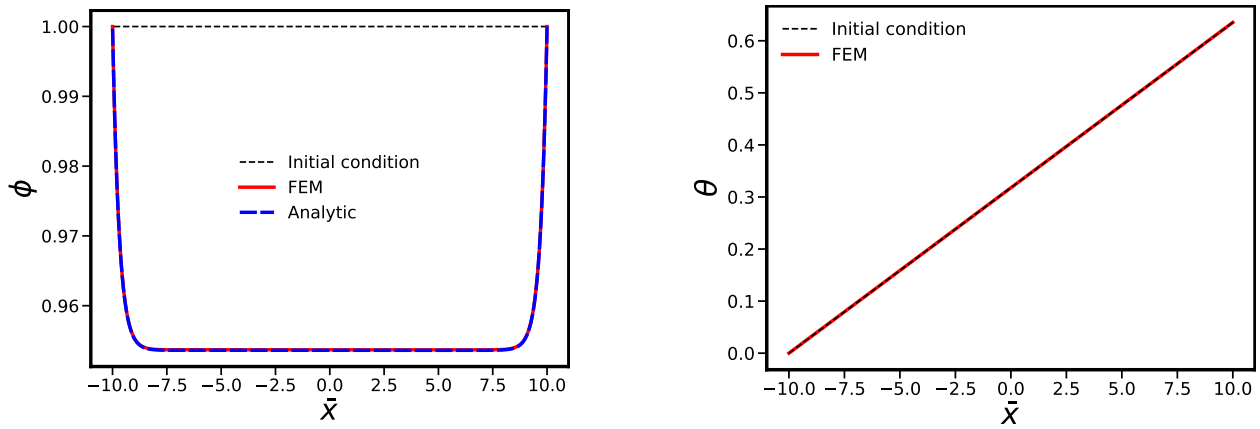

Figure 4.9: *Comparison of the analytical and FEM solutions of the equilibrium profile of $\phi(x)$ for an imposed $\theta(\bar{x}) = K\bar{x}$.*

One can notice in figure 4.9 that

$$\phi_0' = \varphi \sim 0 \; \forall x \in \left[-\frac{\ln\left(\frac{\varphi}{Bv_1}\right)}{v_1}, \frac{\ln\left(\frac{\varphi}{Av_1}\right)}{v_1} \right] \tag{4.76}$$

with $\varphi \ll 1$.

The stability analysis performed in section IV.2.2 found the following system:

$$\begin{pmatrix} \delta\dot{\phi} \\ \delta\dot{\theta} \end{pmatrix} = \begin{pmatrix} -\frac{\bar{\alpha}^2k^2 + 1 + 2\bar{s}\,\epsilon\,\theta_0' + \bar{\varepsilon}^2(\theta_0')^2}{Q\bar{\eta}_\phi} & \frac{-2\phi_0 ik(\bar{s}\,\epsilon + \bar{\varepsilon}^2\theta_0')}{Q\bar{\eta}_\phi} \\ \frac{-2P\bar{\eta}_\theta\phi_0\dot{\theta}_0 + 2\bar{\varepsilon}^2[\phi_0'\theta_0' + \phi_0\theta_0''] + 2\bar{s}\,\epsilon\,\phi_0' + 2\phi_0 ik(\bar{s}\,\epsilon + \bar{\varepsilon}^2\theta_0')}{P\bar{\eta}_\theta\phi_0^2} & \frac{2\bar{\varepsilon}^2\phi_0\phi_0' ik - \bar{\varepsilon}^2k^2}{P\bar{\eta}_\theta} \end{pmatrix} \cdot \begin{pmatrix} \delta\phi \\ \delta\theta \end{pmatrix} \tag{4.77}$$

which in this case becomes:

$$\begin{pmatrix} \delta\dot{\phi} \\ \delta\dot{\theta} \end{pmatrix} = \begin{pmatrix} -\frac{\bar{\alpha}^2k^2 + 1 + 2\bar{s}\,\epsilon\,K + \bar{\varepsilon}^2K^2}{Q\bar{\eta}_\phi} & \frac{-2\phi_0 ik(\bar{s}\,\epsilon + \bar{\varepsilon}^2K)}{Q\bar{\eta}_\phi} \\ \frac{2\bar{\varepsilon}^2\phi_0'K + 2\bar{s}\,\epsilon\,\phi_0' + 2\phi_0 ik(\bar{s}\,\epsilon + \bar{\varepsilon}^2K)}{P\bar{\eta}_\theta\phi_0^2} & \frac{2\bar{\varepsilon}^2\phi_0\phi_0' ik - \bar{\varepsilon}^2k^2\phi_0^2}{P\bar{\eta}_\theta\phi_0^2} \end{pmatrix} \cdot \begin{pmatrix} \delta\phi \\ \delta\theta \end{pmatrix} \tag{4.78}$$

The interval $[-L, L]$ is split into two parts: $\left[-L, -\frac{\ln\left(\frac{\varphi}{Bv_1}\right)}{v_1}\right] \cup \left[\frac{\ln\left(\frac{\varphi}{Av_1}\right)}{v_1}, L\right]$ and $\left[-\frac{\ln\left(\frac{\varphi}{Bv_1}\right)}{v_1}, \frac{\ln\left(\frac{\varphi}{Av_1}\right)}{v_1}\right]$.

Let us first consider $x \in \left[-\frac{\ln\left(\frac{\varphi}{Bv_1}\right)}{v_2}, \frac{\ln\left(\frac{\varphi}{Av_1}\right)}{v_1}\right]$, thus $\phi_0' \sim 0$ and $\phi_0 \sim$ constant. We then have:

$$\begin{pmatrix} \delta\dot{\phi} \\ \delta\dot{\theta} \end{pmatrix} = \begin{pmatrix} -\frac{\bar{\alpha}^2k^2 + 1 + 2\bar{s}\,\epsilon\,K + \bar{\varepsilon}^2K^2}{Q\bar{\eta}_\phi} & \frac{-2\phi_0 ik(\bar{s}\,\epsilon + \bar{\varepsilon}^2K)}{Q\bar{\eta}_\phi} \\ \frac{2\phi_0 ik(\bar{s}\,\epsilon + \bar{\varepsilon}^2K)}{P\bar{\eta}_\theta\phi_0^2} & \frac{-\bar{\varepsilon}^2k^2}{P\bar{\eta}_\theta} \end{pmatrix} \cdot \begin{pmatrix} \delta\phi \\ \delta\theta \end{pmatrix} \tag{4.79}$$

which corresponds to the system found in eq. 4.41.

Now considering $\bar{x} = 9.8$ such that $x \in \left[-L, -\frac{\ln\left(\frac{\varphi}{Bv_1}\right)}{v_1}\right] \cup \left[\frac{\ln\left(\frac{\varphi}{Av_1}\right)}{v_1}, L\right]$, the $\lambda - k$ curve is plotted in figure 4.10. The results are rather similar to those obtained for $x \in \left[-\frac{\ln\left(\frac{\varphi}{Bv_1}\right)}{v_2}, \frac{\ln\left(\frac{\varphi}{Av_1}\right)}{v_1}\right]$ as the term ϕ_0' becomes non negligible for somewhat large values of K.

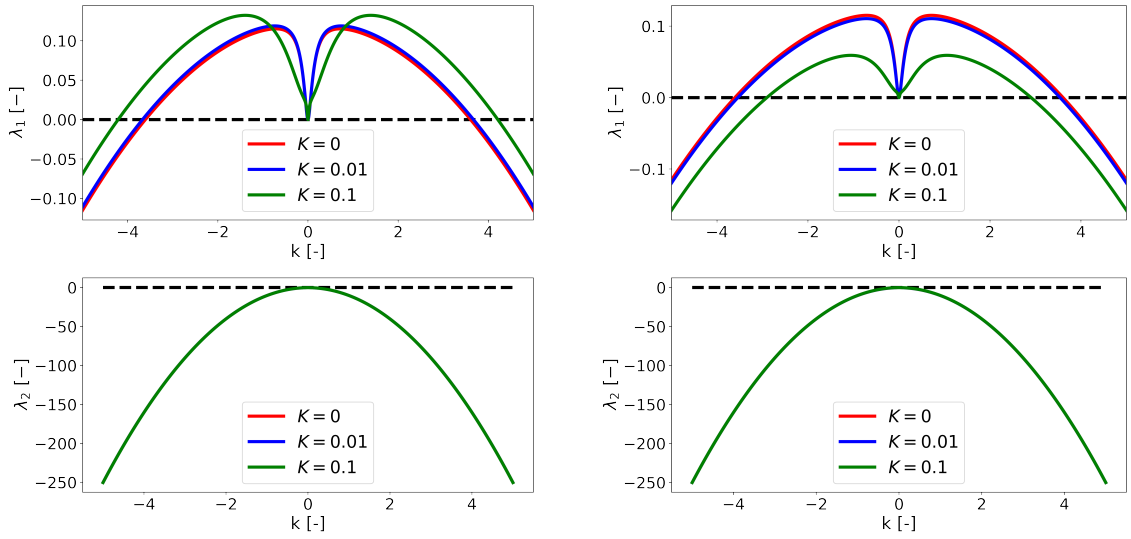

$\epsilon = 1$ $\epsilon = -1$

Figure 4.10: *Eiegenvalues as functions of the wavenumber for the near equilibrium solution in the non-quadratic regime.*

IV.3 Stability of lattice curvature fields: numerical study

In this section the capability of the KWC model to handle grain nucleation in single crystals is assessed numerically using the finite element method. To this end several nucleation cases due to orientation gradients are studied, accounting for different initial and boundary conditions.

IV.3.1 Uniform orientation gradient

The first configuration considered is that of a spatially uniform initial orientation gradient in a single crystal of total length $2L = 20$. These initial conditions (IC) are summarized in Eq. (4.80) with $\Delta\theta = 0.3$. They describe a uniform orientation gradient of $\nabla\theta = \dfrac{\Delta\theta}{2\bar{L}} = \dfrac{0.3}{20} = 0.015\mu m^{-1}$, which, using Nye's formula, corresponds to a GND density of $\rho_{GND} = \dfrac{\nabla\theta}{b} = \dfrac{0.015}{0.2556\times 10^{-3}} \simeq 58.7\times 10^{12} m^{-2}$. Note that the initial uniform field $\phi = 1$ is not in equilibrium in the orientation gradient field.

Dirichlet boundary conditions (BC) are imposed on the left and right edges of the domain for the phase field and the orientation field (Eq. (4.81)). This type of boundary condition for θ enforces the presence of a lattice orientation gradient. Alternatively, zero flux Neumann BC can be prescribed. Multiple point constraints are also enforced at the top and bottom edges to ensure periodicity along the vertical direction.

$$\text{IC:} \begin{cases} \theta(\bar{t}=0,\bar{x}) = \Delta\theta\dfrac{\bar{x}+\bar{L}}{2\bar{L}} \\ \phi(\bar{t}=0,\bar{x}) = 1 \end{cases} \tag{4.80}$$

$$\text{BC:} \begin{cases} \theta(\bar{t},\bar{x}=-\bar{L}) = 0, \quad \theta(\bar{t},\bar{x}=\bar{L}) = \Delta\theta \\ \phi(\bar{t},\bar{x}=-\bar{L}) = \phi(\bar{t},\bar{x}=\bar{L}) = 1 \\ \textbf{or} \\ \underline{\bar{\xi}}_{\phi}(\bar{t},\bar{x}=-\bar{L})\cdot\underline{n} = \underline{\bar{\xi}}_{\phi}(\bar{t},\bar{x}=\bar{L})\cdot\underline{n} = 0 \end{cases} \tag{4.81}$$

Unless specified, all simulations are conducted with the parameters listed in Table 4.2.

Parameter	$\bar{\alpha}$	$\bar{s}$	$\bar{\varepsilon}$	$\bar{\eta}_\phi$	$\bar{\eta}_\theta$	$\bar{\mu}_p$	β_p	C_D	$\bar{C}_1$	$\bar{\gamma}$	γ_g
Value	0.31	0.75	1	10	0.1	10^6	10^2	100	1	10^4	10^{-4}

Table 4.2: *Model parameters used in the simulations with the KWC model.*

IV.3.1.1 Nucleation process

The nucleation process is first studied in the case of Dirichlet boundary conditions prescribed for both ϕ and θ. The profiles of ϕ and θ are plotted at different times in Fig. 4.11. First, as can be seen in Fig. 4.11a, the crystal order field reaches its equilibrium value around $\bar{t} = 100$ and grain boundaries begin to form near the left and right boundaries. At $\bar{t} = 350$, fluctuations of the order and orientation fields are observed in the linear central zone. These fluctuations reveal the unstable character of the linear orientation distribution. Next, the linear profile of the lattice orientation splits into a series of piece-wise constant regions that can be interpreted as subgrains with low angle grain boundaries. Initially, the distance between the neighboring grain boundaries is smaller than ℓ_ϕ. Consequently, the exponential tails of the phase field profiles of neighboring grains interact strongly and the subgrains merge to form grains with larger misorientations (Fig. 4.11c). The process evolves toward well separated grains with larger misorientations (Fig. 4.11d). The interfaces considered here are flat so that the observed motion of low angle grain boundaries is not due to GB curvature nor stored energy. The coalescence results from the overlap of the diffuse grain boundary regions of neighboring newly formed grains. Thus, the interface width ℓ_ϕ imposes a constraint on the maximum number of grains N that can be nucleated along the initial single crystal of total length $2\bar{L}$: $N < 2\bar{L}/\ell_\phi$.

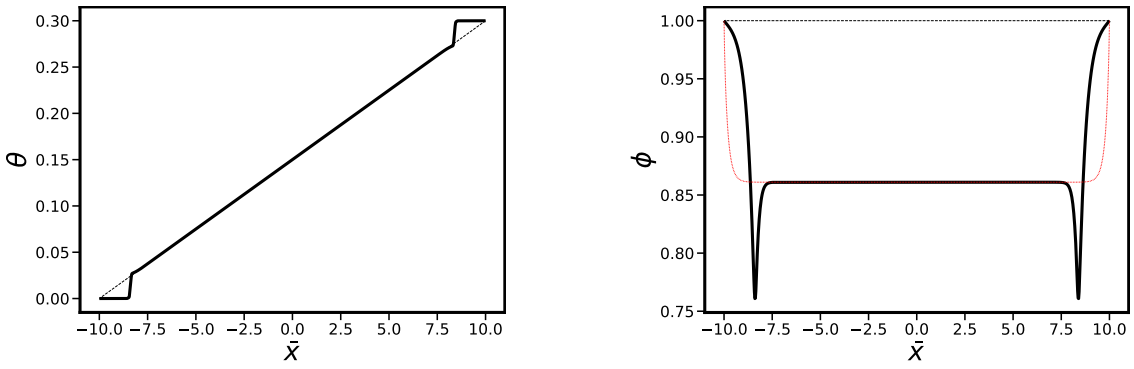

(a) $\bar{t} = 100$

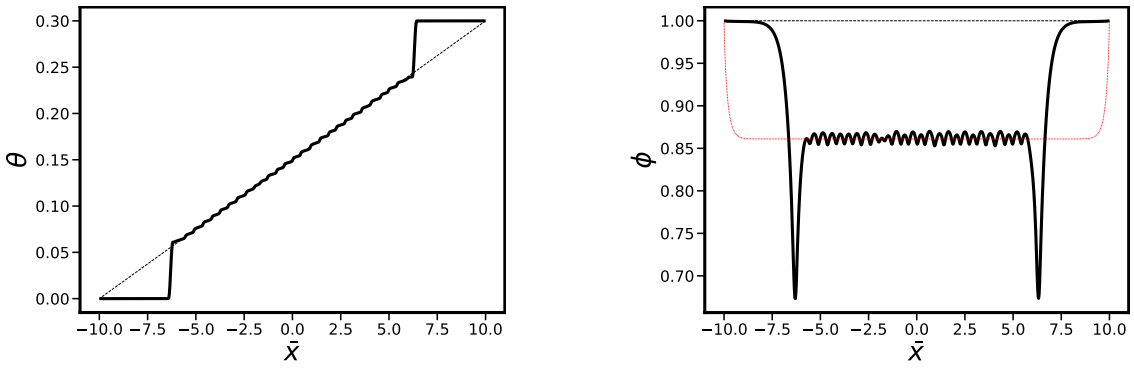

(b) $\bar{t} = 350$

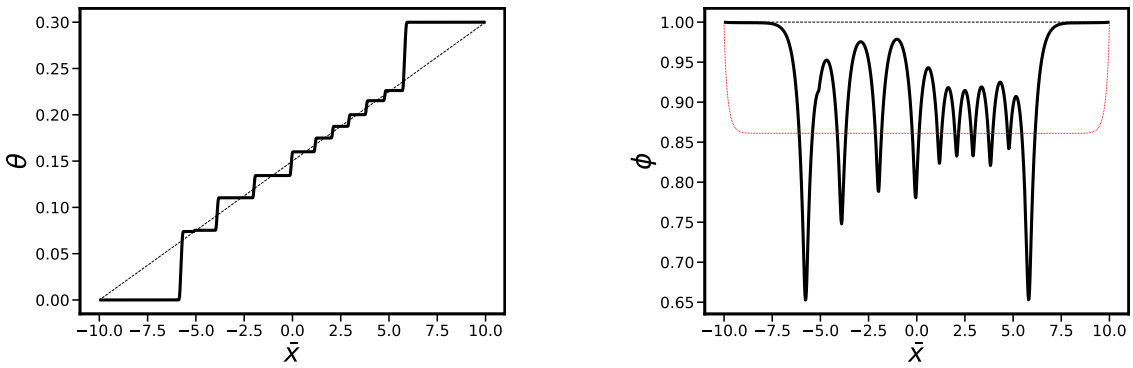

(c) $\bar{t} = 600$

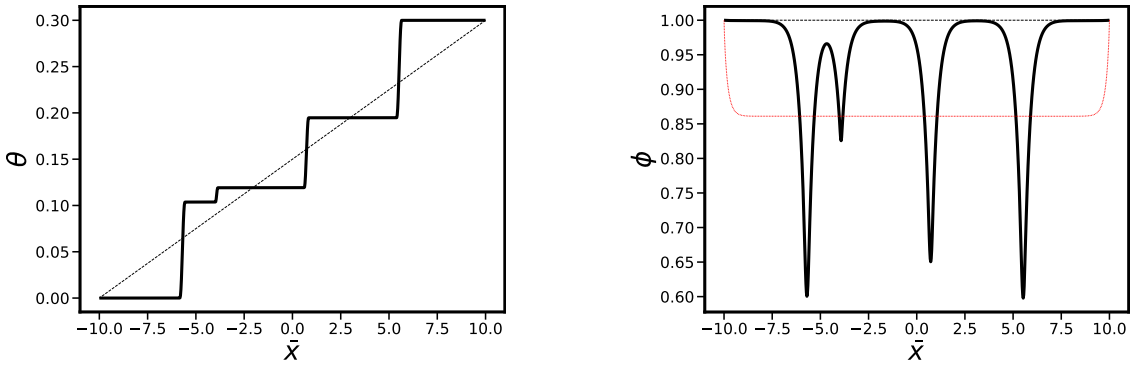

(d) $\bar{t} = 10000$

Figure 4.11: *Snapshots at different times $\bar{t}$ of the θ (left) and ϕ (right) profiles for a single crystal subjected to an initial uniform orientation gradient. The initial conditions are indicated by thin black dashed lines. The phase field ϕ at equilibrium with respect to a linear orientation field prescribed at all points is represented by thin red dotted lines.*

IV.3.1.2 Effect of boundary conditions

The evaluation of boundary conditions for ϕ at the left and right edges is presented. Either Dirichlet or zero flux boundary conditions are applied. Dirichlet boundary conditions for θ are enforced in both cases. The results are shown in figure 4.12. It can be seen that nucleation proceeds in a similar way, with equilibration of the crystal order field, the emergence and propagation of fluctuations leading to subgrain formation, and finally the formation of grains with increased misorientation due to subgrain merging. The main difference lies in the early stage of the process. Indeed, when Neumann BC are prescribed, the crystal order field is not constrained at the left and right boundaries. The decrease of ϕ is therefore homogeneous in the whole domain, contrary to the situation when Dirichlet BC are imposed.

IV.3.1.3 Influence of $g(\phi)$ and the mobility function

Dirichlet boundary conditions for both phase-fields have been arbitrarily chosen for the following simulations. The influence of the selected mobility function $P(\nabla\theta)$ (given by Eq. 3.21) and $g(\phi)$ (Eq . 3.4) is then evaluated. It should be reminded that it was suggested by Warren et al. [2003] to choose either $g(\phi) = \phi^2$ or $g(\phi) = -2(\log(1-\phi)+\phi)$, the choice of the latter being motivated by a grain boundary energy that is mathematically closer to a Read-Schockley model. As for P, it should be noted that, depending on its mathematical expression, it can differentiate the behaviour in the bulk from that at the grain boundary, potentially inhibiting spurious rotation. Specifically, when $P = 1$, both rotation and shrinkage can occur for a circular grain embedded in a larger matrix, whereas using the expression given by Eq. 3.21, only shrinkage may occur. Fig. 4.13 illustrates the impact of g and P selection on nucleation behavior. When P remains

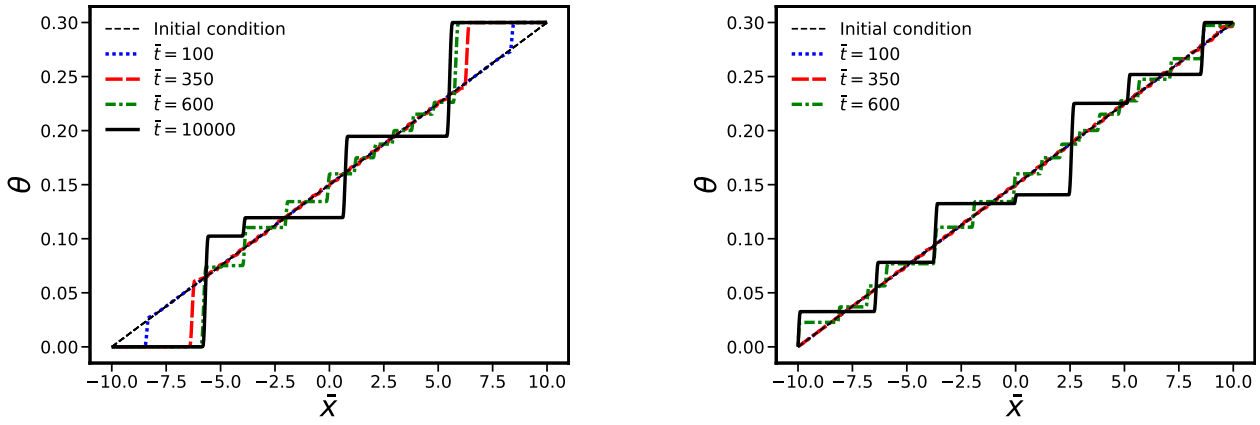

(a) *Profile of θ for Dirichlet (left) and Neumann zero flux (right) boundary conditions.*

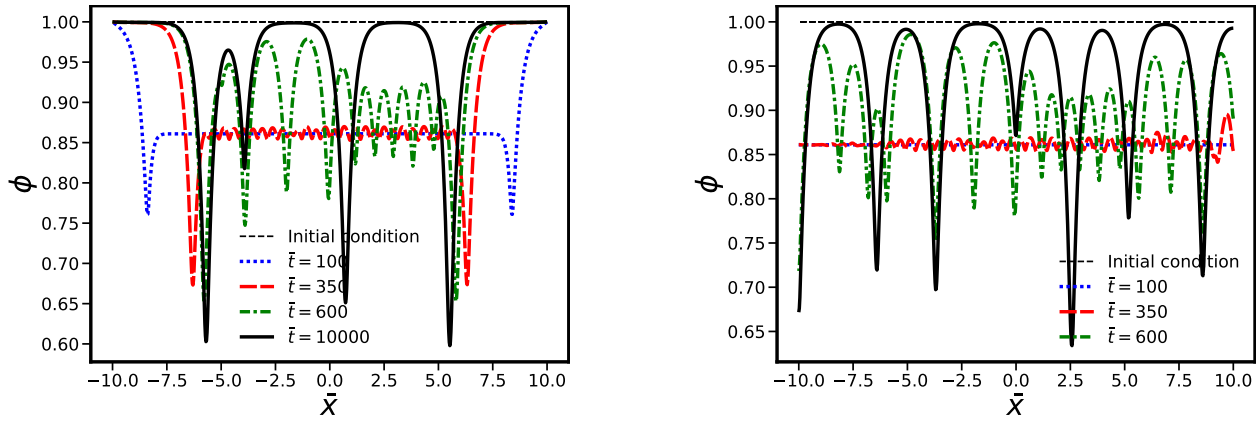

(b) *Profile of ϕ for Dirichlet (left) and Neumann zero flux (right) boundary conditions.*

Figure 4.12: *Profiles of ϕ and θ for Dirichlet (left) or Neumann zero flux (right) boundary conditions for ϕ during nucleation in a single crystal subjected to a uniform initial orientation gradient. Dirichlet BC are imposed on θ in both instances.*

constant, a bicrystal nucleates regardless of the choice of g. Conversely, utilizing $P(\nabla\theta)$ results in multiple grain nucleation for a logarithmic $g(\phi)$ while nucleation is visibly postponed when $g(\phi) = \phi^2$. Thus, selecting a logarithmic form of $g(\phi)$ together with $P(\nabla\theta)$ not only avoids spurious rotations and aligns well with a Read-Shockley energy, but also facilitates the nucleation of more grains. Therefore, it will be adopted from now on.

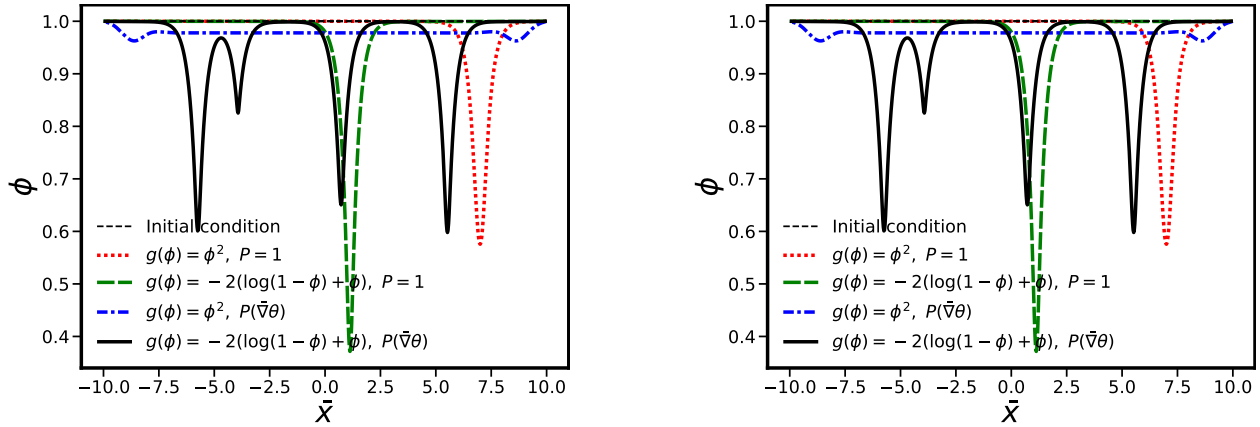

Figure 4.13: *profiles of ϕ and θ at $\bar{t} = 10000$ for different combinations of $g(\phi)$ and inverse mobility function P.*

IV.3.1.4 Effect of the magnitude of the orientation gradient

To assess the existence of a threshold of the orientation gradient to trigger nucleation in the KWC model, simulations were performed with different magnitudes of the orientation gradient $\Delta\theta \in \{0.01, 0.3, 0.6\}$. As can be seen in Fig. 4.14, it appears that (sub)grains are nucleated even for very low orientation gradients. Furthermore, as expected from the analysis in [Lobkovsky and Warren, 2001], the misorientation between grains as well as the minimum value of ϕ are found to depend on the value of the initial orientation gradient.

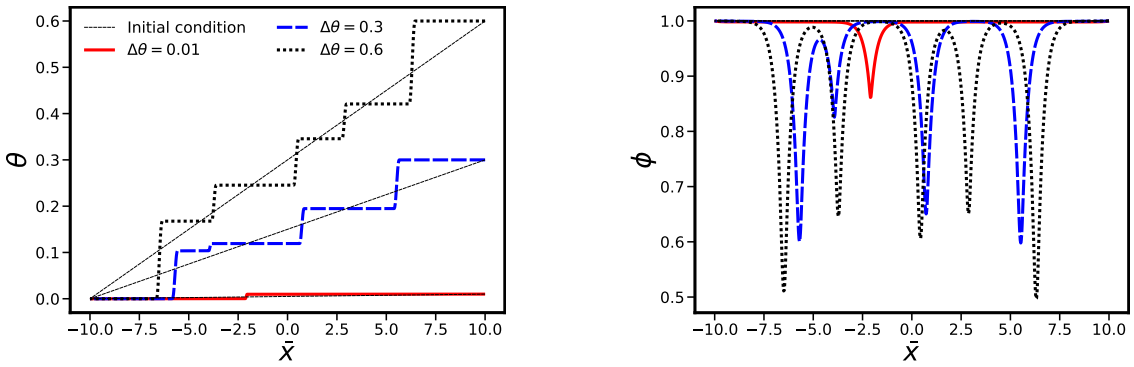

Figure 4.14: *Profiles of θ (left) and ϕ (right) at $\bar{t} = 10000$ for single crystals with initial homogeneous orientation gradients of different magnitudes.*

IV.3.1.5 Nucleation statistics and time evolution of the total energy

A study of the time evolution of the microstructure was carried out by following the evolution of indicators for $\bar{t} \in [0, 10^7]$ with data acquisition every 1000 increment of $\bar{t}$. At each time steps, we have collected the sets of values of (i) ϕ at the cusps defining the very center of the grain (sub-)boundaries, noted $\min(\phi)$; (ii) misorientation defined as the amplitude of the local jump of θ, noted $\Delta\theta$; (iii) the number and (iv) the size of the grains defined by the segments in the θ profiles where $\bar{\nabla}\theta$ is below 10^{-4}. The average, the minimum and the maximum in these sets are plotted in Fig. 6 with solid black, blue and red lines respectively. The grey filling spans the interval [average $\pm$ standard deviation] for the considered quantity at time $\bar{t}$. Grains are defined as regions with uniform orientations. From Fig. 4.15a and 4.15b it is clear that the single crystal is rapidly fragmented into a large number of very small grains which then merge to form fewer and larger grains until only a bicrystal remains as $\bar{t} \to \infty$. This phenomenon is due to the Dirichlet boundary conditions which force the existence of a lattice orientation gradient. However, if zero flux boundary conditions were imposed for θ, the final state would be a single crystal, as this is the configuration with the lowest total energy due to the absence of interfaces. In Fig. 4.15c the minimum value of ϕ decreases globally as grains are merging, increasing the misorientation as seen in Fig. 4.15d. The peaks in the maximum value of $\min(\phi)$ (blue curve) are associated with these mergers: when two grains merge, the misorientation between them decreases, resulting in less deep ϕ cusps.

In the case of an initial uniform gradient of θ with a sine perturbation with period $\bar{\lambda} = 1$ and $\bar{\lambda} \to \infty$ (no perturbation), the time evolution of the total energy, computed numerically by integrating the free energy density over the whole domain, is also shown in Fig. 4.16. This confirms that the nucleation and merger processes due to orientation gradients lead to a global decrease in the total energy of the system. This is expected since the evolution equations of the KWC model are based on a minimization of the total energy. This also explains why, between $\bar{t} = 6 \times 10^5$ and $\bar{t} = 1.5 \times 10^6$, the tri-crystal slowly reorients towards the more energetically favorable bicrystal. Note that energy of the final state corresponds to the grain boundary energy calculated with the matched asymptotics analysis of Lobkovsky and Warren [2001] that is briefly recalled in III.2.2.2.

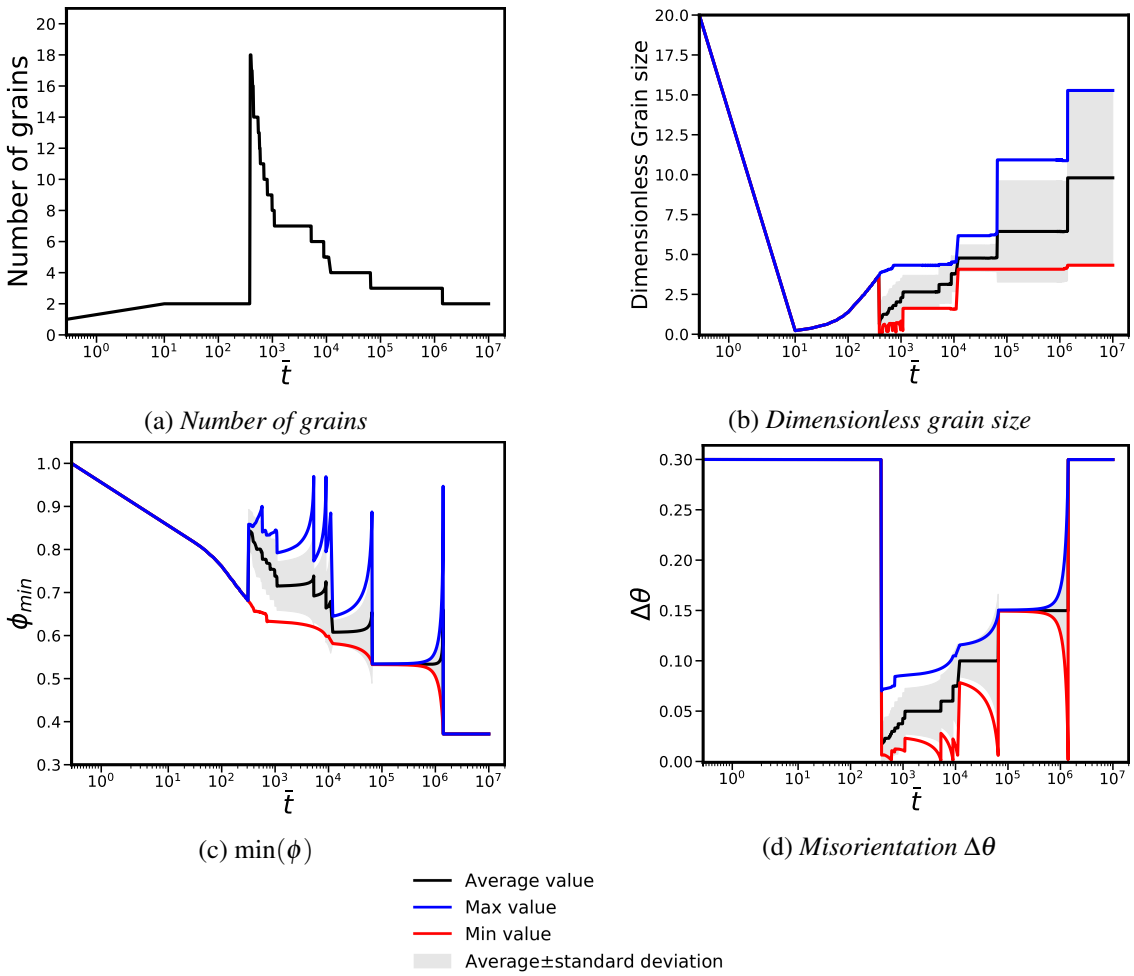

(a) *Number of grains* (b) *Dimensionless grain size*

(c) $\min(\phi)$ (d) *Misorientation* $\Delta\theta$

Figure 4.15: *Time evolution of the number of grains (top left), dimensionless grain size (top right) as well as minimum value of* ϕ *(bottom left) and misorientation* $\Delta\theta$ *(bottom right) for a single crystal subjected to a uniform orientation gradient with the KWC model.*

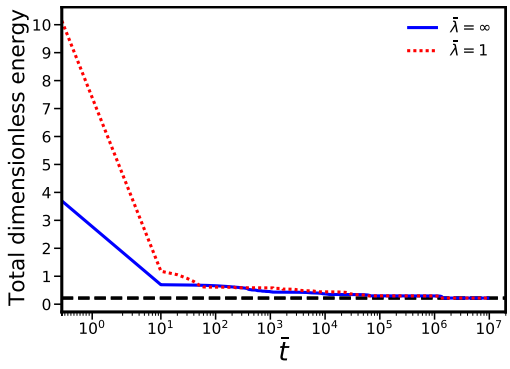

Figure 4.16: *Time evolution of the total dimensionless energy for a single crystal subjected to an initial uniform orientation gradient with a sinusoidal perturbation of period* $\bar{\lambda}$*. The horizontal dashed line corresponds to the grain boundary energy of a bicrystal computed with the asymptotic analysis of Lobkovsky and Warren [2001].*

IV.3.2 Orientation gradient with a perturbation

IV.3.2.1 Sinusoidal perturbation of an initially uniform orientation gradient

The initial condition on the orientation field is now modified by adding a sinusoidal perturbation of spatial period $\bar{\lambda}$ and amplitude A:

$$\text{IC:} \begin{cases} \theta(\bar{t}=0,\bar{x}) = \Delta\theta \dfrac{\bar{x}+\bar{L}}{2\bar{L}} + A\sin\left(\dfrac{2\pi}{\bar{\lambda}}\bar{x}\right) \\ \phi(\bar{t}=0,\bar{x}) = 1 \end{cases} \tag{4.82}$$

Fig. 4.17

shows the profiles of ϕ and θ for two values of the perturbation spatial period. It can be seen that the fluctuations of θ are captured by ϕ and the number of grains initially nucleated depends on $\bar{\lambda}$. However, the resulting microstructure exhibits overlapping diffuse grain boundaries that tend to coalesce. As in section IV.3.1.1 the width of the diffuse grain boundary zone for ϕ therefore sets a maximum value for the final number of grains.

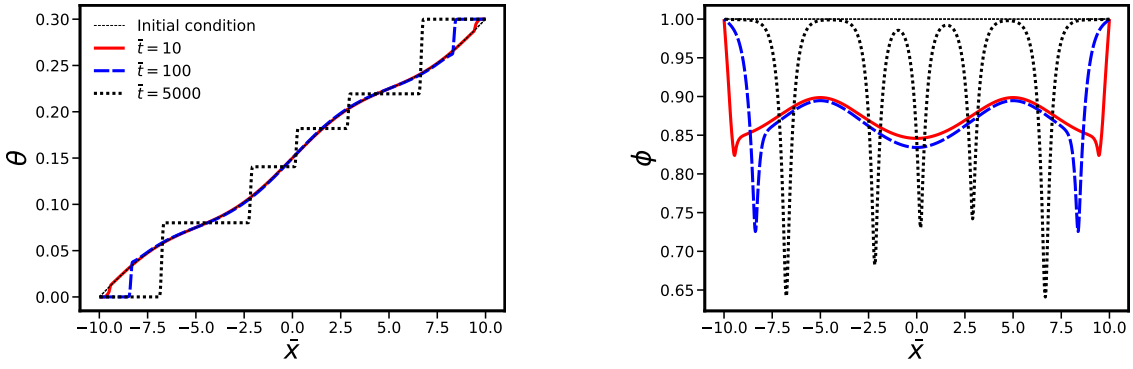

(a) $\bar{\lambda} = 10$

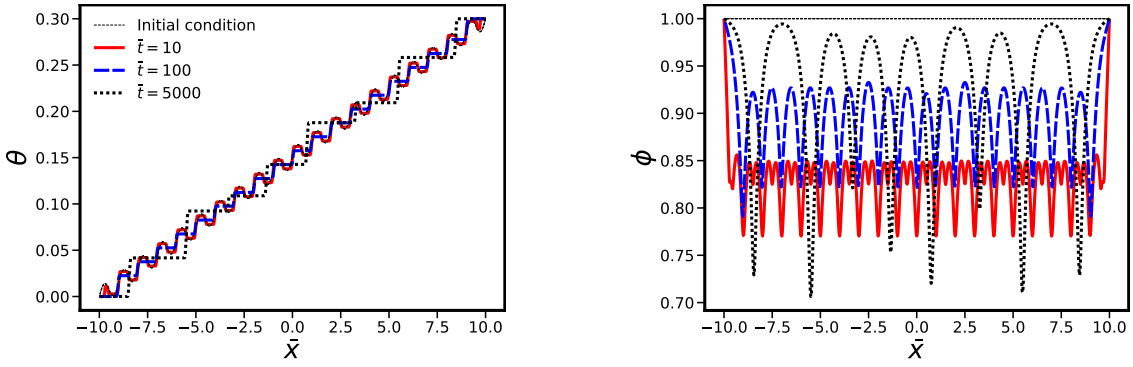

(c) $\bar{\lambda} = 1$

Figure 4.17: *Profiles of θ (left) and ϕ (right) for a single crystal with an initial orientation gradient with a sinusoidal perturbation of spatial period (a) $\bar{\lambda} = 10$, (b) $\bar{\lambda} = 1$ and amplitude $A = 0.01$.*

IV.3.2.2 Sinusoidal perturbation of a 0-average valued initial orientation gradient

A different initial condition for the orientation is then prescribed in the form of a fluctuation with 0 average value:

$$\theta(\bar{t}=0,\bar{x}) = A\sin\left(\frac{\pi}{L}x+\frac{\pi}{2}\right) \tag{4.83}$$

Periodicity is enforced for both ϕ and θ at the top/bottom and left/right edges. Several combinations of $g(\phi)$ and P are considered in Fig. 4.18. Regardless of the choice of g, nucleation does not occur when P is uniform, in contrast to the situation where a uniform orientation gradient is imposed. However, if P depends on the orientation gradient, nucleation occurs regardless of the choice of g. Interestingly, the process of nucleation appears to be triggered initially in the area with the maximum absolute value of the initial orientation gradient. This is evident from the plots of ϕ at $\bar{t}=10$. This is likely due to the terms $\bar{s}g_{,\phi}|\bar{\nabla}\theta|$ and $\bar{\varepsilon}^2/2|\bar{\nabla}\theta|^2$ included in the evolution equation for ϕ (Eq. 3.19). A similar situation has been examined in the context of KWC-strain gradient plasticity by Admal et al. [2018]. A rectangular single crystal was subjected to sinusoidal vertical displacement, generating a sinusoidal lattice rotation distribution. The bulk dislocations produced during the loading procedure subsequently reorganised into grain boundaries in the regions with the highest lattice orientation gradient values. These simulations therefore show the intrinsic ability of the orientation phase-field models to account for spontaneous (sub)grain nucleation in relation to intragranular lattice orientation gradients.

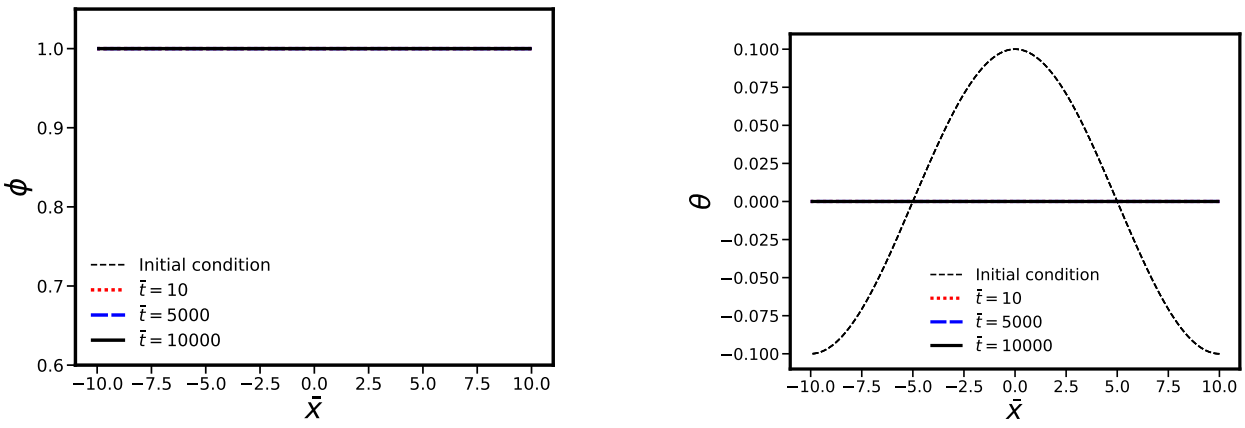

(a) $g(\phi)=\phi^2$, $P=1$

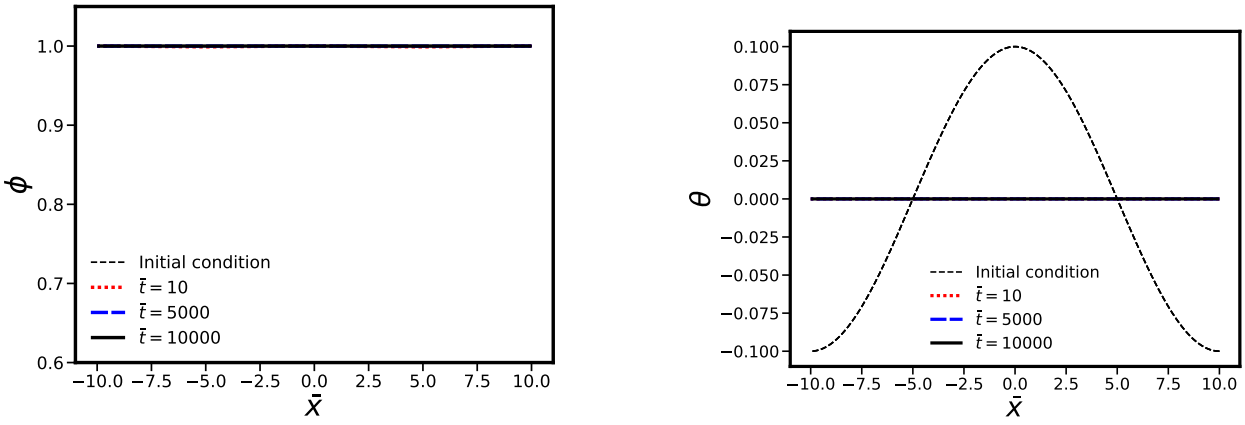

(b) $g(\phi)=-2(\log(1-\phi)+\phi)$, $P=1$

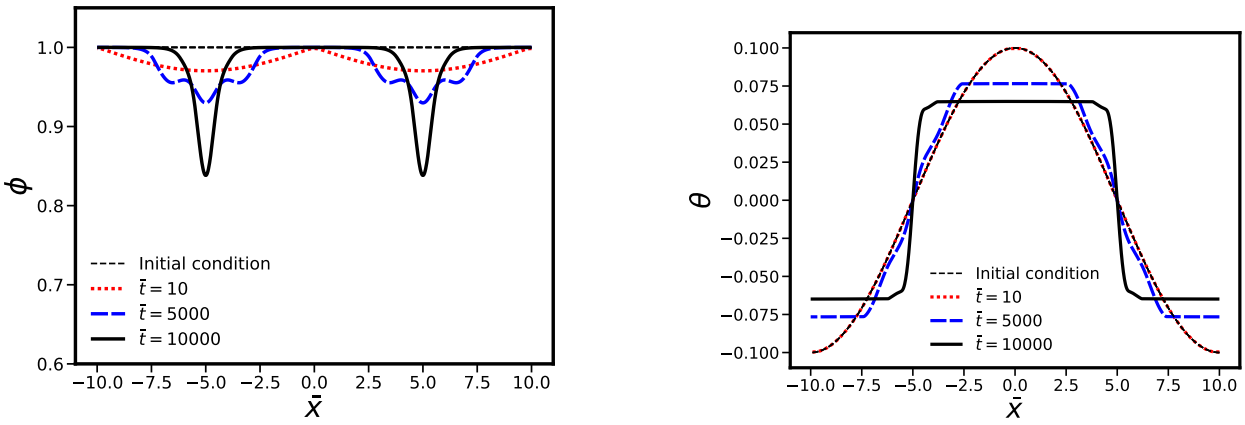

(c) $g(\phi) = \phi^2$, $P(\bar{\nabla}\theta)$

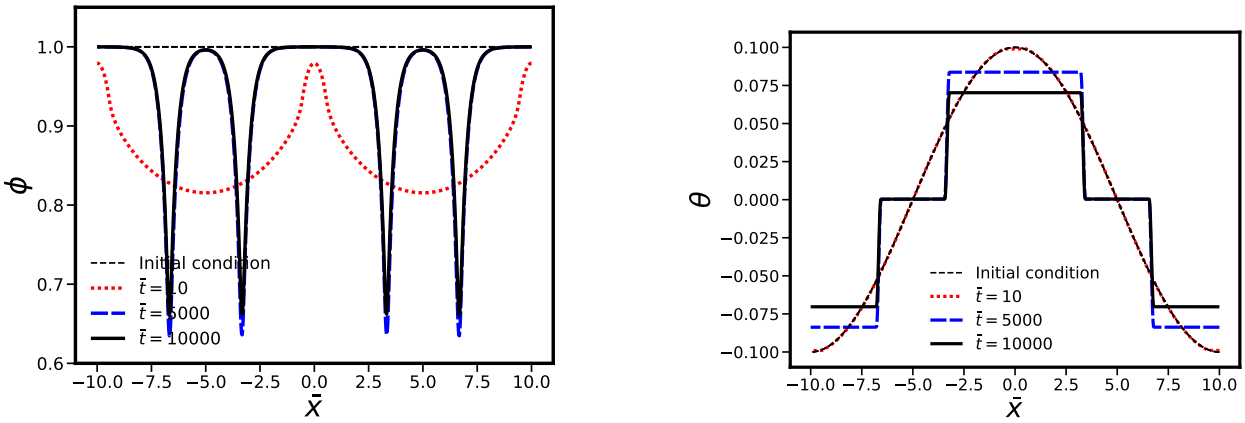

(d) $g(\phi) = -2(\log(1-\phi)+\phi)$, $P(\bar{\nabla}\theta)$

Figure 4.18: *Profiles of ϕ and θ for an initial orientation field with 0 average value and different combinations of $g(\phi)$ and P.*

IV.3.3 Influence of a stored energy gradient

Gradients of stored energy $\bar{E}$ are known to promote GB migration. In this section, we investigate the stability of such a gradient in the KWC-Cosserat medium. In this study, the initial crystal orientation is assumed to be homogeneous. Simultaneous gradients of orientation and stored energy $\bar{E}$ are then considered. The parameters given in table 3.4 are used in all the simulations with $C_D = 100$ and $\bar{C}_A = 1$ to account for full recovery behind the moving grain boundary.

IV.3.3.1 Stability of an SSD density gradient

Similar to section IV.3.1, the effect of a constant SSD-based stored energy gradient on nucleation is studied with the KWC model. For that purpose, a linear profile of slope $\Delta\bar{E}$ is prescribed in a single crystal with a uniform lattice orientation. Zero flux boundary conditions are applied for both ϕ and θ. As shown in Fig. 4.19, no grain has been formed and ϕ simply follows Eq. (3.38) away from the domain boundaries where the boundary conditions impose $\bar{\nabla}\phi \cdot \underline{n} = 0$, $\underline{n}$ being the outward normal vector. The lattice orientation remains uniform and equal to its initial value, meaning that a decrease in the crystal order due to the presence of defects (here the SSD) does not lead to a lattice reorientation. This outcome is to be expected from the KWC evolution equation for θ (Eq. 3.44) as it does not depend on $\bar{\nabla}\phi$. Hence, grain boundaries can be nucleated from an initial state with $\phi = 1$, $\bar{\nabla}\theta \neq 0$ but not with $\bar{\nabla}\theta = 0$, $\bar{\nabla}\phi \neq 0$. To assert this statement, an FEM simulation is carried out. The initial orientation is 0 and the initial crystal order field is that of a bicrystal with misorientation $\Delta\theta = 0.3$. Zero flux BCs are prescribed for θ on the left and right edges while

Dirichlet BCs $\phi = 1$ are enforced. The results plotted in Fig. 4.20 show that the final state is a homogeneous $\phi(\bar{x}) = 1$. This indicates that no grain boundary will nucleate in the absence of orientation gradients.

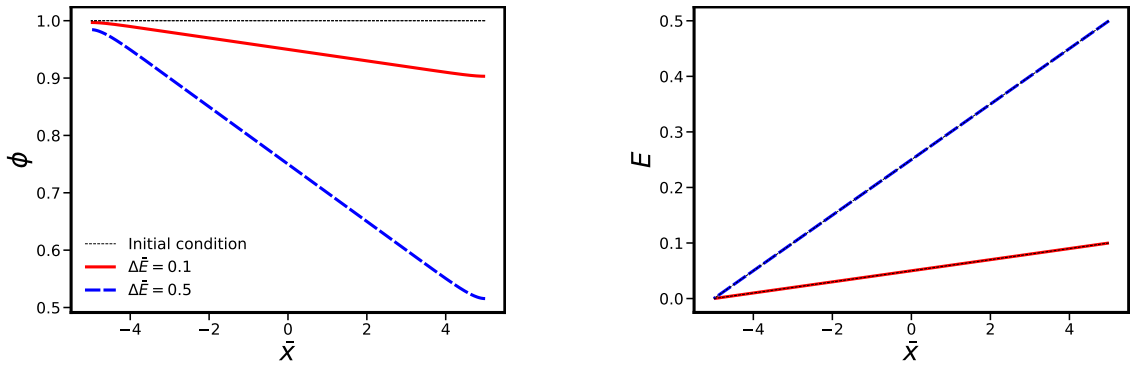

Figure 4.19: *Profiles of ϕ (left) and $\bar{E}$ (right) for a single crystal with uniform initial gradients of stored energy of different magnitudes. The orientation θ is uniform and equal to 0. The simulations are performed with the KWC model.*

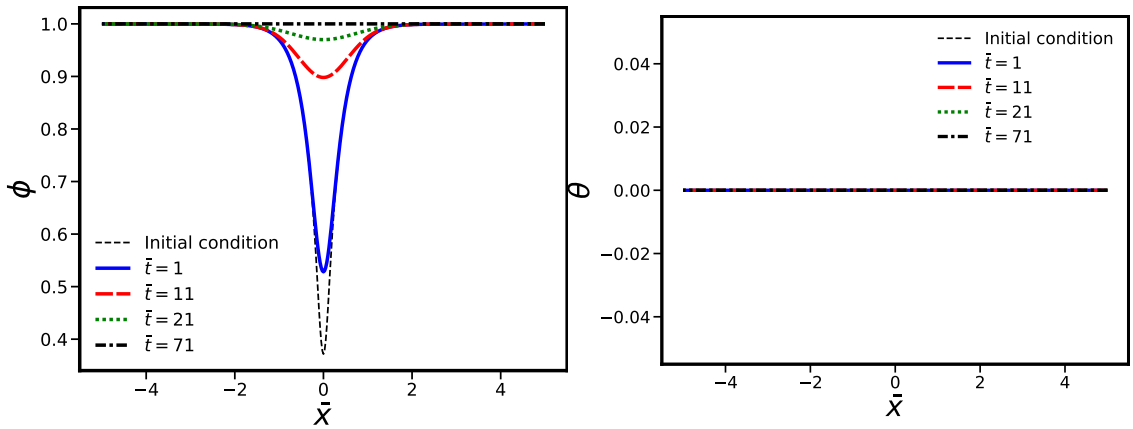

Figure 4.20: *Profiles of ϕ (left) and θ (right) for a microstructure with 0 misorientation and initial crystal order field at equilibrium for a grain boundary with misorientation $\Delta\theta = 0.3$.*

IV.3.3.2 Stability of superimposed SSD and GND density gradients

Now combining uniform initial gradients of both orientation and stored energy, the former triggers grain nucleation whereas the latter provides a driving force for grain boundary motion. Fig. 4.21 shows such simulations with the KWC model comparing the influence of the magnitude of the stored energy gradient on the resulting microstructure. The presence of stored energy promotes grain boundary motion and grain coalescence that did not occur in its absence. During the early stages of nucleation, when grain boundaries are not well defined, the phase-fields fluctuate and the presence of stored energy affect these fluctuations. The subsequent grain coalescence therefore differ from that in the absence of stored energy, which explains the difference in the profiles of ϕ in Fig. 4.21a at $\bar{t} = 51$. At a later stage, when the grain boundaries are better established, the presence of stored energy can cause grain boundary motion that promotes grain merger. Such a phenomenon can be seen in Fig. 4.21c, where the grain boundaries at $\bar{x} = -2.8$ and $\bar{x} = -1.1$ at $\bar{t} = 51$ have coalesced in part by being brought closer together by stored energy driven migration. The fact that migration occurred in part due to stored energy is evident in the stored energy profile of Fig. 4.21b, as a decrease in stored energy indicates recovery in the wake of the moving grain boundary. These figures also show stored energy driven migration without grain coalescence, as the grain boundary located at $\bar{x} = 1.6$ has moved to the edge of the domain at $\bar{t} = 2001$.

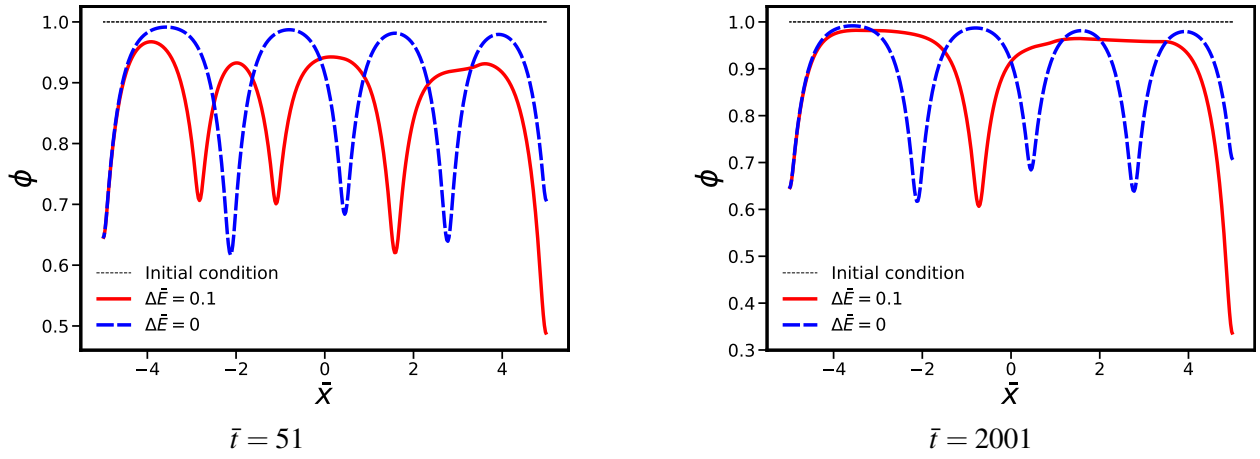

(a) *Crystal order* ϕ.

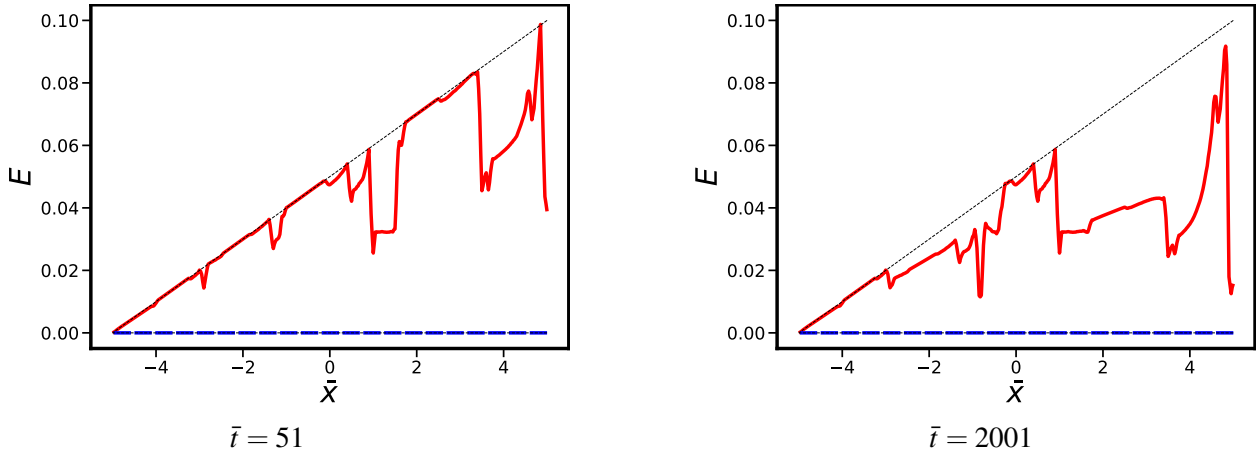

(b) *Stored energy* $\bar{E}$.

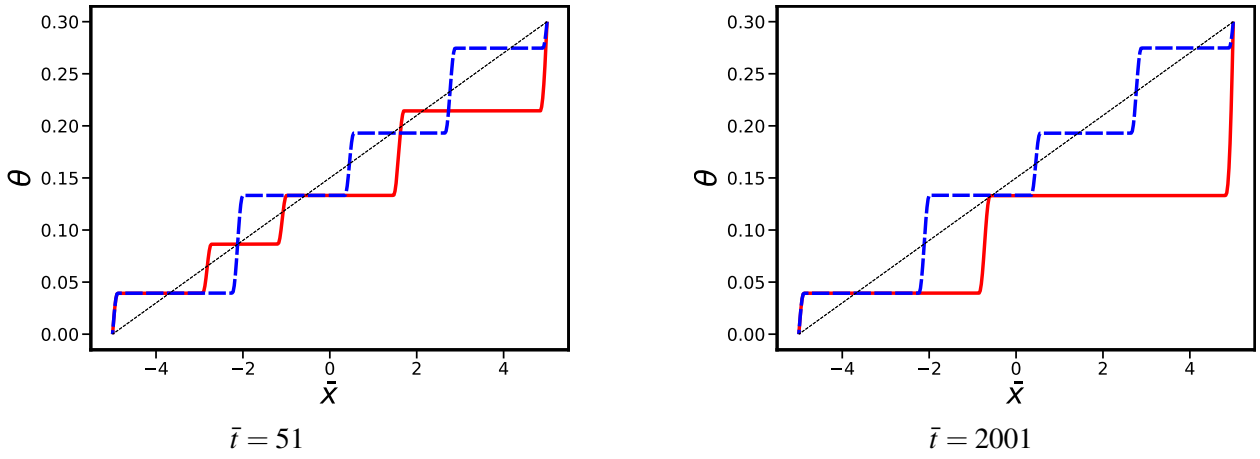

(c) *Lattice orientation* θ.

Figure 4.21: *Profiles of* ϕ *(top),* $\bar{E}$ *(middle) and* θ *(bottom) for a single crystal with uniform initial gradients of stored energy and orientation. The simulations are performed with the KWC model and are plotted at* $\bar{t} = 51$ *on the left and* $\bar{t} = 2001$ *on the right.*

IV.3.4 Grain nucleation with the KWC-Cosserat model in the absence of crystal plasticity

The numerical stability analysis of section IV.3 is revisited by including mechanical aspects in the problem, in particular the effect of skew-symmetric stresses. In this section, we employ the Maxwell type and

Norton with threshold relaxation laws. As a reminder, these formulations result in the following evolution equations for the eigenrotation:

$$\underline{\dot{\theta}}^{\star} = -\frac{1}{\bar{\eta}^{\star} P(\bar{\nabla}\theta)} \overset{\times}{\bar{\underline{\sigma}}} = \overset{\cdot}{\underline{e}}^{e} - \underline{\omega}^{e} + \underline{\dot{\theta}} \quad \text{Maxwell law} \tag{4.84}$$

$$\dot{\theta}^{\star} = -\frac{1}{\bar{\eta}^{\star} P(\bar{\nabla}\theta)} \left\langle |\overset{\times}{\bar{\sigma}}| - \bar{\sigma}_c \right\rangle \operatorname{sgn}(\overset{\times}{\bar{\sigma}}) \quad \text{Norton law with threshold} \tag{4.85}$$

The nucleation behaviour of the KWC-Cosserat model is assessed here for a single crystal subjected to a uniform orientation gradient. A first simulation is run with the KWC model to determine the equilibrium profile of ϕ with respect to the initial orientation field by imposing a linear θ. The obtained fields then serve as initial conditions in subsequent computations in order to limit oscillations caused by too far from equilibrium initial conditions. Then the stability of a uniform orientation gradient is investigated again by adding elastic and viscoelastic/viscoplastic effects in the grain boundaries with Young's modulus $E^e = 130$ GPa and Poisson's ratio $\nu = 0.3$. The full list of parameters is given in table 3.4. For the Maxwell relaxation law, no significant differences are observed with regards to the original KWC model, as shown in Fig. 4.22a. When a Norton relaxation model with threshold is chosen, the existence of the yield stress can substantially delay grain boundary nucleation as shown in Fig. 4.22b. For example, for a value of $\bar{\sigma}_c = 0.5$ or $\bar{\sigma}_c = 0.25$ the nucleation process is still in its early stages at $\bar{t} = 1000$ as the profiles in the central zone away from the left and right boundaries of the domain are the same as the initial conditions. In comparison, lower values of the threshold, such as $\bar{\sigma}_c = 0.05$, allow nucleation to occur at the same $\bar{t}$. As expected, for $\bar{\sigma}_c \to 0$ the behavior is similar to the KWC model. The introduction of residual stresses can therefore delay or even impede the GB formation and migration.

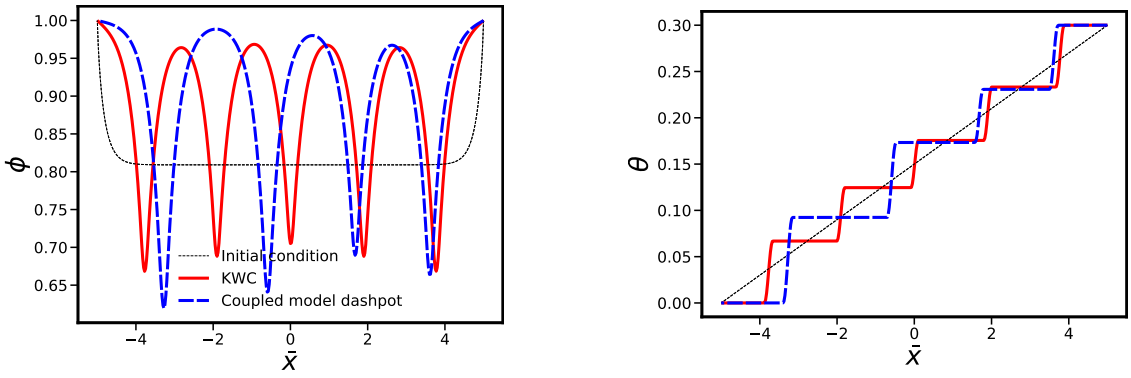

(a) *KWC-Cosserat model with Maxwell relaxation law.*

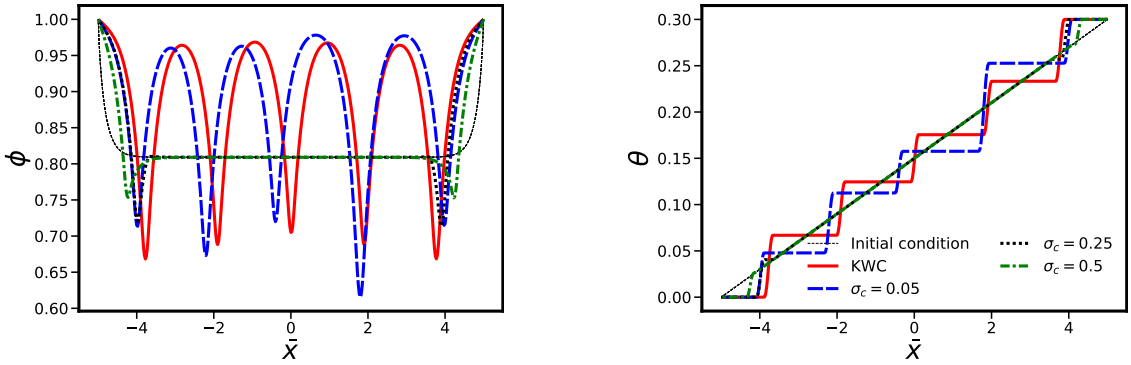

(b) *KWC-Cosserat model with Norton GB relaxation law with threshold.*

Figure 4.22: *Profiles of ϕ (left) and θ (right) at $\bar{t} = 1000$ for a single crystal with a uniform initial orientation gradient for the KWC-Cosserat model with Maxwell relaxation law (top) and Norton law with threshold (bottom).*

IV.4 Grain nucleation during torsion of a single crystal rod

The KWC-Cosserat approach to grain nucleation and GB migration is now applied to a 3D structural problem for which orientation and SSD density gradients will be naturally induced by crystal plasticity in an initially homogeneous single crystal. The torsion of a cylindrical bar with circular cross-section made of a copper single crystal is computed by the finite element method. A 3D simulation framework is required by the anisotropy of the problem. Longitudinal rotation gradients are induced by torsion. Strain gradients are expected from the center to outer surface of the bar. In addition, the cubic symmetry of the FCC crystal leads to a gradient of plastic slip along the circumference of each cross-section as demonstrated numerically and experimentally by Nouailhas and Cailletaud [1995]. This is due to the varying resolved shear stress on each slip system along the circumference. Torsion of elastic-plastic Cosserat bars was recently considered in the isotropic case by Ghiglione and Forest [2022], and in the case of strain gradient crystal plasticity by Scherer et al. [2020]; Phalke et al. [2021] where various crystal orientation effects on crystal hardening were investigated. Torsion of a single crystal bar with square cross-section was performed using Cosserat crystal plasticity at finite strains by Blesgen [2015]. The present simulations of KWC-Cosserat single crystal bars are the first of this kind. They are performed to show whether gradients produced by torsion in a single crystal are sufficient to trigger GB formation and grain nucleation.

IV.4.1 Problem setting

As shown in the above sections, the ability of the KWC model to handle grain nucleation in the presence of orientation gradients is naturally inherited in the coupled model. So far, these gradients were prescribed as initial conditions. In contrast, in this section the orientation gradients are produced through mechanical loading. Indeed we will show through numerical examples that the torsion of a single crystal rod with circular cross-section leads to a uniform orientation gradient along the axis of the cylinder. The computation is made of two loading sequences: first, a torsional loading is applied in order to generate orientation gradients, then the deformation is held constant to let the microstructure evolve to simulate relaxation of the bar. The structure considered here is a cylinder with circular cross-section of radius $\bar{R} = 1$ and length $\bar{L} = 20$. Torsion is applied about the $[111]$ direction coinciding with the cylinder axis z. Under these conditions, only the 3 slip systems in the plane (111) are active: $[10\bar{1}](111)$, $[1\bar{1}0](111)$, $[01\bar{1}](111)$. All slip systems have an initial SSD density of $\rho_0 = 10^{11} m^{-2}$. The mesh is made of 25920 elements with quadratic shape functions and reduced integration resulting in 109169 nodes and 103680 Gauss points. Since each node is endowed with 7 degrees of freedom, namely displacements $\bar{u}_x, \bar{u}_y, \bar{u}_z$, lattice orientations $\theta_x, \theta_y, \theta_z$ and order parameter ϕ, the size of the problem to be solved at each time step is 764183 DOFs. The computation took 53 days on 24 Intel Xeon CPUs, requiring 112 GB of memory. The long computation time associated with very fine time steps required by the strongly nonlinear KWC-Cosserat model explains while recent attempts have been made to implement more efficient solvers for the model by Blesgen [2015]; He and Admal [2021]. The initial conditions are uniform $\phi = 1$ and $\underline{\theta} = \underline{0}$. Dirichlet displacement boundary conditions are imposed on $\bar{u}_x$, $\bar{u}_y$, $\bar{u}_z$ corresponding to a rigid rotation of the top/bottom surfaces of $\pm\vartheta$ around the z axis. Dirichlet boundary conditions $\theta_z = \pm\vartheta$ are also imposed on the top/bottom surfaces. Neumann conditions $m_{xz} = m_{yz} = 0$ are applied at the top/bottom as well. On the whole surface Neumann conditions are imposed for the order parameter ϕ such that $\underline{\xi}_{\phi} \cdot \underline{n} = 0$, where $\underline{n}$ is the exterior normal. Finally, the lateral surfaces of the cylinder are free of all forces (zero traction and surface couples). After torsional loading at the prescribed angle ϑ the deformation is maintained according to table 4.3 to simulate relaxation. The simulation was performed with the KWC-Cosserat model with a Maxwell relaxation law in the GB region and parameters are given in table 4.4. They correspond to pure copper at about $200°C$ where only self hardening is enabled ($h_{ij} = \delta_{ij}$). However, isotropic elasticity ($E = 130\ GPa,\ \nu = 0.3$) was adopted for simplicity. For more details about the choice of parameters, see sections III.2.4-III.3.5.

$\bar{t}$	0	1	730
Prescribed rotation ϑ	0	15°	15°

Table 4.3: *Loading table for torsional loading*

Parameter	$\bar{E}^e$	ν	$\bar{K}$	n	K_r	$\bar{d}$	χ	$\bar{\tau}_c$	$\bar{b}$	$\bar{\mu}$	h_1	h_2	h_3
Value	56×10^3	0.3	4.35	10	10	1×10^{-3}	0.3	0	0.2556×10^{-3}	21750	1	0	0

Parameter	$\bar{\alpha}$	$\bar{s}$	$\bar{\varepsilon}$	$\bar{\eta}_\phi$	$\bar{\eta}^\star$	$\bar{\mu}_p$	β_p	C_D	$\bar{C}_A$	$\bar{\gamma}$	γ_g
Value	0.31	0.75	1	10	0.1	10^6	10^2	100	1	10^4	10^{-4}

Table 4.4: *Model parameters used in the simulation of a single crystal bar under torsional loading.*

IV.4.2 Results

After deformation, tangential, radial and longitudinal rotation gradients are generated as shown in Fig. 4.23. In this figure the curvature tensor is computed in cylindrical coordinates and the magnitude of the radial, tangential and longitudinal components are given by $|\bar{\underset{\sim}{\kappa}}\cdot\underline{e}_r|$, $|\bar{\underset{\sim}{\kappa}}\cdot\underline{e}_\theta|$ and $|\bar{\underset{\sim}{\kappa}}\cdot\underline{e}_z|$ respectively. The six-fold symmetry of the the curvature and plastic deformation patterns is due to crystal symmetry of the shear (111) plane and associated slip systems. It is clear that the dominant gradient is that along the vertical direction, which is about two orders of magnitude larger than the others. It is fairly uniform except close to the ends of the bar and is reminiscent of the initial conditions given in section IV.3.4. The cumulative plastic slip $\gamma^{tot}=\sum_{\alpha=1}^{3}|\gamma^\alpha|$ is shown in the cross-section of the middle of the rod in Fig. 4.23a. It can be seen that the cumulative plastic slip is made of concentric hexagons whose magnitude increases linearly from the center to the outer region of the cross-section up to about 3%. As illustrated in Fig. 4.24, the stored energy field generated by the loading is heterogeneous in the cross-section but its magnitude is rather low ($\max(\bar{E})\sim10^{-2}$), partly due to the fact that only self hardening was considered ($h_{ij}=\delta_{ij}$). Thus, according to Eq. (3.38), one expects local variations of ϕ of about 0.01 in the cross-section, which explains why the crystal order is mostly impacted by the longitudinal torsion. After subsequent relaxation, grain nucleation is observed in Fig. 4.25 in the form of a stack of pancake grains. As in section IV.3.3.2 grain nucleation is triggered by the rotation gradient. The SSD-based stored energy being low, the grains are rather homogeneous in the cross-section. We expect that increasing the magnitude of the torsion angle should still result in grains stacking along the rod, but the crystal order field should consist of concentric hexagons whose magnitude decreases linearly along the radius. The nucleation process being triggered by rotation gradients, it is not expected that grains will nucleate along the radius of the rod. Such a nucleation process would require the presence of multiple grains in the cross-section, or an additional mechanical loading prompting rotation gradients around the x or y axis. Another requirement would be to increase the radius of the rod, as the interface width ℓ_ϕ is larger than the radius ($\ell_\phi/R\sim1.6$ in this computation). The profiles of ϕ and θ_z along the axis of the cylinder are shown in Fig. 4.26 and are very similar to those in section IV.3.4. The nucleation process in this figure is still quite in its early stage with misorientations ranging between $1^\circ-3^\circ$. The model being computationally expensive, a later simulation stage is not available at the time and a rather coarse mesh has been used. However, we think that using a finer mesh will give quite similar qualitative results compared with the current mesh. In addition, it is expected that upon further relaxation the different grains will merge along the vertical axis to accommodate the interface width ℓ_ϕ with misorientation between grains increasing up to forming a bicrystal for $\bar{t}\to\infty$, as with the KWC model. Given the boundary conditions of the simulation, the bicrystal should have a final misorientation of about 30°.

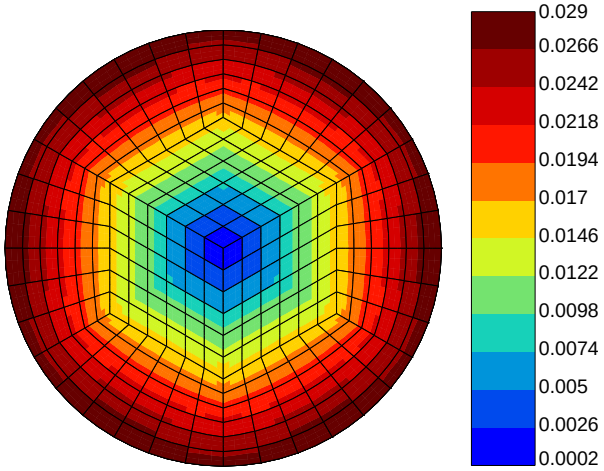

(a) *Cumulative plastic slip on all 3 slip systems.*

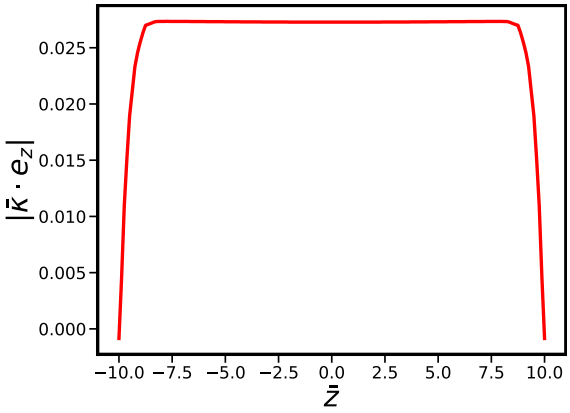

(b) *Magnitude of the longitudinal curvature* $|\bar{\underset{\sim}{\kappa}} \cdot \underline{e}_z|$ *along the vertical direction.*

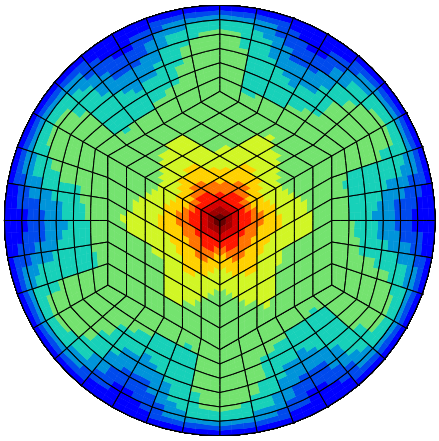

(c) *Magnitude of the radial curvature* $|\bar{\underset{\sim}{\kappa}} \cdot \underline{e}_r|$ *in the middle cross-section.*

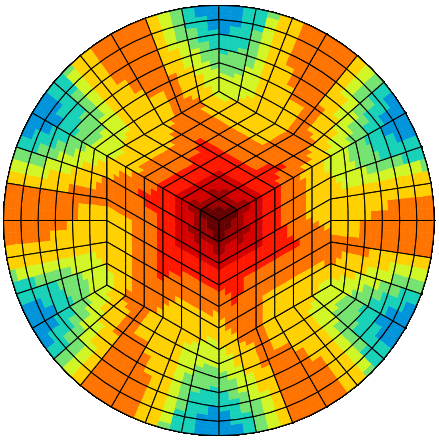

(d) *Magnitude of the tangential curvature* $|\bar{\underset{\sim}{\kappa}} \cdot \underline{e}_\theta|$ *in the middle cross-section.*

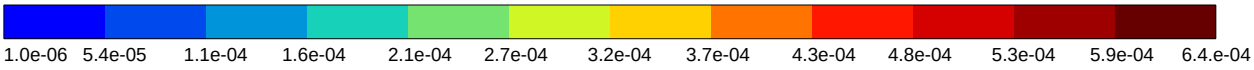

Figure 4.23: *Magnitudes of the curvatures in cylindrical coordinates in the longitudinal (top), radial (bottom left) and tangential (bottom right) directions after torsional loading of a single crystal rod.*

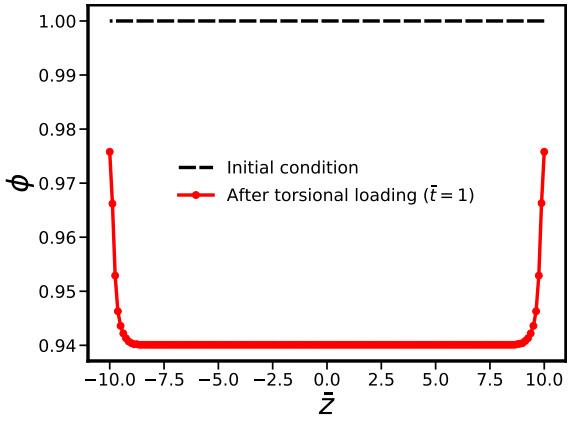

(a) *Profile of* ϕ *along the vertical axis of the rod.*

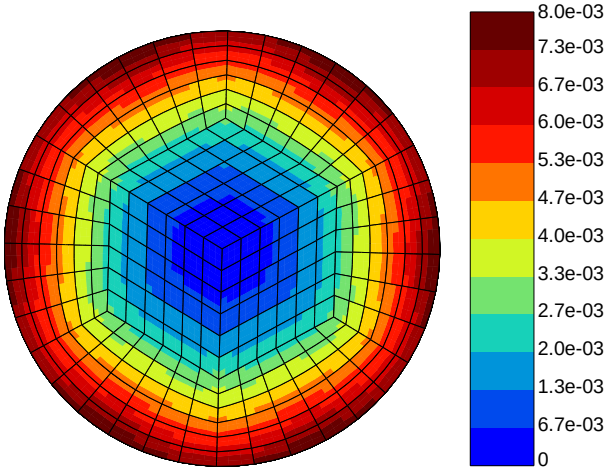

(b) *Stored energy in the middle cross-section.*

Figure 4.24: *Crystal order* ϕ *(left) and stored energy* $\bar{E}$ *(right) after torsional loading of a single crystal rod.*

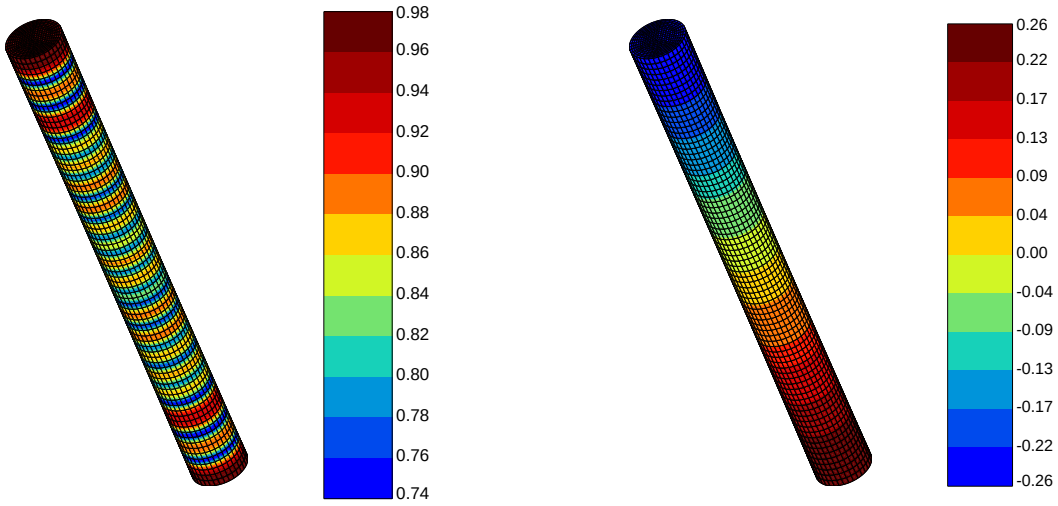

(a) *Crystal order* ϕ. (b) *Microrotation about* $\underline{e}_z$.

Figure 4.25: *Crystal order* ϕ *(left) and* θ_z *component of the lattice orientation (right) after torsional loading and subsequent relaxation of a single crystal rod.*

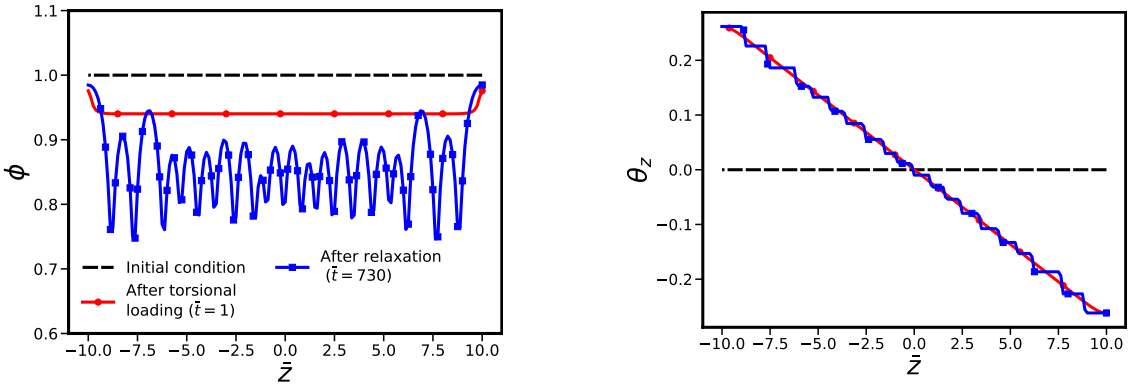

Figure 4.26: *Profiles of* ϕ *(left) and* θ_z *(right) along the axis of the cylinder after torsional loading and subsequent relaxation* ($\bar{t} = 730$).

IV.4.3 Comparison with experimental results from the literature

The presented simulations suggest that single crystal copper bars under torsion at sufficiently high temperature will recrystallize and a bamboo grain microstructure is expected to form. Torsion tests at high temperature are routinely performed for polycrystalline metals and alloys [Montheillet et al., 1984]. They show typical oscillatory torque/angle responses due to successive recrystallization processes and strong crystallographic texture and grain morphology evolution. However, few published papers deal with torsion of single crystal wires at high temperature. High pressure torsion of HCP Magnesium single crystals lead to recrystallization as shown in Bonarski et al. [2008] but the observed grain morphology was not described. Compression of aluminum single crystals and torsion of aluminum polycrystals also lead to recrystallization phenomena observed by Gourdet and Montheillet [2000]. Kassner [1989] performed large strain torsion experiments on Al single crystals with the torsion axis parallel to the [111], exactly the physical situation investigated in our simulations. This led to the early formation of geometrically necessary boundaries (GNBs) parallel to the slip plane and perpendicular to the torsion axis, in agreement with the present simulation results. The bamboo structure in the twisted rod can be observed in Fig. 4.27 that is taken from Fig. 3 of [Kassner, 1989] and is comparable to the simulation results of Fig. 4.25a. Despite the very large strains of about 16 under creep loading, only about 10% of the subgrain facets were found to be high angle boundaries (HABs) [Kassner and Barrabes, 2005]. The experimental results of Kassner [1989] therefore bring

some experimental validation of the predicted microstructure evolution. However, the building-up of a low angle boundary bamboo grain structure predicted by the present simulations during torsion therefore calls for more systematic experimental validation.

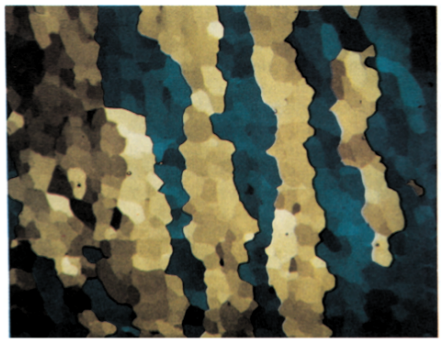

Figure 4.27: *Optical micrograph of a tangential section of an Al single crystal under torsional deformation [Kassner, 1989]. The torsion axis is parallel to the horizontal axis of the micrograph. The microstructure exhibits the same banded aspect as the simulations with the KWC-Cosserat model.*

IV.5 Summary

The ability of the KWC model to spontaneously simulate grain nucleation in a single crystal in the presence of orientation gradients was demonstrated in this chapter both through analytical and numerical stability analysis of orientation gradients in the one-dimensional case. The role of gradients of stored energy was also assessed for the KWC and KWC-Cosserat phase-field models by means of 1D numerical computations. According to the simulations, the initial single crystal is fragmented into a multitude of grains with low misorientation (LAB) that grow and merge together due to interaction between diffuse grain boundary zones. By tracking the time evolution of the total energy, it was shown that grain nucleation contributes to the minimization of total energy. It was demonstrated that the presence of orientation gradients is necessary to trigger grain nucleation, as a gradient of stored energy in a single crystal cannot lead by itself to the formation of new grains, according to the model. Gradients of stored energy influence the mobility of newly formed grain and subgrain boundaries. A similar study was carried out with the KWC-Cosserat model of Ask et al. [2020] to investigate mechanical effects on grain nucleation, firstly in the absence of overall loading. Special attention was drawn to the development and relaxation of skew-symmetric stresses during the formation and the migration of grain boundaries. Two different types of evolution law of the reference orientation – required to relax skew-symmetric stresses at the grain boundaries – were considered: a Maxwell viscoelastic model and a Norton viscoplastic model with threshold. The introduction of a threshold in the relaxation law leads to residual stresses that delay grain boundary motion and nucleation. Sufficiently high values of the threshold can impede grain nucleation within an orientation gradient.
A 3D structural finite element simulation combining crystal plasticity and grain boundary formation was then performed for the torsion of a single crystal bar with circular cross-section. Initial quasi-static torsion was followed by simulation of a relaxation stage. The torsion axis was aligned with the [111] direction of the FCC crystal. The torsional loading generated a significant rotation gradient along the cylinder axis that was sufficient to trigger grain nucleation in the form of a stack of cylindrical grains with low angle grain boundaries, in agreement with the 1D stability analysis. The radial and circumferential gradients of SSD-based stored energy induced by heterogeneous plastic slip in the cross-sections are too low in magnitude to trigger subgrain formation in the cross-section. This results in a bamboo-like subgrain microstructure in the wire. Experimental support of the torsion simulation result was found in the case of torsion of aluminum single crystals under creep loading in [Kassner, 1989; Kassner and Barrabes, 2005] where stacks of LABs were observed parallel to the (111) planes.

Chapter V

Phase-field Cosserat modelling of microstructure evolution in polycrystalline aggregates

Résumé en français

Dans ce chapitre nous présentons plusieurs applications des modèles à champs de phase de type Kobayashi-Warren-Carter et KWC-Cosserat. La première partie est dédiée au cisaillement d'un polycristal périodique à 10 grains avec un seul système de glissement par grain. Selon l'orientation du système de glissement par rapport à l'orientation cristalline du grain, différentes formes de localisation de la déformation plastique peuvent apparaitre, telles que des bandes en genou et des bandes de glissement. En particulier, pour les bandes en genou une localisation de la courbure de réseau est observée, ce qui résulte en l'apparition de nouveaux sous-joints de grains, en accord avec des simulations similaires par Ask et al. [2020]. En revanche, les bandes de glissement observées ne sont pas nécessairement associées à une forte réorientation du réseau et ne peuvent donc pas provoquer la germination de nouveaux sous-joints de grain avec ces modèles.

La seconde application concerne le passage d'un joint de grain à travers un vide. La simulation est dans un premier temps effectuée avec le modèle KWC. On observe un comportement similaire au cisaillement d'un précipité par une dislocation. En outre, on observe une similitude notable avec les simulations basées sur un modèle multi-champs de phase de type Chen-Yang dans les travaux de Zhang et al. [2022], ce malgré des approches relativement différentes entre les deux modèles.
Dans un second temps, ce cas d'application est étendu en ajoutant un chargement mécanique de compression. On observe une réduction signifiative de la contrainte de compression à mesure que le grain se déplace sous l'effet de la différence d'énergie stockée par les dislocations, en accord avec des simulations éléments finis de plasticité cristalline par Wang et al. [2023].

Enfin, la troisième et dernière application traite de la torsion de bicristaux. L'interface est localisée au milieu de la barre et les grains sont désorientés uniquement par rapport à l'axe du cylindre. De façon similaire à la torsion du monocristal présentée au chapitre IV, Le chargement en torsion génère de fort gradient d'orientation du réseau cristallin, ce qui entraine la germination de nouveaux grains. La différence ici est que l'existence à l'état initial d'un joint de grain entraine sa persistance après chargement mécanique. Un deuxième cas présente un bicristal dont la normale au plan du joint est perpendiculaire à l'axe du cylindre. Le chargement mécanique entraine une réorientation du plan de joint, dont la normale après relaxation est parallèle à l'axe du cylindre.
Des analyses supplémentaires sont nécessaires pour examiner plus en détails ces simulations mais il apparaît clairement que l'approche peut être étendue à d'autres applications plus complexes. Cela requerra cependant d'améliorer le coût calcul très élevé de l'implémentation actuelle du modèle KWC-Cosserat, surtout en ce qui concerne la simulation de polycristaux.

Contents

V.1 Introduction

Orientation phase-field models have mainly been applied to single crystals in the previous chapters. This chapter showcases a range of applications of orientation phase-field models to bi and polycrystals. These simulations should be considered as preliminary investigations for modelling microstructure evolution of polycrystalline aggregates during thermomechanical processing. The chapter is organised as follows. Section V.2 demonstrates the periodic shear of a periodic polycrystal with a single slip system per grain. The study investigates the localisation of plastic strain, curvature, and the resulting microstructure evolution. Section V.3 examines the migration of a grain boundary across a void, while section V.4 extends the case of the torsion of a single crystal to bicrystals.

V.2 Periodic shear of a periodic polycrystal

V.2.1 Introduction

Plastic deformation of polycrystals frequently triggers slip localization at the mesoscale. In the literature, two primary modes of localization involving a single slip system are identified: slip and kink banding. Slip bands refer to the localisation of intense plastic slip activity on a few crystallographic planes very close to each other. These planes take the form of bands that are parallel to the glide plane. Slip bands are responsible for the emergence of macroscopic shear bands [Korbel and Martin, 1986]. The alternative mode of localization, namely kink banding, is linked to significant lattice rotation, resulting in bands that are perpendicular to the glide direction.
Within the context of continuum modelling, the theory developed by Asaro and Rice [1977] demonstrates that slip and kink bands emerge from bifurcations in the constitutive equations when a previously homogeneous pattern of deformation is disrupted in the presence of material softening. The theory predicts that slip and kink bands may appear simultaneously, even though they represent distinct localization modes from a physical standpoint. Forest [1998] dealt with this problem by employing generalized continua to enhance the microstructure description. The study demonstrated that the incorporation of curvature effects through Cosserat crystal plasticity enables the distinction between slip and kink banding.
KWC-Cosserat modelling of kink banding and subsequent subgrain boundary nucleation has been studied by Ask et al. [2020] but slip banding was not observed. In this section, we show through finite element simmulations that the model handles slip localization in the form of slip and kink banding as well as subsequent subrain boundary nucleation when applicable.

V.2.2 Problem set-up

Subgrain nucleation due to mechanical loading is studied numerically using the two-dimensional finite element implementation of the coupled model with Maxwell grain boundary relaxation. Similarly to the work of Ask et al. [2020] a 2D periodic polycrystal is subjected to a periodic shear by imposing a displacement field of the form

$$\underline{u} = \underset{\sim}{\boldsymbol{B}} \cdot \underline{x} + \underline{p}\,(\underline{x}) \tag{5.1}$$

with

$$\underset{\sim}{\boldsymbol{B}} = \begin{pmatrix} 0 & 0 & 0 \\ B_{21} & 0 & 0 \\ 0 & 0 & 0 \end{pmatrix} \tag{5.2}$$

and $\underline{p}\,(\underline{x})$ a periodic fluctuation having the same values at opposite nodes of the boundary.

It is assumed that each grain has only one slip system to facilitate plastic strain localization. The grains are oriented at an angle θ relative to the laboratory reference frame, and the slip system $(\underline{l}, \underline{n})$ of each grain is oriented at an angle a relative to the crystal frame, as seen in figure 5.1a. Different values of a are

considered to induce distinct types of plastic strain localisation. The corresponding microstructure is shown in figure 5.1. The orientation of each grain is in the range $0-30°$.

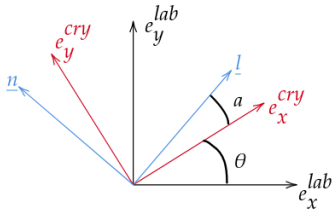

(a) *Laboratory, crystal frames and slip systems.*

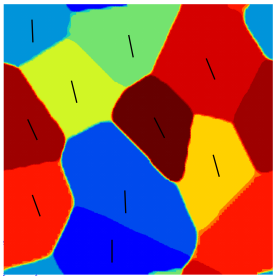

(b) *Polycrystal with angle* $a = 90°$ *between the crystal frame and the slip system.*

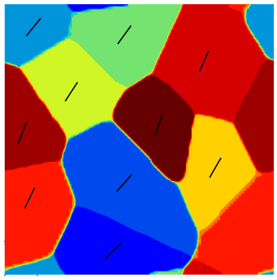

(c) *Polycrystal with angle* $a = 45°$ *between the crystal frame and the slip system.*

Figure 5.1: *Periodic polycrystal with 10 grains used to study subgrain nucleation due to plastic strain localization. Black lines denote the slip direction of each grain.*

The polycrystal is generated using Neper software [Quey et al., 2011]. The subsequent simulations are performed using a 50x50 square mesh of 10000 reduced elements with quadratic shape functions and 30401 nodes. Each grain is described using a set of elements and is given a random uniform initial orientation between $0°$ and $30°$. As the crystal order is still unknown at this stage and the grain boundaries are faceted because of discretization, an initial simulation using the KWC model is performed to both refine the orientation field and reach equilibrium for the crystal order. The fields resulting from this simulation then serve as initial conditions for subsequent computations with the coupled model. Figure 5.2 provides an overview of this process. The parameters used in the simulations are the same as those in Ask et al. [2020] and are recalled in table 5.1. The targeted material is pure copper at around $150-160°C$ ($f_0 = 1.15MPa$).

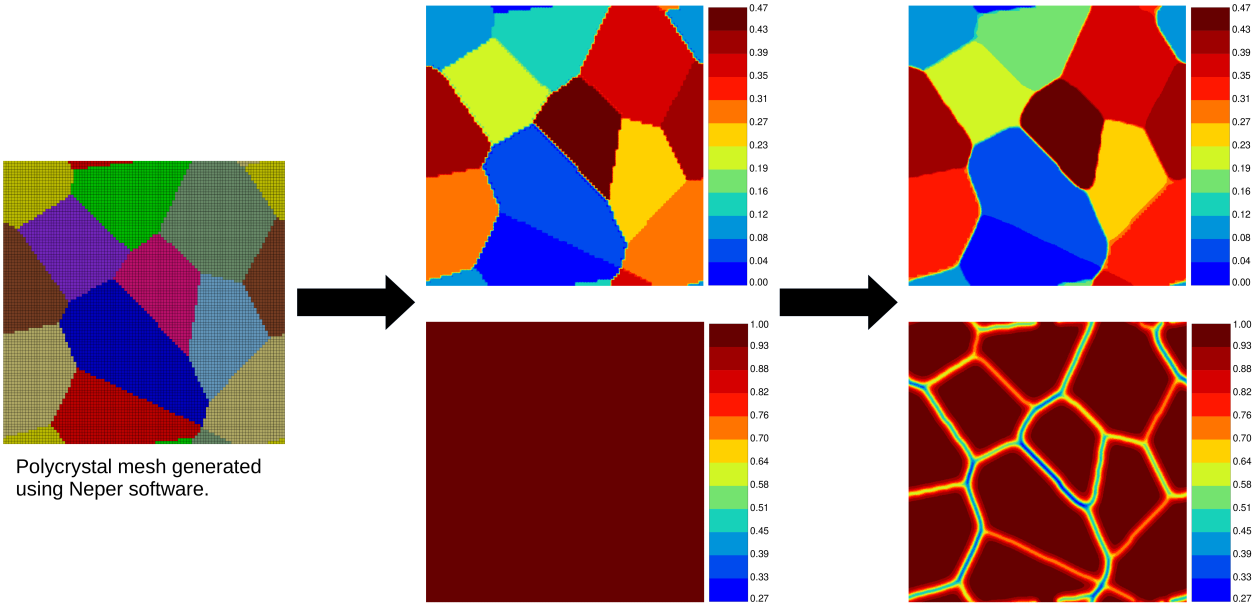

Figure 5.2: *Microstructure initialisation procedure.*

Parameter	$\bar{C}_{11}$	$\bar{C}_{12}$	$\bar{C}_{44}$	$\bar{K}$	n	K_r	$\bar{d}$	χ	$\bar{\tau}_0$	$\bar{b}$	$\bar{\mu}$
Value	139×10^3	95.6×10^3	65.2×10^3	8.7	10	10	1×10^{-3}	0.3	0	0.2556×10^{-3}	4×10^4

Parameter	$\bar{\alpha}$	$\bar{s}$	$\bar{\varepsilon}$	$\bar{\eta}_\phi$	$\bar{\eta}^\star$	$\bar{\mu}_p$	β_p	C_D	$\bar{C}_A$	$\bar{\gamma}$	γ_g
Value	0.62	1.5	2	100	10	10^9	10^2	100	1	10^4	10^{-4}

Table 5.1: *Model parameters used in the simulation of a single crystal bar under torsional loading.*

V.2.3 Results

The microstructure generated using the above procedure is now subjected to periodic shear loading using the KWC-Cosserat model with Maxwell type relaxation for the skew-symmetric stress at the grain boundaries. Simulations are conducted for two different situations: one with the slip system angled at 90° relative to the grain orientation and the other with $a = 45^\circ$. The applied average deformation linearly increases from 0 to 5% between $\bar{t} = 0$ and $\bar{t} = 10$. It is subsequently held constant from $\bar{t} = 10$ to $\bar{t} = 7200$ to simulate relaxation.

V.2.3.1 Localization in the form of kink bands

Kink bands formation after deformation

With $a = 90^\circ$ the shear loading induces significant plastic strain localization that occurs perpendicularly to the slip direction, which is indicative of the formation of kink bands. Figure 5.3 shows that the SSD density and curvature norm demonstrate intense localization at the bottom grains of the polycrystal. The presence of orientation gradients and dislocations visibly reduces the value of the crystal order in these regions.

Subgrain formation in kink bands after relaxation

The microstructure following relaxation is depicted in Figure 5.4. The kink bands display higher curvature than immediately after deformation. Additionally, there is a significant decrease in crystal order in these regions, primarily among the grains positioned at the bottom. The crystal order is sufficiently low to classify these as new subgrain boundaries that result from grain fragmentation. Circular regions with different orientations from the matrix are observed in the bottom right grain and could indicate potential nuclei. These regions are linked to a local reduction in dislocation density. However, due to the stored energy being mostly concentrated within the band, these nuclei are unable to grow as there is no difference in stored energy to prompt grain boundary motion. This phenomenon was also noted by Ask et al. [2020].

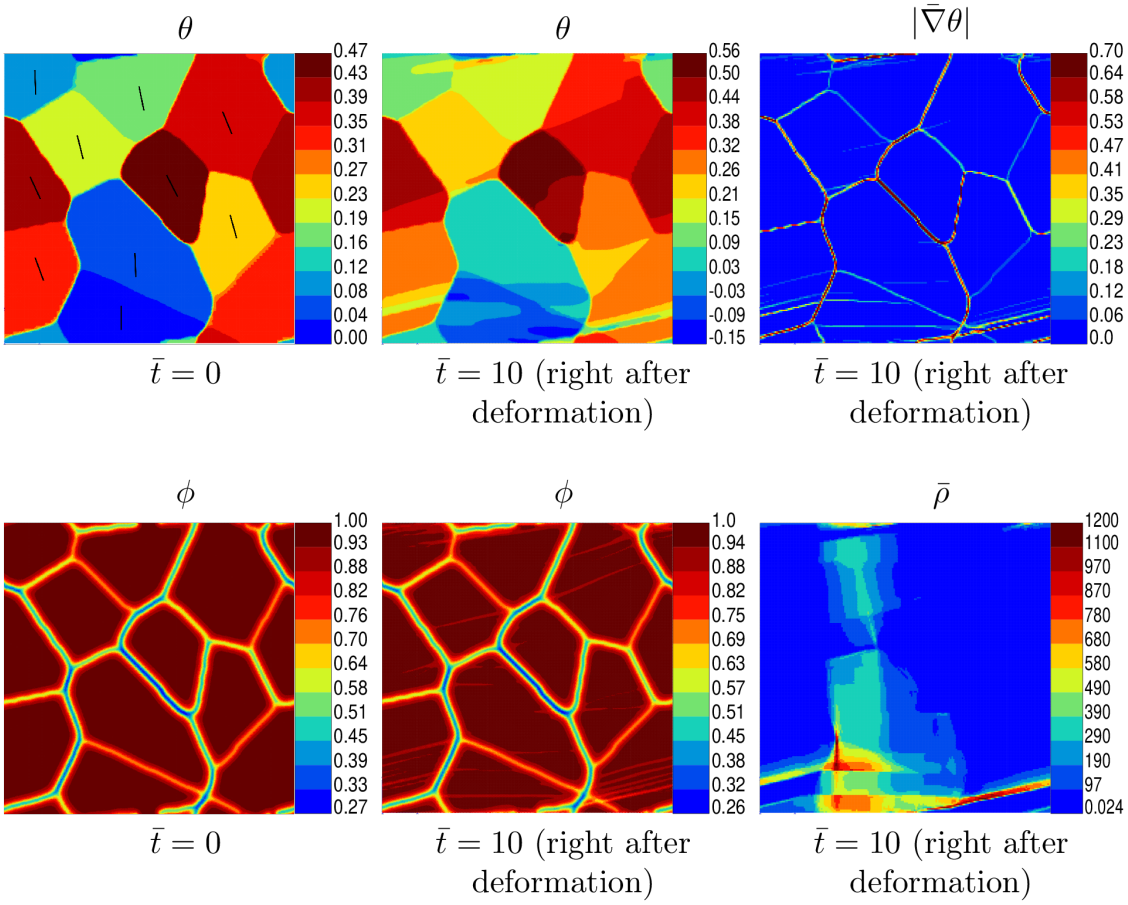

Figure 5.3: *Kink bands formation*

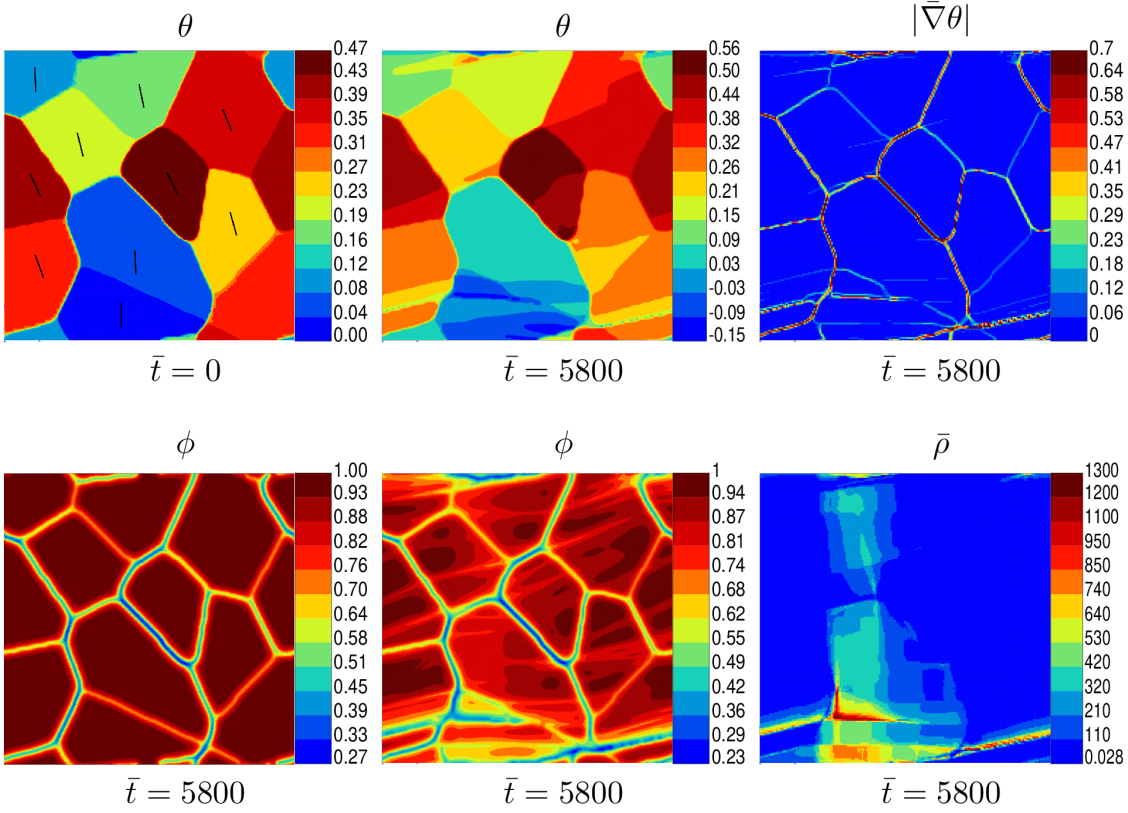

Figure 5.4: *Subgrain formation in kink bands*

V.2.3.2 Localization in the form of slip bands

Slip bands formation

After deformation and at $a = 45°$, plastic strain localisation now occurs in the form of bands parallel to the slip direction (indicating slip bands), either at grain boundaries or through the grains, as seen in Fig. 5.5. They are generally not associated with strong orientation gradients. The presence of lattice rotation in the large grain at the top right is thought to be accommodation of deformation incompatibilities that occur due to interactions with surrounding slip bands or boundary conditions.

Microstructure changes after relaxation

After relaxation the crystal order is lower in these bands of large statistically stored dislocation density as shown in Fig. 5.6 in the central grains where ϕ goes as low as 0.2. For the two large grains at the bottom, these localisation bands are not correlated with lattice reorientation and the fragmented aspect of the grains on the crystal order field results solely from the accumulation of SSD. The absence of misorientation on both sides of the decrease in local order suggests that this is not a new subgrain boundary. That is expected as a local decrease in ϕ due to the presence of SSDs does not lead to an orientation gradient, as discussed in section IV.3.3.1, where it was shown that the presence of orientation gradients is required for boundary nucleation with the orientation phase-field models. On the contrary, the large grain at the top right is fragmented due to lattice rotation.

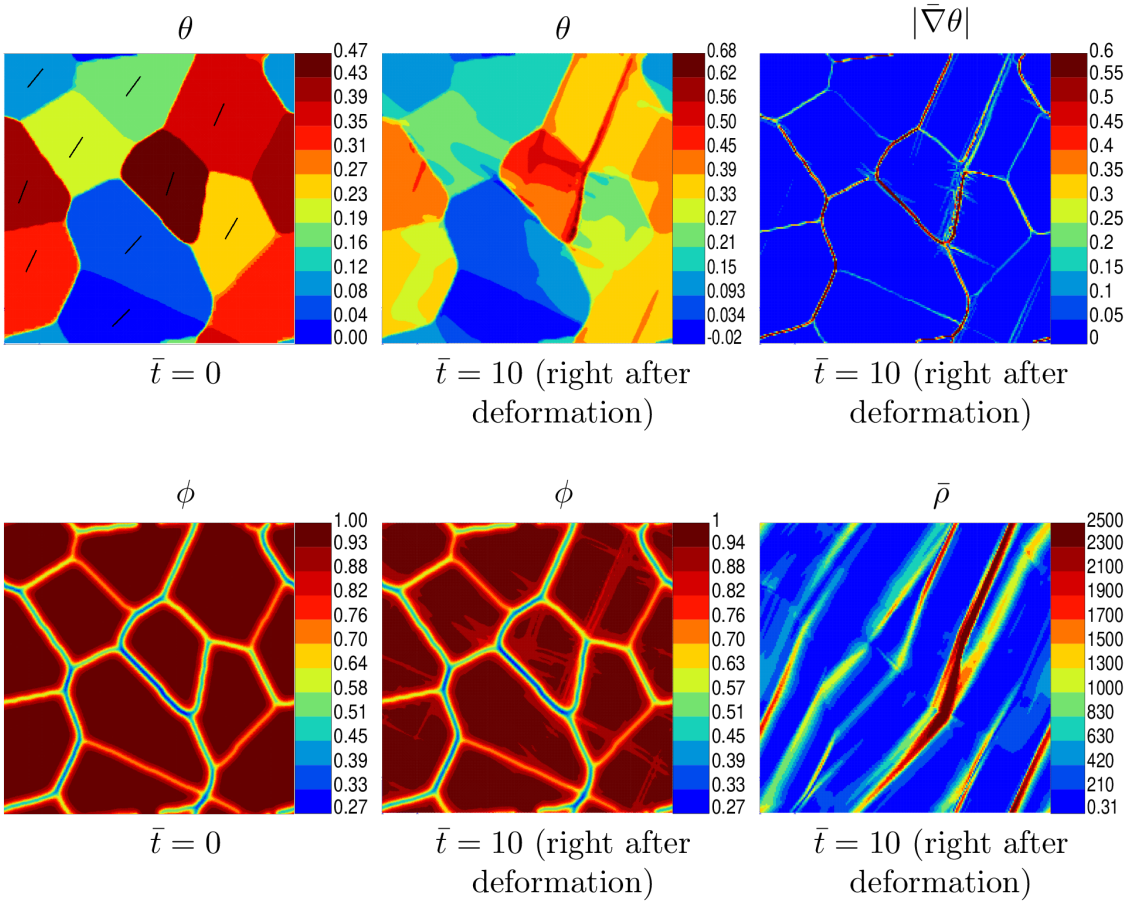

Figure 5.5: *Slip bands formation*

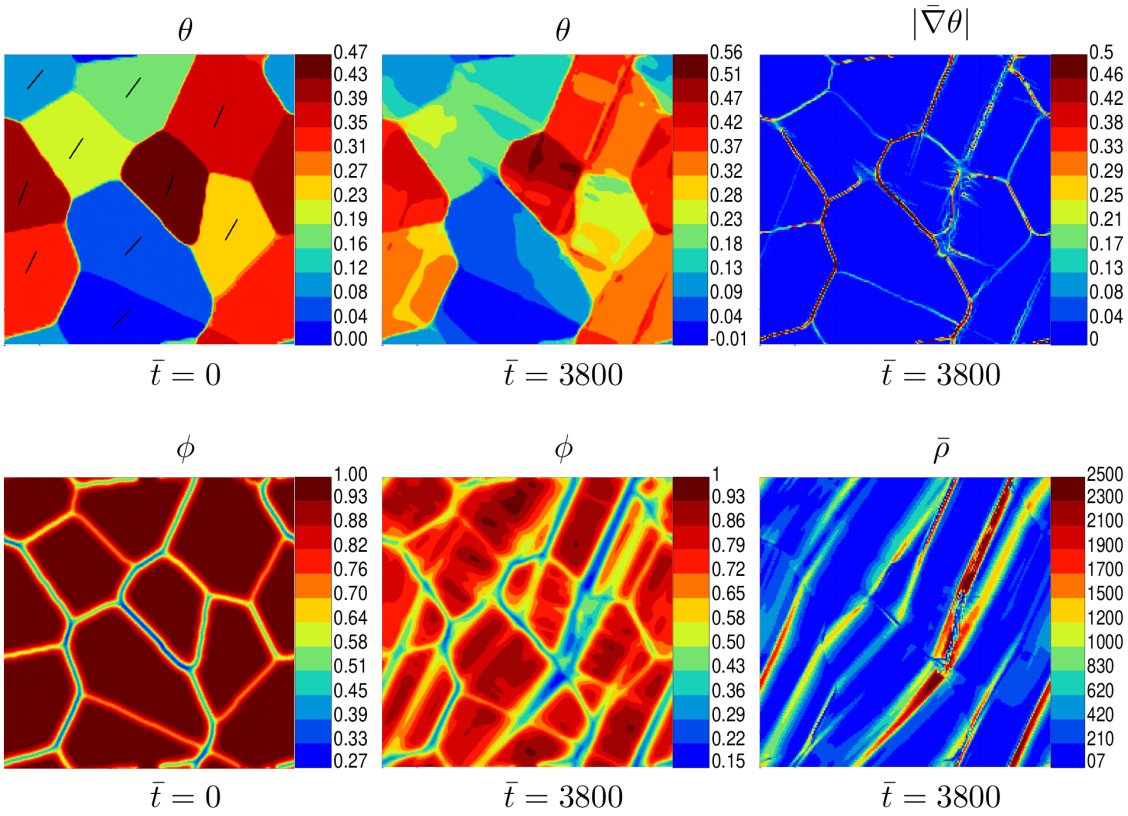

Figure 5.6: *Subgrain formation in slip bands*

V.3 Grain boundary migration in the presence of a void

V.3.1 Introduction

The generation of intragranular voids, as seen in additive manufacturing processes, can lead to stress concentration which is known to promote the fracture of crystalline materials [Bourcier et al., 1986]. The interaction between these voids and migrating grain boundaries is complex. For instance, much like the Zener pinning effect, voids can impact grain boundary behaviour during the process of recrystallization [Zhang et al., 2022]. Migration of the grain boundary across a void can reduce stress concentration and prevent crack formation and propagation [Wang et al., 2023]. From the industrial viewpoint, it is therefore essential to comprehend the interaction between voids and migrating grain boundaries to design dependable safety components through additive manufacturing techniques. We investigate here the ability of the KWC and KWC-Cosserat models to simulate the motion of grain boundaries across voids.

V.3.2 Problem set-up

Consider a 15×10 rectangular domain with a hole of radius $\bar{R} = 1.25$. The mesh, made of 4800 quadratic elements with reduced integration and 14800 nodes, is visible in Fig. 5.7.

A grain boundary is initialized at the left side of the structure so that the hole is fully contained in the grain on the right side of the boundary. A stored energy difference is applied so that the grain boundary will pass through the hole. Zero flux boundary conditions are enforced for both ϕ and θ at all the boundaries (including the hole surface) except for the top and bottom edges where periodicity is prescribed. The simulation is performed with the KWC model and the parameters given in table 5.2, which correspond to pure copper at about $220^{\circ}C$.

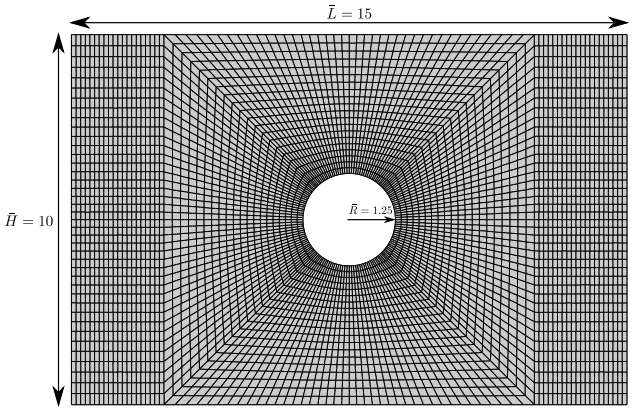

Figure 5.7: *Mesh used in the simulation of stored energy driven migration of a grain boundary in a perforated plate.*

Parameter	$\bar{\alpha}$	$\bar{s}$	$\bar{\varepsilon}$	$\bar{\eta}_\phi$	$\bar{\eta}_\theta$	$\bar{\mu}_p$	β_p	$\bar{\gamma}$	γ_g
Value	0.31	0.75	1	10	1	10^6	10^3	10^4	10^{-4}

Table 5.2: *Model parameters used in the simulation of stored energy driven migration of a grain boundary in a perforated plate.*

V.3.3 Results

Snapshots of the orientation and crystal order fields can be seen in Fig. 5.8. The curvature of the grain boundary becomes more noticeable as it approaches the hole, due to the interaction of ϕ with the void's free surface. As it passes through the hole, the zero flux boundary conditions ($\bar{\nabla}\phi \cdot \underline{n} = 0$ with $\underline{n}$ the outwards normal) on the void require the phase-fields to be orthogonal to the tangent of the void, resulting in the curvature of the grain boundary. A reorientation takes place around the void area, which leads to the reduction of the value of ϕ in that region. Once both the top and bottom portions of the grain boundary have passed through the void, they unite, resulting in a straight grain boundary again. At the final state, only a single crystal remains due to the grain boundary sweeping across the entire domain. Notably, a similar behaviour has been modelled by Zhang et al. [2022] via a modified multi phase-field model of Chen-Yang type, as depicted in Fig. 5.9. The degrees of freedom in their research represent the recrystallized grains and deformed microstructure, rather than the grain orientation and crystal order. Notably, rather than a non-meshed area, the void was represented through the inclusion of a parameter in the free energy density that modified the grain boundary and stored energy contributions. Although the approaches used differ fundamentally, there is significant similarity in the qualitative behaviour exhibited by the grain boundary. Our simulation presented in this section is merely an initial step and requires further investigation. Firstly, a greater number of grains should be included, as demonstrated in [Zhang et al., 2022]. Subsequently, the KWC-Cosserat model must be applied in order to evaluate the influence of bulk and grain boundary mechanical behaviour on the outcomes.

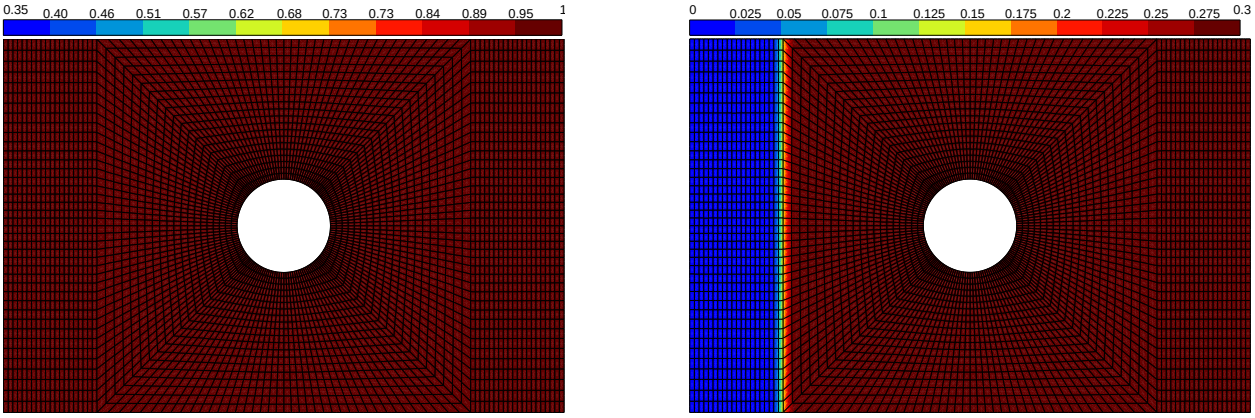

(a) ϕ *and* θ *at* $\bar{t} = 0$.

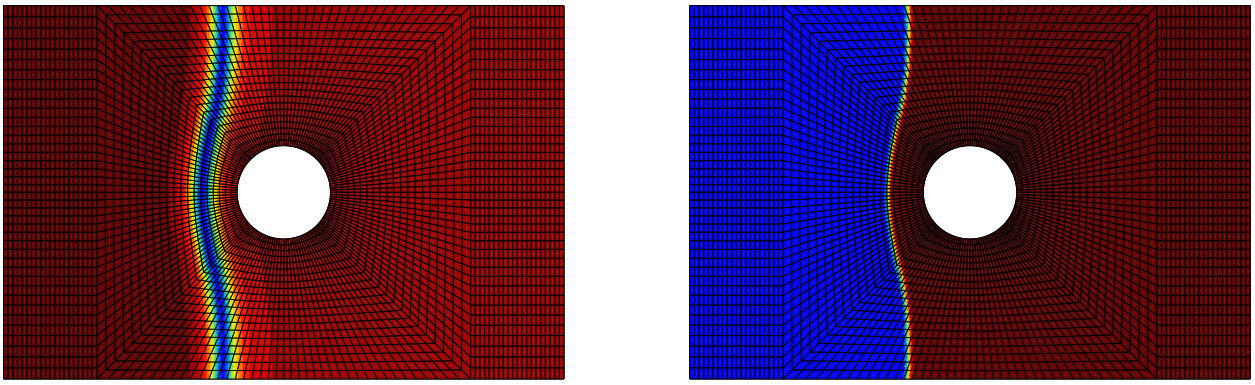

(b) ϕ *and* θ *at* $\bar{t} = 7500$.

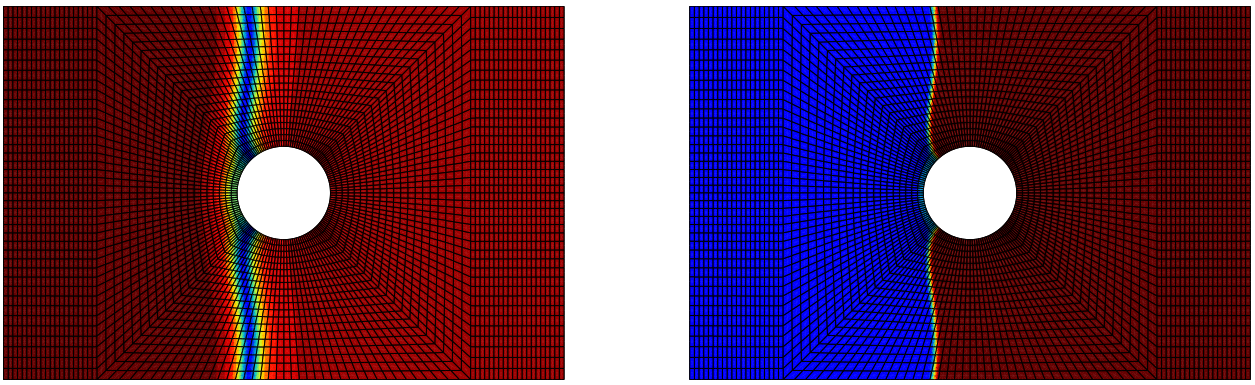

(c) ϕ *and* θ *at* $\bar{t} = 7700$.

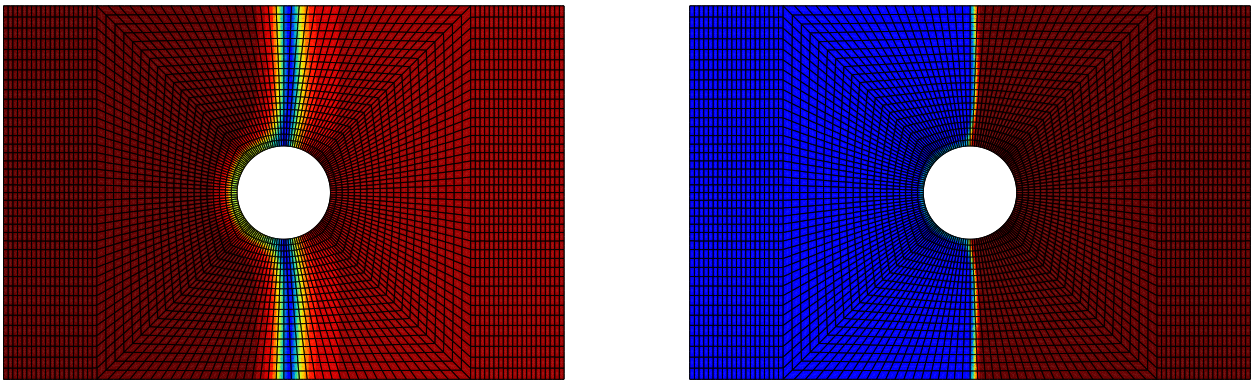

(d) ϕ *and* θ *at* $\bar{t} = 8100$.

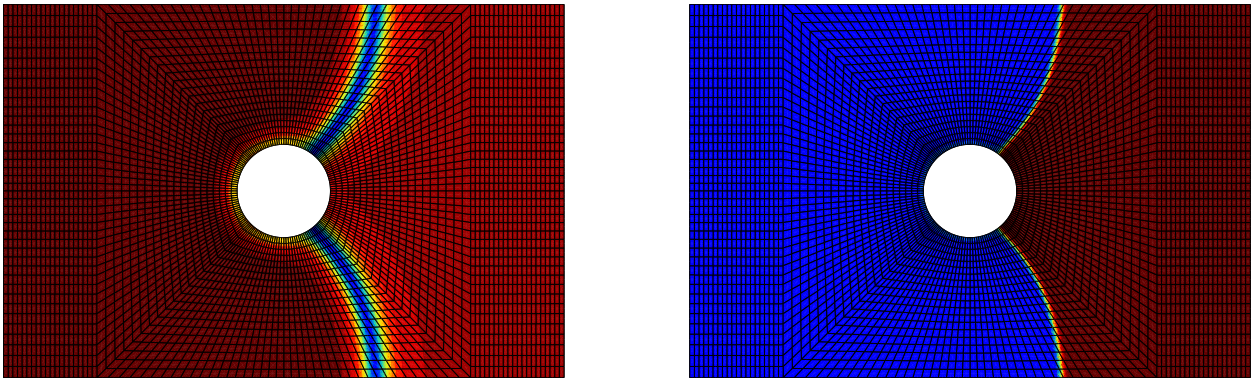

(e) ϕ *and* θ *at* $\bar{t} = 9100$.

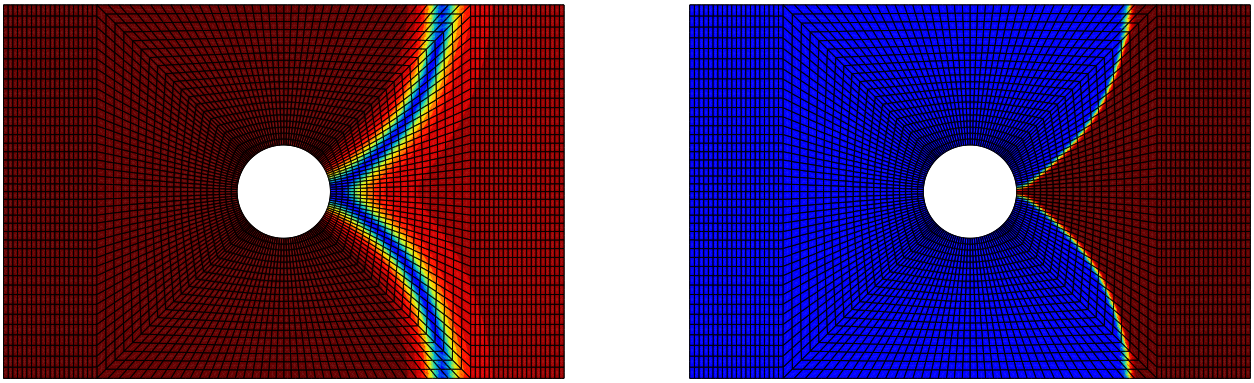

(f) ϕ *and* θ *at* $\bar{t} = 10550$.

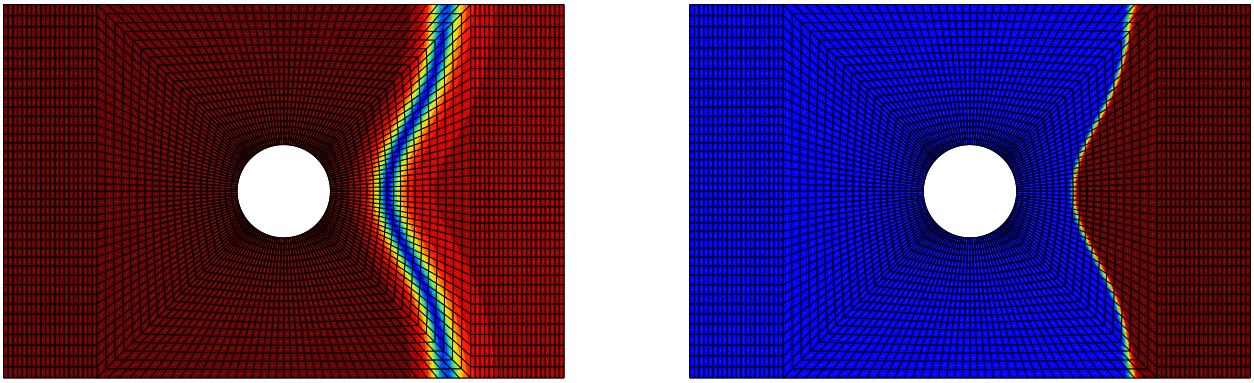

(g) ϕ *and* θ *at* $\bar{t} = 10600$.

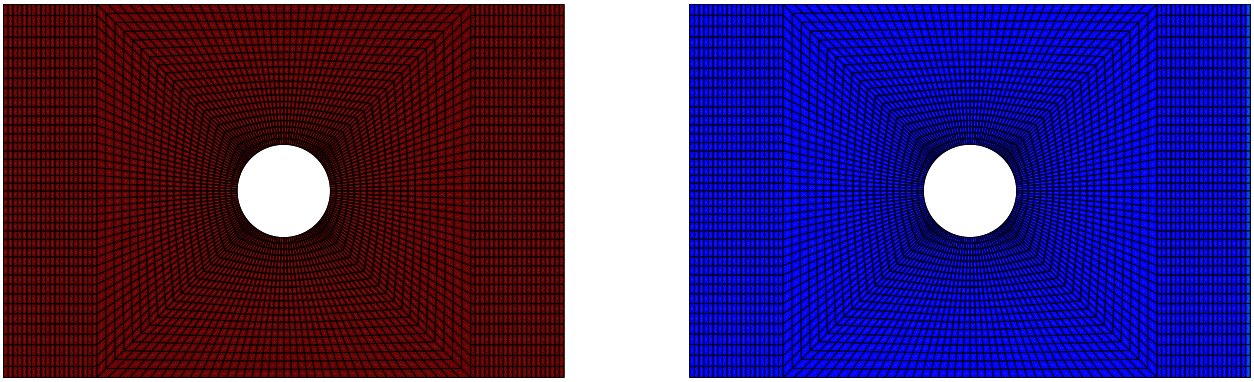

(h) ϕ *and* θ *at* $\bar{t} = 16100$.

Figure 5.8: *Snapshots of the crystal order (ϕ, on the left) and orientation (θ, on the right) fields during simulation of grain boundary migration through a void with the KWC model.*

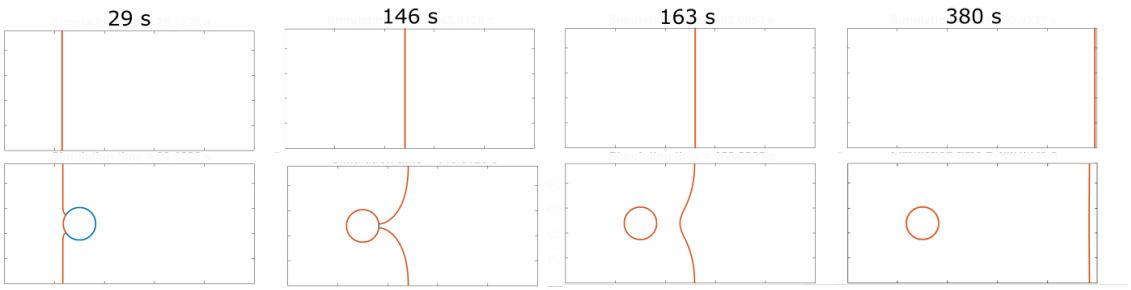

Figure 5.9: *Multi phase-field simulation of grain boundary migration through a void, after Zhang et al. [2022] (supplementary material).*

V.3.4 Inclusion of mechanical effects

The study is now extended by using the KWC-Cosserat model. The initial state, shown in Fig. 5.10, still consists in a grain boundary with a stored energy difference on each side of the interface. The bicrystal is now subjected to compression and subsequent relaxation by imposing a vertical displacement at the top surface that linearly increases from $\bar{u}_y(\bar{t}=0)=0$ to $\bar{u}_y(\bar{t}=20)=-0.1$ and is then held constant. The simulation is in "2.5D" such that the structure can expand axially along the z direction, i.e ε_{zz} is homogeneous and $\varepsilon_{xz}=\varepsilon_{yz}=0$. The parameters used are indicative of pure copper at about $200^{\circ}C$ and are given in table 5.3. All 12 FCC slip systems are considered and the interaction matrix $[h]$ is given by

$$h_{ij}=\begin{cases}\omega_1 \text{ if } i\neq j\\ 1+\omega_1-\omega_2 \text{ else}\end{cases} \tag{5.3}$$

Parameter	$\bar{C}_{11}$	$\bar{C}_{12}$	$\bar{C}_{44}$	$\bar{\mu}_c$	$\bar{K}$	n	$\bar{\tau}_c$	χ	$\bar{\mu}$	K_r	$\bar{d}$	$\bar{b}$	ω_1	ω_2
Value	69600	47800	32600	10000	4.35	10	4.35	0.3	20000	71.4	10^{-3}	0.256	1.5	1.2

Table 5.3: *Material parameters used for the simulation of a bicrystal containing a void and subjected to compression.*

The deformed state is shown in Fig. 5.11. As the grain boundary is parallel to the loading, a compression stress develops within the interface. As expected, stress concentration is observed close to the void, with a magnitude larger than that in the grain boundary. After relaxation, migration of the grain boundary is seen in Fig. 5.12 to occur as per the KWC model studied before. The KWC-Cosserat model provides further information. Notably, grain boundary motion through the void is shown to significantly reduce the stress concentration in the region swept by the interface. Conversely, away from this zone, the stress does not exhibit a drastic decrease in magnitude. In the recent work of Wang et al. [2023], experimental investigations showed that grain boundary migration through voids prevented the nucleation and propagation of micro-cracks through the voids. They explained this phenomenon, through crystal plasticity finite element (CPFE) simulations, by alleviation of stress concentration in the vicinity of the voids, i.e exactly the case studied in this section. However, in their work grain boundary motion was not explicitly accounted for since their approach was based on a 'hard-soft grain pair'. The simulation with the KWC-Cosserat model therefore provides qualitative agreement with their conclusions, but also allows to go beyond the limitations of CPFE through the incorporation of the dynamics of the grain boundary.

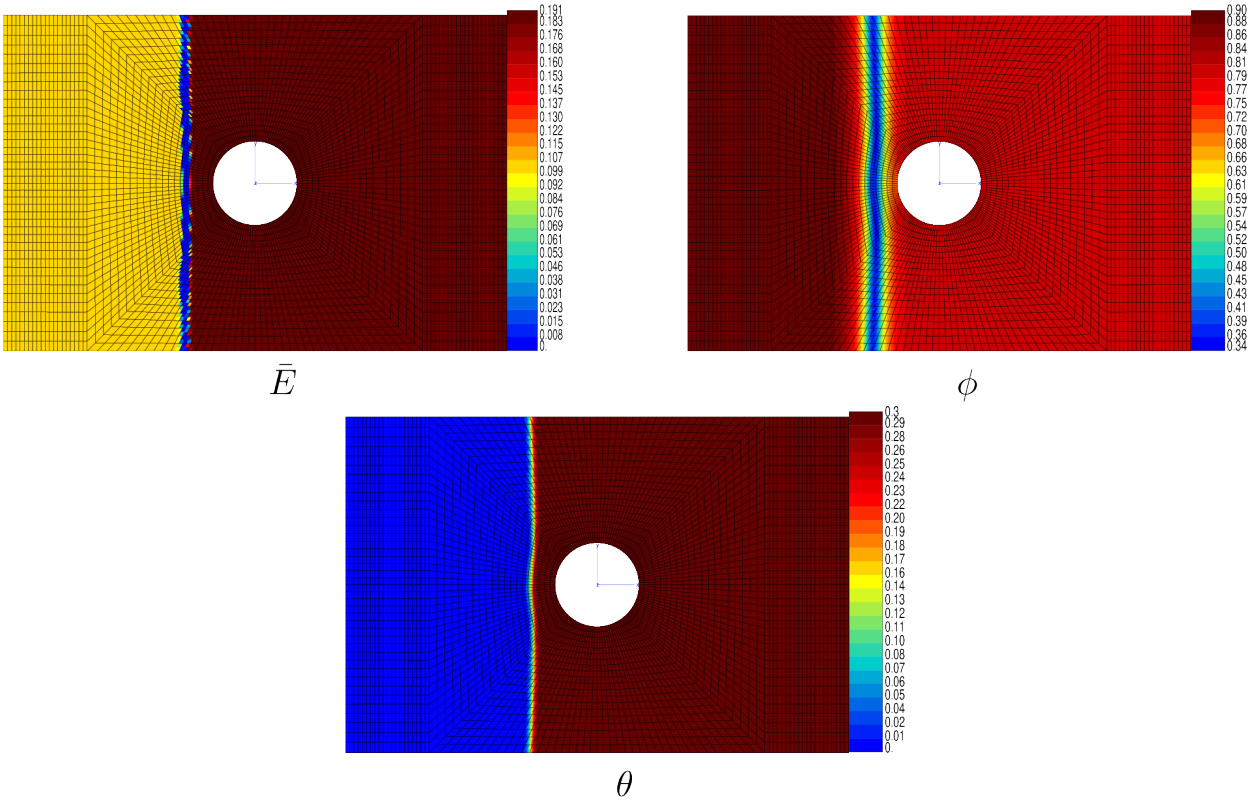

Figure 5.10: *Initial microstructure to study grain boundary migration through a void subjected to compression and subsequent relaxation.*

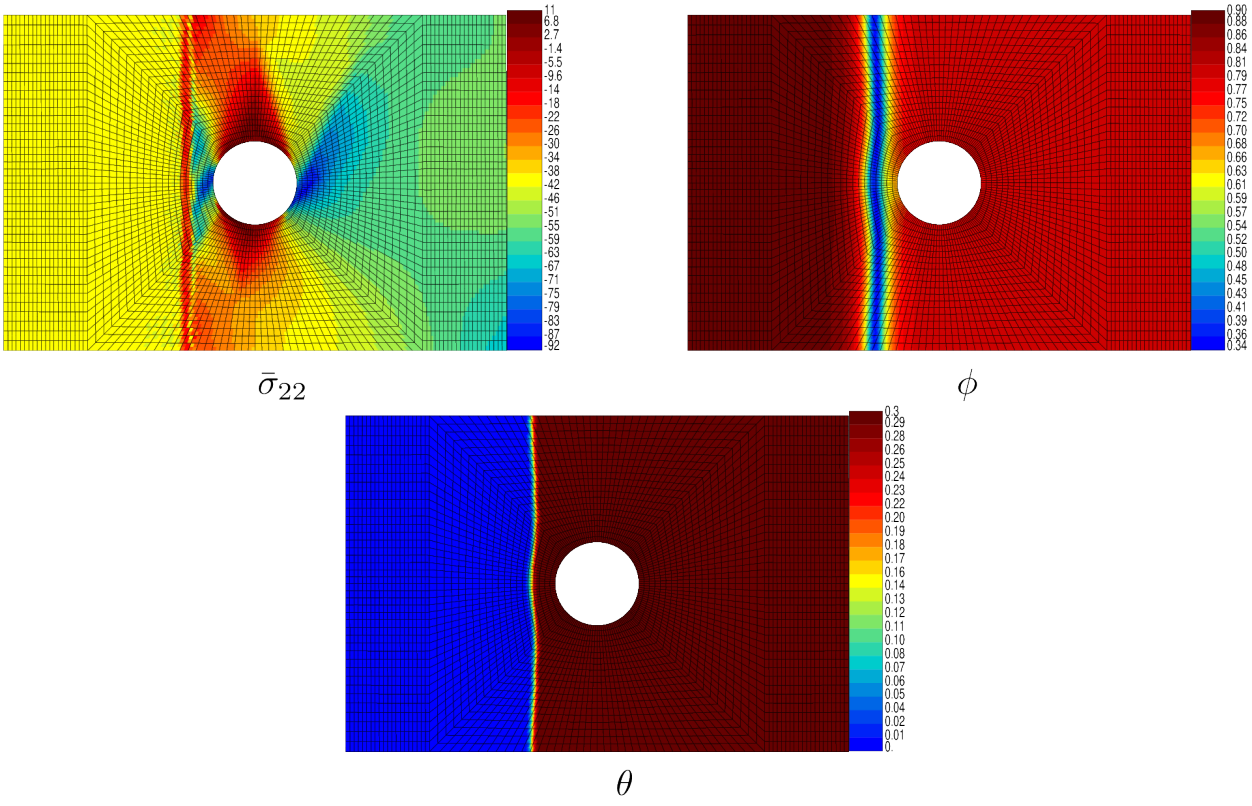

Figure 5.11: *bicrystal with intragranular void after compression ($\bar{t} = 20$)*

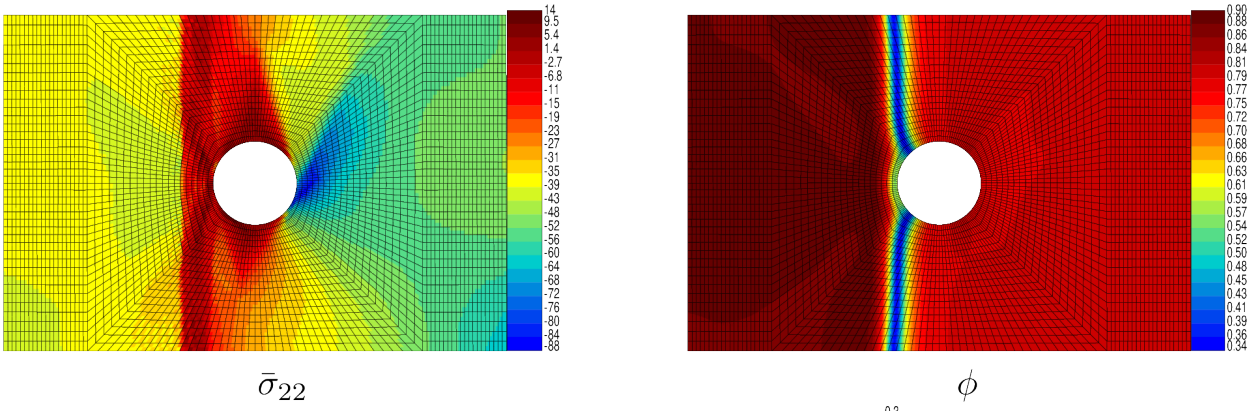

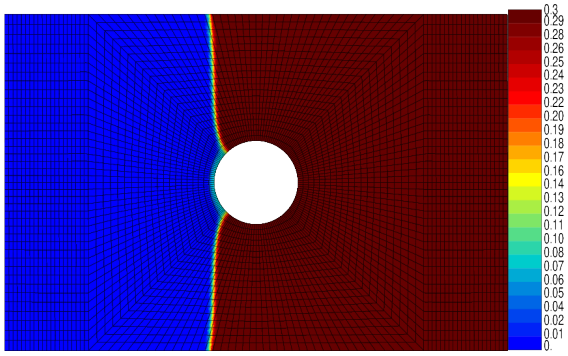

(a) $\bar{t} = 200$

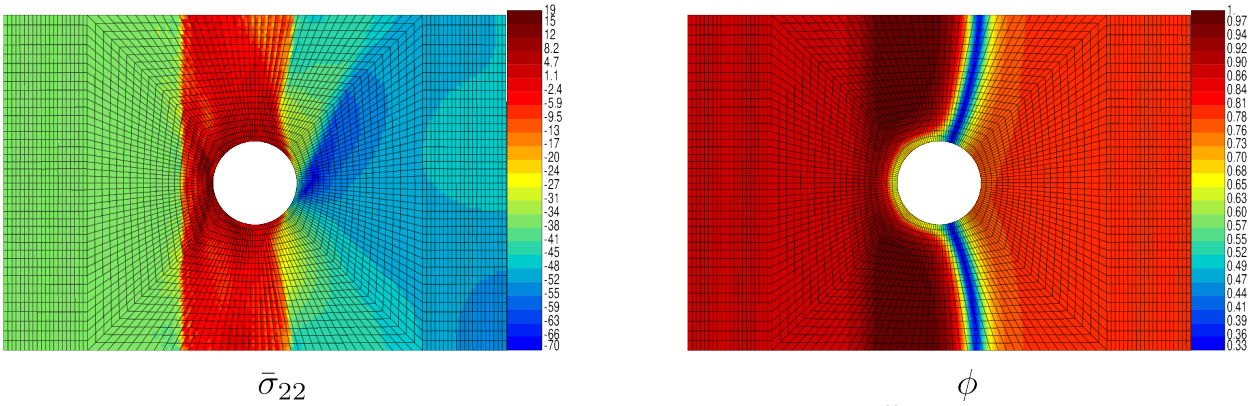

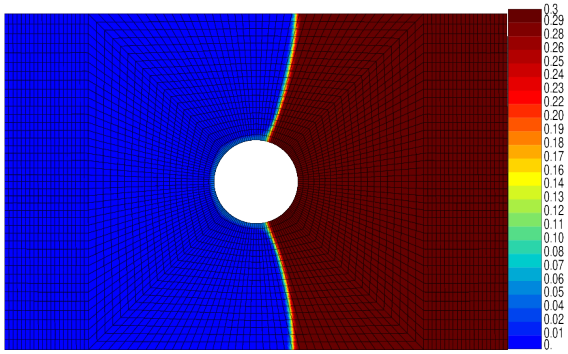

(b) $\bar{t} = 990$

Figure 5.12: *bicrystal with intragranular void after compression and subsequent relaxation*

V.4 Torsion of bicrystals

V.4.1 Misorientation about the rod's axis and GB plane normal parallel to the rod's axis

The case explored in section IV.4 is now reconsidered for a bicrystal. A rod with height $\bar{H} = 10$ and radius $\bar{R} = 1$ is meshed with 1260 quadratic elements with reduced integration and 55089 nodes, resulting in 330534 DOFs. The initial bigrain is obtained from a three-dimensional KWC simulation, which results in a bicrystal with misorientation $\Delta\theta_z = 0.3$. The interface is located at the middle of the rod, as illustrated in Fig. 5.13. The other components of $\underline{\theta}$ are set to 0. The bicrystal is subsequently subjected to torsional loading and relaxation. The boundary conditions and parameters are the same as those in section IV.4 except that at the top and bottom surfaces the boundary condition for θ_z is now of zero flux type. The computation took approximately 117 days on 24 Intel Xeon CPUs and requiring 54GB of memory.

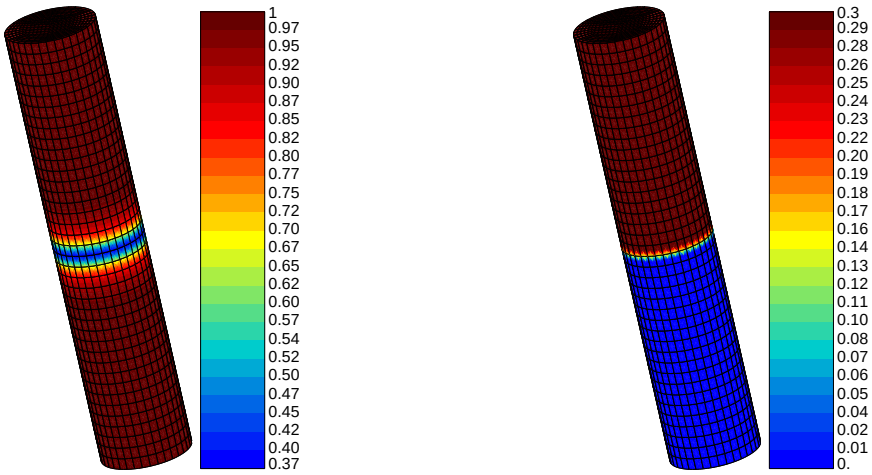

Figure 5.13: *Initial bicrystal obtained with a 3D KWC simulation. The crystal order field is on the left and the lattice orientation θ_z is on the right. The other components of $\underline{\theta}$ are set to 0.*

The results displayed in Fig. 5.14 show that torsional loading generates orientation gradients around the rod's vertical axis, promoting nucleation, just as in single crystals. In comparison with the initial state, a rather uniform lattice orientation gradient is induced in each grain by the mechanical loading. It is also evident that the initial grain boundary remains even after the loading and subsequent relaxation processes. In the early stages of nucleation, newly formed grains with very low misorientation can be observed on either side of the original grain boundary. In addition, they are symmetrically distributed with respect to the centre of the rod. Subsequently, as expected, the grains merge and two subrains remain on each side of the initial grain boundary. The observed symmetry might result from the position of the initial grain boundary. it is assumed that upon further relaxation, the subgrains with low misorientations will merge to form a bicrystal. This computation represents a first step towards KWC-Cosserat modelling of recrystallization in polycrystalline aggregates during torsion. Additional simulations, encompassing columnar bicrystals and tricrystals, need to be conducted. In particular, simulations that explore grains that are not purely misoriented about the rod's axis are required.

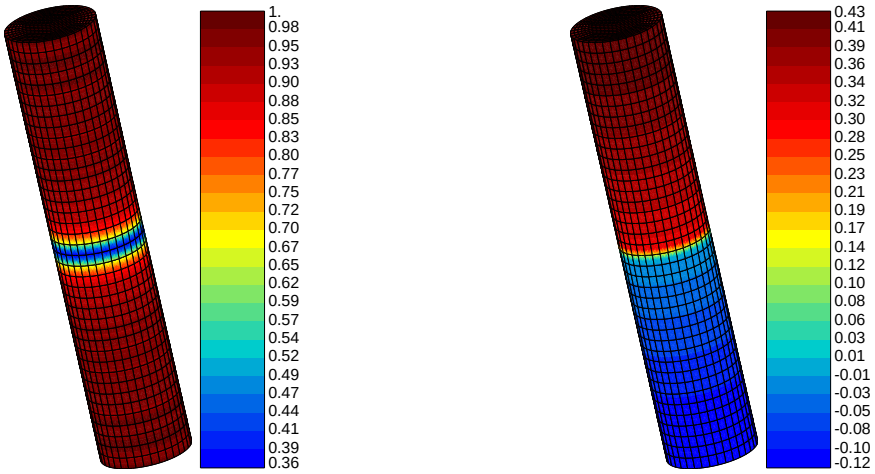

(a) *Crystal order and lattice orientation after torsional loading ($\bar{t} = 1$).*

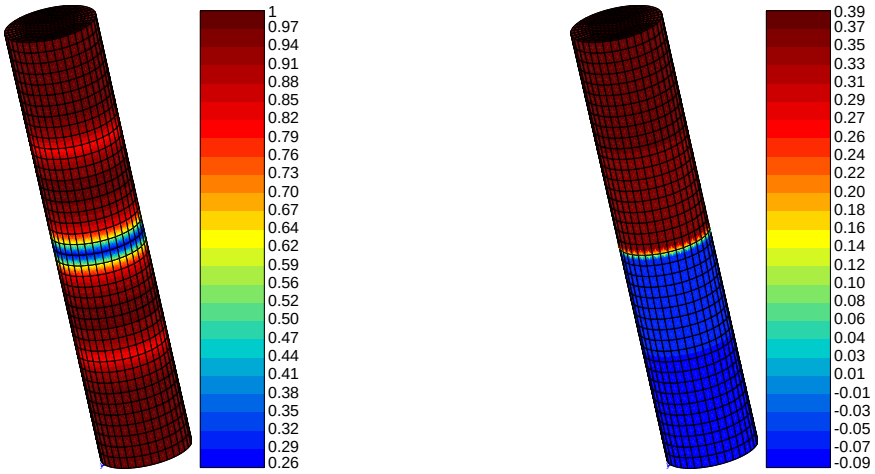

(b) *Crystal order and lattice orientation after torsional loading followed by relaxation ($\bar{t} = 3471$).*

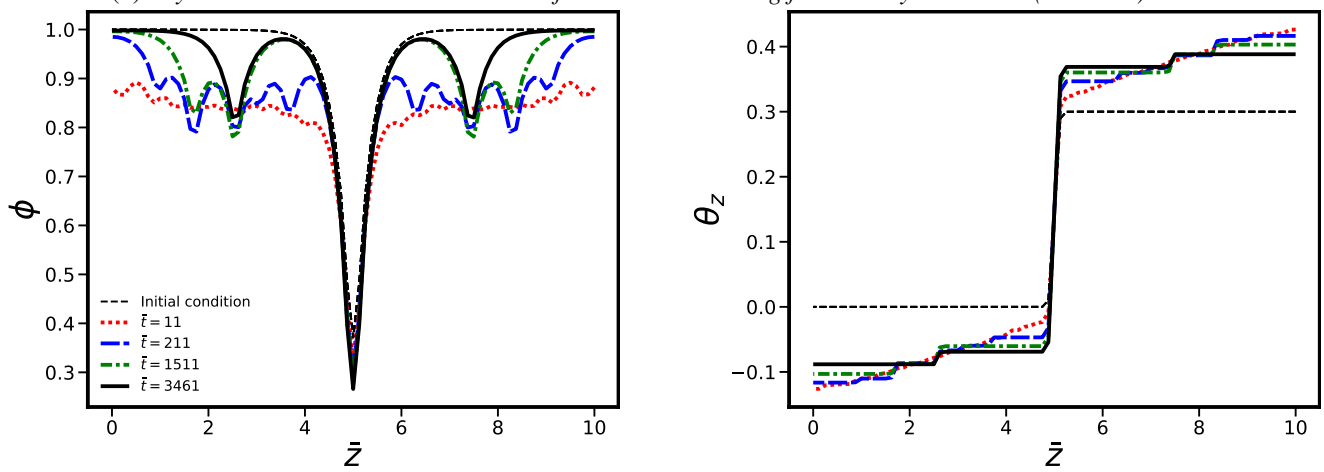

(c) *Profiles along the z axis.*

Figure 5.14: *Crystal order ϕ (left) and lattice orientation θ_z (right) after torsional loading of a bicrystal.*

V.4.2 Misorientation about the rod's axis and GB plane normal orthogonal to the rod's axis

The previous problem is now reconsidered for an initial grain boundary parallel to the rod's axis, with the misorientation still only about the rod's axis. The initial microstructure is shown in Fig. 5.15.

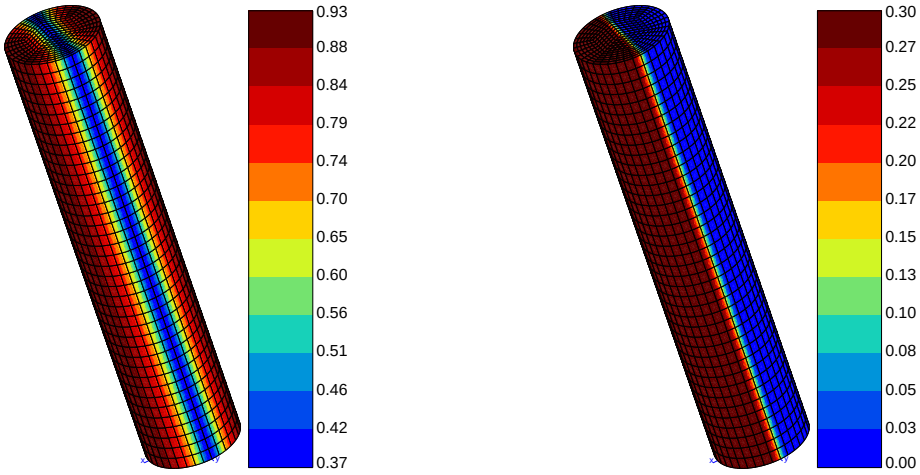

Figure 5.15: *Initial bicrystal obtained with a 3D KWC simulation. The crystal order field is on the left and the lattice orientation θ_z is on the right. The other components of $\underline{\theta}$ are set to 0.*

As usual, mechanical loading induces a strong orientation gradient about the rod's axis. Figure 5.16 shows that the field θ_z after loading is in the form of stacks that are not homogeneous in the cross-section due to the presence of the initial grain boundary. During relaxation, the boundary plane gradually changes over time due to the strong orientation gradient $\theta_{z,z}$. As a result, the boundary normal aligns with the rod's axis, leading to the formation of a bamboo microstructure as in the previous cases.

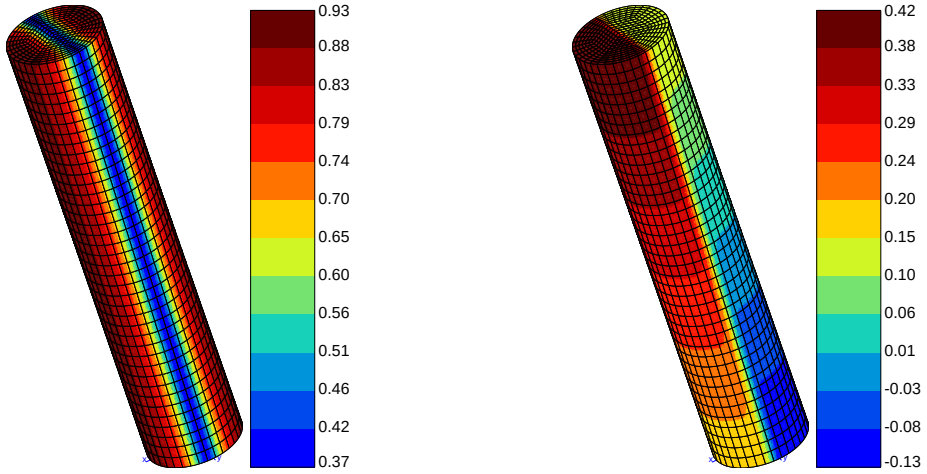

(a) *Crystal order and lattice orientation after torsional loading ($\bar{t} = 1$).*

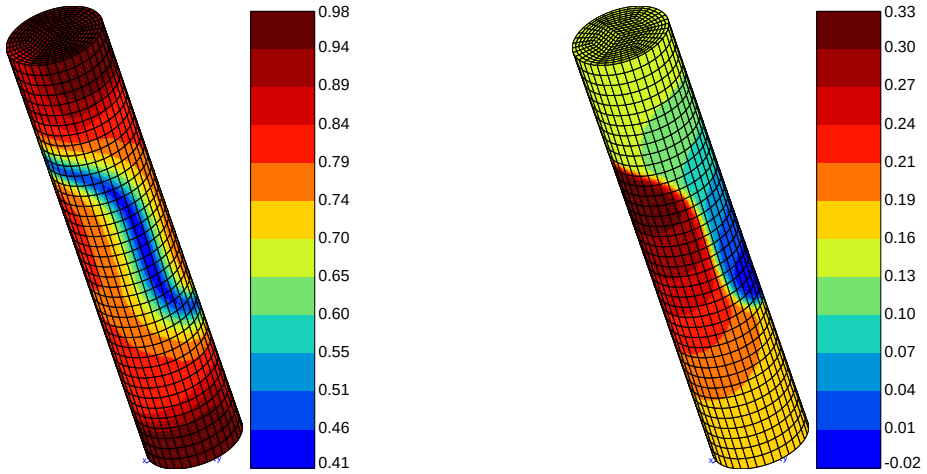

(b) *Crystal order and lattice orientation after torsional loading followed by relaxation ($\bar{t} = 141$).*

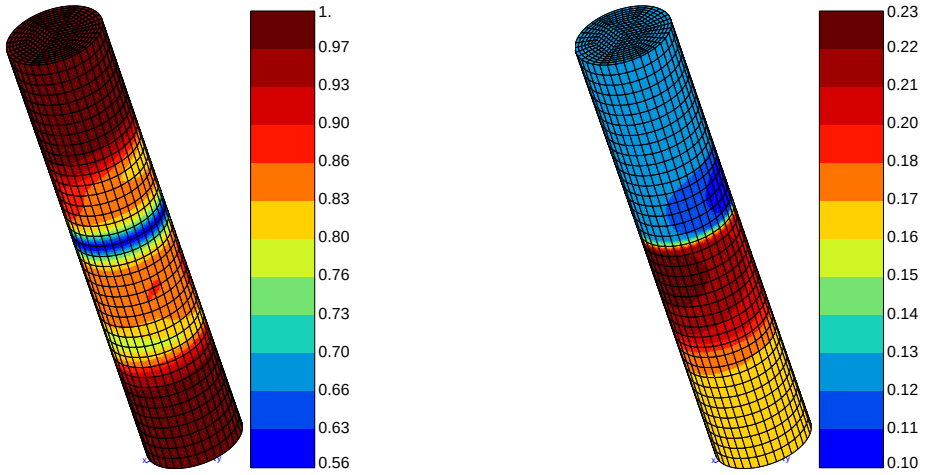

(c) *Crystal order and lattice orientation after torsional loading followed by relaxation ($\bar{t} = 241$).*

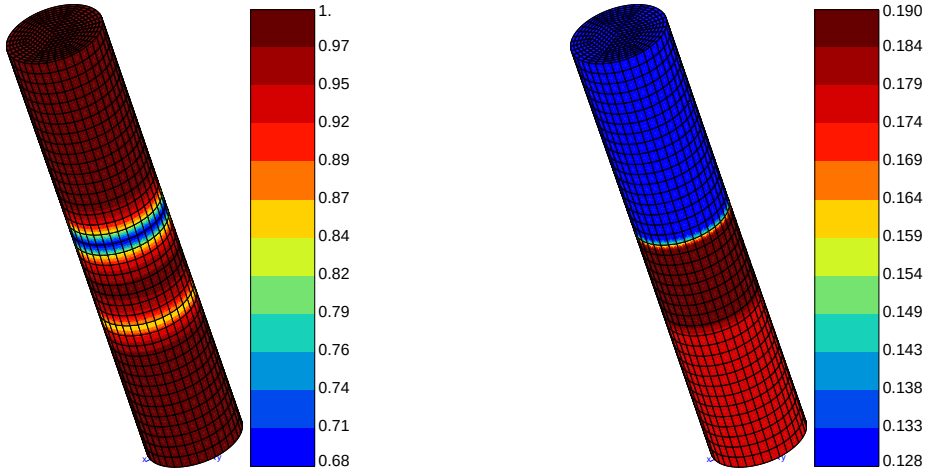

(d) *Crystal order and lattice orientation after torsional loading followed by relaxation ($\bar{t} = 1711$).*

Figure 5.16: *Crystal order ϕ (left) and lattice orientation θ_z (right) after torsional loading of a bicrystal.*

V.5 Summary

Several applications of orientation phase-field models are presented in this chapter as first steps towards modelling microstructure evolution of polycrystalline aggregates. Through the simulation of a periodic polycrystal subjected to periodic shear, the model is shown to account for plastic strain and curvature localization. Kink bands formed mechanically cause subgrain boundary nucleation, resulting in grain fragmentation, as anticipated, which supports previous investigations by Ask et al. [2020]. In contrast, slip bands are unrelated to lattice curvature and therefore cannot result in subgrain nucleation as per the orientation phase-field models.
The KWC model was also used to examine the interaction between a non-meshed intragranular void and a migrating grain boundary. The behaviour is comparable to that of a dislocation passing through a precipitate. Comparison with the work of Zhang et al. [2022] based on a modified Chen-Yang multi-phase-field model demonstrates notable qualitative agreement, despite the fundamentally different modelling approaches. The study was then extended to the compression of a bicrystal containing an intragranular void using the KWC-Cosserat model. The simulation shows a significant reduction of the stress concentration in the region swept by the grain boundary which supports crystal plasticity finite element simulations by Wang et al. [2023].
Additionally, we presented an extension of our research on the torsion of single crystal rods to bicrystals. The interface was located in the centre of the rod and the grains were misoriented solely with respect to the rod's axis. Upon torsional loading, orientation gradients are created, thereby promoting grain nucleation as anticipated. The existence of an initial grain boundary within the microstructure compels, in this particular study, the persistence of the grain boundary even after torsion and relaxation. When the GB plane normal is orthogonal to the rod's axis, the orientation gradient induced by the mechanical loading forces the alignment of the interface normal with the rod's axis.
Additional analysis is necessary to further examine these simulations, but it is clear that the approach can be extended for use in a wider range of applications. One important issue that needs addressing in order to simulate large polycrystalline aggregates is the high computational cost of the current implementation.

Conclusions and prospects

Résumé en français

Cette thèse s'intéresse à la simulation en champs complets d'évolution microstructurales dans les métaux à l'échelle mésoscopique. Pour ce faire, le modèle proposé par Ask et al. [2018b] est utilisé. Celui-ci combine la théorie de Cosserat en plasticité cristalline et le modèle à champs de phase de croissance de grains de Kobayashi-Warren-Carter. Les principaux apports de cette thèse concernent d'un côté la mécanique des milieux de Cosserat et de l'autre la simulation d'évolutions microstructurales. Ainsi, nous proposons dans ce travail de nouvelles solutions analytiques aux problèmes de torsion d'un barreau en plasticité de von Mises généralisée et au cisaillement d'un monocristal. Pour le second cas différentes dépendances du potentiel d'énergie libre vis-à-vis du tenseur de courbure sont considérées.

Nous étendons également le modèle de Ask et al. [2018b] par l'introduction d'une contrainte seuil pour la relaxation aux joints de grains, ce qui résulte en la présence de contraintes résiduelles pouvant gêner le mouvement des interfaces.
Par ailleurs, nous montrons que la présence d'un gradient d'orientation peut entrainer la germination de nouveaux grains de façon "spontanée" (sans introduction ad hoc de nouveaux grains) avec le modèle KWC. Dans cette étude, le gradient d'orientation induit une division du monocristal en une multitude de grains faiblement désorientés qui vont ensuite fusionner, en raison de la diffusivité des joints de grains. Nous illustrons ensuite ce phénomène en simulant la torsion et relaxation d'un monocristal de cuivre avec le modèle KWC-Cosserat, qui mène à une microstructure en bambou. Un accord qualitatif avec des expériences menées sur des monocristaux d'aluminium trouvées dans la littérature est observé.

Les perspectives de ces travaux pourront tenter de remédier aux limites actuelles du modèle utilisé. A court terme, celles-ci concernent principalement l'établissement d'une procédure de calibration plus robuste concernant les paramètres de mobilité et l'amélioration des temps de calcul par décomposition de domaines et intégration implicite de type $\theta-$method pour les lois de comportement. L'extension au grandes déformations, rotations et courbure s'avérera probablement nécessaire pour la modélisation des procédés de mise en forme. Enfin, l'étude de la germination en torsion devra être étendue aux polycristaux et la simulation des mécanismes de type SIBM ou grain coarsening devra être étudiée.

Sur le long terme, la prise en compte explicite de la température pourra s'avérer intéressante pour modéliser l'effet de gradients thermiques. Il pourrait également être utile de considérer une approche par multiplicateurs de Lagrange pour appliquer la contrainte $\overset{\times}{\underline{e}}^{e} = \underline{0}$ plutôt que la pénalisation actuellement utilisée. En outre, une prise en compte de l'anisotropie des propriétés des joints de grains (vis-à-vis du plan de joint par exemple) sera requise pour augmenter la pertinence du modèle. Enfin, il serait intéressant d'appliquer le modèle au design de microstructures bimodales.

Main results

The current thesis focuses on the mesoscale full-field simulation of microstructure evolution in metals. To achieve this, we employed and further developed the model formulated by Ask et al. [2018b]. This particular model combines Cosserat crystal plasticity and the Kobayashi-Warren-Carter phase-field model of grain growth. The individual frameworks for each segment of the model are presented and subsequently the unified model is recalled. The main original contributions found in this work concern two topics: on the one hand, Cosserat continuum mechanics and on the other hand, simulating microstructure evolution with the KWC-Cosserat model. The main results of the thesis can be summarized as follows:

- **Cosserat continuum mechanics of isotropic elastic-plastic structures**: new analytical solutions have been developed for the torsion problem of isotropic elastic-plastic rods. The framework only includes the symmetric part of the deviatoric stress tensor and uses a reduced form of the extended von Mises yield criterion. However, the stress tensor itself is non-symmetric in general. The torsional response of this model naturally exhibits a size effect of the normalized torque that is proportional to the inverse of the rod's radius and dependent on the twist angle. Comparison with results obtained using the Finite Element Method through Zset software demonstrates perfect agreement.

- **Cosserat crystal plasticity**: new analytical solutions are derived for a single crystal under shear loading. Different dependencies of the Helmholtz free energy density on the curvature tensor are assessed, including quadratic, rank one, and combined quadratic-rank one. Analytical solutions are demonstrated in both elasticity and crystal plasticity, with comparisons made to strain gradient plasticity that is based on the dislocation density tensor $\mathrm{Curl}\,(H^p)$. In crystal plasticity, these solutions exhibit a noticeable size effect that is directly proportional to L^{-2} and L^{-1}, where L is the half length of the material strip, depending on whether the dependence of the free energy on the curvature tensor is quadratic or rank one.

- **KWC-Cosserat modelling of grain boundaries**: our work discusses the development and relaxation of stresses during grain boundary formation and migration. It assesses the role of the selected function in relaxing skew-symmetric stresses for stationary and mobile grain boundaries. These skew-symmetric stresses are relaxed in a stable grain boundary. The relaxation function includes a stress threshold in two distinct models: a viscoplastic Norton law with a threshold and a rate-independent law based on isotropic plasticity. Incorporating a threshold into the relaxation law leads to residual stresses that could hinder both formation and movement of the grain boundary. The bicrystal's stress profiles exhibit similarities to the elasto-plastic theory of dislocations and disclinations [Taupin et al., 2013]. Afterwards, the finite element implementation of a 3D version of the KWC-Cosserat model with Maxwell relaxation, programmed in the Z-set software, is presented. The three-dimensional version was tested against the two-dimensional one in various scenarios, including the formation of grain boundaries and periodic shear of a periodic bicrystal.

- **Modelling grain nucleation with the KWC model**: a linear perturbation analysis and finite element simulations demonstrate that the existence of a lattice orientation gradient in a single crystal results in (sub)grain formation to accommodate the gradient. This nucleation proceeds depending on material parameter values that are indicative of temperature. The simulations reveal that the original single crystal is divided into a multitude of grains with low misorientation (LAB), which, due to interaction between diffuse grain boundary zones, grow and merge together. Tracking the time evolution of the total energy demonstrated that grain nucleation aids in the minimisation of the total energy. Conversely, a gradient of the crystal order field, caused by a heterogeneous SSD distribution, does not lead to the formation of new (sub)grain boundaries.

- **Modelling grain nucleation with the KWC-Cosserat model**: a three-dimensional finite element simulation, which incorporated crystal plasticity and grain boundary formation, was conducted on a single crystal bar with a circular cross-section to study torsion. Firstly, initial quasi-static torsion was

performed, after which simulation of relaxation was carried out during a relaxation stage. The torsion axis was aligned with the [111] direction of the FCC crystal. The application of torsion caused a substantial gradient of rotation along the cylinder axis. This was adequate to initiate the formation of grains in the shape of a stack of cylinders with low angle boundaries between them, which matches the 1D stability analysis. Consequently, a bamboo-style subgrain microstructure was developed within the wire. Experimental evidence supporting the torsion simulation result was discovered during the study of the torsion of aluminum single crystals under creep loading in [Kassner, 1989; Kassner and Barrabes, 2005]. It was observed that stacks of Low Angle Boundaries (LABs) were parallel to the (111) planes.

- **Applications of the orientation phase-field models**: simulations of periodic polycrystalline aggregates with a single slip system per grain subjected to periodic shear loading evidenced the capability of the KWC-Cosserat model to account for strain localization. The formation of kink bands and subsequent subgrain boundary nucleation was observed and support previous investigations by Ask et al. [2020]. Plastic slip localization in the form of slip bands was also captured but did not lead to nucleation of new boundaries. Finally, the interaction of a grain boundary and an intragranular void showed remarkable qualitative agreement with the modified Chen-Yang multi phase-field in the work of Zhang et al. [2022].

Numerical implementations in the finite element code Z-set

During the work carried out in this PhD thesis, the following implementations were added in the Z-set software:

- **Time implicit integration of isotropic Cosserat (visco)plasticity**: isotropic Cosserat (visco)plasticity was implemented in Zset only for time explicit integration using Runge-Kutta's method. In this work we added a time implicit integration using the θ-method that is detailed in A.
- **Relaxation laws in KWC-Cosserat models**: in addition to Maxwell's law, viscoplastic isotropic and Norton laws as well as rate-independent viscoplasticity were programmed.
- **Three-dimensional KWC-Cosserat model**: the 2D KWC-Cosserat finite element implementation was extended to 3D based on the weak form of the balance equations.

Current limitations

- **Parameter identification procedure**: currently, the outcomes achieved with the KWC-Cosserat model remain rather qualitative. The first step towards more quantitative predictions would be to develop a proper parameter calibration procedure based on experimental results. Currently, the mechanical parameters are not identified on the basis of experiments carried out over a specific temperature range, but are taken from the literature. Furthermore, the phase-field parameters are fitted based on a 0K grain boundary energy, despite the simulated phenomena occurring during material heating. The most challenging aspect, however, lies in the identification of mobility parameters, as the current procedure is inadequate. Indeed, the mobility parameters are chosen based on numerical tests of stored energy driven of a flat interface.
- **Computational cost**: the substantial computational cost in the present model implementation posed a challenge. It is still unclear whether this is an inherent feature of the model or a consequence of the implementation. The finite element scheme involves seven degrees of freedom for each node, and the nonlinear equations to solve are very stiff.
- **Infinitesimal deformation framework**: the current model assumes infinitesimal deformations, which is inappropriate for metal forming as it occurs mainly at large strains and curvatures.

Prospects

Various enhancements can be made based on the current limitations of this work and are proposed in the following:

Short term prospects

- **Parameter identification procedure**: stored energy and curvature driven grain boundary migration experiments in bicrystals as described by Gottstein and Shvindlerman [2009] could be carried out. A large amount of simulations that aim at reproducing these experiments could then be carried out to retrieve the mobility parameters.

- **Reduction of the computational cost**: parallel computing based on domain decomposition might be a way to deal with this issue. Furthermore, the explicit Runge-Kutta method is currently used to integrate the constitutive laws of the KWC-Cosserat model, necessitating small time steps. Yet, the implicit θ–method could conceivably reduce computation time by allowing for larger time steps. Additionally, the optimum element type and form of shape functions were not examined in this thesis. Alternative numerical methods, including fast Fourier transforms, might be worth investigating.

- **Extension to Finite Strains, Rotation and Curvature**: a proposed extension to the model by Ask et al. [2019] tackles this issue theoretically, but numerical implementation is yet to be done. The changeover to finite deformations entails additional numerical complexity due to the nonlinearity of rotations compared to the present deformation framework. In addition, remeshing operations might be needed. Yet, this extension is imperative to ensure accurate simulation of thermomechanical processes. The PhD thesis of Russo [2022] presents theoretical and numerical aspects of finite deformation Cosserat mechanics that could be used for the numerical implementation of the KWC-Cosserat model at finite deformation.

- **Grain nucleation during torsion**: further experimental and numerical studies are required to investigate nucleation caused by curvature heterogeneities induced by mechanical loading in the torsion of crystals. Conducting numerical creep tests could help bring the simulations closer to the experimental results of Kassner [1989]. An extension of the study to a bicrystal has been presented, but additional investigation regarding the location of the grain boundary is needed. The case of tricrystals and polycrystals could also be explored.

- **Modelling physical mechanisms of grain nucleation**: we believe that orientation phase-field models may be able to model physical mechanisms of grain nucleation, such as Strain Induced Boundary Migration and subgrain coarsening. A first attempt at simulating SIBM with the KWC model can be found in Abrivard [2009]. In this simulation the stored energy difference results from a heterogeneous initial distribution of stored energy and not from mechanical loading. Similarly, Takaki and Tomita [2010] modelled subgrain growth using a multi phase-field approach. Simulations of both mechanisms with a unified model that combines crystal plasticity and grain growth remain to be done.

- **Modeling nucleation at preferential sites**: grain boundaries and triple junctions are likely nucleation sites during recrystallization. As demonstrated in this work, the model captures nucleation in the presence of lattice orientation gradients. In the literature, such large lattice orientation gradients have been reported near triple junctions [Humphreys, 2004]. It would be interesting to see if the model is able to reproduce such phenomenon. This would probably require the orientation gradient to extend over a region that is multiple times larger than the diffuse interface width.

Long term prospects

- **Explicit incorporation of temperature**: currently, temperature is related to the mobility of grain boundaries. Although adding an extra degree of freedom would increase the already high computational cost, it could enhance the physical relevance of the model and potentially allow to explore

anisothermal effects and microstructure evolution induced by thermal gradients. Another approach could be to express the material parameters as functions of temperature (typically Arrhenius laws) not as a degree of freedom, but rather as a parameter derived from previous thermal calculations.

- **Fine tuning the relaxation behaviour of the grain boundaries**: restriction of the relaxation behaviour to the grain boundaries is currently achieved by using a function that depends on the orientation gradient. Alternatively, a more appropriate approach could be to use a rule of mixtures. In addition, the formulation of the inverse mobility/localization function might also be changed to, for instance, allow for grain rotation to occur below a certain grain size.

- **Enforcing the internal constraint** $\overset{\times}{\underline{e}}^{e} = \underline{0}$: nullity of the skew symmetric part of the elastic strain is achieved via the Cosserat coupling modulus μ_c acting as a penalization parameter. An alternative would be to resort to Lagrange multiplier. We believe that this could potentially help in reducing the stress oscillations that develop in the grain boundaries. The effect of not enforcing this constraint locally might also be worth investigating.

- **Accounting for anisotropic properties of the grain boundaries**: even though misorientation dependence of properties such as grain boundary energy is accounted for, the same cannot be said for the boundary plane. Building on early considerations of this issue by Kobayashi et al. [2000]; Warren et al. [2003], a fully anisotropic 3D KWC model that accounts for the orientation axis and the inclination of the grain boundary plane was developed by Admal et al. [2019].

- **Application to the design of bimodal microstructures**: the orientation phase-field models are yet to be used to design microstructures combining two distinct grain sizes, i.e allowing both ductility and sufficient hardening. Examples of numerical bimodal microstructures taken from [Flipon et al., 2020] are shown in Fig 5.17.

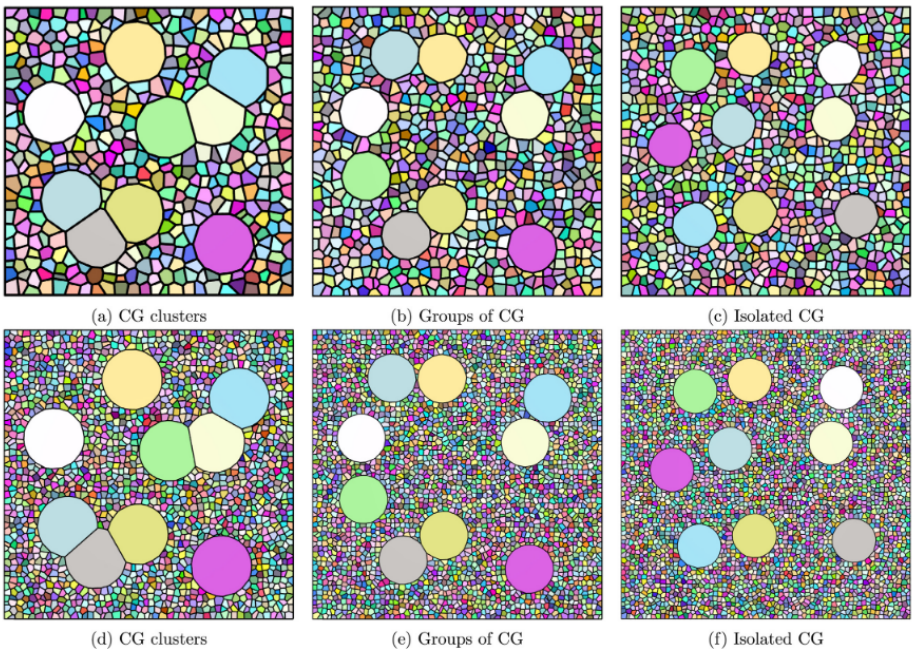

Figure 5.17: *Example of numerical bimodal microstructures after Flipon et al. [2020] for different coarse grain distributions. Grain size ratio of 5 (a-c) and 10 (d-f).*

Appendices

Appendix A

Time implict integration of Cosserat (visco)plasticity

Contents

I.1 Introduction

In this section the objective is to derive the expressions of the consistent tangent matrices for Prandtl-Reuss (isotropic law with isotropic hardeining) viscoplasticity and rate-independent plasticity of a Cosserat medium using the θ-method based on [Besson et al., 2009] (pp 337-343). The consistent tangent matrices $\begin{bmatrix} \underset{\approx}{L}_c^{\sigma} \\ \underset{\approx}{L}_c^{m} \end{bmatrix}$ to determine are given by $\begin{bmatrix} \Delta\underset{\sim}{\sigma} \\ \Delta\underset{\sim}{m} \end{bmatrix} = \begin{bmatrix} \underset{\approx}{L}_c^{\sigma} & 0 \\ 0 & \underset{\approx}{L}_c^{m} \end{bmatrix} : \begin{bmatrix} \Delta\underset{\sim}{e}^e \\ \Delta\underset{\sim}{\kappa}^e \end{bmatrix}$ with $\begin{bmatrix} \Delta\underset{\sim}{e}^e \\ \Delta\underset{\sim}{\kappa}^e \\ \Delta p \end{bmatrix} = [J]^{-1} \begin{bmatrix} \Delta\underset{\sim}{e} \\ \Delta\underset{\sim}{\kappa} \\ 0 \end{bmatrix}$ where $[J]$ is the Jacobian matrix.

For an increment $\Delta\underset{\sim}{e}$ non purely elastic, the system to solve is

$$\begin{bmatrix} \underset{\sim}{r}_e^{\sigma} \\ \underset{\sim}{r}_e^{m} \\ \underset{\sim}{r}^{p} \end{bmatrix} = \begin{bmatrix} \Delta\underset{\sim}{e} \\ \Delta\underset{\sim}{\kappa} \\ 0 \end{bmatrix}$$

where $\underset{\sim}{r}_e^{\sigma}$ is the elastic residual with respect to $\underset{\sim}{e}$, $\underset{\sim}{r}_e^{m}$ the elastic residual with respect to $\underset{\sim}{\kappa}$ and $\underset{\sim}{r}^{p}$ the inelastic residual. $\Delta\underset{\sim}{e}$, $\Delta\underset{\sim}{\kappa}$, Δp are respectively the increments of total strain, total curvature and accumulated plastic strain. The expressions of the residuals are:

$$\begin{bmatrix} \underset{\sim}{r}_e^{\sigma} \\ \underset{\sim}{r}_e^{m} \\ r^{p} \end{bmatrix} = \begin{bmatrix} \Delta\underset{\sim}{e}^e + \Delta p \underset{\sim}{n}_{\theta}^{\sigma} \\ \Delta\underset{\sim}{\kappa}^e + \Delta p \underset{\sim}{n}_{\theta}^{m} \\ f\left(\underset{\sim}{\sigma}_{t+\theta\Delta t},\ \underset{\sim}{m}_{t+\theta\Delta t}\right) \end{bmatrix}$$

The Jacobian matrix is then given by:

$$[J] = \begin{bmatrix} \dfrac{\partial \underset{\sim}{r}^{\sigma}_{e}}{\partial \Delta \underset{\sim}{e}^{e}} & \dfrac{\partial \underset{\sim}{r}^{\sigma}_{e}}{\partial \Delta \underset{\sim}{\kappa}^{e}} & \dfrac{\partial \underset{\sim}{r}^{\sigma}_{e}}{\partial \Delta p} \\ \dfrac{\partial \underset{\sim}{r}^{\tilde{m}}_{e}}{\partial \Delta \underset{\sim}{e}^{e}} & \dfrac{\partial \underset{\sim}{r}^{\tilde{m}}_{e}}{\partial \Delta \underset{\sim}{\kappa}^{e}} & \dfrac{\partial \underset{\sim}{r}^{m}_{e}}{\partial \Delta p} \\ \dfrac{\partial r^{\tilde{p}}}{\partial \Delta \underset{\sim}{e}^{e}} & \dfrac{\partial r^{\tilde{p}}}{\partial \Delta \underset{\sim}{\kappa}^{e}} & \dfrac{\partial r^{p}}{\partial \Delta p} \end{bmatrix}$$

The inverse of the Jacobian matrix is made of blocks:

$$\begin{bmatrix} \Delta \underset{\sim}{e}^{e} \\ \Delta \underset{\sim}{\kappa}^{e} \\ \Delta p \end{bmatrix} = \begin{bmatrix} \underset{\approx}{J}^{\sigma\star} & \bullet & \bullet \\ \bullet & \underset{\approx}{J}^{m\star} & \bullet \\ \bullet & \bullet & \bullet \end{bmatrix} \cdot \begin{bmatrix} \Delta \underset{\sim}{e} \\ \Delta \underset{\sim}{\kappa} \\ 0 \end{bmatrix}$$

The tangent matrices are then:

$$\begin{bmatrix} \underset{\approx}{L}^{\sigma}_{c} \\ \underset{\approx}{L}^{m}_{c} \end{bmatrix} = \begin{bmatrix} \underset{\approx}{\Lambda}^{\sigma}_{\theta} & 0 \\ 0 & \underset{\approx}{\Lambda}^{m}_{\theta} \end{bmatrix} : \begin{bmatrix} \underset{\approx}{J}^{\sigma\star} \\ \underset{\approx}{J}^{m\star} \end{bmatrix}$$

where $\begin{bmatrix} \underset{\approx}{\Lambda}^{\sigma}_{\theta} \\ \underset{\approx}{\Lambda}^{m}_{\theta} \end{bmatrix} = \begin{bmatrix} \dfrac{\partial \underset{\sim}{\sigma}(t+\theta\Delta t)}{\partial \underset{\sim}{e}^{e}(t+\theta\Delta t)} \\ \dfrac{\partial \underset{\sim}{m}(t+\theta\Delta t)}{\partial \underset{\sim}{\kappa}^{e}(t+\theta\Delta t)} \end{bmatrix}$

For a Cosserat medium with an isotropic elasticity law they can be retrieved knowing that

$$\underset{\sim}{\sigma} = \lambda \mathrm{tr}(\underset{\sim}{e}^{e})\underset{\sim}{I} + 2\mu \frac{\underset{\sim}{e}^{e} + \underset{\sim}{e}^{e^{T}}}{2} + 2\mu_{c} \frac{\underset{\sim}{e}^{e} - \underset{\sim}{e}^{e^{T}}}{2}$$

which is equivalent to

$$\underset{\sim}{\sigma} = \lambda \mathrm{tr}(\underset{\sim}{e}^{e})\underset{\sim}{I} + 2(\mu + \mu_{c})\underset{\sim}{e}^{e} + 2(\mu - \mu_{c})\underset{\sim}{e}^{e^{T}}$$

which can be rewritten as

$$\boxed{\underset{\sim}{\sigma} = \underset{\approx}{\Lambda}^{\sigma} : \underset{\sim}{e}^{e}}$$

with

$$\boxed{\underset{\approx}{\Lambda}^{\sigma} = \lambda \underset{\sim}{I} \otimes \underset{\sim}{I} + 2(\mu + \mu_{c})\underset{\approx}{I} + 2(\mu - \mu_{c})\underset{\approx}{I}^{T}}$$

where

$$\underset{\approx}{I} = \delta_{ik}\delta_{jl}, \ \underset{\approx}{I}^{T} = \delta_{jk}\delta_{il}$$

Similarly we have

$$\boxed{\underset{\sim}{m} = \underset{\approx}{\Lambda}^{m} : \underset{\sim}{\kappa}^{e}}$$

with

$$\boxed{\underset{\approx}{\Lambda}^{m} = \alpha \underset{\sim}{I} \otimes \underset{\sim}{I} + 2(\beta + \gamma)\underset{\approx}{I} + 2(\beta - \gamma)\underset{\approx}{I}^{T}}$$

Finally:

$$\begin{aligned}
\underset{\sim}{e}^e_{t+\Delta t} &= \underset{\sim}{e}^e_{t+\theta\Delta t} + (1-\theta)\Delta\underset{\sim}{e}^e \\
\underset{\sim}{\kappa}^e_{t+\Delta t} &= \underset{\sim}{\kappa}^e_{t+\theta\Delta t} + (1-\theta)\Delta\underset{\sim}{\kappa}^e \\
p_{t+\Delta t} &= p_{t+\theta\Delta t} + (1-\theta)\Delta p
\end{aligned}$$

I.2 Prandtl-Reuss rate indepedent elastoplasticity

I.2.1 Single criterion framework

The Prandtl-Reuss law for a Cosserat medium is given by

$$\boxed{f(\underset{\sim}{\sigma},\ \underset{\sim}{m}) = J_2(\underset{\sim}{\sigma},\ \underset{\sim}{m}) - R(p)}$$

where $J_2(\underset{\sim}{\sigma},\ \underset{\sim}{m})$ is the extended von Mises equivalent stress Forest [2005]

$$\boxed{J_2(\underset{\sim}{\sigma},\ \underset{\sim}{m}) = \sqrt{a_1\underset{\sim}{\sigma}' : \underset{\sim}{\sigma}' + a_2\underset{\sim}{\sigma}' : \underset{\sim}{\sigma}'^T + b_1\underset{\sim}{m} : \underset{\sim}{m} + b_2\underset{\sim}{m} : \underset{\sim}{m}^T}}$$

The plastic strain rate and curvature rate tensors are then given by

$$\dot{\underset{\sim}{e}}^p = \dot{p}\frac{\partial f}{\partial \underset{\sim}{\sigma}},\ \dot{\underset{\sim}{\kappa}}^p = \dot{p}\frac{\partial f}{\partial \underset{\sim}{m}}$$

where the normals to the yield surface appear:

$$\boxed{\underset{\sim}{n}^\sigma := \frac{\partial f}{\partial \underset{\sim}{\sigma}} = \frac{a_1\underset{\sim}{\sigma}' + a_2\underset{\sim}{\sigma}'^T}{J_2(\underset{\sim}{\sigma},\ \underset{\sim}{m})},\ \underset{\sim}{n}^m := \frac{\partial f}{\partial \underset{\sim}{m}} = \frac{b_1\underset{\sim}{m} + b_2\underset{\sim}{m}^T}{J_2(\underset{\sim}{\sigma},\ \underset{\sim}{m})}}$$

Let us now compute the components of the Jacobian matrix at time $t+\theta\Delta t$ where $X_t = X(t)$ and $X_\theta = x(t+\theta\Delta t)$. First, let us compute the derivatives of $\underset{\sim}{r}^\sigma_e$

$$\begin{aligned}
\frac{\partial \underset{\sim}{r}^\sigma_e}{\partial \Delta\underset{\sim}{e}^e} &= \frac{\partial}{\partial \Delta\underset{\sim}{e}^e}\left(\Delta\underset{\sim}{e}^e + \Delta\underset{\sim}{e}^p\right) \\
&= \frac{\partial}{\partial \Delta\underset{\sim}{e}^e}\left(\Delta\underset{\sim}{e}^e + \Delta p\underset{\sim}{n}^\sigma_\theta\right) \\
&= \underset{\approx}{I} + \Delta p\frac{\partial \underset{\sim}{n}^\sigma_\theta}{\partial \underset{\sim}{\sigma}_\theta} : \frac{\partial \underset{\sim}{\sigma}_\theta}{\partial \underset{\sim}{e}^e_\theta} : \frac{\partial \underset{\sim}{e}^e_\theta}{\partial \Delta\underset{\sim}{e}^e}
\end{aligned}$$

knowing that

$$\frac{\partial \underset{\sim}{e}^e_\theta}{\partial \Delta\underset{\sim}{e}^e} = \frac{\partial \underset{\sim}{e}^e_t + \theta\Delta\underset{\sim}{e}^e}{\partial \Delta\underset{\sim}{e}^e} = \theta\underset{\approx}{I}$$

as well as

$$\frac{\partial \underset{\sim}{\sigma}_\theta}{\partial \underset{\sim}{e}^e_\theta} = \underset{\approx}{\Lambda}^\sigma_\theta$$

and

$$\begin{aligned}
\frac{\partial \underset{\sim}{\boldsymbol{n}}^{\sigma}_{\theta}}{\partial \underset{\sim}{\boldsymbol{\sigma}}_{\theta}} &= \frac{\partial}{\partial \underset{\sim}{\boldsymbol{\sigma}}_{\theta}} \left(\frac{a_1 \underset{\sim}{\boldsymbol{\sigma}}'_{\theta} + a_2 \underset{\sim}{\boldsymbol{\sigma}}'^{T}{}_{\theta}}{J_2(\underset{\sim}{\boldsymbol{\sigma}}_{\theta},\, \underset{\sim}{\boldsymbol{m}}_{\theta})} \right) \\
&= \frac{J_2(\underset{\sim}{\boldsymbol{\sigma}}_{\theta},\, \underset{\sim}{\boldsymbol{m}}_{\theta}) \frac{\partial}{\partial \underset{\sim}{\boldsymbol{\sigma}}_{\theta}} \left(a_1 \underset{\sim}{\boldsymbol{\sigma}}'_{\theta} + a_2 \underset{\sim}{\boldsymbol{\sigma}}'^{T}{}_{\theta} \right) - \left(a_1 \underset{\sim}{\boldsymbol{\sigma}}'_{\theta} + a_2 \underset{\sim}{\boldsymbol{\sigma}}'^{T}{}_{\theta} \right) \otimes \frac{\partial J_2(\underset{\sim}{\boldsymbol{\sigma}}_{\theta},\, \underset{\sim}{\boldsymbol{m}}_{\theta})}{\partial \underset{\sim}{\boldsymbol{\sigma}}_{\theta}}}{J_2^2(\underset{\sim}{\boldsymbol{\sigma}}_{\theta},\, \underset{\sim}{\boldsymbol{m}}_{\theta})} \\
&= \frac{J_2(\underset{\sim}{\boldsymbol{\sigma}}_{\theta},\, \underset{\sim}{\boldsymbol{m}}_{\theta}) \left(a_1 \underset{\approx}{\boldsymbol{P}}^{dev} + a_2 \underset{\approx}{\boldsymbol{P}}^{dev^T} \right) - \left(a_1 \underset{\sim}{\boldsymbol{\sigma}}'_{\theta} + a_2 \underset{\sim}{\boldsymbol{\sigma}}'^{T}{}_{\theta} \right) \otimes \underset{\sim}{\boldsymbol{n}}^{\sigma}_{\theta}}{J_2^2(\underset{\sim}{\boldsymbol{\sigma}}_{\theta},\, \underset{\sim}{\boldsymbol{m}}_{\theta})} \\
\frac{\partial \underset{\sim}{\boldsymbol{n}}^{\sigma}_{\theta}}{\partial \underset{\sim}{\boldsymbol{\sigma}}_{\theta}} &= \frac{1}{J_2(\underset{\sim}{\boldsymbol{\sigma}}_{\theta},\, \underset{\sim}{\boldsymbol{m}}_{\theta})} \left(a_1 \underset{\approx}{\boldsymbol{P}}^{dev} + a_2 \underset{\approx}{\boldsymbol{P}}^{dev^T} \right) - \frac{\frac{a_1 \underset{\sim}{\boldsymbol{\sigma}}'_{\theta} + a_2 \underset{\sim}{\boldsymbol{\sigma}}'^{T}{}_{\theta}}{J_2(\underset{\sim}{\boldsymbol{\sigma}}_{\theta},\, \underset{\sim}{\boldsymbol{m}}_{\theta})} \otimes \underset{\sim}{\boldsymbol{n}}^{\sigma}_{\theta}}{J_2(\underset{\sim}{\boldsymbol{\sigma}}_{\theta},\, \underset{\sim}{\boldsymbol{m}}_{\theta})} \\
\frac{\partial \underset{\sim}{\boldsymbol{n}}^{\sigma}_{\theta}}{\partial \underset{\sim}{\boldsymbol{\sigma}}_{\theta}} &= \frac{1}{J_2(\underset{\sim}{\boldsymbol{\sigma}}_{\theta},\, \underset{\sim}{\boldsymbol{m}}_{\theta})} \left(a_1 \underset{\approx}{\boldsymbol{P}}^{dev} + a_2 \underset{\approx}{\boldsymbol{P}}^{dev^T} - \underset{\sim}{\boldsymbol{n}}^{\sigma}_{\theta} \otimes \underset{\sim}{\boldsymbol{n}}^{\sigma}_{\theta} \right)
\end{aligned}$$

$$\boxed{\frac{\partial \underset{\sim}{\boldsymbol{n}}^{\sigma}_{\theta}}{\partial \underset{\sim}{\boldsymbol{\sigma}}_{\theta}} := \underset{\approx}{\boldsymbol{N}}^{\sigma}_{\theta} = \frac{1}{J_2(\underset{\sim}{\boldsymbol{\sigma}}_{\theta},\, \underset{\sim}{\boldsymbol{m}}_{\theta})} \left(a_1 \underset{\approx}{\boldsymbol{P}}^{dev} + a_2 \underset{\approx}{\boldsymbol{P}}^{dev^T} - \underset{\sim}{\boldsymbol{n}}^{\sigma}_{\theta} \otimes \underset{\sim}{\boldsymbol{n}}^{\sigma}_{\theta} \right)}$$

where $\underset{\approx}{\boldsymbol{P}}^{dev}$ and $\underset{\approx}{\boldsymbol{P}}^{dev^T}$ are the deviatoric projectors:

$$\underset{\approx}{\boldsymbol{P}}^{dev} = \underset{\approx}{\boldsymbol{I}} - \frac{1}{3} \underset{\sim}{\boldsymbol{I}} \otimes \underset{\sim}{\boldsymbol{I}},\ \underset{\approx}{\boldsymbol{P}}^{dev^T} = \underset{\approx}{\boldsymbol{I}}^{T} - \frac{1}{3} \underset{\sim}{\boldsymbol{I}} \otimes \underset{\sim}{\boldsymbol{I}}$$

Thus we find:

$$\begin{aligned}
\frac{\partial \underset{\sim}{\boldsymbol{r}}^{\sigma}_{e}}{\partial \Delta \underset{\sim}{\boldsymbol{e}}^{e}_{\theta}} &= \underset{\approx}{\boldsymbol{I}} + \frac{\partial \underset{\sim}{\boldsymbol{n}}^{\sigma}_{\theta}}{\partial \underset{\sim}{\boldsymbol{\sigma}}_{\theta}} : \frac{\partial \underset{\sim}{\boldsymbol{\sigma}}_{\theta}}{\partial \underset{\sim}{\boldsymbol{e}}^{e}_{\theta}} : \frac{\partial \underset{\sim}{\boldsymbol{e}}^{e}_{\theta}}{\partial \Delta \underset{\sim}{\boldsymbol{e}}^{e}} \\
&= \underset{\approx}{\boldsymbol{I}} + \Delta p \underset{\approx}{\boldsymbol{N}}^{\sigma}_{\theta} : \underset{\approx}{\boldsymbol{\Lambda}}^{\sigma}_{\theta} : \theta \underset{\approx}{\boldsymbol{I}}
\end{aligned}$$

$$\boxed{\frac{\partial \underset{\sim}{\boldsymbol{r}}^{\sigma}_{e}}{\partial \Delta \underset{\sim}{\boldsymbol{e}}^{e}} = \underset{\approx}{\boldsymbol{I}} + \theta \Delta p \underset{\approx}{\boldsymbol{N}}^{\sigma}_{\theta} : \underset{\approx}{\boldsymbol{\Lambda}}^{\sigma}_{\theta}}$$

$$\frac{\partial \underset{\sim}{\boldsymbol{r}}^{\sigma}_{e}}{\partial \Delta p} = \frac{\partial}{\partial \Delta p} \left(\Delta \underset{\sim}{\boldsymbol{e}}^{e} + \Delta p \underset{\sim}{\boldsymbol{n}}^{\sigma}_{\theta} \right)$$

$$\boxed{\frac{\partial \underset{\sim}{\boldsymbol{r}}^{\sigma}_{e}}{\partial \Delta p} = \underset{\sim}{\boldsymbol{n}}^{\sigma}_{\theta}}$$

$$\begin{aligned}
\frac{\partial \underset{\sim}{\boldsymbol{r}}^{\sigma}_{e}}{\partial \Delta \underset{\sim}{\boldsymbol{\kappa}}^{e}} &= \frac{\partial}{\partial \Delta \underset{\sim}{\boldsymbol{\kappa}}^{e}} \left(\Delta \underset{\sim}{\boldsymbol{e}}^{e} + \Delta p \underset{\sim}{\boldsymbol{n}}^{\sigma}_{\theta} \right) \\
&= \Delta p \frac{\partial \underset{\sim}{\boldsymbol{n}}^{\sigma}_{\theta}}{\partial \Delta \underset{\sim}{\boldsymbol{\kappa}}^{e}} \\
&= \Delta p \frac{\partial \underset{\sim}{\boldsymbol{n}}^{\sigma}_{\theta}}{\partial \underset{\sim}{\boldsymbol{m}}_{\theta}} : \frac{\partial \underset{\sim}{\boldsymbol{m}}_{\theta}}{\partial \underset{\sim}{\boldsymbol{\kappa}}^{e}_{\theta}} : \frac{\partial \underset{\sim}{\boldsymbol{\kappa}}^{e}_{\theta}}{\partial \Delta \underset{\sim}{\boldsymbol{\kappa}}^{e}}
\end{aligned}$$

knowing that

$$\frac{\partial \underset{\sim}{\boldsymbol{\kappa}}^e_\theta}{\partial \Delta \underset{\sim}{\boldsymbol{\kappa}}^e} = \frac{\partial \underset{\sim}{\boldsymbol{\kappa}}^e_t + \theta \Delta \underset{\sim}{\boldsymbol{\kappa}}^e}{\partial \Delta \underset{\sim}{\boldsymbol{\kappa}}^e} = \theta \underset{\approx}{\boldsymbol{I}}$$

as well as

$$\frac{\partial \underset{\sim}{\boldsymbol{m}}_\theta}{\partial \underset{\sim}{\boldsymbol{\kappa}}^e_\theta} = \underset{\approx}{\boldsymbol{\Lambda}}^m_\theta$$

and

$$\begin{aligned}
\frac{\partial \underset{\sim}{\boldsymbol{n}}^\sigma_\theta}{\partial \underset{\sim}{\boldsymbol{m}}_\theta} &= \frac{\partial}{\partial \underset{\sim}{\boldsymbol{m}}_\theta} \left(\frac{a_1 \underset{\sim}{\boldsymbol{\sigma}}' + a_2 \underset{\sim}{\boldsymbol{\sigma}}'^T}{J_2(\underset{\sim}{\boldsymbol{\sigma}},\, \underset{\sim}{\boldsymbol{m}})} \right) \\
&= \frac{-\left(a_1 \underset{\sim}{\boldsymbol{\sigma}}' + a_2 \underset{\sim}{\boldsymbol{\sigma}}'^T\right) \otimes \frac{\partial J_2(\underset{\sim}{\boldsymbol{\sigma}}_\theta,\, \underset{\sim}{\boldsymbol{m}}_\theta)}{\partial \underset{\sim}{\boldsymbol{m}}_\theta}}{J_2^2(\underset{\sim}{\boldsymbol{\sigma}}_\theta,\, \underset{\sim}{\boldsymbol{m}}_\theta)} \\
&= \frac{-\frac{\left(a_1 \underset{\sim}{\boldsymbol{\sigma}}' + a_2 \underset{\sim}{\boldsymbol{\sigma}}'^T\right)}{J_2(\underset{\sim}{\boldsymbol{\sigma}}_\theta,\, \underset{\sim}{\boldsymbol{m}}_\theta)} \otimes \underset{\sim}{\boldsymbol{n}}^m_\theta}{J_2(\underset{\sim}{\boldsymbol{\sigma}}_\theta,\, \underset{\sim}{\boldsymbol{m}}_\theta)} \\
&= \frac{-\underset{\sim}{\boldsymbol{n}}^\sigma_\theta \otimes \underset{\sim}{\boldsymbol{n}}^m_\theta}{J_2(\underset{\sim}{\boldsymbol{\sigma}}_\theta,\, \underset{\sim}{\boldsymbol{m}}_\theta)}
\end{aligned}$$

We find

$$\frac{\partial \underset{\sim}{\boldsymbol{r}}^\sigma_e}{\partial \Delta \underset{\sim}{\boldsymbol{\kappa}}^e} = -\Delta p \frac{\underset{\sim}{\boldsymbol{n}}^\sigma_\theta \otimes \underset{\sim}{\boldsymbol{n}}^m_\theta}{J_2(\underset{\sim}{\boldsymbol{\sigma}}_\theta,\, \underset{\sim}{\boldsymbol{m}}_\theta)} : \underset{\approx}{\boldsymbol{\Lambda}}^m_\theta : \theta \underset{\approx}{\boldsymbol{I}}$$

$$\boxed{\frac{\partial \underset{\sim}{\boldsymbol{r}}^\sigma_e}{\partial \Delta \underset{\sim}{\boldsymbol{\kappa}}^e} = -\theta \Delta p \frac{\underset{\sim}{\boldsymbol{n}}^\sigma_\theta \otimes \underset{\sim}{\boldsymbol{n}}^m_\theta}{J_2(\underset{\sim}{\boldsymbol{\sigma}}_\theta,\, \underset{\sim}{\boldsymbol{m}}_\theta)} : \underset{\approx}{\boldsymbol{\Lambda}}^m_\theta}$$

Let us now compute the derivatives of $\underset{\sim}{\boldsymbol{r}}^m_e$:

$$\begin{aligned}
\frac{\partial \underset{\sim}{\boldsymbol{r}}^m_e}{\partial \Delta \underset{\sim}{\boldsymbol{\kappa}}^e} &= \frac{\partial}{\partial \Delta \underset{\sim}{\boldsymbol{\kappa}}^e} \left(\Delta \underset{\sim}{\boldsymbol{\kappa}}^e + \Delta \underset{\sim}{\boldsymbol{\kappa}}^p \right) \\
&= \frac{\partial}{\partial \Delta \underset{\sim}{\boldsymbol{\kappa}}^e} \left(\Delta \underset{\sim}{\boldsymbol{\kappa}}^e + \Delta p \underset{\sim}{\boldsymbol{n}}^m_\theta \right) \\
&= \underset{\approx}{\boldsymbol{I}} + \Delta p \frac{\partial \underset{\sim}{\boldsymbol{n}}^m_\theta}{\partial \underset{\sim}{\boldsymbol{m}}_\theta} : \frac{\partial \underset{\sim}{\boldsymbol{m}}_\theta}{\partial \underset{\sim}{\boldsymbol{\kappa}}^e_\theta} : \frac{\partial \underset{\sim}{\boldsymbol{\kappa}}^e_\theta}{\partial \Delta \underset{\sim}{\boldsymbol{\kappa}}^e}
\end{aligned}$$

with

$$\begin{aligned}
\frac{\partial \underset{\sim}{\boldsymbol{n}}^m_\theta}{\partial \underset{\sim}{\boldsymbol{m}}_\theta} &= \frac{\partial}{\partial \underset{\sim}{\boldsymbol{m}}_\theta}\left(\frac{b_1\underset{\sim}{\boldsymbol{m}}_\theta + b_2\underset{\sim}{\boldsymbol{m}}^T_\theta}{J_2(\underset{\sim}{\boldsymbol{\sigma}}_\theta,\ \underset{\sim}{\boldsymbol{m}}_\theta)}\right)\\
&= \frac{J_2(\underset{\sim}{\boldsymbol{\sigma}}_\theta,\ \underset{\sim}{\boldsymbol{m}}_\theta)\frac{\partial}{\partial \underset{\sim}{\boldsymbol{m}}_\theta}\left(b_1\underset{\sim}{\boldsymbol{m}}_\theta + b_2\underset{\sim}{\boldsymbol{m}}^T_\theta\right) - \left(b_1\underset{\sim}{\boldsymbol{m}}_\theta + b_2\underset{\sim}{\boldsymbol{m}}^T_\theta\right)\otimes\frac{\partial J_2(\underset{\sim}{\boldsymbol{\sigma}}_\theta,\ \underset{\sim}{\boldsymbol{m}}_\theta)}{\partial \underset{\sim}{\boldsymbol{m}}_\theta}}{J_2^2(\underset{\sim}{\boldsymbol{\sigma}}_\theta,\ \underset{\sim}{\boldsymbol{m}}_\theta)}\\
&= \frac{J_2(\underset{\sim}{\boldsymbol{\sigma}}_\theta,\ \underset{\sim}{\boldsymbol{m}}_\theta)\left(b_1\underset{\approx}{\boldsymbol{I}} + b_2\underset{\approx}{\boldsymbol{I}}^T\right) - \left(b_1\underset{\sim}{\boldsymbol{m}}_\theta + b_2\underset{\sim}{\boldsymbol{m}}^T_\theta\right)\otimes\underset{\sim}{\boldsymbol{n}}^m_\theta}{J_2^2(\underset{\sim}{\boldsymbol{\sigma}}_\theta,\ \underset{\sim}{\boldsymbol{m}}_\theta)}\\
\frac{\partial \underset{\sim}{\boldsymbol{n}}^m_\theta}{\partial \underset{\sim}{\boldsymbol{m}}_\theta} &= \frac{1}{J_2(\underset{\sim}{\boldsymbol{\sigma}}_\theta,\ \underset{\sim}{\boldsymbol{m}}_\theta)}\left(b_1\underset{\approx}{\boldsymbol{I}} + b_2\underset{\approx}{\boldsymbol{I}}^T\right) - \frac{\frac{b_1\underset{\sim}{\boldsymbol{m}}_\theta + b_2\underset{\sim}{\boldsymbol{m}}^T_\theta}{J_2(\underset{\sim}{\boldsymbol{\sigma}}_\theta,\ \underset{\sim}{\boldsymbol{m}}_\theta)}\otimes\underset{\sim}{\boldsymbol{n}}^m_\theta}{J_2(\underset{\sim}{\boldsymbol{\sigma}}_\theta,\ \underset{\sim}{\boldsymbol{m}}_\theta)}\\
\frac{\partial \underset{\sim}{\boldsymbol{n}}^m_\theta}{\partial \underset{\sim}{\boldsymbol{m}}_\theta} &= \frac{1}{J_2(\underset{\sim}{\boldsymbol{\sigma}}_\theta,\ \underset{\sim}{\boldsymbol{m}}_\theta)}\left(b_1\underset{\approx}{\boldsymbol{I}} + b_2\underset{\approx}{\boldsymbol{I}}^T - \underset{\sim}{\boldsymbol{n}}^m_\theta\otimes\underset{\sim}{\boldsymbol{n}}^m_\theta\right)
\end{aligned}$$

$$\boxed{\frac{\partial \underset{\sim}{\boldsymbol{n}}^m_\theta}{\partial \underset{\sim}{\boldsymbol{m}}_\theta} := \underset{\approx}{\boldsymbol{N}}^m_\theta = \frac{1}{J_2(\underset{\sim}{\boldsymbol{\sigma}}_\theta,\ \underset{\sim}{\boldsymbol{m}}_\theta)}\left(b_1\underset{\approx}{\boldsymbol{I}} + b_2\underset{\approx}{\boldsymbol{I}}^T - \underset{\sim}{\boldsymbol{n}}^m_\theta\otimes\underset{\sim}{\boldsymbol{n}}^m_\theta\right)}$$

Thus we find:

$$\begin{aligned}
\frac{\partial \underset{\sim}{\boldsymbol{r}}^m_e}{\partial \Delta\underset{\sim}{\boldsymbol{\kappa}}^e_\theta} &= \underset{\approx}{\boldsymbol{I}} + \frac{\partial \underset{\sim}{\boldsymbol{n}}^m_\theta}{\partial \underset{\sim}{\boldsymbol{m}}_\theta} : \frac{\partial \underset{\sim}{\boldsymbol{m}}_\theta}{\partial \underset{\sim}{\boldsymbol{\kappa}}^e_\theta} : \frac{\partial \underset{\sim}{\boldsymbol{\kappa}}^e_\theta}{\partial \Delta\underset{\sim}{\boldsymbol{\kappa}}^e}\\
&= \underset{\approx}{\boldsymbol{I}} + \Delta p\underset{\approx}{\boldsymbol{N}}^m_\theta : \underset{\approx}{\boldsymbol{\Lambda}}^m_\theta : \theta\underset{\approx}{\boldsymbol{I}}
\end{aligned}$$

$$\boxed{\frac{\partial \underset{\sim}{\boldsymbol{r}}^m_e}{\partial \Delta\underset{\sim}{\boldsymbol{\kappa}}^e} = \underset{\approx}{\boldsymbol{I}} + \theta\Delta p\underset{\approx}{\boldsymbol{N}}^m_\theta : \underset{\approx}{\boldsymbol{\Lambda}}^m_\theta}$$

$$\begin{aligned}
\frac{\partial \underset{\sim}{\boldsymbol{r}}^m_e}{\partial \Delta\underset{\sim}{\boldsymbol{e}}^e} &= \frac{\partial}{\partial \Delta\underset{\sim}{\boldsymbol{e}}^e}\left(\Delta\underset{\sim}{\boldsymbol{\kappa}}^e + \Delta p\underset{\sim}{\boldsymbol{n}}^m_\theta\right)\\
&= \Delta p\frac{\partial \underset{\sim}{\boldsymbol{n}}^m_\theta}{\partial \underset{\sim}{\boldsymbol{\sigma}}_\theta} : \frac{\partial \underset{\sim}{\boldsymbol{\sigma}}_\theta}{\partial \underset{\sim}{\boldsymbol{e}}^e_\theta} : \frac{\partial \underset{\sim}{\boldsymbol{e}}^e_\theta}{\partial \Delta\underset{\sim}{\boldsymbol{e}}^e}
\end{aligned}$$

with

$$\begin{aligned}
\frac{\partial \underset{\sim}{\boldsymbol{n}}^m_\theta}{\partial \underset{\sim}{\boldsymbol{\sigma}}_\theta} &= \frac{\partial}{\partial \underset{\sim}{\boldsymbol{\sigma}}_\theta}\left(\frac{b_1\underset{\sim}{\boldsymbol{m}} + b_2\underset{\sim}{\boldsymbol{m}}^T}{J_2(\underset{\sim}{\boldsymbol{\sigma}},\ \underset{\sim}{\boldsymbol{m}})}\right)\\
&= \frac{-\left(b_1\underset{\sim}{\boldsymbol{m}} + b_2\underset{\sim}{\boldsymbol{m}}^T\right)\otimes\frac{\partial J_2(\underset{\sim}{\boldsymbol{\sigma}}_\theta,\ \underset{\sim}{\boldsymbol{m}}_\theta)}{\partial \underset{\sim}{\boldsymbol{\sigma}}_\theta}}{J_2^2(\underset{\sim}{\boldsymbol{\sigma}}_\theta,\ \underset{\sim}{\boldsymbol{m}}_\theta)}\\
&= \frac{-\frac{\left(b_1\underset{\sim}{\boldsymbol{m}} + b_2\underset{\sim}{\boldsymbol{m}}^T\right)}{J_2(\underset{\sim}{\boldsymbol{\sigma}}_\theta,\ \underset{\sim}{\boldsymbol{m}}_\theta)}\otimes\underset{\sim}{\boldsymbol{n}}^\sigma_\theta}{J_2(\underset{\sim}{\boldsymbol{\sigma}}_\theta,\ \underset{\sim}{\boldsymbol{m}}_\theta)}\\
&= \frac{-\underset{\sim}{\boldsymbol{n}}^m_\theta\otimes\underset{\sim}{\boldsymbol{n}}^\sigma_\theta}{J_2(\underset{\sim}{\boldsymbol{\sigma}}_\theta,\ \underset{\sim}{\boldsymbol{m}}_\theta)}
\end{aligned}$$

In the end

$$\boxed{\frac{\partial \underset{\sim}{r}_e^m}{\partial \Delta \underset{\sim}{e}^e} = -\theta \Delta p \frac{\underset{\sim}{n}_\theta^m \otimes \underset{\sim}{n}_\theta^\sigma}{J_2(\underset{\sim}{\sigma}_\theta,\, \underset{\sim}{m}_\theta)} : \underset{\approx}{\Lambda}_\theta^\sigma}$$

$$\frac{\partial \underset{\sim}{r}_e^m}{\partial \Delta p} = \frac{\partial}{\partial \Delta p}\left(\Delta \underset{\sim}{\kappa}^e + \Delta p \underset{\sim}{n}_\theta^m\right)$$

$$\boxed{\frac{\partial \underset{\sim}{r}_e^m}{\partial \Delta p} = \underset{\sim}{n}_\theta^m}$$

Finally, let us compute the derivatives of r^p:

$$\begin{aligned}\frac{\partial r^p}{\partial \Delta p} &= \frac{\partial}{\partial \Delta p}\left(J_2(\underset{\sim}{\sigma}_\theta,\, \underset{\sim}{m}_\theta) - R(p)\right)\\ &= -\frac{\partial R}{\partial \Delta p}\\ &:= -H_\theta\end{aligned}$$

$$\boxed{\frac{\partial r^p}{\partial \Delta p} = -H_\theta}$$

$$\begin{aligned}\frac{\partial r^p}{\partial \Delta \underset{\sim}{e}_\theta^e} &= \frac{\partial}{\partial \Delta \underset{\sim}{e}_\theta^e}\left(J_2(\underset{\sim}{\sigma}_\theta,\, \underset{\sim}{m}_\theta) - R(p)\right)\\ &= \frac{\partial J_2(\underset{\sim}{\sigma}_\theta,\, \underset{\sim}{m}_\theta)}{\partial \underset{\sim}{\sigma}_\theta} : \frac{\partial \underset{\sim}{\sigma}_\theta}{\partial \underset{\sim}{e}_\theta^e} : \frac{\partial \underset{\sim}{e}_\theta^e}{\partial \Delta \underset{\sim}{e}^e}\\ &= \underset{\sim}{n}_\theta^\sigma : \underset{\approx}{\Lambda}_\theta^\sigma : \theta \underset{\approx}{I}\end{aligned}$$

$$\boxed{\frac{\partial r^p}{\partial \Delta \underset{\sim}{e}_\theta^e} = \theta \underset{\sim}{n}_\theta^\sigma : \underset{\approx}{\Lambda}_\theta^\sigma}$$

$$\begin{aligned}\frac{\partial r^p}{\partial \Delta \underset{\sim}{\kappa}^e} &= \frac{\partial}{\partial \Delta \underset{\sim}{\kappa}^e}\left(J_2(\underset{\sim}{\sigma}_\theta,\, \underset{\sim}{m}_\theta) - R(p)\right)\\ &= \frac{\partial J_2(\underset{\sim}{\sigma}_\theta,\, \underset{\sim}{m}_\theta)}{\partial \underset{\sim}{m}_\theta} : \frac{\partial \underset{\sim}{m}_\theta}{\partial \underset{\sim}{\kappa}_\theta^e} : \frac{\partial \underset{\sim}{\kappa}_\theta^e}{\partial \Delta \underset{\sim}{\kappa}^e}\\ &= \underset{\sim}{n}_\theta^m : \underset{\approx}{\Lambda}_\theta^m : \theta \underset{\approx}{I}\end{aligned}$$

$$\boxed{\frac{\partial r^p}{\partial \Delta \underset{\sim}{\kappa}^e} = \theta \underset{\sim}{n}_\theta^m : \underset{\approx}{\Lambda}_\theta^m}$$

Finally, the Jacobian matrix is given by

$$\boxed{\begin{bmatrix} \frac{\partial \underset{\sim}{r}_e^\sigma}{\partial \Delta \underset{\sim}{e}^e} = \underset{\approx}{I} + \theta \Delta p \underset{\approx}{N}_\theta^\sigma : \underset{\approx}{\Lambda}_\theta^\sigma & \frac{\partial \underset{\sim}{r}_e^\sigma}{\partial \Delta \underset{\sim}{\kappa}^e} = -\theta \Delta p \frac{\underset{\sim}{n}_\theta^\sigma \otimes \underset{\sim}{n}_\theta^m}{J_2(\underset{\sim}{\sigma}_\theta,\, \underset{\sim}{m}_\theta)} : \underset{\approx}{\Lambda}_\theta^m & \frac{\partial \underset{\sim}{r}_e^\sigma}{\partial \Delta p} = \underset{\sim}{n}_\theta^\sigma \\ \frac{\partial \underset{\sim}{r}_e^m}{\partial \Delta \underset{\sim}{e}^e} = -\theta \Delta p \frac{\underset{\sim}{n}_\theta^m \otimes \underset{\sim}{n}_\theta^\sigma}{J_2(\underset{\sim}{\sigma}_\theta,\, \underset{\sim}{m}_\theta)} : \underset{\approx}{\Lambda}_\theta^\sigma & \frac{\partial \underset{\sim}{r}_e^m}{\partial \Delta \underset{\sim}{\kappa}^e} = \underset{\approx}{I} + \theta \Delta p \underset{\approx}{N}_\theta^m : \underset{\approx}{\Lambda}_\theta^m & \frac{\partial \underset{\sim}{r}_e^m}{\partial \Delta p} = \underset{\sim}{n}_\theta^m \\ \frac{\partial r^p}{\partial \Delta \underset{\sim}{e}^e} = \theta \underset{\approx}{N}_\theta^\sigma : \underset{\approx}{\Lambda}_\theta^\sigma & \frac{\partial r^p}{\partial \Delta \underset{\sim}{\kappa}^e} = \theta \underset{\approx}{N}_\theta^m : \underset{\approx}{\Lambda}_\theta^m & \frac{\partial r^p}{\partial \Delta p} = -H_\theta \end{bmatrix}}$$

with

$$\underset{\approx}{\boldsymbol{N}}_{\theta}^{\sigma}=\frac{\partial \underset{\sim}{\boldsymbol{n}}_{\theta}^{\sigma}}{\partial \underset{\sim}{\boldsymbol{\sigma}}_{\theta}}:=\underset{\approx}{\boldsymbol{N}}_{\theta}^{\sigma}=\frac{1}{J_2(\underset{\sim}{\boldsymbol{\sigma}}_{\theta},\,\underset{\sim}{\boldsymbol{m}}_{\theta})}\left(a_1\underset{\approx}{\boldsymbol{P}}^{dev}+a_2\underset{\approx}{\boldsymbol{P}}^{dev^T}-\underset{\sim}{\boldsymbol{n}}_{\theta}^{\sigma}\otimes\underset{\sim}{\boldsymbol{n}}_{\theta}^{\sigma}\right),\ \underset{\approx}{\boldsymbol{N}}_{\theta}^{m}=\frac{1}{J_2(\underset{\sim}{\boldsymbol{\sigma}}_{\theta},\,\underset{\sim}{\boldsymbol{m}}_{\theta})}\left(a_1\underset{\approx}{\boldsymbol{I}}+a_2\underset{\approx}{\boldsymbol{I}}^{T}-\underset{\sim}{\boldsymbol{n}}_{\theta}^{m}\otimes\underset{\sim}{\boldsymbol{n}}_{\theta}^{m}\right)$$

I.2.2 Multi-criterion framework

In this case two yield functions are adopted so as to decouple the contributions of $\underset{\sim}{\boldsymbol{\sigma}}$ and $\underset{\sim}{\boldsymbol{m}}$. However, a new plastic multiplier κ is introduced:

$$f(\underset{\sim}{\boldsymbol{\sigma}},R)=J_2(\underset{\sim}{\boldsymbol{\sigma}})-R(p,\kappa),\ \ f^m(\underset{\sim}{\boldsymbol{m}},R^m)=J_2(\underset{\sim}{\boldsymbol{m}})-R^m(p,\kappa)$$

$$J_2(\underset{\sim}{\boldsymbol{\sigma}})=\sqrt{a_1\underset{\sim}{\boldsymbol{\sigma}}'+a_2\underset{\sim}{\boldsymbol{\sigma}}'^T},\ \ J_2(\underset{\sim}{\boldsymbol{m}})=\sqrt{b_1\underset{\sim}{\boldsymbol{m}}+b_2\underset{\sim}{\boldsymbol{m}}^T}$$

The normals to the yield surfaces are then given by:

$$\underset{\sim}{\boldsymbol{n}}^{\sigma}:=\frac{\partial f}{\partial \underset{\sim}{\boldsymbol{\sigma}}}=\frac{a_1\underset{\sim}{\boldsymbol{\sigma}}'+a_2\underset{\sim}{\boldsymbol{\sigma}}'^T}{J_2(\underset{\sim}{\boldsymbol{\sigma}})},\ \underset{\sim}{\boldsymbol{n}}^{m}:=\frac{\partial f^m}{\partial \underset{\sim}{\boldsymbol{m}}}=\frac{b_1\underset{\sim}{\boldsymbol{m}}+b_2\underset{\sim}{\boldsymbol{m}}^T}{J_2(\underset{\sim}{\boldsymbol{m}})}$$

The rates of the plastic deformation and plastic curvature are thus given by:

$$\dot{\underset{\sim}{\boldsymbol{e}}}^{p}=\dot{p}\frac{\partial f}{\partial \underset{\sim}{\boldsymbol{\sigma}}},\ \ \dot{\underset{\sim}{\boldsymbol{\kappa}}}^{p}=\dot{\kappa}\frac{\partial f^m}{\partial \underset{\sim}{\boldsymbol{m}}}$$

The residuals are then given by:

$$\begin{bmatrix}\underset{\sim}{\boldsymbol{r}}_{e}^{\sigma}\\ \underset{\sim}{\boldsymbol{r}}_{e}^{m}\\ r_p^{\sigma}\\ r_p^{m}\end{bmatrix}=\begin{bmatrix}\Delta\underset{\sim}{\boldsymbol{e}}^{e}+\Delta p\underset{\sim}{\boldsymbol{n}}_{\theta}^{\sigma}\\ \Delta\underset{\sim}{\boldsymbol{\kappa}}^{e}+\Delta\kappa\underset{\sim}{\boldsymbol{n}}_{\theta}^{m}\\ f\left(\underset{\sim}{\boldsymbol{\sigma}}_{t+\theta\Delta t}\right)\\ f^m\left(\underset{\sim}{\boldsymbol{m}}_{t+\theta\Delta t}\right)\end{bmatrix}$$

Let us now compute the derivatives of $\underset{\sim}{\boldsymbol{r}}_{e}^{\sigma}$. One can see that $\dfrac{\partial \underset{\sim}{\boldsymbol{r}}_{e}^{\sigma}}{\partial \Delta\underset{\sim}{\boldsymbol{e}}^{e}}$ and $\dfrac{\partial \underset{\sim}{\boldsymbol{r}}_{e}^{\sigma}}{\partial \Delta p}$ are the same as for the single criterion case. However, $\dfrac{\partial \underset{\sim}{\boldsymbol{r}}_{e}^{\sigma}}{\partial \Delta\underset{\sim}{\boldsymbol{\kappa}}^{e}}$ is now null since $J_2(\underset{\sim}{\boldsymbol{\sigma}})$ does not depend on $\underset{\sim}{\boldsymbol{m}}$ anymore. Finally, it can be seen that $\underset{\sim}{\boldsymbol{r}}_{e}^{\sigma}$ does not depend on $\Delta\kappa$ thus $\dfrac{\partial \underset{\sim}{\boldsymbol{r}}_{e}^{\sigma}}{\partial \Delta\kappa}=0$.

$$\begin{pmatrix}\dfrac{\partial \underset{\sim}{\boldsymbol{r}}_{e}^{\sigma}}{\partial \Delta\underset{\sim}{\boldsymbol{e}}^{e}}\\ \dfrac{\partial \underset{\sim}{\boldsymbol{r}}_{e}^{\sigma}}{\partial \Delta\underset{\sim}{\boldsymbol{\kappa}}^{e}}\\ \dfrac{\partial \underset{\sim}{\boldsymbol{r}}_{e}^{\sigma}}{\partial \Delta p}\\ \dfrac{\partial \underset{\sim}{\boldsymbol{r}}_{e}^{\sigma}}{\partial \Delta\kappa}\end{pmatrix}=\begin{pmatrix}\underset{\approx}{\boldsymbol{I}}+\theta\Delta p\underset{\approx}{\boldsymbol{N}}_{\theta}^{\sigma}:\underset{\approx}{\boldsymbol{\Lambda}}_{\theta}^{\sigma}\\ \underset{\approx}{\boldsymbol{0}}\\ \underset{\sim}{\boldsymbol{n}}_{\theta}^{\sigma}\\ \underset{\sim}{\boldsymbol{0}}\end{pmatrix}$$

An analogical reasoning can be made for $\underset{\sim}{r}^m_e$. One gets:

$$\boxed{\begin{pmatrix} \frac{\partial \underset{\sim}{r}^m_e}{\partial \Delta \underset{\sim}{e}^e} \\ \frac{\partial \underset{\sim}{r}^m_e}{\partial \Delta \underset{\sim}{\kappa}^e} \\ \frac{\partial \underset{\sim}{r}^m_e}{\partial \Delta p} \\ \frac{\partial \underset{\sim}{r}^m_e}{\partial \Delta \kappa} \end{pmatrix} = \begin{pmatrix} \underset{\approx}{0} \\ \underset{\approx}{I} + \theta \Delta p \underset{\approx}{N}^m_\theta : \underset{\approx}{\Lambda}^m_\theta \\ \underset{\sim}{0} \\ \underset{\sim}{n}^m_\theta \end{pmatrix}}$$

Let us now focus on the plastic residuals and compute the derivatives of r^σ_p. It can be seen that $\frac{\partial r^\sigma_p}{\partial \Delta \underset{\sim}{e}^e} = \frac{\partial r^p}{\partial \Delta \underset{\sim}{e}^e}$ and $\frac{\partial r^\sigma_p}{\partial \Delta p} = \frac{\partial r^p}{\partial \Delta p}$. Moreover

$$\begin{aligned} \frac{\partial r^p}{\partial \Delta \kappa} &= \frac{\partial}{\partial \Delta \kappa} \left(J_2(\underset{\sim}{\sigma}_\theta) - R(p, \kappa) \right) \\ &= -\frac{\partial R}{\partial \kappa} \end{aligned}$$

$\frac{\partial R}{\partial \kappa}$ is defined as the hardening modulus H^{pc} Forest [2005]; Forest and Sievert [2003] and such that $H^{pc} = \frac{\partial R}{\partial \kappa} = \frac{\partial R^m}{\partial p}$. Finally

$$\begin{aligned} \frac{\partial r^p}{\partial \Delta \underset{\sim}{\kappa}^e} &= \frac{\partial}{\partial \Delta \underset{\sim}{\kappa}^e_\theta} \left(J_2(\underset{\sim}{\sigma}_\theta) - R(p, \kappa) \right) \\ &= \underset{\sim}{0} \end{aligned}$$

In the end,

$$\boxed{\begin{pmatrix} \frac{\partial r^\sigma_p}{\partial \Delta \underset{\sim}{e}^e} \\ \frac{\partial r^\sigma_p}{\partial \Delta \underset{\sim}{\kappa}^e} \\ \frac{\partial r^\sigma_p}{\partial \Delta p} \\ \frac{\partial r^\sigma_p}{\partial \Delta \kappa} \end{pmatrix} = \begin{pmatrix} \theta \underset{\approx}{N}^\sigma_\theta : \underset{\approx}{\Lambda}^\sigma_\theta \\ \underset{\sim}{0} \\ -H_\theta \\ -H^{pc}_\theta \end{pmatrix}}$$

Similarly, it can be found that:

$$\boxed{\begin{pmatrix} \frac{\partial r^m_p}{\partial \Delta \underset{\sim}{e}^e} \\ \frac{\partial r^m_p}{\partial \Delta \underset{\sim}{\kappa}^e} \\ \frac{\partial r^m_p}{\partial \Delta p} \\ \frac{\partial r^m_p}{\partial \Delta \kappa} \end{pmatrix} = \begin{pmatrix} \underset{\sim}{0} \\ \theta \underset{\approx}{N}^m_\theta : \underset{\approx}{\Lambda}^m_\theta \\ -H^{pc}_\theta \\ -H^m_\theta \end{pmatrix}}$$

The expression of the Jacobian matrix is therefore:

$$[J] = \begin{bmatrix} \dfrac{\partial \underset{\sim}{r}_e^\sigma}{\partial \Delta \underset{\sim}{e}^e} = \underset{\approx}{I} + \theta \Delta p \underset{\approx}{N}_\theta^\sigma : \underset{\approx}{\Lambda}_\theta^\sigma & \dfrac{\partial \underset{\sim}{r}_e^\sigma}{\partial \Delta \underset{\sim}{\kappa}^e} = \underset{\approx}{0} & \dfrac{\partial \underset{\sim}{r}_e^\sigma}{\partial \Delta p} = \underset{\sim}{n}_\theta^\sigma & \dfrac{\partial \underset{\sim}{r}_e^\sigma}{\partial \Delta \kappa} = \underset{\sim}{0} \\ \dfrac{\partial \underset{\sim}{r}_e^m}{\partial \Delta \underset{\sim}{e}^e} = \underset{\approx}{0} & \dfrac{\partial \underset{\sim}{r}_e^m}{\partial \Delta \underset{\sim}{\kappa}^e} = \underset{\approx}{I} + \theta \Delta p \underset{\approx}{N}_\theta^m : \underset{\approx}{\Lambda}_\theta^m & \dfrac{\partial \underset{\sim}{r}_e^m}{\partial \Delta p} = \underset{\sim}{0} & \dfrac{\partial \underset{\sim}{r}_e^m}{\partial \Delta \kappa} = \underset{\sim}{n}_\sigma^m \\ \dfrac{\partial r_p^\sigma}{\partial \Delta \underset{\sim}{e}^e} = \theta \underset{\approx}{N}_\theta^\sigma : \underset{\approx}{\Lambda}_\theta^\sigma & \dfrac{\partial r_p^\sigma}{\partial \Delta \underset{\sim}{\kappa}^e} = \underset{\sim}{0} & \dfrac{\partial r_p^\sigma}{\partial \Delta p} = -H_\theta & \dfrac{\partial r_p^\sigma}{\partial \Delta \kappa} = -H_\theta^{pc} \\ \dfrac{\partial r_p^m}{\partial \Delta \underset{\sim}{e}^e} = \underset{\sim}{0} & \dfrac{\partial r_p^m}{\partial \Delta \underset{\sim}{\kappa}^e} = \theta \underset{\approx}{N}_\theta^m : \underset{\approx}{\Lambda}_\theta^m & \dfrac{\partial r_p^m}{\partial \Delta p} = -H_\theta^{pc} & \dfrac{\partial r_p^m}{\partial \Delta \kappa} = -H_\theta^m \end{bmatrix}$$

I.3 Prandtl-Reuss viscoplasticity

I.3.1 Single criterion framework

In this case

$$\dot{p} = \left\langle \frac{J_2(\underset{\sim}{\sigma}_\theta, \underset{\sim}{m}_\theta) - R(p)}{K} \right\rangle^n$$
$$\frac{\Delta p}{\Delta t} = \left\langle \frac{J_2(\underset{\sim}{\sigma}_\theta, \underset{\sim}{m}_\theta) - R(p)}{K} \right\rangle^n$$

The elastic residuals $\underset{\sim}{r}_e^\sigma$ and $\underset{\sim}{r}_e^m$ are the same as for rate-independent plasticity with single criterion. However, the inelastic one r_p is not:

$$r_p = \Delta p - \Delta t \left\langle \frac{J_2(\underset{\sim}{\sigma}_\theta, \underset{\sim}{m}_\theta) - R(p)}{K} \right\rangle^n = 0$$

$$\begin{aligned} \frac{\partial r_p}{\partial \Delta \underset{\sim}{e}^e} &= \frac{\partial}{\partial \Delta \underset{\sim}{e}^e} \left(\Delta p - \Delta t \left\langle \frac{J_2(\underset{\sim}{\sigma}_\theta, \underset{\sim}{m}_\theta) - R(p)}{K} \right\rangle^n \right) \\ &= -\Delta t \frac{n}{K} \left\langle \frac{J_2(\underset{\sim}{\sigma}_\theta, \underset{\sim}{m}_\theta) - R(p)}{K} \right\rangle^{n-1} \frac{\partial J_2(\underset{\sim}{\sigma}_\theta, \underset{\sim}{m}_\theta)}{\partial \Delta \underset{\sim}{e}^e} \\ &= -\Delta t \frac{n}{K} \left\langle \frac{J_2(\underset{\sim}{\sigma}_\theta, \underset{\sim}{m}_\theta) - R(p)}{K} \right\rangle^{n-1} \frac{\partial J_2(\underset{\sim}{\sigma}_\theta, \underset{\sim}{m}_\theta)}{\partial \underset{\sim}{\sigma}_\theta} : \frac{\partial \underset{\sim}{\sigma}_\theta}{\partial \underset{\sim}{e}_\theta^e} : \frac{\partial \underset{\sim}{e}_\theta^e}{\partial \Delta \underset{\sim}{e}^e} \\ &= -\Delta t \frac{n}{K} \left\langle \frac{J_2(\underset{\sim}{\sigma}_\theta, \underset{\sim}{m}_\theta) - R(p)}{K} \right\rangle^{n-1} \underset{\sim}{n}_\theta^\sigma : \underset{\approx}{\Lambda}_\theta^\sigma : \theta \underset{\approx}{I} \end{aligned}$$

$$\frac{\partial r_p}{\partial \Delta \underset{\sim}{e}^e} = -\Delta t \theta \frac{n}{K} \left\langle \frac{J_2(\underset{\sim}{\sigma}_\theta, \underset{\sim}{m}_\theta) - R(p)}{K} \right\rangle^{n-1} \underset{\sim}{n}_\theta^\sigma : \underset{\approx}{\Lambda}_\theta^\sigma$$

$$
\begin{aligned}
\frac{\partial r_p}{\partial \Delta \underset{\sim}{\boldsymbol{\kappa}}^e} &= \frac{\partial}{\partial \Delta \underset{\sim}{\boldsymbol{\kappa}}^e}\left(\Delta p - \Delta t \left\langle \frac{J_2(\underset{\sim}{\boldsymbol{\sigma}}_\theta,\, \underset{\sim}{\boldsymbol{m}}_\theta) - R(p)}{K} \right\rangle^n\right) \\
&= -\Delta t \frac{n}{K} \left\langle \frac{J_2(\underset{\sim}{\boldsymbol{\sigma}}_\theta,\, \underset{\sim}{\boldsymbol{m}}_\theta) - R(p)}{K} \right\rangle^{n-1} \frac{\partial J_2(\underset{\sim}{\boldsymbol{\sigma}}_\theta,\, \underset{\sim}{\boldsymbol{m}}_\theta)}{\partial \Delta \underset{\sim}{\boldsymbol{\kappa}}^e} \\
&= -\Delta t \frac{n}{K} \left\langle \frac{J_2(\underset{\sim}{\boldsymbol{\sigma}}_\theta,\, \underset{\sim}{\boldsymbol{m}}_\theta) - R(p)}{K} \right\rangle^{n-1} \frac{\partial J_2(\underset{\sim}{\boldsymbol{\sigma}}_\theta,\, \underset{\sim}{\boldsymbol{m}}_\theta)}{\partial \underset{\sim}{\boldsymbol{m}}_\theta} : \frac{\partial \underset{\sim}{\boldsymbol{m}}_\theta}{\partial \underset{\sim}{\boldsymbol{\kappa}}^e_\theta} : \frac{\partial \underset{\sim}{\boldsymbol{\kappa}}^e_\theta}{\partial \Delta \underset{\sim}{\boldsymbol{\kappa}}^e} \\
&= -\Delta t \frac{n}{K} \left\langle \frac{J_2(\underset{\sim}{\boldsymbol{\sigma}}_\theta,\, \underset{\sim}{\boldsymbol{m}}_\theta) - R(p)}{K} \right\rangle^{n-1} \underset{\sim}{\boldsymbol{n}}^m_\theta : \underset{\approx}{\boldsymbol{\Lambda}}^m_\theta : \theta \underset{\approx}{\boldsymbol{I}}
\end{aligned}
$$

$$
\boxed{\frac{\partial r_p}{\partial \Delta \underset{\sim}{\boldsymbol{\kappa}}^e} = -\Delta t \theta \frac{n}{K} \left\langle \frac{J_2(\underset{\sim}{\boldsymbol{\sigma}}_\theta,\, \underset{\sim}{\boldsymbol{m}}_\theta) - R(p)}{K} \right\rangle^{n-1} \underset{\sim}{\boldsymbol{n}}^m_\theta : \underset{\approx}{\boldsymbol{\Lambda}}^m_\theta}
$$

$$
\begin{aligned}
\frac{\partial r_p}{\partial \Delta p} &= \frac{\partial}{\partial \Delta p}\left(\Delta p - \Delta t \left\langle \frac{J_2(\underset{\sim}{\boldsymbol{\sigma}}_\theta,\, \underset{\sim}{\boldsymbol{m}}_\theta) - R(p)}{K} \right\rangle^n\right) \\
&= 1 - \Delta t \left(-\frac{\partial R}{\partial p}\frac{\partial p}{\partial \Delta p}\frac{n}{K} \left\langle \frac{J_2(\underset{\sim}{\boldsymbol{\sigma}}_\theta,\, \underset{\sim}{\boldsymbol{m}}_\theta) - R(p)}{K} \right\rangle^{n-1}\right) \\
&= 1 + \Delta t \frac{\partial R}{\partial p} \theta \frac{n}{K} \left\langle \frac{J_2(\underset{\sim}{\boldsymbol{\sigma}}_\theta,\, \underset{\sim}{\boldsymbol{m}}_\theta) - R(p)}{K} \right\rangle^{n-1}
\end{aligned}
$$

$$
\boxed{\frac{\partial r_p}{\partial \Delta p} = 1 + \theta \Delta t \frac{\partial R}{\partial p}\frac{n}{K} \left\langle \frac{J_2(\underset{\sim}{\boldsymbol{\sigma}}_\theta,\, \underset{\sim}{\boldsymbol{m}}_\theta) - R(p)}{K} \right\rangle^{n-1}}
$$

I.3.2 Multi criterion framework

As for rate independent plasticity with multi criterion there are two inelastic residuals:

$$
\boxed{r^\sigma_p = \Delta p - \Delta t \left\langle \frac{J_2(\underset{\sim}{\boldsymbol{\sigma}}_\theta) - R(p,\kappa)}{K} \right\rangle^n = 0}
$$

and

$$
\boxed{r^m_p = \Delta \kappa - \Delta t \left\langle \frac{J_2(\underset{\sim}{\boldsymbol{m}}_\theta) - R^m(p,\kappa)}{K} \right\rangle^n = 0}
$$

As for the single criterion visoplasticity case we find that:

$$
\boxed{\frac{\partial r^\sigma_p}{\partial \Delta \underset{\sim}{\boldsymbol{e}}^e} = -\Delta t \theta \frac{n}{K} \left\langle \frac{J_2(\underset{\sim}{\boldsymbol{\sigma}}_\theta) - R(p,\kappa)}{K} \right\rangle^{n-1} \underset{\sim}{\boldsymbol{n}}^\sigma_\theta : \underset{\approx}{\boldsymbol{\Lambda}}^\sigma_\theta}
$$

as well as:

$$
\boxed{\frac{\partial r^\sigma_p}{\partial \Delta p} = 1 + \theta \Delta t \frac{\partial R}{\partial p}\frac{n}{K} \left\langle \frac{J_2(\underset{\sim}{\boldsymbol{\sigma}}_\theta) - R(p,\kappa)}{K} \right\rangle^{n-1}}
$$

The derivative of r_p^σ with respect to $\Delta\kappa$ is given by:

$$\begin{aligned}\frac{\partial r_p^\sigma}{\partial \Delta\kappa} &= \frac{\partial}{\partial \Delta\kappa}\left(\Delta p - \Delta t \left\langle \frac{J_2(\underset{\sim}{\sigma}_\theta) - R(p,\kappa)}{K}\right\rangle^n\right)\\ &= -\Delta t\left(-\frac{\partial R}{\partial \kappa}\frac{\partial \kappa}{\partial \Delta\kappa}\frac{n}{K}\left\langle \frac{J_2(\underset{\sim}{\sigma}_\theta) - R(p,\kappa)}{K}\right\rangle^{n-1}\right)\\ &= \Delta t \frac{\partial R}{\partial \kappa}\theta\frac{n}{K}\left\langle \frac{J_2(\underset{\sim}{\sigma}_\theta) - R(p,\kappa)}{K}\right\rangle^{n-1}\end{aligned}$$

$$\boxed{\frac{\partial r_p^\sigma}{\partial \Delta\kappa} = \theta\Delta t H_\theta^{pc}\frac{n}{K}\left\langle \frac{J_2(\underset{\sim}{\sigma}_\theta) - R(p,\kappa)}{K}\right\rangle^{n-1}}$$

finally we have:

$$\boxed{\frac{\partial r_p^\sigma}{\partial \Delta\underset{\sim}{\kappa}^e} = \underset{\sim}{0}}$$

The derivatives of r_σ^m can be computed using the same method. We find:

$$\boxed{\frac{\partial r_p^m}{\partial \Delta\underset{\sim}{e}^e} = \underset{\sim}{0}}$$

$$\boxed{\frac{\partial r_p^m}{\partial \Delta\underset{\sim}{\kappa}^e} = -\Delta t\,\theta\frac{n}{K}\left\langle \frac{J_2(\underset{\sim}{m}_\theta) - R^m(p,\kappa)}{K}\right\rangle^{n-1}\underset{\sim}{n}_\theta^m : \underset{\approx}{\Lambda}_\theta^m}$$

$$\boxed{\frac{\partial r_p^m}{\partial \Delta\kappa} = 1 + \theta\Delta t\frac{\partial R^m}{\partial \kappa}\frac{n}{K}\left\langle \frac{J_2(\underset{\sim}{m}_\theta) - R^m(p,\kappa)}{K}\right\rangle^{n-1}}$$

$$\boxed{\frac{\partial r_p^m}{\partial \Delta p} = \theta\Delta t H_\theta^{pc}\frac{n}{K}\left\langle \frac{J_2(\underset{\sim}{m}_\theta) - R(p,\kappa)}{K}\right\rangle^{n-1}}$$

I.4 Crystal plasticity

We consider the case where there is no plastic curvature. We have

$$\underset{\sim}{e} = \underset{\sim}{e}^e + \underset{\sim}{e}^p$$

with

$$\underset{\sim}{e}^p = \sum_{s=1}^{N}\gamma^s\underset{\sim}{P}^s$$

where

$$\underset{\sim}{P}^s = \underline{l}^s \otimes \underline{n}^s$$

is the orientation tensor and

$$\dot{\gamma}^s = \left\langle \frac{|\underset{\sim}{\sigma} : \underset{\sim}{P}^s| - r^s}{K}\right\rangle^n \operatorname{sgn}(\underset{\sim}{\sigma} : \underset{\sim}{P}^s)$$

The derivatives of the elastic residuals are:

$$\frac{\partial \underset{\sim}{\boldsymbol{r}}_e^{\sigma}}{\partial \Delta \underset{\sim}{\boldsymbol{e}}^e} = \frac{\partial}{\partial \Delta \underset{\sim}{\boldsymbol{e}}^e} \left(\Delta \underset{\sim}{\boldsymbol{e}}^e + \sum_{s=1}^{N} \Delta \gamma^s \underset{\sim}{\boldsymbol{P}}^s \right)$$

$$\boxed{\frac{\partial \underset{\sim}{\boldsymbol{r}}_e^{\sigma}}{\partial \Delta \underset{\sim}{\boldsymbol{e}}^e} = \underset{\approx}{\boldsymbol{I}}}$$

$$\frac{\partial \underset{\sim}{\boldsymbol{r}}_e^{\sigma}}{\partial \Delta \underset{\sim}{\boldsymbol{\kappa}}} = \frac{\partial}{\partial \Delta \underset{\sim}{\boldsymbol{\kappa}}} \left(\Delta \underset{\sim}{\boldsymbol{e}}^e + \sum_{s=1}^{N} \Delta \gamma^s \underset{\sim}{\boldsymbol{P}}^s \right)$$

$$\boxed{\frac{\partial \underset{\sim}{\boldsymbol{r}}_e^{\sigma}}{\partial \Delta \underset{\sim}{\boldsymbol{\kappa}}} = \underset{\approx}{\boldsymbol{0}}}$$

$$\begin{aligned} \frac{\partial \underset{\sim}{\boldsymbol{r}}_e^{\sigma}}{\partial \Delta \gamma^s} &= \frac{\partial}{\partial \Delta \gamma^s} \left(\Delta \underset{\sim}{\boldsymbol{e}}^e + \sum_{s=1}^{N} \Delta \gamma^s \underset{\sim}{\boldsymbol{P}}^s \right) \\ &= \frac{\partial}{\partial \Delta \gamma^s} \left(\sum_{s=1}^{N} \Delta \gamma^s \underset{\sim}{\boldsymbol{P}}^s \right) \end{aligned}$$

$$\boxed{\frac{\partial \underset{\sim}{\boldsymbol{r}}_e^{\sigma}}{\partial \Delta \gamma^s} = \sum_{s=1}^{N} \underset{\sim}{\boldsymbol{P}}^s}$$

$$\frac{\partial \underset{\sim}{\boldsymbol{r}}_e^{m}}{\partial \Delta \underset{\sim}{\boldsymbol{e}}^e} = \frac{\partial}{\partial \Delta \underset{\sim}{\boldsymbol{e}}^e} \left(\Delta \underset{\sim}{\boldsymbol{\kappa}} + \sum_{s=1}^{N} \Delta \gamma^s \underset{\sim}{\boldsymbol{P}}^s \right)$$

$$\boxed{\frac{\partial \underset{\sim}{\boldsymbol{r}}_e^{m}}{\partial \Delta \underset{\sim}{\boldsymbol{e}}^e} = \underset{\approx}{\boldsymbol{0}}}$$

$$\frac{\partial \underset{\sim}{\boldsymbol{r}}_e^{m}}{\partial \Delta \underset{\sim}{\boldsymbol{\kappa}}} = \frac{\partial}{\partial \Delta \underset{\sim}{\boldsymbol{\kappa}}} \left(\Delta \underset{\sim}{\boldsymbol{\kappa}} + \sum_{s=1}^{N} \Delta \gamma^s \underset{\sim}{\boldsymbol{P}}^s \right)$$

$$\boxed{\frac{\partial \underset{\sim}{\boldsymbol{r}}_e^{m}}{\partial \Delta \underset{\sim}{\boldsymbol{\kappa}}} = \underset{\approx}{\boldsymbol{I}}}$$

$$\begin{aligned} \frac{\partial \underset{\sim}{\boldsymbol{r}}_e^{m}}{\partial \Delta \gamma^s} &= \frac{\partial \Delta \underset{\sim}{\boldsymbol{\kappa}}}{\partial \Delta \gamma^s} \\ &= \underset{\sim}{\boldsymbol{0}} \end{aligned}$$

$$\boxed{\frac{\partial \underset{\sim}{\boldsymbol{r}}_e^{m}}{\partial \Delta \gamma^s} = \underset{\sim}{\boldsymbol{0}}}$$

$$\frac{\partial r_p}{\partial \Delta\gamma^s} = \frac{\partial}{\partial \Delta\gamma^s}\left(\Delta\gamma^s - \Delta t \left\langle \frac{|\underset{\sim}{\sigma} : \underset{\sim}{P}^s| - r^s}{K} \right\rangle^n \operatorname{sgn}(\underset{\sim}{\sigma} : \underset{\sim}{P}^s)\right)$$
$$= 1 - \Delta t \frac{\partial r^s}{\partial \gamma^s}\frac{\gamma^s}{\Delta\gamma^s}\frac{n}{K}\left\langle \frac{|\underset{\sim}{\sigma} : \underset{\sim}{P}^s| - r^s}{K} \right\rangle^{n-1} \operatorname{sgn}(\underset{\sim}{\sigma} : \underset{\sim}{P}^s)$$

$$\boxed{\frac{\partial r_p}{\partial \Delta\gamma^s} = 1 - \theta\Delta t \frac{\partial r^s}{\partial \gamma^s}\frac{n}{K}\left\langle \frac{|\underset{\sim}{\sigma} : \underset{\sim}{P}^s| - r^s}{K} \right\rangle^{n-1} \operatorname{sgn}(\underset{\sim}{\sigma} : \underset{\sim}{P}^s)}$$

$$\frac{\partial r_p}{\partial \Delta \underset{\sim}{e}^e} = \frac{\partial}{\partial \underset{\sim}{e}^e}\left(\Delta\gamma^s - \Delta t \left\langle \frac{|\underset{\sim}{\sigma} : \underset{\sim}{P}^s| - r^s}{K} \right\rangle^n \operatorname{sgn}(\underset{\sim}{\sigma} : \underset{\sim}{P}^s)\right)$$
$$= -\Delta t \frac{n}{K}\left\langle \frac{|\underset{\sim}{\sigma} : \underset{\sim}{P}^s| - r^s}{K} \right\rangle^{n-1} \frac{\partial |\underset{\sim}{\sigma} : \underset{\sim}{P}^s|}{\partial \underset{\sim}{\sigma}_\theta} : \frac{\partial \underset{\sim}{\sigma}_\theta}{\partial \underset{\sim}{e}^e_\theta} : \frac{\partial \underset{\sim}{e}^e_\theta}{\partial \Delta \underset{\sim}{e}^e} \operatorname{sgn}(\underset{\sim}{\sigma} : \underset{\sim}{P}^s)$$
$$= -\Delta t \frac{n}{K}\left\langle \frac{|\underset{\sim}{\sigma} : \underset{\sim}{P}^s| - r^s}{K} \right\rangle^{n-1} \frac{\underset{\sim}{\sigma} : \underset{\sim}{P}^s}{|\underset{\sim}{\sigma} : \underset{\sim}{P}^s|} \underset{\sim}{P}^s : \underset{\approx}{\Lambda}_\theta : \theta \underset{\approx}{I} \operatorname{sgn}(\underset{\sim}{\sigma} : \underset{\sim}{P}^s)$$

$$\boxed{-\theta\Delta t \frac{n}{K}\left\langle \frac{|\underset{\sim}{\sigma} : \underset{\sim}{P}^s| - r^s}{K} \right\rangle^{n-1} \underset{\sim}{P}^s : \underset{\approx}{\Lambda}_\theta \operatorname{sgn}(\underset{\sim}{\sigma} : \underset{\sim}{P}^s) \operatorname{sgn}(\underset{\sim}{\sigma} : \underset{\sim}{P}^s)}$$

$$\frac{\partial r_p}{\partial \Delta \underset{\sim}{\kappa}} = \frac{\partial}{\partial \underset{\sim}{\kappa}}\left(\Delta\gamma^s - \Delta t \left\langle \frac{|\underset{\sim}{\sigma} : \underset{\sim}{P}^s| - r^s}{K} \right\rangle^n \operatorname{sgn}(\underset{\sim}{\sigma} : \underset{\sim}{P}^s)\right)$$
$$= \underset{\sim}{0}$$

$$\boxed{\frac{\partial r_p}{\partial \Delta \underset{\sim}{\kappa}} = \underset{\sim}{0}}$$

Appendix B

KWC model using microforce formalism

The energy functional of the system is defined by

$$\mathscr{F} = \int_V f(\phi, \nabla\phi, \theta, \nabla\theta) dV = \int_V f_0(\phi) + \frac{\alpha^2}{2}|\nabla\phi|^2 + sg(\phi)|\nabla\theta| d\phi$$

This free energy corresponds to a KWC model with $\varepsilon = 0$. Let us determine the evolution equations based on the approach proposed by Gurtin [1996], which uses the principle of virtual powers. To do so, let us first introduce the generalized stress measures which are power-conjugate to the fields of virtual order parameters $\phi^\star(\underline{x}, t)$ and $\theta^\star(\underline{x}, t)$ and their first gradient:

- The internal microforce π_ϕ associated to $\phi^\star$
- The internal microforce π_θ associated to $\theta^\star$
- The microstress vector $\underline{\xi}_\theta$ associated to $\nabla\phi^\star$
- The microstress vector $\underline{\xi}_\theta$ associated to $\nabla\theta^\star$
- The external microforce γ_ϕ associated to $\phi^\star$
- The external microforce γ_θ associated to $\theta^\star$
- The volume density of microforce $\underline{\gamma}_\phi$ associated to $\phi^\star$
- The volume density of microforce $\underline{\gamma}_\theta$ associated to $\theta^\star$
- The surface density of microtraction ζ_ϕ associated to $\phi^\star$
- The surface density of microtraction ζ_θ associated to $\theta^\star$

The virtual power of internal generalized forces is given by:

$$\mathscr{P}^i = \int_V \pi_\phi \dot{\phi}^\star + \pi_\theta \dot{\theta}^\star - \left(\underline{\xi}_\phi \cdot \nabla\dot{\phi}^\star + \underline{\xi}_\theta \cdot \nabla\dot{\theta}^\star\right) dV$$

Recalling the identity

$$\nabla \cdot \left(\underline{\xi}_\bullet \bullet\right) = \bullet \nabla \cdot \underline{\xi}_\bullet + \underline{\xi}_\bullet \cdot \nabla\bullet$$

where $\bullet = \{\phi^\star, \theta^\star\}$, we get:

$$\begin{aligned}\mathscr{P}^i &= \int_V \pi_\phi \dot{\phi}^\star + \pi_\theta \dot{\theta}^\star - \left(\nabla \cdot \left(\underline{\xi}_\phi \dot{\phi}^\star\right) - \dot{\phi}^\star \nabla \cdot \underline{\xi}_\phi + \nabla \cdot \left(\underline{\xi}_\theta\right) - \dot{\theta}^\star \nabla \cdot \underline{\xi}_\theta\right) dV \\ &= \int_V \left(\pi_\phi + \nabla \cdot \underline{\xi}_\phi\right) \dot{\phi}^\star + \left(\pi_\theta + \nabla \cdot \underline{\xi}_\theta\right) \dot{\theta}^\star - \left(\nabla \cdot \left(\underline{\xi}_\phi \dot{\phi}^\star\right) + \nabla \cdot \left(\underline{\xi}_\theta \dot{\theta}^\star\right)\right) dV\end{aligned}$$

Making use of the divergence theorem $\int_V \nabla \cdot \xi dV = \int_{\partial V} \xi \cdot \underline{n}\, dS$ we get:

$$\boxed{\mathscr{P}^i = \int_V \left(\pi_\phi + \nabla \cdot \underline{\xi}_\phi\right) \dot{\phi}^\star + \left(\pi_\theta + \nabla \cdot \underline{\xi}_\theta\right) \dot{\theta}^\star dV - \int_{\partial V} \left(\underline{\xi}_\phi \dot{\phi}^\star + \underline{\xi}_\theta \dot{\theta}^\star\right) \cdot \underline{n}\, dS}$$

The virtual power of external forces applied to the considered body is defined by:

$$\mathscr{P}^e = \int_V \gamma_\phi \dot{\phi}^\star + \underline{\gamma}_\phi \cdot \nabla \dot{\phi}^\star + \gamma_\theta \dot{\theta}^\star + \underline{\gamma}_\theta \cdot \nabla \dot{\theta}^\star dV$$
$$\mathscr{P}^e = \int_V \left(\gamma_\phi - \nabla \cdot \underline{\gamma}_\phi\right) \dot{\phi}^\star + \left(\gamma_\theta - \nabla \cdot \underline{\gamma}_\phi\right) \dot{\phi}^\star dV + \int_{\partial V} \left(\dot{\phi}^\star \underline{\gamma}_\phi + \dot{\theta}^\star \underline{\gamma}_\theta\right) \underline{n}\, dS$$

where the divergence theorem was used. Finally, let us express the contact power:

$$\boxed{\mathscr{P}^c = \int_V \zeta_\phi \dot{\phi}^\star + \zeta_\theta \dot{\theta}^\star dV}$$

Neglecting the inertial microforces, the principle of virtual powers reads:

$$\mathscr{P}^i + \mathscr{P}^e + \mathscr{P}^c = 0$$

which gives:

$$\int_V \left(\pi_\phi + \nabla \cdot \underline{\xi}_\phi + \gamma_\phi - \nabla \cdot \underline{\gamma}_\phi\right) \dot{\phi}^\star dV + \int_V \left(\pi_\theta + \nabla \cdot \underline{\xi}_\theta + \gamma_\theta - \nabla \cdot \underline{\gamma}_\theta\right) \dot{\theta}^\star dV$$
$$+ \int_{\partial V} \left(\left(\underline{\gamma}_\phi - \underline{\xi}_\phi\right) \cdot \underline{n} + \zeta_\phi\right) \dot{\phi}^\star + \left(+\left(\underline{\gamma}_\theta - \underline{\xi}_\theta\right) \cdot \underline{n} + \zeta_\theta\right) \dot{\theta}^\star dS = 0$$

which can be satisfied $\forall \phi^\star, \forall \theta^\star$ and $\forall V$ if and only if:

$$\begin{cases} \nabla \cdot \left(\underline{\xi}_\phi - \underline{\gamma}_\phi\right) + \pi_\phi + \gamma_\phi = 0 \\ \nabla \cdot \left(\underline{\xi}_\theta - \underline{\gamma}_\theta\right) + \pi_\theta + \gamma_\theta = 0 \end{cases} \text{ in } V \text{ (balance equations)}$$
$$\begin{cases} \left(\gamma_\phi - \underline{\xi}_\phi\right) \cdot \underline{n} + \zeta_\phi = 0 \\ \left(\gamma_\theta - \underline{\xi}_\theta\right) \cdot \underline{n} + \zeta_\theta = 0 \end{cases} \text{ on } \partial V \text{ (boundary conditions)}$$

In the remainder of this work, $\gamma_\phi = \gamma_\theta = 0$ and $\underline{\gamma}_\phi = \underline{\gamma}_\theta = \underline{0}$. The balance equations and boundary conditions thus reduce to:

$$\begin{cases} \nabla \cdot \underline{\xi}_\phi + \pi_\phi = 0 \\ \nabla \cdot \underline{\xi}_\theta + \pi_\theta = 0 \end{cases} \text{ in } V \text{ (balance equations)}$$
$$\begin{cases} \zeta_\phi = 0 \\ \zeta_\theta = 0 \end{cases} \text{ on } \partial V \text{ (boundary conditions)}$$

Without accounting for inertia and volumetric heat sources, the first principle of thermodynamics states that:

$$\dot{E} = \mathscr{P}^{ext} + \mathscr{Q}$$

where $\mathscr{P}^{ext}$ is the power of external forces such that $\mathscr{P}^{int} + \mathscr{P}^{ext} = 0$, $\dot{E} = \int_V \dot{e} dV$ is the time variation of the internal energy and $\dot{e}$ its volume density. $\mathscr{Q} = -\int_{\partial V} \underline{q} \cdot \underline{n}\, dS$ is the heat rate and $\underline{q}$ the heat flux. Using

the identity $\mathscr{P}^{int} + \mathscr{P}^{ext} = 0$ allows to rewrite the first principle such that:

$$\dot{E} = -\mathscr{P}^{int} + \mathscr{Q}$$

This gives:

$$\begin{aligned}\int_V \rho \dot{e} dV &= -\int_V \pi_\phi \dot{\phi} + \pi_\theta \dot{\theta} - \left(\underline{\xi}_\phi \cdot \nabla\dot{\phi} + \underline{\xi}_\theta \cdot \nabla\dot{\theta}\right) dV - \int_{\partial V} \underline{q} \cdot \underline{n} \, dS \\ &= \int_V -\pi_\phi \dot{\phi} - \pi_\theta \dot{\theta} + \underline{\xi}_\phi \cdot \nabla\dot{\phi} + \underline{\xi}_\theta \cdot \nabla\dot{\theta} - \nabla \cdot \underline{q} \, dV\end{aligned}$$

The local form of the internal energy is thus:

$$\rho \dot{e} = \underbrace{-\pi_\phi \dot{\phi} - \pi_\theta \dot{\theta} + \underline{\xi}_\phi \cdot \nabla\dot{\phi} + \underline{\xi}_\theta \cdot \nabla\dot{\theta}}_{-p^i} - \nabla \cdot \underline{q} \tag{2.1}$$

Neglecting volumetric heat sources, the second principle of thermodynamics states that:

$$\int_V \rho \dot{s} dV \geq -\int_{\partial V} \frac{\underline{\underline{q}} \cdot \underline{n}}{T} dS \tag{2.2}$$

where s is the entropy per unit mass. The entropy inequality can be rewritten as:

$$\begin{aligned}&\int_V \rho \dot{s} dV + \int_{\partial V} \frac{\underline{\underline{q}} \cdot \underline{n}}{T} dS \geq 0 \\ \iff &\int_V \rho \dot{s} + \nabla \cdot \frac{\underline{\underline{q}}}{T} dV \geq 0\end{aligned}$$

The local form of the inequality is thus, for isothermal processes:

$$\rho \dot{s} + \nabla \cdot \frac{\underline{\underline{q}}}{T} \geq 0 \tag{2.3}$$

$$\rho \dot{s} + \frac{\nabla \cdot \underline{q}}{T} - \frac{\underline{\underline{q}} \cdot \nabla T}{T^2} \geq 0 \tag{2.4}$$

Multiplying this inequality by $T > 0$ and using $\nabla \cdot \underline{q} = \dot{e} + p^i$, the inequality becomes:

$$\rho(T\dot{s} - \dot{e}) - p^i - \frac{\underline{\underline{q}} \cdot \nabla T}{T^2} \geq 0 \tag{2.5}$$

The time variation of the free energy density $\psi(\phi, \nabla\phi, \theta, \nabla\theta)$ is given by

$$\dot{\psi} = \dot{e} - T\dot{s} = \frac{\partial \psi}{\partial \phi}\dot{\phi} + \frac{\partial \psi}{\partial \nabla\phi} \cdot \nabla\dot{\phi} + \frac{\partial \psi}{\partial \theta}\dot{\theta} + \frac{\partial \psi}{\partial \nabla\theta} \cdot \nabla\dot{\theta}$$

Combining $T\dot{s} = \dot{e} - \dot{\psi}$ with the local entropy inequality gives the Clausius-Duhem inequality:

$$\begin{aligned}-\rho\dot{\psi} - p^i - \frac{\underline{\underline{q}} \cdot \nabla T}{T^2} &\geq 0 \\ -\rho\left(\frac{\partial \psi}{\partial \phi}\dot{\phi} + \frac{\partial \psi}{\partial \nabla\phi} \cdot \nabla\dot{\phi} + \frac{\partial \psi}{\partial \theta}\dot{\theta} + \frac{\partial \psi}{\partial \nabla\theta} \cdot \nabla\dot{\theta}\right) - \pi_\phi\dot{\phi} - \pi_\theta\dot{\theta} + \underline{\xi}_\phi \cdot \nabla\dot{\phi} + \underline{\xi}_\theta \cdot \nabla\dot{\theta} - \frac{\underline{\underline{q}} \cdot \nabla T}{T^2} &\geq 0 \\ -\left(\pi_\phi + \frac{\partial \psi}{\partial \phi}\right)\dot{\phi} + \left(\underline{\xi}_\phi - \frac{\partial \psi}{\partial \nabla\phi}\right) \cdot \nabla\dot{\phi} - \left(\pi_\theta + \frac{\partial \psi}{\partial \theta}\right)\dot{\theta} + \left(\underline{\xi}_\theta - \frac{\partial \psi}{\partial \nabla\theta}\right) \cdot \nabla\dot{\theta} - \frac{\underline{\underline{q}} \cdot \nabla T}{T^2} &\geq 0\end{aligned}$$

This inequality must hold $\forall(\phi, \nabla\phi, \theta, \nabla\theta)$. The micros stresses $\underline{\xi}_\phi(\phi, \nabla\phi)$ and $\underline{\xi}_\theta(\theta, \nabla\theta)$ are assumed

independent of $\dot{\phi}, \nabla\dot{\phi}, \dot{\theta}, \nabla\dot{\theta}$. Thus:

$$\boxed{\underline{\xi}_{\phi} = \frac{\partial \psi}{\partial \nabla \phi}, \ \underline{\xi}_{\theta} = \frac{\partial \psi}{\partial \nabla \theta}}$$

It is assumed that π_ϕ, π_θ contains energetic and dissipative contributions:

$$\pi_\phi = \pi_\phi^{eq} + \pi_\phi^{neq}, \quad \pi_\theta = \pi_\theta^{eq} + \pi_\theta^{neq} \tag{2.6}$$

$$\pi_\phi = \frac{\partial \psi}{\partial \phi} + \pi_\phi^{neq}, \quad \pi_\theta = \frac{\partial \psi}{\partial \theta} + \pi_\theta^{neq} \tag{2.7}$$

Let us assume the existence of a dissipation potential $\Omega\left(\pi_\phi^{neq}, \pi_\theta^{neq}\right)$ of the form

$$\Omega = \frac{1}{2}\frac{1}{Q\tau_\phi}\left(\pi_\phi^{neq}\right)^2 + \frac{1}{2}\frac{1}{P\tau_\theta}\left(\pi_\theta^{neq}\right)^2$$

where Q and P are functions of $(\phi, \nabla\phi, \theta, \nabla\theta, T)$ and τ_ϕ, τ_θ are material parameters. The convexity of this potential is ensured by the choice of quadratic terms. This convexity ensures the positivity of the dissipation. The evolution laws derive from this potential:

$$\begin{cases} \dot{\phi} = \dfrac{-\partial\Omega}{\partial \pi_\phi^{neq}} \\ \dot{\theta} = \dfrac{-\partial\Omega}{\partial \pi_\theta^{neq}} \end{cases}$$

$$\iff \begin{cases} \dot{\phi} = -\dfrac{1}{Q\tau_\phi}\pi_\phi^{neq} \\ \dot{\theta} = -\dfrac{1}{P\tau_\theta}\pi_\theta^{neq} \end{cases}$$

$$\iff \begin{cases} \pi_\phi = -Q\tau_\phi\dot{\phi} - \dfrac{\partial\psi}{\partial\phi} \\ \pi_\theta = -P\tau_\theta\dot{\theta} - \dfrac{\partial\psi}{\partial\theta} \end{cases}$$

Then:

$$\begin{cases} \pi_\phi = -Q\tau_\phi\dot{\phi} - \dfrac{\partial\psi}{\partial\phi} \\ \pi_\theta = -P\tau_\theta\dot{\theta} - \dfrac{\partial\psi}{\partial\theta} \end{cases}$$

Finally, combining these equations with the balance equations $\begin{cases} \nabla\cdot\underline{\xi}_{\phi} + \pi_\phi = 0 \\ \nabla\cdot\underline{\xi}_{\theta} + \pi_\theta = 0 \end{cases}$ and $\begin{cases} \underline{\xi}_{\phi} = \dfrac{\partial\psi}{\partial\nabla\phi} \\ \underline{\xi}_{\theta} = \dfrac{\partial\psi}{\partial\nabla\theta} \end{cases}$

the evolution equations are:

$$
\begin{aligned}
&\begin{cases}
\nabla\cdot\left(\dfrac{\partial\psi}{\partial\nabla\phi}\right)-Q\tau_\phi\dot{\phi}-\dfrac{\partial\psi}{\partial\phi}=0\\
\nabla\cdot\left(\dfrac{\partial\psi}{\partial\nabla\theta}\right)-P\tau_\theta\dot{\theta}-\dfrac{\partial\psi}{\partial\theta}=0
\end{cases}\\
\Longleftrightarrow\ &\begin{cases}
\nabla\cdot\left(\dfrac{\partial\psi}{\partial\nabla\phi}\right)-\dfrac{\partial\psi}{\partial\phi}=Q\tau_\phi\dot{\phi}\\
\nabla\cdot\left(\dfrac{\partial\psi}{\partial\nabla\theta}\right)-\dfrac{\partial\psi}{\partial\theta}=P\tau_\theta\dot{\theta}
\end{cases}\\
\Longleftrightarrow\ &\begin{cases}
Q\tau_\phi\dot{\phi}=-\dfrac{\delta\mathscr{F}}{\delta\phi}\\
P\tau_\theta\dot{\theta}=-\dfrac{\delta\mathscr{F}}{\delta\theta}
\end{cases}
\end{aligned}
$$

where $\dfrac{\delta\mathscr{F}}{\delta\bullet}=\dfrac{\partial f}{\partial\bullet}-\nabla\cdot\dfrac{\partial f}{\nabla\bullet}$ is the functional derivative with respect to variable $\bullet$.

Appendix C

Interface with sharp orientation field

Contents

III.1 1D stationary equations

Let us choose

$$f_0(\phi) = \frac{1}{2}(1-\phi)^2,\ g(\phi) = h(\phi) = \phi^2$$

for the free energy density. The 1D equilibrium equations are thus:

$$\begin{cases} 0 = -\dfrac{\delta \mathscr{F}}{\delta \phi} \\ 0 = -\dfrac{\delta \mathscr{F}}{\delta \theta} \end{cases}$$

$$\iff \begin{cases} 0 = -\left(\dfrac{\partial f_0(\phi)}{\partial \phi} + s\dfrac{\partial g(\phi)}{\partial \phi}|\nabla\theta|\right) - \dfrac{\partial}{\partial x}\left(\dfrac{\alpha^2}{2}\dfrac{\partial}{\partial \nabla\phi}|\nabla\phi|^2\right) \\ 0 = -\left(-\dfrac{\partial}{\partial x}\left(\dfrac{\partial}{\partial \nabla\theta} s g(\phi)|\nabla\theta|\right)\right) \end{cases}$$

$$\iff \begin{cases} 0 = (1-\phi) - 2\phi s|\nabla\theta| + \alpha^2\Delta\phi \\ 0 = s\dfrac{\partial}{\partial x}\left(\phi^2 \dfrac{\partial}{\partial \nabla\theta}\sqrt{(\nabla\theta)^2}\right) \end{cases}$$

$$\iff \begin{cases} 0 = (1-\phi) - 2\phi s|\nabla\theta| + \alpha^2\Delta\phi \\ 0 = s\dfrac{\partial}{\partial x}\left(\phi^2 \dfrac{\frac{\partial (\nabla\theta)^2}{\partial \nabla\theta}}{2\sqrt{(\nabla\theta)^2}}\right) \end{cases}$$

$$\iff \boxed{\begin{cases} 0 = (1-\phi) - 2\phi s|\nabla\theta| + \alpha^2\Delta\phi \\ 0 = s\dfrac{\partial}{\partial x}\left(\phi^2 \dfrac{\nabla\theta}{|\nabla\theta|}\right) \end{cases}}$$

It has been mentioned by Kobayashi et al. [2000] that the solution for θ of this system of equations can be showed to be Kobayashi and Giga [1999]:

$$\theta(x) = \begin{cases} \theta^-,\ x < 0 \\ \theta^+,\ x > 0 \end{cases} \tag{3.1}$$

Moreover,

$$\left|\frac{\partial\theta}{\partial x}\right| = \Delta\theta\,\delta(x)$$

with $\Delta\theta$ the misorientation angle and $\delta(x)$ the Dirac delta function. It has the property

$$\int_{-\infty}^{+\infty} f(x)\delta(x)dx = f(0)$$

.

III.2 Determination of $\phi(x)$

Let us now consider $x \in]-\infty, 0[\cup]0, +\infty[$ such that $\nabla\theta = 0$. The equation on ϕ is now given by:

$$0 = (1-\phi) + \alpha^2\Delta\phi$$

The homogeneous equation associated to this differential equation is

$$0 = \alpha^2\Delta\phi - \phi$$

The characteristic equation is

$$\alpha^2 y^2 - 1 = 0$$

whose solutions are $y = \pm\sqrt{\frac{1}{\alpha^2}} = \pm\frac{1}{\alpha}$
the solution to the homogeneous equation is given by:

$$\phi_h = A_1 \exp\left(-\frac{1}{\alpha}|x|\right) + A_2 \exp\left(\frac{1}{\alpha}|x|\right)$$

Let us find a particular solution ϕ_p to the equation $0 = (1-\phi) + \alpha^2\Delta\phi$. Seeking it in the form of $\phi_p = cst$ we get $y_p = 1$. Thus

$$\phi(|x|) = \phi_h + \phi_p = A_1 \exp\left(-\frac{1}{\alpha}|x|\right) + A_2 \exp\left(\frac{1}{\alpha}|x|\right) + 1$$

The boundary condition $\phi(x = \pm\infty) = 1$ gives:

$$\lim_{x\to\infty}\phi(x) = 1 \Rightarrow \lim_{x\to\infty} A_2 \exp\left(\frac{1}{\alpha}|x|\right) = 0$$
$$\Rightarrow A_2 = 0$$

Thus

$$\phi(x) = A_1 \exp\left(-\frac{1}{\alpha}|x|\right) + 1$$

A_1 can be determined from the condition $\phi(x=0) = \phi_{min}$:

$$A_1 + 1 = \phi_{min}$$
$$\iff A_1 = \phi_{min} - 1$$

Finally,

$$\phi(x) = (\phi_{min} - 1)\exp\left(-\frac{1}{\alpha}|x|\right) + 1$$

An equivalent form used in Kobayashi et al. [2000] is

$$\boxed{\phi(x) = 1 - (1-\phi_{min})\exp\left(-\frac{1}{\alpha}|x|\right)}$$

III.3 Determination of ϕ_{min}

Using the newly found expression for $\phi(x)$ and making use of the property of the Dirac distribution, we can compute ϕ_{min} by integrating the equation on ϕ between 0^+ and 0^-:

$$\begin{aligned}
\alpha^2 \int_{0^-}^{0^+} \phi'' dx &= -\int_{0^-}^{0^+} 1 dx + \int_{0^-}^{0^+} \phi dx + 2s \int_{0^-}^{0^+} \phi |\theta'| dx \\
\alpha^2 [\phi']_{0^-}^{0^+} &= -\int_{0^-}^{0^+} 1 dx + \int_{0^-}^{0^+} \phi dx + 2s \int_{0^-}^{0^+} \phi \Delta\theta \delta(x) dx \\
&= -\int_{0^-}^{0^+} 1 dx + \int_{0^-}^{0^+} \phi dx + 2s\Delta\theta\phi(0) \\
&= -\int_{0^-}^{0^+} 1 dx + \int_{0^-}^{0^+} \phi dx + 2s\Delta\theta\phi_{min} \\
&= -\int_{0^-}^{0^+} 1 dx + \left(\int_{0^-}^{0^+} 1 - (1-\phi_{min})\exp\left(-\frac{1}{\alpha}|x|\right) dx\right) + 2s\Delta\theta\phi_{min} \\
&= -\int_{0^-}^{0^+} 1 dx + \int_{0^-}^{0^+} 1 dx - (1-\phi_{min})\left[-\frac{\alpha}{\text{sign}(x)}\exp\left(-\frac{1}{\alpha}|x|\right)\right]_{0^-}^{0^+} + 2s\Delta\theta\phi_{min} \\
&= -(1-\phi_{min})(-\alpha - -\alpha) + 2s\Delta\theta\phi_{min}
\end{aligned}$$

Finally, we get

$$\alpha^2 [\phi']_{0^-}^{0^+} = 2s\phi_{min}\Delta\theta$$

with the expression $\phi'(x) = \left(-\frac{\text{sign}(x)}{\alpha}\right)\left(-(1-\phi_{min})\exp\left(\frac{1}{\alpha}|x|\right)\right)$ we can compute ϕ_{min}:

$$\begin{aligned}
\alpha^2\left(\frac{1}{\alpha}(1-\phi_{min}) - -\frac{1}{\alpha}(1-\phi_{min})\right) &= 2s\phi_{min}\Delta\theta \\
\iff 2\alpha(1-\phi_{min}) &= 2s\phi_{min}\Delta\theta \\
\iff \phi_{min}\left(1+\frac{s\Delta\theta}{\alpha}\right) &= 1
\end{aligned}$$

In the end:

$$\boxed{\phi_{min} = \frac{1}{1+\frac{s\Delta\theta}{\alpha}} = \frac{\alpha}{\alpha + s\Delta\theta}}$$

III.4 Determination of γ_{GB}

The 1D energy functional is given by:

$$\begin{aligned}
\mathscr{F} &= \int_{-\infty}^{+\infty} f(\phi) + \frac{\alpha^2}{2}\left|\frac{\partial\phi}{\partial x}\right|^2 + sg(\phi)\left|\frac{\partial\theta}{\partial x}\right| dx \\
&= \int_{-\infty}^{+\infty} \frac{1}{2}(1-\phi)^2 + \frac{\alpha^2}{2}\left|\frac{\partial\phi}{\partial x}\right|^2 + s\phi^2\left|\frac{\partial\theta}{\partial x}\right| dx \\
&= \int_{-\infty}^{+\infty} \frac{1}{2}(1-\phi)^2 + \frac{\alpha^2}{2}\left|\frac{\partial\phi}{\partial x}\right|^2 dx + \int_{-\infty}^{+\infty} s\phi^2\left|\frac{\partial\theta}{\partial x}\right| dx \\
&= \int_{-\infty}^{+\infty} \frac{1}{2}(1-\phi)^2 + \frac{\alpha^2}{2}\left|\frac{\partial\phi}{\partial x}\right|^2 dx + \int_{-\infty}^{+\infty} s\Delta\theta\phi^2\delta(x)dx \\
&= \int_{-\infty}^{+\infty} \frac{1}{2}(1-\phi)^2 + \frac{\alpha^2}{2}\left|\frac{\partial\phi}{\partial x}\right|^2 dx + s\Delta\theta\phi^2(x=0) \\
&= \int_{-\infty}^{+\infty} \frac{1}{2}(1-\phi)^2 + \frac{\alpha^2}{2}\left|\frac{\partial\phi}{\partial x}\right|^2 dx + s\Delta\theta\phi_{min}^2
\end{aligned}$$

Focusing on

$$\int_{-\infty}^{+\infty} \frac{1}{2}(1-\phi)^2 + \frac{\alpha^2}{2}\left|\frac{\partial\phi}{\partial x}\right|^2 dx = \int_{-\infty}^{0} \frac{1}{2}(1-\phi)^2 + \frac{\alpha^2}{2}\left|\frac{\partial\phi}{\partial x}\right|^2 dx + \int_{0}^{+\infty} \frac{1}{2}(1-\phi)^2 + \frac{\alpha^2}{2}\left|\frac{\partial\phi}{\partial x}\right|^2 dx$$

let us express

$$\begin{aligned}
\frac{1}{2}(1-\phi)^2 + \frac{\alpha^2}{2}\left|\frac{\partial\phi}{\partial x}\right|^2 &= \frac{1}{2}\left(1-2\phi+\phi^2\right) + \frac{\alpha^2}{2}\left|\frac{\partial\phi}{\partial x}\right|^2 \\
&= \frac{1}{2}\left(1-2\left(1-(1-\phi_{min})\exp\left(-\frac{1}{\alpha}|x|\right)\right) + \left(1-(1-\phi_{min})\exp\left(-\frac{1}{\alpha}|x|\right)\right)^2\right) \\
&+ \frac{\alpha^2}{2}\left|\left(-\frac{\text{sign}(x)}{\alpha}\right)\left(-(1-\phi_{min})\exp\left(\frac{1}{\alpha}|x|\right)\right)\right|^2 \\
&= \frac{1}{2}(1-\phi_{min})^2\exp\left(-\frac{2}{\alpha}|x|\right) + \frac{\alpha^2}{2}\frac{1}{\alpha^2}(1-\phi_{min})^2\exp\left(-\frac{2}{\alpha}|x|\right) \\
&= (1-\phi_{min})^2\exp\left(-\frac{2}{\alpha}|x|\right)
\end{aligned}$$

Thus we have:

$$\begin{aligned}
\int_{-\infty}^{+\infty} \frac{1}{2}(1-\phi)^2 + \frac{\alpha^2}{2}\left|\frac{\partial\phi}{\partial x}\right|^2 dx &= (1-\phi_{min})^2\left(\int_{-\infty}^{0}\exp\left(-\frac{2}{\alpha}|x|\right)dx + \int_{0}^{+\infty}\exp\left(-\frac{2}{\alpha}|x|\right)dx+\right) \\
&= (1-\phi_{min})^2\left(\left[-\frac{\alpha}{2\text{sign}(x)}\exp\left(-\frac{2}{\alpha}|x|\right)\right]_{-\infty}^{0} + \left[-\frac{\alpha}{2\text{sign}(x)}\exp\left(-\frac{2}{\alpha}|x|\right)\right]_{0}^{+\infty}\right) \\
&= (1-\phi_{min})^2\left(\left[\frac{\alpha}{2}-0\right] + \left[0--\frac{\alpha}{2}\right]\right) \\
&= \alpha(1-\phi_{min})^2
\end{aligned}$$

We get

$$\mathscr{F} = \gamma_{GB} = \alpha(1-\phi_{min})^2 + s\Delta\theta\phi_{min}^2$$

Using $\phi_{min} = \dfrac{\alpha}{\alpha + s\Delta\theta}$ we find:

$$\begin{aligned}
\gamma_{GB} &= \alpha\left(1 - \frac{\alpha}{\alpha + s\Delta\theta}\right)^2 + s\Delta\theta\left(\frac{\alpha}{\alpha + s\Delta\theta}\right)^2 \\
&= \alpha\left(1 - 2\frac{2\alpha}{\alpha + s\Delta\theta} + \frac{\alpha^2}{(\alpha + s\Delta\theta)^2}\right) + \frac{s\Delta\theta\alpha^2}{(\alpha + s\Delta\theta)^2} \\
&= \frac{\alpha\left((\alpha + s\Delta\theta)^2 - 2\alpha(\alpha + s\Delta\theta) + \alpha^2\right) + s\Delta\theta\alpha^2}{(\alpha + s\Delta\theta)^2} \\
&= \frac{\alpha\left(\alpha^2 + 2s\Delta\theta\alpha + (s\Delta\theta)^2 - 2\alpha^2 - 2\alpha s\Delta\theta + \alpha^2\right) + s\Delta\theta\alpha^2}{(\alpha + s\Delta\theta)^2} \\
&= \frac{\alpha(s\Delta\theta)^2 + s\Delta\theta\alpha^2}{(\alpha + s\Delta\theta)^2} \\
&= \frac{\alpha s\Delta\theta(s\Delta\theta + \alpha)}{(\alpha + s\Delta\theta)^2}
\end{aligned}$$

Finally

$$\boxed{\gamma_{GB} = \frac{\alpha s\Delta\theta}{\alpha + s\Delta\theta}}$$

Bibliography

Abrivard, G. (2009). *A coupled crystal plasticity–phase field formulation to describe microstructural evolution in polycrystalline aggregates*. PhD thesis, Mines ParisTech.

Abrivard, G., Busso, E., Forest, S., and Appolaire, B. (2012a). Phase field modelling of grain boundary motion driven by curvature and stored energy gradients. part i: theory and numerical implementation. *Philosophical Magazine*, 92:3618–3642.

Abrivard, G., Busso, E., Forest, S., and Appolaire, B. (2012b). Phase field modelling of grain boundary motion driven by curvature and stored energy gradients. part ii: Application to recrystallisation. *Philosophical Magazine*, 92:3643–3664.

Admal, N. C., Po, G., and Marian, J. (2018). A unified framework for polycrystal plasticity with grain boundary evolution. *International Journal of Plasticity*, 106:1–30.

Admal, N. C., Segurado, J., and Marian, J. (2019). A three-dimensional misorientation axis-and inclination-dependent kobayashi–warren–carter grain boundary model. *Journal of the Mechanics and Physics of Solids*, 128:32–53.

Ahmadian, A., Scheiber, D., Zhou, X., Gault, B., Liebscher, C. H., Romaner, L., and Dehm, G. (2021). Aluminum depletion induced by co-segregation of carbon and boron in a bcc-iron grain boundary. *Nature Communications*, 12(1):6008.

Anand, L., Gurtin, M. E., and Reddy, B. D. (2015). The stored energy of cold work, thermal annealing, and other thermodynamic issues in single crystal plasticity at small length scales. *International Journal of Plasticity*, 64:1 – 25.

Anderson, M., Srolovitz, D., Grest, G., and Sahni, P. (1984). Computer simulation of grain growth–i. kinetics. *Acta metallurgica*, 32(5):783–791.

Asaro, R. J. and Rice, J. (1977). Strain localization in ductile single crystals. *Journal of the Mechanics and Physics of Solids*, 25(5):309–338.

Ashby, M. (1970). The deformation of plastically non-homogeneous materials. *The Philosophical Magazine: A Journal of Theoretical Experimental and Applied Physics*, 21(170):399–424.

Ask, A., Forest, S., Appolaire, B., and Ammar, K. (2018a). Cosserat crystal plasticity with dislocation–driven grain boundary migration. *Journal of Micromechanics and Molecular Physics*, 3:1840009.

Ask, A., Forest, S., Appolaire, B., and Ammar, K. (2019). A Cosserat–phase-field theory of crystal plasticity and grain boundary migration at finite deformation. *Continuum Mechanics and Thermodynamics*, 31(4):1109–1141.

Ask, A., Forest, S., Appolaire, B., and Ammar, K. (2020). Microstructure evolution in deformed polycrystals predicted by a diffuse interface Cosserat approach. *Advanced Modeling and Simulation in Engineering Sciences*, 7(1):1–28.

Ask, A., Forest, S., Appolaire, B., Ammar, K., and Salman, O. U. (2018b). A Cosserat crystal plasticity and phase field theory for grain boundary migration. *Journal of the Mechanics and Physics of Solids*, 115:167–194.

Avrami, M. (1939). Kinetics of phase change. i general theory. *The Journal of chemical physics*, 7(12):1103–1112.

Avrami, M. (1940). Kinetics of phase change. ii transformation-time relations for random distribution of nuclei. *The Journal of chemical physics*, 8(2):212–224.

Bailey, J. and Hirsch, P. B. (1962). The recrystallization process in some polycrystalline metals. *Proceedings of the Royal Society of London. Series A. Mathematical and Physical Sciences*, 267(1328):11–30.

Bainbridge, D. W., Choh, H. L., and Edwards, E. H. (1954). Recent observations on the motion of small angle dislocation boundaries. *Acta metallurgica*, 2(2):322–333.

Beck, P. A. (1949). The formation of recrystallization nuclei. *Journal of Applied Physics*, 20(6):633–634.

Beck, P. A. and Sperry, P. R. (1950). Strain induced grain boundary migration in high purity aluminum. *Journal of applied physics*, 21(2):150–152.

Beheshti, A. (2018). A numerical analysis of Saint-Venant torsion in strain-gradient bars. *European Journal of Mechanics - A/Solids*, 70:181–190.

Beltran, O., Huang, K., and Logé, R. E. (2015). A mean field model of dynamic and post-dynamic recrystallization predicting kinetics, grain size and flow stress. *Computational Materials Science*, 102:293–303.

Bernacki, M., Chastel, Y., Coupez, T., and Logé, R. E. (2008). Level set framework for the numerical modelling of primary recrystallization in polycrystalline materials. *Scripta Materialia*, 58(12):1129–1132.

Bernard, P., Bag, S., Huang, K., and Logé, R. E. (2011). A two-site mean field model of discontinuous dynamic recrystallization. *Materials Science and Engineering: A*, 528(24):7357–7367.

Besdo, D. (1974). Ein beitrag zur nichtlinearen theorie des Cosserat-kontinuums. *Acta Mechanica*, 20(1):105–131.

Besson, J., Cailletaud, G., Chaboche, J.-L., Forest, S., and Blétry, M. (2009). *Non–Linear Mechanics of Materials*. Solid Mechanics and Its Applications 167. Springer-Verlag Berlin Heidelberg.

Besson, J. and Foerch, R. (1997). Large scale object–oriented finite element code design. *Computer Methods in Mechanical Engineering*, 142:165–187.

Bilby, B. (1955). Types of dislocation source. In *Report of Bristol conference on defects in crystalline solids*, pages 124–133. The Physical Society, Bristol, 1954, London.

Bilby, B. A., Bullough, R., and Smith, E. (1955). Continuous distributions of dislocations: a new application of the methods of non-riemannian geometry. *Proceedings of the Royal Society of London. Series A. Mathematical and Physical Sciences*, 231(1185):263–273.

Blesgen, T. (2015). On rotation deformation zons for finite-strain Cosserat plasticity. *Acta Mechanica*, 226:2421–2434.

Bonarski, B., Schafler, E., Mikulowski, B., and Zehetbauer, M. (2008). Texture evolution of magnesium single crystals deformed by high-pressure torsion. *Materials Science Forum*, 584-586:263–268.

Bourcier, R., Koss, D., Smelser, R., and Richmond, O. (1986). The influence of porosity on the deformation and fracture of alloys. *Acta Metallurgica*, 34(12):2443–2453.

Burke, J. and Turnbull, D. (1952). Recrystallization and grain growth. *Progress in metal physics*, 3:220–292.

Cahn, R. (1950). A new theory of recrystallization nuclei. *Proceedings of the Physical Society. Section A*, 63(4):323.

Chen, L., Chen, J., Lebensohn, R., Ji, Y., Heo, T., Bhattacharyya, S., Chang, K., Mathaudhu, S., Liu, Z., and Chen, L.-Q. (2015). An integrated fast fourier transform-based phase-field and crystal plasticity approach to model recrystallization of three dimensional polycrystals. *Computer Methods in Applied Mechanics and Engineering*, 285:829–848.

Chen, L.-Q. (2002). Phase-field models for microstructure evolution. *Annual review of materials research*, 32(1):113–140.

Chen, L.-Q. and Yang, W. (1994). Computer simulation of the domain dynamics of a quenched system with a large number of nonconserved order parameters: The grain-growth kinetics. *Physical Review B*, 50(21):15752.

Cheong, K. and Busso, E. (2004). Discrete dislocation density modelling of single phase FCC polycrystal aggregates. *Acta Materialia*, 52:5665–5675.

Cordero, N. M., Gaubert, A., Forest, S., Busso, E., Gallerneau, F., and Kruch, S. (2010). Size effects in generalised continuum crystal plasticity for two–phase laminates. *Journal of the Mechanics and Physics of Solids*, 58:1963–1994.

Cosserat, E. and Cosserat, F. (1909). *Théorie des corps déformables*. Hermann, Paris.

Cram, D., Zurob, H. S., Brechet, Y., and Hutchinson, C. (2009). Modelling discontinuous dynamic recrystallization using a physically based model for nucleation. *Acta Materialia*, 57(17):5218–5228.

Cruz-Fabiano, A. L., Logé, R., and Bernacki, M. (2014). Assessment of simplified 2d grain growth models from numerical experiments based on a level set framework. *Computational materials science*, 92:305–312.

Després, A., Greenwood, M., and Sinclair, C. (2020). A mean-field model of static recrystallization considering orientation spreads and their time-evolution. *Acta Materialia*, 199:116–128.

Diepolder, W., Mannl, V., and Lippman, H. (1991). The Cosserat continuum, a model for grain rotations in metals? *International journal of plasticity*, 7(4):313–328.

Dimokrati, A., Le Bouar, Y., Benyoucef, M., and Finel, A. (2020). S-PFM model for ideal grain growth. *Acta Materialia*, 201:147–157.

Dluzewski, P. (1992). Finite elastic-plastic deformations of oriented media. In Benallal, A. and Marquis, D., editors, *MECAMAT'92, Int. Seminar on Multiaxial Plasticity*. Cachan.

Doherty, R., Hughes, D., Humphreys, F., Jonas, J. J., Jensen, D. J., Kassner, M., King, W., McNelley, T., McQueen, H., and Rollett, A. (1997). Current issues in recrystallization: a review. *Materials Science and Engineering: A*, 238(2):219–274.

Drugan, W. and Lakes, R. (2018). Torsion of a Cosserat elastic bar with square cross section: theory and experiment. *Zeitschrift für angewandte Mathematik und Physik*, 69(2):1–14.

Elder, K., Grant, M., Provatas, N., and Kosterlitz, J. (2001). Sharp interface limits of phase-field models. *Physical Review E*, 64(2):021604.

Eringen, A. (1976). *Polar and non local fields theories,* in *Continuum Physics*, volume IV. Academic Press.

Eringen, A. (1999). *Microcontinuum field theories*. Springer, New York.

Fan, D., Geng, C., and Chen, L.-Q. (1997). Computer simulation of topological evolution in 2-d grain growth using a continuum diffuse-interface field model. *Acta materialia*, 45(3):1115–1126.

Ferdinand Knipschildt, E. F. (2022). Nucleation of recrystallization. *Materials Science and Technology*, 38(12):765–779.

Finel, A., Le Bouar, Y., Dabas, B., Appolaire, B., Yamada, Y., and Mohri, T. (2018). Sharp phase field method. *Physical review letters*, 121(2):025501.

Finel, A., Le Bouar, Y., Gaubert, A., and Salman, U. (2010). Phase field methods: Microstructures, mechanical properties and complexity. *Comptes Rendus Physique*, 11:245–256.

Fleck, N., Muller, G., Ashby, M. F., and Hutchinson, J. W. (1994). Strain gradient plasticity: theory and experiment. *Acta Metallurgica et materialia*, 42(2):475–487.

Flipon, B., Keller, C., Quey, R., and Barbe, F. (2020). A full-field crystal-plasticity analysis of bimodal polycrystals. *International Journal of Solids and Structures*, 184:178–192.

Forest, S. (1998). Modeling slip, kink and shear banding in classical and generalized single crystal plasticity. *Acta materialia*, 46(9):3265–3281.

Forest, S. (2005). Mechanics of Cosserat media–an introduction. *Ecole des Mines de Paris, Paris*, pages 1–20.

Forest, S. (2013). Questioning size effects as predicted by strain gradient plasticity. *Journal of the Mechanical Behavior of Materials*, 22:101–110.

Forest, S., Barbe, F., and Cailletaud, G. (2000). Cosserat modelling of size effects in the mechanical behaviour of polycrystals and multiphase materials. *International Journal of Solids and Structures*, 37:7105–7126.

Forest, S., Cailletaud, G., and Sievert, R. (1997). A Cosserat theory for elastoviscoplastic single crystals at finite deformation. *Archives of Mechanics*, 49(4):705–736.

Forest, S. and Ghiglione, F. (2023). Size effects in cosserat crystal plasticity. In *Sixty Shades of Generalized Continua: Dedicated to the 60th Birthday of Prof. Victor A. Eremeyev*, pages 211–234. Springer.

Forest, S. and Guéninchault, N. (2013). Inspection of free energy functions in gradient crystal plasticity. *Acta Mechanica Sinica*, 29:763–772.

Forest, S., Mayeur, J. R., and McDowell, D. L. (2018). Micromorphic crystal plasticity. In Voyiadjis, G. Z., editor, *Handbook of Nonlocal Continuum Mechanics for Materials and Structures*, pages 1–44. Springer International Publishing.

Forest, S. and Sievert, R. (2003). Elastoviscoplastic constitutive frameworks for generalized continua. *Acta Mechanica*, 160:71–111.

Fressengeas, C., Taupin, V., and Capolungo, L. (2011). An elasto-plastic theory of dislocation and disclination fields. *International Journal of Solids and Structures*, 48(25-26):3499–3509.

Gao, J. and Thompson, R. (1996). Real time-temperature models for monte carlo simulations of normal grain growth. *Acta materialia*, 44(11):4565–4570.

Gauthier, R. and Jahsman, W. (1975). A quest for micropolar elastic constants. *Journal of Applied Mechanics*.

Gérard, C., Bacroix, B., Bornert, M., Cailletaud, G., Crépin, J., and Leclercq, S. (2009). Hardening description for FCC materials under complex loading paths. *Computational Materials Science*, 45:751 – 755.

Ghiglione, F. and Forest, S. (2022). On the torsion of isotropic elastoplastic Cosserat circular cylinders. *Journal of Micromechanics and Molecular Physics*, 6:1–14.

Giga, Y., Okamoto, J., and Uesaka, M. (2023). A finer singular limit of a single-well modica–mortola functional and its applications to the kobayashi–warren–carter energy. *Advances in Calculus of Variations*, 16(1):163–182.

Godio, M., Stefanou, I., Sab, K., and Sulem, J. (2014). Cosserat elastoplastic finite elements for masonry structures. *Key Engineering Materials*, 624:131–138.

Gottstein, G. and Shvindlerman, L. S. (2009). *Grain boundary migration in metals: thermodynamics, kinetics, applications*. CRC press.

Gourdet, S. and Montheillet, F. (2000). An experimental study of the recrystallization mechanism during hot deformation of aluminium. *Materials Science and Engineering: A*, 283:274–288.

Grammenoudis, P. and Tsakmakis, C. (2005). Predictions of microtorsional experiments by micropolar plasticity. *Proceedings of the Royal Society A: Mathematical, Physical and Engineering Sciences*, 461(2053):189–205.

Grammenoudis, P. and Tsakmakis, C. (2009). Isotropic hardening in micropolar plasticity. *Archive of Applied Mechanics*, 79(4):323–334.

Gruber, J., George, D. C., Kuprat, A. P., Rohrer, G. S., and Rollett, A. D. (2005). Effect of anisotropic grain boundary properties on grain boundary plane distributions during grain growth. *Scripta materialia*, 53(3):351–355.

Günther, W. (1958). Zur statik und kinematik des cosseratschen kontinuums. *Abh. Braunschweig. Wiss. Ges*, 10(213):1.

Gurtin, M. (1996). Generalized Ginzburg–Landau and Cahn–Hilliard equations based on a microforce balance. *Physica D*, 92:178–192.

Gurtin, M. (2003). On a framework for small–deformation viscoplasticity: free energy, microforces, strain gradients. *International Journal of Plasticity*, 19:47–90.

Gurtin, M. and Anand, L. (2009). Thermodynamics applied to gradient theories involving the accumulated plastic strain: The theories of Aifantis and Fleck & Hutchinson and their generalization. *Journal of the Mechanics and Physics of Solids*, 57:405–421.

Hallberg, H. (2011). Approaches to modeling of recrystallization. *Metals*, 1(1):16–48.

Hallberg, H. (2013). A modified level set approach to 2d modeling of dynamic recrystallization. *Modelling and Simulation in Materials Science and Engineering*, 21(8):085012.

Hallberg, H. (2014). Influence of anisotropic grain boundary properties on the evolution of grain boundary character distribution during grain growth—a 2d level set study. *Modelling and Simulation in Materials Science and Engineering*, 22(8):085005.

Hallberg, H. and Bulatov, V. V. (2019). Modeling of grain growth under fully anisotropic grain boundary energy. *Modelling and Simulation in Materials Science and Engineering*, 27(4):045002.

Hallberg, H. and Ristinmaa, M. (2013). Microstructure evolution influenced by dislocation density gradients modeled in a reaction–diffusion system. *Computational Materials Science*, 67:373–383.

Han, J., Thomas, S. L., and Srolovitz, D. J. (2018). Grain-boundary kinetics: A unified approach. *Progress in Materials Science*, 98:386–476.

Hasson, G. and Goux, C. (1971). Interfacial energies of tilt boundaries in aluminium. experimental and theoretical determination. *Scripta metallurgica*, 5(10):889–894.

He, J. and Admal, N. (2021). Polycrystal plasticity with grain boundary evolution: a numerically efficient dislocation-based diffuse-interface model. *Modelling and Simulation in Materials Science and Engineering*, 30:025006.

Herring, C. and Kingston, W. (1951). The physics of powder metallurgy. *WE Kingston, Edition: McGraw Hill, New York*.

Hesselbarth, H. W. and Göbel, I. (1991). Simulation of recrystallization by cellular automata. *Acta Metallurgica et Materialia*, 39(9):2135–2143.

Hirth, J. and Lothe, J. (1982). *Theory of Dislocations*. Wiley Intersciences.

Hirth, J. P., Hirth, G., and Wang, J. (2020). Disclinations and disconnections in minerals and metals. *Proceedings of the National Academy of Sciences*, 117(1):196–204.

Holm, E. A., Miodownik, M. A., and Rollett, A. D. (2003). On abnormal subgrain growth and the origin of recrystallization nuclei. *Acta Materialia*, 51(9):2701–2716.

Huang, Y. and Humphreys, F. (2000). Subgrain growth and low angle boundary mobility in aluminium crystals of orientation $\{110\}<001$. *Acta materialia*, 48(8):2017–2030.

Huang, Y., Humphreys, F., and Ferry, M. (2000). The annealing behaviour of deformed cube-oriented aluminium single crystals. *Acta Materialia*, 48(10):2543–2556.

Humphreys, F. (1997). A unified theory of recovery, recrystallization and grain growth, based on the stability and growth of cellular microstructures–i. the basic model. *Acta materialia*, 45(10):4231–4240.

Humphreys, J. F. (2004). Nucleation in recrystallization. In *Materials Science Forum*, volume 467, pages 107–116. Trans Tech Publ.

Hurley, P. and Humphreys, F. (2003). Modelling the recrystallization of single-phase aluminium. *Acta materialia*, 51(13):3779–3793.

Ieşan, D. (1971). Torsion of micropolar elastic beams. *International Journal of Engineering Science*, 9(11):1047–1060.

Iesan, D. (2013). Deformation of chiral rods in the strain gradient theory of thermoelasticity. *European Journal of Mechanics - A/Solids*, 37:351 – 360.

Janssens, K. G. F., Raabe, D., Kozeschnik, E., Miodownik, M. A., and Nestler, B. (2007). *Computational materials engineering: an introduction to microstructure evolution*. Academic Press.

Jensen, D. J. (1992). Modelling of microstructure development during recrystallization. *Scripta metallurgica et materialia*, 27(11):1551–1556.

Johnson, W. and Mehl, R. (1939). Reaction kinetics in processes of nucleation and growth. *Trans. Metall. Soc. AIME*, 135:416–442.

Kafadar, C. and Eringen, A. (1971). Micropolar media: I the classical theory. *Int. J. Engng Sci.*, 9:271–305.

Kaiser, T., Forest, S., and Menzel, A. (2021). A finite element implementation of the stress gradient theory. *Meccanica*, 56:1109–1128.

Kaplunov, J. and Lippmann, H. (1995). Elastic-plastic torsion of a Cosserat-type rod. *Acta mechanica*, 113(1):53–62.

Kassner, M. and Barrabes, S. (2005). New developments in geometric dynamic recrystallization. *Materials Science and Engineering: A*, 410-411:152–155.

Kassner, M. E. (1989). Large-strain deformation of aluminum single crystals at elevated temperature as a test of the geometric-dynamic-recrystallization concept. *Metallurgical Transactions A*, 20:2182–2185.

Kawasaki, K., Nagai, T., and Nakashima, K. (1989). Vertex models for two-dimensional grain growth. *Philosophical Magazine B*, 60(3):399–421.

Kim, B. and Eringen, A. (1973). Stress distribution around an elliptic hole in an infinite micropolar elastic plate. *Letters in Applied and Engineering Sciences*, 1:381–390.

Kobayashi, R. and Giga, Y. (1999). Equations with singular diffusivity. *Journal of statistical physics*, 95(5):1187–1220.

Kobayashi, R., Warren, J. A., and Carter, W. C. (2000). A continuum model of grain boundaries. *Physica D: Nonlinear Phenomena*, 140(1-2):141–150.

Kolmogorov, A. N. (1937). On the statistics of the crystallization process in metals. *Bull Akad Sci. USSR, Class Sci, Math Nat*, 1:355–359.

Korbel, A. and Martin, P. (1986). Microscopic versus macroscopic aspect of shear bands deformation. *Acta Metallurgica*, 34(10):1905–1909.

Kröner, E. (1963). On the physical reality of torque stresses in continuum mechanics. *Int. J. Engng. Sci.*, 1:261–278.

Kunin, I. A. (1968). The theory of elastic media with microstructure and the theory of dislocations. In *Mechanics of Generalized Continua: Proceedings of the IUTAM-Symposium on The Generalized Cosserat Continuum and the Continuum Theory of Dislocations with Applications, Freudenstadt and Stuttgart (Germany) 1967*, pages 321–329. Springer.

Kunin, I. A. (1982). *Elastic media with microstructure I: One-dimensional models*. Springer.

Kunin, I. A. (1983). *Elastic media with microstructure II: Three-dimensional models*. Springer.

Kuprat, A. (2000). Modeling microstructure evolution using gradient-weighted moving finite elements. *Siam Journal on Scientific Computing*, 22(2):535–560.

Kuprat, A., George, D., Straub, G., and Demirel, M. C. (2003). Modeling microstructure evolution in three dimensions with grain3d and lagrit. *Computational Materials Science*, 28(2):199–208.

Lakes, R. (1987). Foam structures with a negative Poisson's ratio. *Science*, 235:1038–1040.

Lazopoulos, K. and Lazopoulos, A. (2012). On the torsion problem of strain gradient elastic bars. *Mechanics Research Communications*, 45:42–47.

Li, Y., Hu, S., Barker, E., Overman, N., Whalen, S., and Mathaudhu, S. (2020). Effect of grain structure and strain rate on dynamic recrystallization and deformation behavior: A phase field-crystal plasticity model. *Computational Materials Science*, 180:109707.

Lippmann, H. (1969). Eine Cosserat-Theorie des plastischen Fließens. *Acta Mechanica*, 8:255–284.

Lippmann, H. (1995). Cosserat plasticity and plastic spin. *Appl. Mech. Rev.*, 48:753–762.

Liu, P. and Lusk, M. T. (2002). Parametric links among monte carlo, phase-field, and sharp-interface models of interfacial motion. *Physical Review E*, 66(6):061603.

Liu, Y., Baudin, T., and Penelle, R. (1996). Simulation of normal grain growth by cellular automata. *Scripta Materialia*, 34(11).

Lobkovsky, A. E. and Warren, J. A. (2001). Sharp interface limit of a phase-field model of crystal grains. *Physical Review E*, 63(5):051605.

Luan, Q., Lee, J., Zheng, J.-H., Hopper, C., and Jiang, J. (2020). Combining microstructural characterization with crystal plasticity and phase-field modelling for the study of static recrystallization in pure aluminium. *Computational Materials Science*, 173:109419.

Mahin, K. W., Hanson, K., and Morris Jr, J. (1980). Comparative analysis of the cellular and johnson-mehl microstructures through computer simulation. *Acta Metallurgica*, 28(4):443–453.

Maire, L., Fausty, J., Bernacki, M., Bozzolo, N., De Micheli, P., and Moussa, C. (2018). A new topological approach for the mean field modeling of dynamic recrystallization. *Materials & Design*, 146:194–207.

Masiani, R. and Trovalusci, P. (1996). Cosserat and cauchy materials as continuum models of brick masonry. *Meccanica*, 31:421–432.

Mason, J. (2015). Grain boundary energy and curvature in monte carlo and cellular automata simulations of grain boundary motion. *Acta materialia*, 94:162–171.

Mason, J., Lind, J., Li, S., Reed, B., and Kumar, M. (2015). Kinetics and anisotropy of the monte carlo model of grain growth. *Acta Materialia*, 82:155–166.

Mayeur, J. and McDowell, D. (2014). A comparison of gurtin type and micropolar theories of generalized single crystal plasticity. *International Journal of Plasticity*, 57:29–51.

Mayeur, J., McDowell, D., and Bammann, D. (2011). Dislocation–based micropolar single crystal plasticity: Comparison of multi– and single criterion theories. *Journal of the Mechanics and Physics of Solids*, 59:398–422.

Mayeur, J. R., McDowell, D. L., and Forest, S. (2018). Micropolar crystal plasticity. In Voyiadjis, G. Z., editor, *Handbook of Nonlocal Continuum Mechanics for Materials and Structures*, pages 1–47. Springer International Publishing.

McClintock, F., André, P., Schwerdt, K., and Stoeckly, R. (1958). Interface couples in crystals. *Nature*, 4636:652–653.

Mellbin, Y., Hallberg, H., and Ristinmaa, M. (2015). A combined crystal plasticity and graph-based vertex model of dynamic recrystallization at large deformations. *Modelling and Simulation in Materials Science and Engineering*, 23(4):045011.

Mesarovic, S., Forest, S., and Zbib Editors, H. (2019). *Mesoscale Models. From Micro-Physics to Macro-Interpretation*. Springer, CISM International Centre for Mechanical Sciences, vol. 587, ISBN: 978-3-319-94186-8, 344 pages.

Moelans, N., Blanpain, B., and Wollants, P. (2008). An introduction to phase-field modeling of microstructure evolution. *Calphad*, 32(2):268–294.

Montheillet, F. (2009). Métallurgie en mise en forme à chaud.

Montheillet, F., Cohen, M., and Jonas, J. (1984). Axial stresses and texture development during the torsion testing of Al, Cu and α-Fe. *Acta Metallurgica*, 32:2077–2089.

Montheillet, F., Lurdos, O., and Damamme, G. (2009). A grain scale approach for modeling steady-state discontinuous dynamic recrystallization. *Acta Materialia*, 57(5):1602–1612.

Mühlhaus, H.-B. and Vardoulakis, I. (1987). The thickness of shear bands in granular materials. *Geotechnique*, 37(3):271–283.

Muramatsu, M., Aoyagi, Y., Tadano, Y., and Shizawa, K. (2014). Phase-field simulation of static recrystallization considering nucleation from subgrains and nucleus growth with incubation period. *Computational materials science*, 87:112–122.

Neuber, H. (1966). Ueber Probleme der Spannungskonzentration im Cosserat-Koerper. *Acta Mechanica*, 2:48–69.

Neuber, H. (1968). On the effect of stress concentration in Cosserat continua. In Kröner, E., editor, *Mechanics of Generalized Continua*, pages 109–113, Berlin, Heidelberg. Springer Berlin Heidelberg.

Nouailhas, D. and Cailletaud, G. (1995). Tension-torsion behavior of single-crystal superalloys - Experiment and finite-element analysis. *Int. J. Plasticity*, 8:451–470.

Nowacki, W. (1986). *Theory of asymmetric elasticity*. Pergamon.

Ohno, N. and Okumura, D. (2007). Higher–order stress and grain size effects due to self–energy of geometrically necessary dislocations. *Journal of the Mechanics and Physics of Solids*, 55:1879–1898.

Onck, P. (2002). Cosserat modeling of cellular solids. *Comptes Rendus Mecanique*, 330:717–722.

Phalke, V., Kaiser, T., Scherer, J. M., and Forest, S. (2021). Modeling size effects in microwire torsion: A comparison between a lagrange multiplier-based and a CurlF^p gradient crystal plasticity model. *European Journal of Mechanics A/Solids*, 94:104550.

Piękoś, K., Tarasiuk, J., Wierzbanowski, K., and Bacroix, B. (2008). Generalized vertex model of recrystallization–application to polycrystalline copper. *Computational materials science*, 42(4):584–594.

Plapp, M. (2011). Remarks on some open problems in phase-field modelling of solidification. *Philosophical Magazine*, 91(1):25–44.

Priester, L. (2012). *Grain boundaries: from theory to engineering*, volume 172. Springer Science & Business Media.

Quey, R., Dawson, P., and Barbe, F. (2011). Large-scale 3d random polycrystals for the finite element method: Generation, meshing and remeshing. *Computer Methods in Applied Mechanics and Engineering*, 200(17-20):1729–1745.

Raabe, D. (1998). Discrete mesoscale simulation of recrystallization microstructure and texture using a stochastic cellular automation approach. In *Materials science forum*, volume 273, pages 169–174. Trans Tech Publ.

Raabe, D. (2000). Scaling monte carlo kinetics of the potts model using rate theory. *Acta Materialia*, 48(7):1617–1628.

Raabe, D. (2014). Recovery and recrystallization: phenomena, physics, models, simulation. *Physical metallurgy*, pages 2291–2397.

Ratanaphan, S., Olmsted, D. L., Bulatov, V. V., Holm, E. A., Rollett, A. D., and Rohrer, G. S. (2015). Grain boundary energies in body-centered cubic metals. *Acta Materialia*, 88:346–354.

Rattez, H., Stefanou, I., Sulem, J., Veveakis, M., and Poulet, T. (2018). Numerical analysis of strain localization in rocks with thermo-hydro-mechanical couplings using cosserat continuum. *Rock Mechanics and Rock Engineering*, 51:3295–3311.

Read, W. (1953). *Dislocations in crystals*. McGraw–Hill, New York.

Read, W. T. and Shockley, W. (1950). Dislocation models of crystal grain boundaries. *Physical review*, 78(3):275.

Reddy, G. V. K. and Venkatasubramanian, N. K. (1976). Saint-Venant's problem for a micropolar elastic circular cylinder. *International Journal of Engineering Science*, 14:1047–1057.

Rios, P. R., Siciliano Jr, F., Sandim, H. R. Z., Plaut, R. L., and Padilha, A. F. (2005). Nucleation and growth during recrystallization. *Materials Research*, 8(3):225–238.

Rohrer, G. S. (2011). Grain boundary energy anisotropy: a review. *Journal of materials science*, 46:5881–5895.

Rollett, A. (1997). Overview of modeling and simulation of recrystallization. *Progress in materials science*, 42(1-4):79–99.

Rollett, A. and Raabe, D. (2001). A hybrid model for mesoscopic simulation of recrystallization. *Computational Materials Science*, 21(1):69–78.

Rollett, A., Rohrer, G. S., and Humphreys, J. (2017). *Recrystallization and Related Annealing Phenomena*. Elsevier.

Russo, R. (2022). *Cosserat thermo-mechanics under finite deformations : theory and finite element implementation*. Theses, Université Paris sciences et lettres ; Universidad del País Vasco.

Russo, R., Girot Mata, F. A., and Forest, S. (2020). Thermomechanics of cosserat medium: Modeling adiabatic shear bands in metals. *Continuum Mechanics and Thermodynamics*.

Rys, M., Stupkiewicz, S., and Petryk, H. (2022). Micropolar regularization of crystal plasticity with the gradient-enhanced incremental hardening law. *International Journal of Plasticity*, 156:103355.

Sakout, S., Weisz-Patrault, D., and Ehrlacher, A. (2020). Energetic upscaling strategy for grain growth. i: Fast mesoscopic model based on dissipation. *Acta Materialia*, 196:261–279.

Sansour, C. (1998). A theory of the elastic–viscoplastic Cosserat continuum. *Archives of Mechanics*, 50:577–597.

Sarrazola, D. R., Maire, L., Moussa, C., Bozzolo, N., Muñoz, D. P., and Bernacki, M. (2020a). Full field modeling of dynamic recrystallization in a cpfem context–application to 304l steel. *Computational Materials Science*, 184:109892.

Sarrazola, D. R., Muñoz, D. P., and Bernacki, M. (2020b). A new numerical framework for the full field modeling of dynamic recrystallization in a cpfem context. *Computational Materials Science*, 179:109645.

Sawczuk, A. (1967). On yielding of Cosserat continua. *Archiwum Mechaniki Stosowanej*, 19(3):471.

Schaefer, H. (1967). Das cosserat kontinuum. *ZAMM-Journal of Applied Mathematics and Mechanics/Zeitschrift für Angewandte Mathematik und Mechanik*, 47(8):485–498.

Scherer, J. M., Phalke, V., Besson, J., Forest, S., Hure, J., and Tanguy, B. (2020). Lagrange multiplier based vs micromorphic gradient-enhanced rate-(in)dependent crystal plasticity modelling and simulation. *Computer Methods in Applied Mechanics and Engineering*, 372:113426.

Scholtes, B., Boulais-Sinou, R., Settefrati, A., Muñoz, D. P., Poitrault, I., Montouchet, A., Bozzolo, N., and Bernacki, M. (2016). 3d level set modeling of static recrystallization considering stored energy fields. *Computational Materials Science*, 122:57–71.

Shakoor, M., Scholtes, B., Bouchard, P.-O., and Bernacki, M. (2015). An efficient and parallel level set reinitialization method–application to micromechanics and microstructural evolutions. *Applied Mathematical Modelling*, 39(23-24):7291–7302.

Sievert, R. (1995). Zur Zerlegung der Verformungsmaße des Cosserat-Kontinuums bei großen inelastischen Deformationen. *Z. Angew. Math. Mech.*, 75:205–206.

Sitko, M., Chao, Q., Wang, J., Perzynski, K., Muszka, K., and Madej, L. (2020). A parallel version of the cellular automata static recrystallization model dedicated for high performance computing platforms–development and verification. *Computational Materials Science*, 172:109283.

Smith, A. (1967). Deformations of micropolar elastic solids. *International Journal of Engineering Science*, 5(8):637–651.

Stefanou, I., Sulem, J., and Rattez, H. (2017). Cosserat approach to localization in geomaterials. *Handbook of nonlocal continuum mechanics for materials and structures*, 730.

Stefanou, I., Sulem, J., and Vardoulakis, I. (2008). Three-dimensional cosserat homogenization of masonry structures: elasticity. *Acta Geotechnica*, 3:71–83.

Steinbach, I. (2009). Phase field models in materials science. *Modelling and Simulation in Materials Science and Engineering*, 17:1–31.

Steinbach, I. and Apel, M. (2006). Multi phase field model for solid state transformation with elastic strain. *Physica D*, 217:153–160.

Steinbach, I. and Pezzolla, F. (1999). A generalized field method for multiphase transformations using interface fields. *Physica D: Nonlinear Phenomena*, 134(4):385–393.

Sulem, J. and Mühlhaus, H.-B. (1997). A continuum model for periodic two-dimensional block structures. *Mechanics of Cohesive-frictional Materials: An International Journal on Experiments, Modelling and Computation of Materials and Structures*, 2(1):31–46.

Sulem, J., Stefanou, I., and Veveakis, E. (2011). Stability analysis of undrained adiabatic shearing of a rock layer with cosserat microstructure. *Granular Matter*, 13:261–268.

Sun, X.-Y., Fressengeas, C., Taupin, V., Cordier, P., and Combe, N. (2018). Disconnections, dislocations and generalized disclinations in grain boundary ledges. *International Journal of Plasticity*, 104:134–146.

Suwa, Y., Saito, Y., and Onodera, H. (2008). Phase-field simulation of recrystallization based on the unified subgrain growth theory. *Computational materials science*, 44(2):286–295.

Suwa, Y., Tomita, M., Tanaka, Y., and Ushioda, K. (2021). Phase-field simulation of recrystallization in cold rolling and subsequent annealing of pure iron exploiting ebsd data of cold-rolled sheet. *ISIJ International*, 61(1):350–360.

Takaki, T., Hirouchi, T., Hisakuni, Y., Yamanaka, A., and Tomita, Y. (2008a). Multi-phase-field model to simulate microstructure evolutions during dynamic recrystallization. *Materials transactions*, 49(11):2559–2565.

Takaki, T., Hisakuni, Y., Hirouchi, T., Yamanaka, A., and Tomita, Y. (2009). Multi-phase-field simulations for dynamic recrystallization. *Computational Materials Science*, 45(4):881–888.

Takaki, T. and Tomita, Y. (2010). Static recrystallization simulations starting from predicted deformation microstructure by coupling multi-phase-field method and finite element method based on crystal plasticity. *International Journal of Mechanical Sciences*, 52(2):320–328.

Takaki, T., Yamanaka, A., Higa, Y., and Tomita, Y. (2008b). Phase-field model during static recrystallization based on crystal-plasticity theory. *Journal of Computer–Aided Materials Design*, 14:75–84.

Taliercio, A. and Veber, D. (2016). Torsion of elastic anisotropic micropolar cylindrical bars. *European Journal of Mechanics-A/Solids*, 55:45–56.

Taupin, V., Capolungo, L., Fressengeas, C., Das, A., and Upadhyay, M. (2013). Grain boundary modeling using an elasto-plastic theory of dislocation and disclination. *Journal of the Mechanics and Physics of Solids*, 61:370–384.

Telley, H., Liebling, T. M., Mocellin, A., and Righetti, F. (1992). Simulating and modelling grain growth as the motion of a weighted voronoi diagram. In *Materials Science Forum*, volume 94, pages 301–306. Trans Tech Publ.

Trovalusci, P. and Masiani, R. (2003). Non-linear micropolar and classical continua for anisotropic discontinuous materials. *International Journal of Solids and Structures*, 40(5):1281–1297.

Trovalusci, P., Ostoja-Starzewski, M., De Bellis, M. L., and Murrali, A. (2015). Scale-dependent homogenization of random composites as micropolar continua. *European Journal of Mechanics-A/Solids*, 49:396–407.

Trovalusci, P. and Pau, A. (2014). Derivation of microstructured continua from lattice systems via principle of virtual works: the case of masonry-like materials as micropolar, second gradient and classical continua. *Acta Mechanica*, 225(1):157–177.

Vandermeer, R., Jensen, D. J., and Woldt, E. (1997). Grain boundary mobility during recrystallization of copper. *Metallurgical and materials transactions A*, 28(3):749–754.

Viswanathan, R. and Bauer, C. (1973). Kinetics of grain boundary migration in copper bicrystals with [001] rotation axes. *Acta Metallurgica*, 21(8):1099–1109.

Voigt, W. (1887). *Theoretische studien über die elasticitätsverhältnisse der krystalle*. Königliche Gesellschaft der Wissenschaften zu Göttingen.

Voigt, W. (1900). L'état actuel de nos connaissances sur l'élasticité des cristaux. In *Rapports présentés au Congrès international de Physique*, pages 277–347.

Voigt, W. (1910). *Lehrbuch der kristallphysik:(mit ausschluss der kristalloptik)*, volume 34. BG Teubner.

Wang, W., Balint, D. S., Shirzadi, A. A., Wang, Y., Lee, J., Aucott, L., and Jiang, J. (2023). Imparted benefits on mechanical properties by achieving grain boundary migration across voids. *Acta Materialia*, page 119103.

Warren, J. A., Kobayashi, R., Lobkovsky, A. E., and Carter, W. C. (2003). Extending phase field models of solidification to polycrystalline materials. *Acta Materialia*, 51(20):6035–6058.

Wei, H., Knapp, G., Mukherjee, T., and DebRoy, T. (2019). Three-dimensional grain growth during multi-layer printing of a nickel-based alloy inconel 718. *Additive Manufacturing*, 25:448–459.

Winning, M., Gottstein, G., and Shvindlerman, L. (2001). Stress induced grain boundary motion. *Acta materialia*, 49(2):211–219.

Woldt, E. and Jensen, D. J. (1995). Recrystallization kinetics in copper: Comparison between techniques. *Metallurgical and Materials Transactions A*, 26:1717–1724.

Wolf, D. (1989). A Read-Shockley model for high-angle grain boundaries. *Scripta metallurgica*, 23(10):1713–1718.

Wolf, D. (1990). Structure-energy correlation for grain boundaries in fcc metals–iii. symmetrical tilt boundaries. *Acta metallurgica et materialia*, 38(5):781–790.

Wulfinghoff, S., Forest, S., and Böhlke, T. (2015). Strain gradient plasticity modeling of the cyclic behavior of laminate microstructures. *Journal of the Mechanics and Physics of Solids*, 79:1–20.

Yang, J. and Lakes, R. (1981). Transient study of couple stress effects in compact bone : torsion. *J. of Biomech. Engng*, 103:275–279.

Z-set (2022). Non-linear material & structure analysis suite.

Zhang, C., Yadav, V., Moelans, N., Jensen, D. J., and Yu, T. (2022). The effect of voids on boundary migration during recrystallization in additive manufactured samples—a phase field study. *Scripta Materialia*, 214:114675.

Zurob, H., Brechet, Y., and Dunlop, J. (2006). Quantitative criterion for recrystallization nucleation in single-phase alloys: Prediction of critical strains and incubation times. *Acta materialia*, 54(15):3983–3990.

RÉSUMÉ

Les traitements thermomécaniques des matériaux cristallins provoquent d'importants changements microstructuraux qu'il convient de maitriser pour contrôler les propriétés macroscopiques qui en résultent. En particulier, la recristallisation, i.e la germination et croissance de grains possédant une faible densité de dislocations, est d'intérêt industriel pour l'optimisation de microstructures lors la mise en forme des métaux. Malgré son importance, la modélisation de ce phénomène reste parcellaire. En effet, si de nombreux modèles ont été développés afin de reproduire efficacement la phase de croissance (méthodes de Monte-Carlo Potts, automates cellulaires, level-sets, champs de phase...), la simulation de la germination passe traditionnellement par l'introduction ad hoc de nouveaux grains sphériques ou circulaires en lien avec une valeur critique de déformation, contrainte ou densité de dislocations. Il convient donc de développer des modèles rendant compte spontanément de l'apparition de nouveaux grains. Lors des procédés thermomécaniques, la déformation (visco)plastique du matériau peut engendrer une réorientation importante du réseau cristallin et une distribution hétérogène d'orientations peut apparaître au sein de grains initialement orientés de façon homogène. À l'échelle mésoscopique, ces phénomènes sont bien pris en compte par des modèles de plasticité cristalline. Une description enrichie de la matière, telle que celle des milieux de Cosserat, permet en outre de prendre en compte des effets de taille. Dans cette théorie, des degrés de liberté additionnels de microrotations sont introduits et peuvent être identifiés aux rotations du réseau cristallins par le biais de contraintes internes. Nous proposons de nouvelles solutions analytiques aux problèmes de la torsion d'un cylindre en elastoplasticité isotrope et du cisaillement d'un monocristal. Pour ce dernier, différentes formulations du potentiel d'énergie libre explorant diverses dépendances vis-à-vis du tenseur de courbure-torsion sont étudiées. Parmi les modèles de croissance de grains, seule l'approche à deux champs de phases proposée par Kobayashi-Warren-Carter (KWC) peut modéliser un gradient d'orientation intragranulaire induit par la déformation. Les modèles à champs de phase s'appuyant sur une formulation thermodynamique, le couplage avec la mécanique via le potentiel d'énergie libre est particulièrement aisé. Le modèle mésoscopique en champs complets utilisé dans cette thèse, développé par Ask et al., combine ainsi la plasticité cristalline des milieux de Cosserat et le modèle à champs de phase de croissance de grains de KWC. Une des particularités du modèle étudié est d'ajouter à la déformation (visco)plastique du grain un comportement inélastique de relaxation du joint de grain. L'influence du choix de la fonction de relaxation aux joints de grain sur la formation et le mouvement de ceux-ci est ainsi étudiée. En particulier, il est montré que la présence d'une contrainte seuil dans la fonction de relaxation peut ralentir la formation et le mouvement des joints. Nous montrons également par des simulations éléments finis que les modèles de type KWC peuvent simuler de façon spontanée de la germination de nouveaux (sous)grains en raison de la présence de gradients d'orientation cristalline. Un calcul tridimensionnel de torsion d'une barre monocristalline de cuivre à section circulaire d'axe [111] montre ainsi la formation de sous-grains le long de la barre en raison du développement d'un gradient d'orientation du réseau dû au chargement. Cette observation est confortée qualitativement par une comparaison aux résultats expérimentaux sur la torsion d'un monocristal d'aluminium obtenus par M.E. Kassner.

MOTS CLÉS

Plasticité cristalline, Champs de phase, Mécanique des milieux de Cosserat, Migration de joint de grains, Recristallisation, éléments finis

ABSTRACT

Thermomechanical treatment of crystalline materials induces significant microstructural changes that must be understood in order to control the resulting macroscopic properties. In particular, recrystallization, i.e. the nucleation and growth of grains with low dislocation density, is of industrial interest for microstructure optimization during metal forming. Despite its importance, the modelling of this phenomenon remains fragmentary. While numerous models have been developed to efficiently simulate the growth phase (Monte-Carlo Potts, cellular automata, level sets, phase-fields, etc.), the simulation of nucleation traditionally involves the ad hoc introduction of new spherical or circular grains linked to a critical value of strain, stress or dislocation density. It is therefore necessary to develop models that spontaneously account for the appearance of new grains. During thermomechanical processes, the (visco)plastic deformation of the material can lead to a significant reorientation of the crystal lattice and a heterogeneous distribution of orientations can appear within grains that are initially homogeneously oriented. At the mesoscopic scale, these phenomena are well accounted for by models of crystal plasticity. An enriched description of matter, such as that of Cosserat continua, also allows size effects to be taken into account. In this theory, additional degrees of freedom are introduced in the form of microrotations, which can be identified with the rotations of the crystal lattice by means of internal constraints. We propose new analytical solutions to the problems of torsion of an isotropic elastic-plastic cylinder and shear of a single crystal. For the latter, different formulations of the free energy potential exploring various dependencies on the curvature-torsion tensor are studied. Among the available grain growth models, only the two-phase-field approach proposed by Kobayashi-Warren-Carter (KWC) can model an intragranular orientation gradient induced by deformation. Since phase-field models are based on a thermodynamic formulation, coupling to mechanics via the free energy potential is particularly straightforward. The full-field mesoscopic model used in this work, developed by Ask et al., thus combines Cosserat crystal plasticity and the KWC phase-field model of grain growth. One of the features of the model studied is the inclusion of inelastic relaxation behaviour at the grain boundary in addition to the (visco)plastic deformation of the grain. Therefore, the choice of the relaxation function on the formation and movement of grain boundaries is investigated. In particular, the existence of a threshold stress in the relaxation function is shown to potentially hinder the formation and movement of grain boundaries. We also show through finite element simulations that KWC-type models can spontaneously simulate the nucleation of new (sub)grains due to the presence of crystal orientation gradients. A three-dimensional torsional calculation of a single-crystal copper rod with a circular cross section of axis [111] shows the nucleation of subgrains along the rod due to lattice orientation gradients induced by mechanical loading. This observation is qualitatively confirmed by comparison with experimental results on the torsion of an aluminium single crystal obtained by M.E. Kassner.

KEYWORDS

Crystal plasticity, Phase field, Cosserat mechanics, Grain boundary migration, Recrystallization, Finite element method